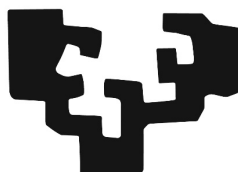


DRESSING ENZYMES WITH TAILORED
NANOGELES AS A VERSATILE APPROACH
FOR THE DEVELOPMENT OF
HETEROGENEOUS BIOCATALYSTS

eman ta zabal zazu



Universidad
del País Vasco

Euskal Herriko
Unibertsitatea

Andoni Rodríguez López de Abetxuko

2022

This dissertation has been performed under the supervision of

Prof. Dr. Mato Knez

Dr. Ana Beloqui Elizazu

The tutor of this dissertation is

Prof. Dr. Jose M. Pitarke de la Torre

Keywords: Single Enzyme Nanogels, Heterogeneous Biocatalysts, Chemoenzymatic Nanomaterials.

An electronic version of this thesis is available at:

<https://www.nanogune.eu/en/publications/phd-theses>.

RESUMEN

Algunas reacciones químicas se producen espontáneamente en condiciones ambientales. Sin embargo, la mayoría de ellas deben ser catalizadas para alcanzar una velocidad significativa. Los sistemas biológicos cuentan con biomoléculas extraordinarias, las enzimas, capaces de acelerar reacciones químicas hasta 10^8 veces con gran especificidad, convirtiéndose así en los principales motores de la vida. Por ejemplo, una bacteria *Escherichia coli* en fase de crecimiento, dispone de más de 1.000 enzimas realizando aproximadamente 2.200 reacciones metabólicas para mantener su metabolismo.

Las enzimas presentan una excelente capacidad catalítica y una amplia selectividad química, permitiendo así una síntesis eficaz de compuestos enantioméricamente puros. A diferencia de los catalizadores químicos, las enzimas realizan su función en condiciones fisiológicas, es decir, a pH y temperaturas moderadas. Además, son biodegradables y respetuosas con el medio ambiente. Estas excepcionales cualidades son el resultado de sus complejas estructuras, formadas a través de cadenas polipeptídicas y de alguna molécula auxiliar (cofactores). Sin embargo, las condiciones de trabajo a las que se enfrentan las enzimas en aplicaciones tecnológicas distan mucho de aquéllas para las que fueron concebidas originalmente, lo cual puede comprometer el equilibrio termodinámico de la enzima y provocar su inactivación.

En las últimas décadas, con el fin de aprovechar el excelente potencial de las enzimas, se han adoptado enfoques multidisciplinarios para mejorar su rendimiento en condiciones no fisiológicas. Estrategias como la ingeniería de proteínas, la modificación química o la inmovilización de proteínas están mejorando su vida útil y la eficacia en toda una serie de aplicaciones tecnológicas e industriales: la química fina,

biosensores, la producción de biocombustibles, el diagnóstico o las tecnologías biomédicas.

En concreto, la modificación química de las enzimas mediante el uso de nanogel enzimáticos, conocidos como *Single Enzyme Nanogels* (SENs), tiene como objetivo proteger la biomolécula en condiciones extremas. Los SENs son estructuras solubles de tipo *core-shell*, con una única enzima en el núcleo, protegida ésta por un hidrogel de muy pocos nanómetros de espesor. El nanogel genera un microambiente favorable al tiempo que mantiene la flexibilidad de la proteína necesaria para realizar la catálisis. Es importante destacar que el nanogel apenas influye en el transporte del sustrato, la cinética de la reacción y la descarga del producto. Las principales razones de la conservación del rendimiento catalítico de los *SENs* están probablemente relacionadas con la encapsulación individual de cada enzima y la porosidad/grosos programables del hidrogel, los cuales pueden ajustarse para minimizar los problemas de difusión.

Las enzimas inmovilizadas permanecen adheridas a materiales insolubles mientras que los sustratos y productos difunden entre las fases sólida y líquida. De este modo, las enzimas insolubles, denominadas biocatalizadores heterogéneos, presentan propiedades diferentes a las de las enzimas libres, como una mayor estabilidad y la posibilidad de ser reutilizadas de manera sencilla. Generalmente, las estrategias de inmovilización se dividen en tres grandes grupos: 1) la inmovilización en soportes prefabricados; 2) el atrapamiento de enzimas en materiales porosos; y 3) el entrecruzamiento de agregados enzimáticos, que no requieren de soporte. Sin embargo, la mayoría de los biocatalizadores heterogéneos actuales aún no son lo suficientemente estables y su reutilización es escasa, lo cual limita, en cierta medida, su aplicabilidad.

El objetivo principal de esta tesis doctoral es diseñar y desarrollar materiales biocatalíticos innovadores, que ayuden a simplificar, facilitar y ampliar el uso de las enzimas en nuestro día a día. Para lograr ese objetivo principal, se han planteado los

siguientes objetivos específicos: 1) la fabricación de los *SENs* y la modulación de sus propiedades mediante la modificación química del nanogel; 2) la formación de biocatalizadores heterogéneos de última generación empleando los *SENs*; y 3) la demostración de la utilidad de estos biocatalizadores heterogéneos en diferentes aplicaciones.

La formación de los agregados enzimáticos entrecruzados (*CLEAs*, por sus siglas en inglés) consiste en la precipitación de las enzimas y su posterior entrecruzamiento químico. De este modo, estos biocatalizadores heterogéneos evitan los caros soportes empleados en la inmovilización de enzimas, previniendo, además, la lixiviación enzimática. Sin embargo, la modificación estructural de la enzima disminuye la actividad de estos sistemas significativamente. En el primer capítulo experimental de esta tesis doctoral (**Chapter 4**), se ha desarrollado una nueva plataforma de inmovilización enzimática sin soporte para la fabricación de biomateriales catalíticos, denominados agregados enzimáticos metal-orgánicos (*MOEAs*, por sus siglas en inglés). Estos se sintetizan a través del entrecruzamiento no covalente de los *SENs* (funcionalizados con imidazol) guiado por cationes metálicos. De esta manera, se evita la pérdida de actividad enzimática, además de proveer el sistema con otras características beneficiosas.

El tamaño y la morfología de los *MOEAs* es variable, desde nanopartículas hasta estructuras macroscópicas muy estables en solución. La versatilidad estructural de los *MOEAs* se define tanto por la naturaleza del catión metálico utilizado para ensamblar los *SENs* como por los ratios catión:*SEN* utilizados en la síntesis. Es importante destacar la capacidad de los *MOEAs* de autoensamblarse en estructuras supramoleculares más complejas, es decir, capas finas. Como veremos, la caracterización de los *MOEAs* evidencia su excepcional integridad, estabilidad y reutilización. Finalmente, el uso de las enzimas glucosa oxidasa y β -Glucosidasa ha

facilitado la fabricación de un biosensor electroquímico de glucosa y el estudio de reacciones enzimáticas en cascada.

En el segundo capítulo experimental (**Chapter 5**) se ha desarrollado otra plataforma destinada a la síntesis de biocatalizadores heterogéneos, denominados nanoesponjas (*NS*). La formación de las *NS* se fundamenta en el atrapamiento de los *SENs* modificados con moléculas de imidazol dentro de una sal metálica de fosfato. La biomineralización es una estrategia *bottom-up*, en la que, en primera instancia, se forman puntos de nucleación para luego ensamblarse y evolucionar en estructuras jerárquicas más complejas. Las proteínas desempeñan un papel muy importante en el proceso de biomineralización, ya que controlan la formación, la morfología y la organización de la fase mineral. Este fenómeno ha atraído la atención de los investigadores para explorar y diseñar nuevos biomateriales catalíticos, por ejemplo, las nanoflores de proteínas (*NF*). Estas estructuras tridimensionales presentan una gran superficie específica beneficiosa en procesos catalíticos y están formadas exclusivamente por enzimas y fosfatos, generalmente de cobre.

En comparación con las *NF*, la estructuración de las *NS* mejora la conversión catalítica, la robustez del material y la estabilidad térmica. Esto se debe a la alta densidad de imidazol presente en la superficie de la proteína, lograda a través de la tecnología de los *SENs*. La presencia de imidazol es de gran transcendencia en este caso, ya que acelera el proceso de biomineralización. Es importante destacar la posibilidad de fabricar *NS* a partir de diversos cationes metálicos (mono-, di- y trivalentes) ampliando así su diversidad química y estructural. En este trabajo se ha empleado la peroxidasa de rábano (HRP) como enzima modelo.

El tercer capítulo experimental (**Chapter 6**) se centra en la fabricación de nanomateriales quimio-enzimáticos multifuncionales (*INRs*, por sus siglas en inglés) para la oxidación controlada de varias moléculas (compuestos aromáticos y cofactores). La combinación de enzimas y catalizadores químicos confinados en una

sola entidad es un campo de investigación en crecimiento. Esto se debe a que las reacciones consecutivas canalizadas pueden aumentar la selectividad y el rendimiento global del proceso, como ocurre en las células.

Estos *INRs* se sintetizan a partir de nanogel de glucosa oxidasa, que son posteriormente modificados con heminas, una protoporfirina de hierro con actividad peroxidasa. Las heminas se unen a los grupos imidazol del nanogel mediante coordinación, imitando el centro activo de algunas hemoproteínas y aumentando así su capacidad catalítica. El nanogel, además de ser un elemento protector de la enzima, sirve de soporte y cobijo para la hemina. Es importante destacar que las propiedades de los *SENs* pueden ser moduladas para activar su entrecruzamiento guiado por la hemina, dando lugar a biocatalizadores heterogéneos sin soportes fácilmente reutilizables. El diseño de los *INRs* ha sido optimizado para aumentar la eficiencia y la canalización del sustrato.

Los *INRs* tienen la capacidad de oxidar cofactores reducidos de nicotinamida naturales (NAD(P)H) y artificiales (BNAH). Estas nicotinamidas son cofactores especialmente importantes en la biosíntesis química, ya que el 90% de las oxidorreductasas son dependientes de ellos. Los cofactores, a diferencia de las enzimas, sufren reacciones químicas durante el proceso de catálisis, y deben ser regenerados debido a su elevado coste. Afortunadamente, con la síntesis química como objetivo, los *INRs* trabajan eficientemente junto a oxidorreductasas dependientes de NAD, siguiendo una estrategia basada en la inyección secuencial de glucosa. Este estudio ha descrito el primer ejemplo de nanomaterial químico-enzimático híbrido capaz de imitar eficientemente sistemas de regeneración de cofactores.

En el último capítulo experimental (**Chapter 7**), se ha incrementado la complejidad de los *SENs*. Para ello se ha modificado una enzima con enorme potencial en la química fina: una ω -transaminasa dependiente del cofactor PLP. En este caso, el nanogel tiene una funcionalidad adicional. Sirve de depósito de PLP, necesario para que la ω -

transaminasa sea catalíticamente activa. Los resultados preliminares muestran que los nanogeles cargados con PLP, en comparación con los no cargados, ofrecen una mayor actividad y estabilidad al sistema. Este es el primer ejemplo en el que los *SENs* han sido empleados como almacén de coenzimas necesarias para la catálisis.

Además, estamos trabajando en la inmovilización de estos *SENs* mediante enlaces covalentes en soportes prefabricados de metacrilato. Esta aproximación es una de las más empleadas en la industria. Por último, hemos empaquetado un reactor de lecho compacto con estos catalizadores heterogéneos. El objetivo final de este proyecto es aumentar el rendimiento de la biocatálisis de flujo, aún en fase de optimización.

SUMMARY

Enzymes are excellent catalysts with enormous specificity. However, they are very sensitive biomacromolecules and can undergo denaturation beyond their natural environment. In addition, their good solubility makes their recovery and reuse problematic. Therefore, enzyme immobilization became a very important research topic and novel approaches for achieving efficient immobilization are rapidly evolving due to advances in biotechnology, polymer chemistry and nanotechnology. Single Enzyme Nanogels (SENs), i.e., core-shell type hybrids with a single enzyme molecule in the core and a protective hydrogel shell, have proven advantageous in enhancing enzyme robustness and facilitating the fabrication of efficient heterogeneous biocatalysts. In this thesis, we have designed and developed four different heterogeneous biocatalysts using the SEN technology and three different immobilization strategies. The metal-driven crosslinking of imidazole-functionalized SENs results in versatile Metal-Organic Enzyme Aggregates (MOEAs), which can be subsequently self-assembled into continuous biocatalytic films for biosensing purposes. Similarly, the entrapment of these SENs upon biomineralization generates robust and very active organic-inorganic protein hybrids. Parallely, carrier-free heterogeneous chemoenzymatic hybrids are developed using the nanogel as scaffold for the chemical catalyst. This configuration has proven to be very promising for cascade oxidation reactions, applicable in biosynthesis. Finally, the complexity of the system is increased by encapsulating the enzyme ω -transaminase, which has great potential in chemical synthesis. These ω -transaminase-SENs are covalently immobilized on prefabricated supports, aiming for an application in flow biocatalysis.

CONTENTS

Chapter 1	General Introduction	1
1.1	Biocatalysis: powerful tool, limited applications	1
1.2	Genetic engineering of enzymes.....	4
1.3	Chemical modification of enzymes	5
1.3.1	Single Enzyme Nanogels (SENs)	8
1.3.1.1	Enzymes implemented with SEN technology.....	10
1.3.1.2	Synthesis of SENs	11
1.3.1.3	Monomers and Crosslinkers	13
1.3.1.4	Post polymerization modifications.....	18
1.4	Enzyme immobilization.....	19
1.4.1	Use of prefabricated carriers	20
1.4.2	Entrapment into (in)organic polymeric matrices	21
1.4.3	Crosslinked of enzyme aggregates	22
1.4.4	Mutifunctional Nanobiocatalysts	23
1.5	Heterogeneous biocatalyst formation from SENs.....	25
Chapter 2	Scope and Objectives	27
2.1	Scientific outcome	31
2.1.1	Other papers	32
2.1.2	Papers in Preparation.....	32
Chapter 3	Materials and methods	33
3.1	Materials	33
3.2	Instrumentation and characterization techniques	35
3.2.1	Dynamic light scattering (DLS)	35

3.2.2	Atomic Force Microscopy (AFM).....	35
3.2.3	Circular Dichroism (CD).....	36
3.2.4	Attenuated Total Reflection Fourier Transform Infrared Spectroscopy (ATR-FTIR).....	36
3.2.5	Scanning Electron Microscopy (SEM).....	37
3.2.6	Transmission electron microscopy (TEM).....	37
3.2.7	Raman spectroscopy.....	38
3.2.8	X-ray photoelectron spectroscopy (XPS).....	38
3.2.9	Inductively coupled plasma mass spectrometry (ICP-MS).....	39
3.2.10	UV-Vis absorption spectroscopy.....	39
3.2.11	Cyclic Voltammetry (CV).....	40
3.2.12	Zeta-potential.....	40
3.2.13	Sodium dodecyl sulfate-polyacrylamide gel electrophoresis (SDS-PAGE).....	41
3.2.14	Proton nuclear magnetic resonance (¹ H NMR).....	41
3.2.15	Ultra-performance liquid chromatography mass spectroscopy.....	42
3.2.16	High performance liquid chromatography.....	42
3.3	Methods.....	43
3.3.1	Acrylation of proteins.....	43
3.3.2	General protocol for the synthesis of SENS.....	44
3.3.3	Post-polymerization modifications of SENS.....	48
3.3.3.1	Grafting imidazole moieties to HRP@pAA-NH ₂	48
3.3.3.2	Integration of hemin molecules to SENS.....	49
3.3.3.3	Integration of PLP into HeWT@pAA-NH ₂	49
3.3.4	Fabrication of heterogeneous biocatalysts.....	49
3.3.4.1	Carrier-free SEN immobilization.....	50
3.3.4.2	SENS entrapped in biominerals.....	51

3.3.4.3	HeWT@pAA-NH ₂ covalently bound to epoxy-functionalized prefabricated carriers.....	51
3.3.5	Expression and purification of recombinant enzymes.....	51
3.3.6	Calculation of SEN immobilization yield.....	53
3.3.7	Calculation of the protein content in heterogeneous biocatalysts (mass fraction).....	54
3.3.8	Characterization of biocatalytic performance.....	54
3.3.8.1	Calculation of apparent catalytic constants of heterogeneous biocatalysts.....	56
3.3.8.2	Degradation of small aromatics and dyes.....	57
3.3.8.3	NanoNO _x performance coupled with NAD-dependent dehydrogenases.....	58
3.3.9	Stability experiments of heterogeneous biocatalysts.....	58
3.3.10	Reusability experiments of heterogeneous biocatalysts.....	60
3.3.11	Flow reactions.....	60
Chapter 4	Metal-Organic Enzyme Aggregates (MOEAs)	63
4.1	Focused introduction.....	64
4.2	Results and discussion.....	65
4.2.1	Synthesis and characterization of single enzyme nanogels (SENs).....	65
4.2.2	Synthesis and Characterization of Metal-Organic Enzyme Aggregates (MOEAs).....	67
4.2.2.1	Catalytic film formation using MOEAs.....	72
4.3	Conclusion.....	81
Chapter 5	Biomaterialized Enzyme Hybrids	83
5.1	Focused Introduction.....	84
5.2	Results and discussion.....	85
5.2.1	Synthesis and characterization of single enzyme nanogels (SENs).....	85

5.2.2	Synthesis and characterization of Nanosponges (NSs).....	86
5.2.3	Kinetics, robustness, and thermal stability of nanosponges.....	91
5.2.4	Broadening the chemical nature and morphology of NSs	94
5.3	Conclusion.....	96
Chapter 6	Integrated Chemoenzymatic Nanoreactors	97
6.1	Focused Introduction	98
6.2	Results and discussion	99
6.2.1	Synthesis and characterization of integrated chemoenzymatic nanoreactors (INRs).....	99
6.2.2	Integrated chemoenzymatic catalysis.....	106
6.2.3	Stability in organic solvents and reusability of INRs.....	110
6.2.4	Removal of small aromatic derivatives and dye pollutants.....	112
6.2.5	In situ regeneration of nicotinamide cofactors	115
6.2.5.1	NanoNO _x performance coupled with NAD- dependent dehydrogenases	120
6.3	Conclusion.....	122
Chapter 7	Cofactor confinement, Prefabricated carriers, Flow	125
7.1	Focused Introduction	126
7.2	Results and discussion	128
7.2.1	Synthesis and characterization of PLP-loaded SENs.....	128
7.2.2	Immobilization of HeWT@pAA-NH ₂ in epoxy- functionalized resins.....	136
7.2.3	Implementation of heterogeneous biocatalyst in flow	138
7.3	Conclusion.....	139
Chapter 8	Concluding remarks	141
	References	143

FIGURES

Figure 1-1. Schematic representation of enzyme catalysis. The enzyme (grey) binds the substrate (orange) and co-substrate (green) specifically forming a reactant-enzyme transition complex. The product (red) is subsequently generated and released with the co-product (pink), and the enzyme returns to its initial state. Enzyme binding site is represented in blue.....	2
Figure 1-2. Research areas with the potential to improve enzyme stability.	4
Figure 1-3. Schematic illustration of the strategies that are carried out for the formation of covalent enzyme-polymer hybrids. A) Non-specific grafting of proteins, using polymers with a single reacting group and several target residues within the protein. B) Multi-point strategy using polymers with multiple anchoring sites. C) Site-specific grafting using a biorthogonal approach. D) <i>Grafting-from</i> approach that entails the conjugation of the macroinitiator to the protein and the subsequent <i>in-situ</i> polymerization after the addition of monomers.....	7
Figure 1-4. Ball model representation of the structure of an unmodified enzyme, i.e., glucose oxidase (GOx, left), and the corresponding Single Enzyme Nanogel (SEN, right). The crosslinked polymeric network is illustrated in blue.	9
Figure 1-5. Representation of the electrostatic surfaces of the main enzymes used for the fabrication of SENs by now. The negatively charged surface areas are shown in red, while the positive ones are blue.....	11
Figure 1-6. Synthesis of single enzyme nanogels (SENs). (A) Covalently entrapped SEN formation consists of two steps: i) acrylation of the enzyme and ii) subsequent <i>in situ</i> radical polymerization in the presence of monomers, crosslinkers, and initiators. (B) Synthesis of non-covalent SEN consists of a single step: the polymerization occurs in the presence of the monomers, crosslinkers, initiators and the unmodified enzyme.....	13
Figure 1-7. Scheme of the most common enzyme immobilization strategies: A) immobilization into prefabricated carriers, B) entrapment or encapsulation, and C) crosslinking of enzyme aggregates or crystals.	20

Figure 1-8. Fabrication workflow and SEM images of A) protein-inorganic nanoflowers (NFs) and B) enzyme-ZIF-8 hybrids.....	22
Figure 1-9. Examples of multifunctional nanobiocatalysts. A) Lipase immobilization into nanoporous gold. B) Supramolecular hybrid nanogel around Fe ₃ O ₄ nanoparticles for SOD and chloroperoxidase immobilization. C) Immobilization of enzymes onto graphene-based nanomaterials. D) Mesoporous-silica nanoparticles used to entrap lipase. Figures adapted with permissions from Plos One (2011, A), Nature Communications (2019, B), Trends in Biotechnology (2014, C), and Nano Research (2017, D). ^{154,156–158}	24
Figure 2-1. Inside cover published in Angewandte Chemie-International Edition 2022-61/39. Picture author: Antonio Reifs.....	32
Figure 3-1. Covalently entrapped SEN detailed synthesis procedure divided in i) enzyme acrylation, ii) monomer adsorption to the enzyme surface and iii) in-situ radical polymerization.....	45
Table 3-2. Synthesis conditions utilized in this thesis for the fabrication of the SENs. The protein concentration was set to 20 μM and sucrose concentration was set to 5 % (m/v). The absence of units refers to the molar excess <i>vs.</i> the enzyme.	46
Figure 3-2. Grafting of imidazole moieties to reactive amines from α-HRP@pAA-NH ₂ . 4-ICA is transformed into an o-acylisourea ester with EDC as coupling agent. NHS-OH transforms the o-acylisourea into an NHS-ester. Finally, the amide bond is formed.	49
Figure 4-1. Workflow for the MOEA formation. a) enzymes are entrapped within imidazole-functionalized SENs, which are b) further crosslinked by coordination to metal ions for the MOEA formation.....	65
Figure 4-2. Structural characterization of GOx and GOx@pAA-I. A) DLS, B) AFM, C) CD, and D) ATR-FTIR spectra of free and GOx@pAA-I samples.66	
Figure 4-3. Structural characterization of MOEAs. A) SEM images of Cu@, Ni@, Zn@, and Co@MOEA nanoparticles (scale bar 2 μm). B) Statistical size distribution of the hydrodynamic diameter of Cu@, Co@, Zn@, and Ni@MOEAs measured by DLS.	67
Figure 4-4. (A) Optical images of pelleted MOEAs. (B) Robustness of MOEA nanoparticles and pellets in water in terms of protein release and their disassembly after addition of EDTA. Inset pictures: Cu@MOEA dissolution over time.	68

Figure 4-5. Compositional characterization of MOEAs. A) ATR-FTIR spectra of GOx@pAA-I, Cu@, Ni@, Co@, and Zn@MOEAs in the 990-980 cm ⁻¹ spectral window. B) XPS of Cu@MOEAs in the Cu2p region.....	69
Figure 4-6. Recycling and thermal stability of MOEAs. A) ON-OFF switching experiment showing the immersion (ON) and withdrawal (OFF) of Cu@MOEAs into and out of the reaction mixture. B) MOEA and GOx-ZIF-8 activity evolution after incubation at 65°C for 1h.....	71
Figure 4-7. Formation workflow and optical pictographs of catalytic films. A) Catalytic film formation entails 1) the drop-casting of MOEAs onto a hydrophilic substrate and 2) the arrangement of the MOEAs during the drying process. Pictographs of films based on GOx@pAA-I (left) and GOx@pHEAA-I (right). Scale bar: 1 mm.....	73
Figure 4-8. Dark-field optical pictographs of catalytic films formed with Zn, Cu, Ni, Co, Pd, and Cr. Scale bar: 1 mm.....	73
Figure 4-9. Morphology of catalytic Zn-containing thin films. SEM image of the film deposited with 0.75 mg ml ⁻¹ in A) top view and B) cross-section view. C) Top view of the film deposited with 2.0 mg ml ⁻¹ . D) Top view of the film deposited with 0.1 mg ml ⁻¹ . The aggregation and compactness of nanoscale structures within the film was evidenced by E) AFM and F) SEM. G) Layered structures are observed in cracked films by SEM. Scale bar: 4 μm.....	74
Figure 4-10. Compositional characterization of films. A) UV-vis, B) CD, and C) ATR-FTIR measurements of Zn@MOEA films and free GOx as reference. E) XPS spectrum of a Zn@MOEA films in the Zn 2p spectral region.....	75
Figure 4-11. Catalytic characterization of MOEA catalytic films. A) Glucose oxidase activity plots of Zn@MOEA films, deposited at a range of protein concentration from 3 mg to 0.09 mg. B) Glucose oxidase activity of assorted Me@MOEA films at different protein concentrations.....	76
Figure 4-12. Reusability and activity in organic solvents of MOEA catalytic films. A) Reusability of all investigated films after 5 long (30 min) catalytic cycles. B) Relative catalytic performance (compared with water) of Zn@MOEA films in the presence of organic solvents after being incubated in the same solvents for 1 h.....	78
Figure 4-13. Catalytic response of Zn films in a temperature window of 30-75 °C.....	78

Figure 4-14. Electrochemical glucose biosensing with Zn@MOEA catalytic films. (A) Cyclic voltammogram obtained at different glucose concentrations (0 – 1.5 mM). B) Recorded intensity at each glucose concentration.79

Figure 4-15. Synthesis and characterization of bi-enzymatic films for cascade catalysis. (A) Scheme of the cascade reaction. (B) Drop-casting of two consecutive films on top of each other. (C) EDX-imaging map of the cross-section of the film with the GOx/ β -Gluc configuration. (D) Catalytic rates measured for all configurations. U defined as $\mu\text{mol}_{\text{glucose}} \text{min}^{-1}$80

Figure 5-1. Schematic of the formation of both heterogeneous biocatalysts presented in this chapter. Nanoflowers (NF, blue) after biomineralization of free HRP. Nanosponges (NS, grey) were fabricated from nanogels modified with imidazole molecules (a-HRP@pAA-I).84

Figure 5-2. Synthesis and characterization of a-HRP@i-aNGs. A) Workflow for the synthesis of a-HRP@i-aNGs consisting of 3 steps: 1) acrylation, 2) polymerization, and 3) grafting. B) Hydrodynamic diameters measured by DLS.86

Figure 5-3. Morphological characterization of NS and NF biomaterials. A) SEM images showing size and morphology of nanosponges (NS) and nanoflowers (NF) (scale bar 20 μm). B) SEM images of NSs grown from different CuSO_4 concentrations (0.1 mM – 10 mM, scale bar: 4 μm).87

Figure 5-4. Calculation of the protein immobilization yield (%) of NSs and NF. A) Evaluation of immobilized protein at increasing Cu(II) concentrations (from 0.1 to 10.0 mM). Inset picture: morphology of the fabricated hybrids (bar: 5 μm) B) Evaluation of the effect of protein concentration on immobilized yields (from 1.5 to 9 μM).88

Figure 5-5. Compositional characterization of NS and NFs. A) HRP:Cu molar ratio (n/n) of formed hybrids at different seeded protein concentrations, measured by ICP-MS. B) ATR-FTIR spectra highlighting three spectral regions: i) protein peaks (1650 – 1550 cm^{-1}), ii) imidazole (1440 – 1410 cm^{-1}), and iii) phosphate stretching peaks (1031 cm^{-1}).89

Figure 5-6. Cyclic voltammograms highlighting peak-to-peak separation of NSs (ΔE_{NS}) and NFs (ΔE_{NF}).90

Figure 5-7. Fitted XPS spectra of NS and NFs. A) XPS of the N 1s region. B) XPS spectra of the Cu 2p_{2/3} region prepared with 0, 10, 50, and 100 mM of imidazole in a 10 mM CuSO_4 in PBS.91

Figure 5-8. Characterization of the catalytic activity of the NSs and the NFs. A) Apparent turnover number ($^{app}k_{cat}$) and B) apparent Michaelis constant ($^{app}K_M$) of both heterogeneous biocatalysts fabricated at increasing $CuSO_4$ concentrations.	92
Figure 5-9. Robustness of heterogeneous biocatalysts. A) Relative activity (%) after incubation of NFs and NSs in various buffers at different pH values. B) Retained initial activity (%) of NFs, NSs, HRP, and a-HRP@pAA-I after incubation at 65 °C for 60 min.....	93
Figure 5-10. SEM images of the resulting hybrid structures after biomineralization with divalent cations: Mn(II), Cu(II), Co(II), Cd(II), Zn(II), Ag(I), Ni(II), and Au(III). Scale bar: 4 μm	94
Figure 5-11. Structure-function relationship of biohybrids. A) Protein immobilization yield (%) using free HRP and a-HRP@pAA-I in PBS and different metal salts ($MnCl_2$, $Co(NO_3)_2$, $NiSO_4$, $CuSO_4$, $Zn(NO_3)_2$, $CdSO_4$, $AgNO_3$, and $HAuCl_4$). B) Specific peroxidase activity ($\mu mol\ min^{-1}$ per mg of protein) of every NS. C) Cyclic voltammograms of $AgNO_3$ solution and $Ag@NSs$. D) UV-Vis spectra of $AgNO_3$ solution and $Ag@NSs$	95
Figure 6-1. Schematic representation of the synthesis procedure and the arrangement of the catalysts within integrated chemoenzymatic nanoreactors (INR). Imidazole-functionalized SENs are synthesized from free GOx and mixed with hemin for the fabrication of chemoenzymatic nanoreactors.....	100
Figure 6-2. ATR-FTIR spectra of SENs. Main peaks are highlighted: #1: 1642 cm^{-1} ; #2: 1060 cm^{-1} ; #3: 917 cm^{-1} ; #4: 655 cm^{-1} ; #5: 1725 cm^{-1} ; #6: 3275 cm^{-1} .	101
Figure 6-3. Raman and ATR-FTIR of INRs. A) Raman spectra of INRs, hemin, and GOx. The characteristic D band (#1) and G band (#3) of hemin are highlighted at 1347 and 1574 cm^{-1} , respectively. The D band present in the INRs is highlighted at 1360 B) ATR-FTIR spectra of hemin and INRs. Significant peaks are highlighted at 1700 (#1) and 710 cm^{-1} (#2).....	102
Figure 6-4. Deconvoluted XPS spectra of INR1. A) Fe 3p region. B) N 1s region.	103
Figure 6-5. UV-Vis analysis of INRs. A) Scaled heat-map representation of the intensity of the UV-Vis spectra of INR1 samples synthesized at a range of hemin:GOx@pHEAA-I molar ratios from 10 to 500. B) Spectra of INRs in comparison to free hemin (non-continuous black line). Zoom at the 500-650 nm region showing the Soret band satellite peaks.	104

Figure 6-6. Structural characterization of INRs. Sample homogeneity and morphology of INR1 was revealed by A) SEM, B) TEM, and C) high-resolution AFM. The inset image shows the 3D reconstruction of a single INR1 particle. D) High-resolution AFM image and the corresponding 3D reconstruction of one small aggregate within the INR3 sample.	105
Figure 6-7. Activity plots of INRs synthesized at increasing hemin loadings. One-pot concurrent reaction of INRs representing initial velocities (V_i) of each INR.....	107
Figure 6-8. Activity plots of INRs synthesized at increasing hemin loadings. A) Peroxidase and B) glucose oxidase activity of INRs.	107
Figure 6-9. Activity plots of the one-pot chemoenzymatic reactions performed at very diluted conditions. A) 0-1000 pM catalyst region. B) Zoom in the 0-25 pM catalyst region. INRs were compared to a mix of GOx and HRP enzymes at equivalent concentrations.....	109
Figure 6-10. Effect of pH on INRs. A) UV-Vis spectra at different pH values and B) pH activity profile.....	109
Figure 6-11. Catalase-like activity of INR3 at alkaline conditions. A) Catalase activity measured at pH 7, 8, and 9. Inset pictures: INR3 sample before and after the addition of glucose at pH 9. B) ABTS oxidation ability of INR3 sample before and after catalase reaction.....	110
Figure 6-12. Relative activity of INRs and free enzyme system in different organic solvents. A) One-pot concurrent cascade activity. B) Peroxidase activity.	111
Figure 6-13. ON-OFF switching experiment in the presence (ON) and absence (OFF) of INR3. The values of k represent the catalytic rate of INR3 in each of the 5 ON phases.	112
Figure 6-14. Degradation kinetics of 1 mM phenol by INR3.....	112
Figure 6-15. Degradation of aromatic dyes by INR3. UV-Vis spectra of 50 μ M of dyes A) methyl orange (MO), B) methylene blues (MB), C) phenol red (PR), and D) rhodamine (Rho) before and after overnight reaction.	115
Figure 6-16. Workflow for NanoNO _x formation. The addition of hemin to GOx@pHEAA-I (formed from $n_{Vi}:n_{GOx} = 4000$) renders solid materials by the hemin-directed crosslinking of individual nanogels (details in SEM inset	

image). In the presence of glucose, a concurrent cascade reaction is implemented, releasing oxidized nicotinamide cofactors to the medium..... 116

Figure 6-17. Calculation of the apparent Michaelis-Menten constant ($^{app}K_M$) of NanoNOx. A) $^{app}K_M$ of glucose and B) $^{app}K_M$ of NADH. 117

Figure 6-18. Bioavailability test of NADH. A) $^1\text{H-NMR}$ spectra of 1,4-NAD⁺, 1,4-NADH, and changes of 1,4-NADH after oxidation with NanoNOx (NADH+NanoNOx). B) Complete NADH oxidation catalyzed by NanoNOx followed by the NAD⁺ reduction accomplished by BsADH using iprOH as substrate. Reactions were followed at 340 nm. 118

Figure 6-19. Calculation of the turnover number and regioselectivity of NanoNOx. A) $^{app}k_{cat,NADPH}$ calculation using NADPH as substrate B) $^{app}k_{cat,BNAH}$ calculation using BNAH as substrate. C) Changes in the $^1\text{H-NMR}$ spectra of NADPH after oxidation with NanoNOx. D) Changes in the $^1\text{H-NMR}$ spectra of BNAH after oxidation with NanoNOx. Stars designate monitored hydrogens (H-2) of the biologically active nicotinamide (oxidized and reduced) moieties..... 119

Figure 6-20. Study of the applicability of NanoNOx in NAD-dependent coupled oxidations. A) Illustration of coupled NanoNOx-BsADH biocatalytic system for the formation of NADH and the concomitant regeneration of NAD⁺ that boosts the oxidation of BnOH. A single dose of glucose generates copious amounts of H₂O₂ in the medium, which halts the reaction progress (left). The sequential addition of small concentrations of glucose generates low levels of H₂O₂, which are directionally channeled to the organometallic catalyst without damaging the biomolecules present in the reaction (right). B) BnOH oxidation kinetics with different glucose addition mode: simultaneous (20 mM), 0.2 mM every 5 min and 15 min, and without NanoNOx. Asterisks represent the point at which [glucose] = 20 mM. C) Evaluation of the cofactor by $^1\text{H NMR}$ after BnOH oxidation with glucose simultaneous addition. 121

Figure 7-1. Reaction mechanism of ω TAs. A) Catalytic cycle of ω TAs consisting of the PLP half-cycle and the PMP half-cycle. B) Model transamination reaction and inactivation mechanism of dimeric ω TAs..... 128

Figure 7-2. Synthesis and characterization of HeWT@pAA-NH₂. A) SDS-PAGE electrophoresis, synthesis conditions, specific and retained activity calculation of HeWT and HeWT@pAA-(NH₂). Lane L: protein ladder; lane 1 and 5: purified HeWT; lane 2: HeWT@pAA; lane 3, 4, and 6: HeWT@pAA-

NH ₂ . B) DLS spectra of HeWT and HeWT@pAA-NH ₂ (lane 6) samples. C) Picture of SENs (lanes 2-4) after dialysis in the presence of PLP.	129
Figure 7-3. UV-Vis spectra of PLP, HeWT and SENs fabricated using AA, (APM), and BIS. A) Spectra fixed at a HeWT concentration of 0.2 mg ml ⁻¹ (1.84 μM). The PLP sample was used for dialysis. B) Normalized UV-Vis spectra.	131
Figure 7-4. UV-vis spectra of HeWT@pAA-NH ₂ loaded with different PLP excess (0 to 250). A) UV-vis spectra of each hybrid. B) Absorption maxima of the PLP peak <i>vs.</i> PLP excess.	132
Figure 7-5. Kinetic characterization and stability of HeWT and HeWT@pAA-NH ₂ . A) Activity of HeWT@pAA-NH ₂ loaded with different PLP excess. One unit of HeWT activity was defined as the amount of enzyme that catalyzes the reaction of 1 μmol acetophenone per minute. B) Long-term stability of HeWT@pAA-NH ₂ loaded with different PLP excess.	133
Figure 7-6. Kinetic characterization of HeWT and HeWT@pAA-NH ₂ . A) Reaction scheme. B) K _{M,pyruvate} calculation. C) K _{M,S-MBA} calculation.	134
Figure 7-7. Relative activity of HeWT and HeWT@pAA-NH ₂ in the presence of 50% (v/v) organic solvents (2-isopropanol (iPrOH), acetonitrile (MeCN), and dimethyl sulfoxide (DMSO)). The activity in 50 mM phosphate buffer pH 8.0 was taken as 100%.	135
Figure 7-8. Catalytic activity evaluation of HeWT@pAA-NH ₂ outside its optimal environment. A) Activity evaluation after incubation overnight in toluene (50%, v/v) and B) aqueous solution with different pH values (8.0 – 10.0).	135
Figure 7-9. SEN immobilization into prefabricated carriers. A) Workflow of the immobilization of HeWT@pAA-NH ₂ into epoxy-functionalized insoluble carriers for the formation of heterogeneous biocatalysts (SEN-(B)MA). B) SDS-PAGE of the immobilization of HeWT and HeWT@pAA-NH ₂ . L: protein ladder; HeWT: free HeWT; HeWT-MA: HeWT immobilized on epoxy-functionalized methacrylate beads; SEN: HeWT@pAA-NH ₂ ; SEN-MA: HeWT@pAA-NH ₂ immobilized on epoxy-functionalized methacrylate beads.	137
Figure 7-10. Continuous flow deamination by immobilized HeWT/HeWT@pAA-NH ₂ on epoxy-methacrylate supports. (A) Schematic of the flow system setup with immobilized HeWT@pAA-NH ₂ loaded with PLP.	

(B) The operational performance of the packed bed reactors. (C) UV-Vis spectra of the 2 washings (W) and first 10 column volumes..... 139

TABLES

Table 1-1. Summary of polymeric monomers used to synthesize Single Enzyme Nanogels (SENs).....	16
Table 1-2 Summary of polymeric crosslinkers used to synthesize SENs.....	17
Table 1-3. List of SENs modified after the polymerization reaction.....	19
Table 3-3. Main features of each SEN and the application they have been used for. In all cases the SENs show higher thermal stability and activity in the presence of organic solvents than the unmodified enzyme.....	47
Table 4-1. Measured apparent catalytic parameters for nanoparticulated MOEAs, ZIF-8 hybrids, and GOx.	70
Table 4-2. Measured apparent catalytic parameters for Me@MOEA catalytic films.....	77
Table 6-1. Shell thickness and zeta-potential values of synthesized SENs.....	101
Table 6-2. Summary of integrated chemoenzymatic nanoreactors (INRs) used in this work.	102
Table 6-3. Diameters measured for INRs using different techniques.	106
Table 6-4. Kinetic parameters measured for INR samples and the free GOx/HRP system.....	108
Table 6-5 Chemical structures of assayed aromatic compounds and degradation efficiency	113
Table 7-1. HeWT and HeWT@pAA-NH ₂ immobilization on epoxy-functionalized methacrylate (MA) and butyl-methacrylate (BMA) supports..	136

ABBREVIATIONS

4-ICA: 4-imidazole carboxylic acid

AA: acrylamide

ABTS: 2,2'-azino-bis(3-ethylbenzothiazoline-6-sulphonic acid)

AFM: atomic force microscopy

AP: acetophenone

APBA: 3-acrylamidophenylboronic acid

APM: N-(3-aminopropyl) methacrylamide

APS: ammonium persulfate

APTAC: (3-acrylamidopropyl) trimethyl ammonium

Aq: aqueous

ATR-FTIR: attenuated total reflection Fourier transform infrared spectroscopy

β -Gluc: β -glucosidase

BAC: N,N'-Bis(acryloyl)cystamine

BBB: blood-brain barrier

BCA: bovine carbonic anhydrase

BChE: butyrylcholinesterase

BIS: N,N'-methylenebisacrylamide

BMA: butyl-methacrylate

BMP-2: bone morphogenetic protein-2

BNA: 1-benzyl-1,4-dihydronicotinamide

BnOH: benzyl alcohol

BRTA: Basque Research and Technology Alliance

BSA: bovine serum albumin

BsADH: alcohol dehydrogenase from *Bacillus stearothermophilus*

CAS3: caspase-3
Cas9: CRISPR-associated protein 9
CAT: catalase
CB: sodium carbonate buffer
CBAA: carboxybetaine acrylamide
CBAAX: Bisacrylated carboxybetaine
CD: circular dichroism
CEAA: 2-Carboxyethyl acrylate
CLEA: crosslinked enzyme aggregates
COVID-19: coronavirus disease 2019
CRISPR: clustered regularly interspaced short palindromic repeats
CV: cyclic voltammetry
DAA: 2'-diallylamino-ethyl
DH: dehydrogenase
DLS: dynamic light scattering
DMF: dimethyl formamide
DMSO: dimethyl sulfoxide
DNase: deoxyribonuclease
EDC: 1-Ethyl-3-(3-dimethylaminopropyl)carbodiimide
EDTA: ethylenediaminetetraacetic acid
EDX: energy dispersive X-ray analysis
FAD: flavin adenine dinucleotide
FEBS: Federation of the European Biochemical Societies
FL: firefly luciferase
FRET: fluorescence resonance energy transfer
GDMA: glycerol dimethacrylate
GFP: green fluorescent protein

GOx: glucose oxidase

GSH: glutathione

HEAA: hydroxyethyl acrylamide

HEPES: (4-(2-hydroxyethyl)-1-piperazineethanesulfonic acid)

HeWT: ω -transaminase from *Halomonas elongate*

¹H NMR: proton nuclear magnetic resonance

HPLC: high performance liquid chromatography

HRP: horseradish peroxidase

ICP-MS: inductively coupled plasma mass spectrometry

INR: integrated chemoenzymatic nanoreactor

IprOH: 2-isopropanol

IPTG: isopropyl β -D-1-thiogalactopyranoside

k_{cat} : turnover number

K_M : Michaelis-Menten constant

L-Ala: L-alanine

LB: Luria-Bertani

MA: methacrylate

MAEP: monoacryloyloxyethyl phosphate

MeCN: acetonitrile

MeOH: methanol

MINECO: ministerio de asuntos económicos y transformación digital

MOEA: metal-organic enzyme aggregate

MOF: metal-organic framework

MPC: 2-methacryloyloxyethyl phosphorylcholine

MWCO: molecular weight cut-off

NAD: β -nicotinamide adenine dinucleotide

NADP: β -nicotinamide adenine dinucleotide phosphate

NAS: N-acryloxysuccinimide
NBC: nanobiocatalyst
NF: protein-inorganic hybrid nanoflower
NHS: N-hydroxysuccinimide
NIPAM: N-isopropyl acrylamide
NS: nanosponge
OPH: organophosphate hydrolase
PA: propenoic acid
pAA: polyacrylamide
PBS: phosphate buffered saline
PCTI: plan de ciencia, tecnología e innovación
PEG: poly(ethylene glycol)
PEG(M)A: poly(ethylene glycol) (meth)acrylate
PET: positron emission tomography
PGA: penicillin G amidase
PhD: doctor of philosophy
PLP: pyridoxal 5'-phosphate
pNIPAAm: poly(N-isopropylacrylamide)
Pyr: pyruvate
RIS3: regional innovation strategy
SDS-PAGE: sodium dodecyl sulfate-polyacrylamide gel electrophoresis
SEM: scanning electron microscopy
SEN: single enzyme nanogel
S-MBA: S-(α)-Methylbenzylamine
SOD: superoxide dismutase
SPECT: single-photon emission computed tomography
TEM: transmission electron microscopy

TEMED: tetramethylethylenediamine
THPP: Meso-tetra(p-hydroxyphenyl) porphine
TNF: tumor necrosis factor
Tol: toluene
Tris: tris(hydroxymethyl)aminomethane
UOx: urate oxidase
UPLC-MS: ultra-performance liquid chromatography mass spectroscopy
UV-Vis: ultraviolet-visible spectroscopy
VEGF: vascular endothelial growth factors
VI: vinyl imidazole
ωTA: ω-transaminase
XPS: x-ray photoelectron spectroscopy
ZIF-8: zeolitic imidazolate framework-8

Chapter 1 GENERAL INTRODUCTION

1.1 BIOCATALYSIS: POWERFUL TOOL, LIMITED APPLICATIONS

Enzymes are the main engines of life. Although some chemical reactions can proceed spontaneously in standard conditions, in most of the cases reactions need to be catalyzed to have a significant rate. Catalysts, a term derived from Greek *kataluein* (loosen), are molecules that speed up chemical reactions by reducing the energy barrier necessary for a reagent to be converted into a product.¹ Ideally, the catalyst is not consumed during the reaction, transforming the substrate continuously and indefinitely. In this regard, biological systems have remarkable molecular devices, i.e., enzymes, capable of accelerating chemical reactions up to 10^8 fold with enormous specificity.² Unlike chemical catalysts, enzymes perform their function in mild conditions, i.e., at moderate pH values and temperatures, and are biodegradable and environmentally friendly.³

Enzymes are essential for the maintenance of life and have narrowed down their substrate specificity through natural evolution over millions of years. Indeed, each of the biochemical reactions in the cellular metabolism is catalyzed by a particular enzyme. For example, if we isolated an *Escherichia coli* bacterium in the growth phase, we would find more than 1000 different enzymes performing over 2200 metabolic reactions to keep the bacteria alive and thriving.⁴ In the case of human cells, the numbers are even more remarkable with approximately 75,000 enzymes working in perfect coordination, carrying out 9×10^9 reactions per second.² These biomacromolecules accommodate reagents specifically by programmed recognition, which depends on the specific

composition and spatial configuration of their catalytic pocket. Finally, the reactant-enzyme transition complex is transformed into the product which is released, while restoring the initial state of the enzyme (see **Figure 1-1**).⁵

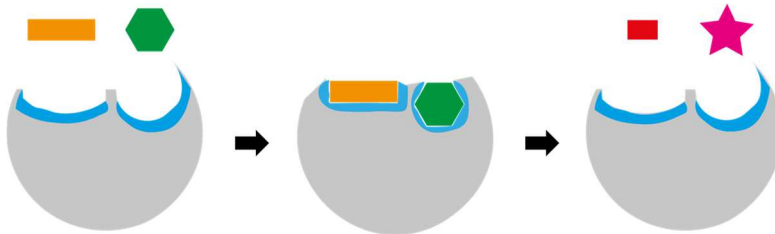


Figure 1-1. Schematic representation of enzyme catalysis. The enzyme (grey) binds the substrate (orange) and co-substrate (green) specifically forming a reactant-enzyme transition complex. The product (red) is subsequently generated and released with the co-product (pink), and the enzyme returns to its initial state. Enzyme binding site is represented in blue.

Most of the features of enzymes are a consequence of their complex molecular structure, which is divided into four different levels: primary, secondary, tertiary, and quaternary structure.^{6,7} The primary structure consists of a specific and genetically determined amino acid sequence that builds up the protein. The secondary structure is a three-dimensional pattern adopted by several domains of the protein, which are mainly determined by hydrogen bonds between the amino acid side chains. The most common secondary structures are α -helix and β -sheet, which are determined by the Ramachandran plot.⁸ Both the primary and secondary structures define the tertiary structure, referred to as the three-dimensional folded form of the protein. In addition, most proteins are composed of more than one polypeptide chain or monomer, which constitute the quaternary structure and plays a key role for its natural function.⁹

Enzymes reach several fields of application. Whole-cell fermentations have long been used by humans for the production of food and beverages, e.g. wine, beer, bread, and cheese, using the native metabolism of the host cells.¹⁰ Since the 1960s, the scientific community has invented several ingenious ways to exploit isolated enzymes, solving several problems encountered with whole-cell biocatalysis.¹⁰ This achievement has permitted

the utilization of enzymes not only in the food industry, but also for other purposes, such as for the synthesis of fine chemicals,¹¹ detergents and pharmaceutical ingredients,¹² biosensing,¹³ bioremediation,¹⁴ biofuel production,¹⁵ diagnostics,¹⁶ and biomedical technologies.¹⁷ Therefore, it is evident that enzymes show an impressive potential in many technological fields and will certainly be also successfully implemented in other key sectors, e.g., eco-friendly biobatteries, very shortly.^{18,19}

Cofactors are often required. Small molecules, termed cofactors, contribute to carrying out enzymatic reactions that cannot occur with the standard set of twenty amino acids. A fair number of enzyme families require the presence of cofactors to transfer hydrogen, electrons, oxygen, or other types of atoms or molecules to the active site of the enzyme and thereby execute the catalytic function. Enzyme cofactors are subdivided into two groups depending on their nature: (1) metals and (2) small organic compounds termed coenzymes. Coenzymes are usually derived from vitamins and may be either tightly or loosely bound to the enzyme.²⁰ Those that are loosely bound are called co-substrates (**Figure 1-1**, green hexagon), since, like substrates and products, they bind to the enzyme and are released after the reaction. One of the most relevant co-substrates in the metabolism are β -nicotinamide adenine dinucleotide (NAD) and its phosphorylated form, i.e., NADP. These coenzymes are involved in redox reactions, accepting and donating electrons and protons from other molecules. Reactions of this type are encompassed by the dehydrogenases (DHs), which show enormous potential in the chemical, pharmaceutical, and food industry.²¹ Importantly, the development of efficient cofactor recycling systems is critical to assess the economic viability and the catalytic performance of DHs in biotechnological applications.^{22,23} We have approached this challenge in a highly innovative way in this thesis.

Utilization of enzymes beyond their comfort zone. While only few families of enzymes, e.g. lipases,¹⁵ are implementable into industrial applications for their stability, cost, and activity, most enzymes need adjustments to be economically viable.²⁴ The structure of

enzymes is the result of a fragile balance between entropic loss and enthalpic contribution, which is caused mainly by hydrogen bonds.²⁵ Small changes, such as heat, pressure, or the presence of organic solvents, can compromise the thermodynamic balance, giving rise to extensive conformational changes that may result in an irreversible deactivation of the enzyme.²⁶ Moreover, in some applications the presence of proteolytic enzymes can also be a threat.²⁷ Hence, several multidisciplinary approaches have been undertaken to broaden the “catalytic window” of enzymes under non-physiological conditions (**Figure 1-2**). Specifically, relevant advances have been performed in the following research fields: (i) genetic and protein engineering, (ii) chemical modification of enzymes, and (iii) enzyme immobilization. In fact, the most fruitful breakthroughs have been achieved by combining technologies adopted from these fields.^{28–30} As a preview, this thesis studies a series of tools to improve the stability and reusability of enzymes, i.e., glucose oxidase (GOx), horseradish peroxidase (HRP), and ω -transaminases (ω TA), for biotechnological purposes.

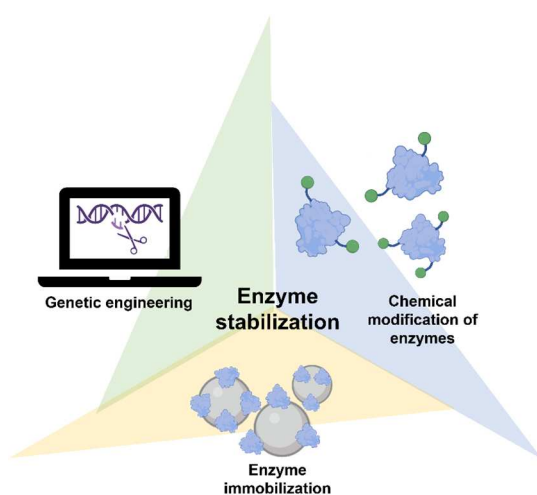


Figure 1-2. Research areas with the potential to improve enzyme stability.

1.2 GENETIC ENGINEERING OF ENZYMES

Molecular biology as a tool to improve enzyme stability. The advances in genome sequencing

and metagenomics are expanding the repertoire of known biocatalytic reactions and facilitating the screening of intrinsically stable enzymes. The enzymes from extremophilic microorganisms are generally stable at high temperatures, in the presence of organic solvents, and resistant to proteolysis.³¹ However, they have a rather narrow reaction spectrum compared to mesophilic enzymes (enzymes that work better at moderate temperature). Therefore, it is of great interest to stabilize mesophilic enzymes with a broad reaction spectrum. Protein engineering based on molecular biology is another avenue for the design and fabrication of enzymes with enhanced stability and very high efficiency making use of molecular biology tools.³² This technology consists of the modification or *de novo* synthesis of enzyme-encoding genes, inserted into competent microorganisms, for the expression and purification of enzymes on a large scale. Protein engineering follows strategies such as the protein rational design, the directed evolution, or the *de novo* design.^{31,33} The stability mechanism of each enzyme is different and varies depending on the environmental conditions.³⁴ Therefore, high-precision computational studies are needed to understand the relationship between the structure and stability of each protein.³⁵ In general, the technologies mentioned so far, i.e., genome sequencing, metagenomics, and protein engineering, are well suited to improve enzymatic efficiency, increase the reaction scope, and improve the enzyme stability. However, they do not allow the separation of enzymes from the medium and their reuse, which is highly demanded in many application fields.

1.3 CHEMICAL MODIFICATION OF ENZYMES

Small molecules are easily conjugated to enzymes. An approach alternative to genetic engineering is the chemical modification of enzymes with small molecules. Chemists and biologists are working side by side to introduce a wide range of functional groups into the protein structure, either to modify its active center or as a reactive loop for conjugation to other (bio)macromolecules or supports. Chemical modification of enzymes is a simple, cheap, and effective strategy to improve the functionality and

stability of the modified variant.³⁶ Moreover, this approach is exploited to change the physical properties, substrate specificity, or reaction type of wild-type and recombinant enzymes.³⁷ Importantly, conjugation reactions must be efficient under mild conditions (neutral pH, room temperature, aqueous systems, etc.) to preserve the structure of the enzyme of interest. Traditional chemical modifications have targeted nucleophilic amino acids, especially lysines and cysteines.³⁸ However, other available residues, such as tyrosine, tryptophan, and methionine are also modifiable.³⁹

The primary amines of lysines (ϵ -amino group) are nucleophilic handles, well suited for the chemical modification of proteins. The high abundance of lysines on the enzyme surface enables the reaction with various chemical moieties such as acid anhydrides of dicarboxylic acids, epoxides, glutaraldehyde-, and glyoxyl-derivatives. The reactivity of the lysines can be tailored with the pH of the reaction medium, as primary amines act as potent nucleophiles (above pK_a) in their deprotonated form, while protonation reduces their reactivity (below pK_a).³⁰ The coupling of hydrophilic groups, i.e., acid anhydrides, to ϵ -amino groups can change the protein charge from positive to negative, in some cases increasing the enzyme resistance under denaturation conditions.^{40–42} However, the effect of the modification cannot be foreseen and must be empirically assessed. Therefore, it is of great importance to make a good optimization for each enzyme, choosing the most suitable chemical moiety, and targeting the correct number of modified lysines.⁴³

Enzyme-polymer hybrids as an attractive solution to the fabrication of stable biocatalysts. The recent years have witnessed a trend to modify enzymes with high molecular weight macromolecules, i.e., (bio)polymers. A covalent conjugation of linear polymers to the amino acid residues on the surface of enzymes, either by a *grafting from* or a *grafting to* approach, allows a successful generation of active and stable enzyme-polymer conjugates (**Figure 1-3**).⁴⁴ Today, many enzymes have been covalently modified with linear (bio)polymers: α -chymotrypsin, lysozyme, L-asparaginase, acetylcholinesterase,

lipase, etc.⁴⁵ In most of the cases, the enzyme activity is reduced (relative to the free enzyme), but in favor of an increase in its thermal stability profile.⁴⁶ Poly(ethylene glycol) (PEG) is the most widely used and described polymer for modifying enzymes. Enzyme-polymer hybrids generally show improved solubility, increased stability against degradation, increased circulation times, and prolonged biological activity as a consequence of the steric shielding effects and the milder microenvironment generated by the associated polymer.^{47,48} Fortunately, nowadays the rapid growth of polymer chemistry offers a wealth of opportunities for the successful combination of enzymes with versatile synthetic polymers. For example, the thermoresponsive poly(N-isopropylacrylamide) (pNIPAAm) polymer is capable of altering the catalytic microenvironment of trypsin, triggering conformational changes of the enzyme that lead to the improvement of the accessibility of the substrates to its active center, thereby significantly enhancing the catalytic activity. In addition, the enzyme conjugates are more stable than the native enzyme in solution.^{45,49} Polymers with pendant carbohydrates, i.e., trehalose-based polymers, have also been used to stabilize enzymes against environmental stressors.⁵⁰

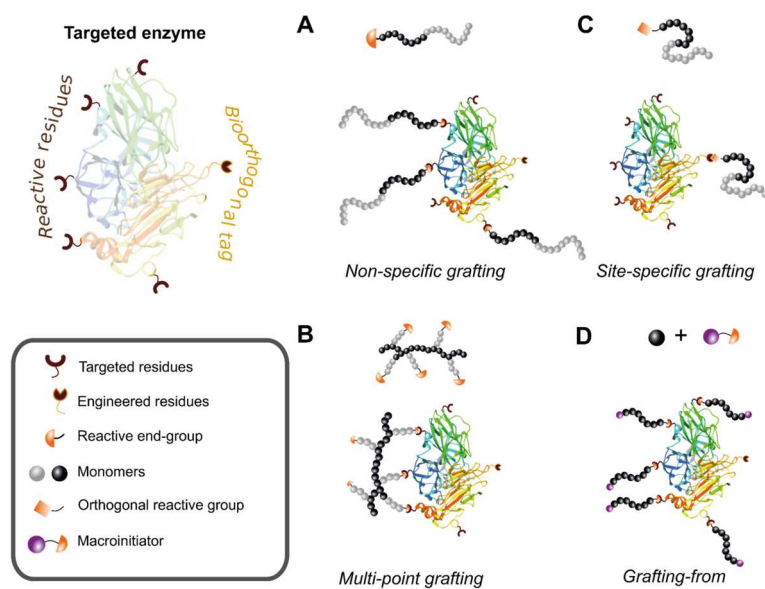


Figure 1-3. Schematic illustration of the strategies that are carried out for the formation of covalent enzyme-polymer hybrids. A) Non-specific grafting of proteins, using polymers with a single

reacting group and several target residues within the protein. B) Multi-point strategy using polymers with multiple anchoring sites. C) Site-specific grafting using a biorthogonal approach. D) *Grafting-from* approach that entails the conjugation of the macroinitiator to the protein and the subsequent *in-situ* polymerization after the addition of monomers.

In the specific case of biocatalysis, the benefits of anchoring polymers to catalytic proteins are multifold.⁵¹ Only through the combination of both, the enzymes can reach unique conformational properties such as nanostructured assembly. The polymeric moiety can be just a mere solid architecture that provides suitable anchoring sites for the enzyme (widely used in the field of heterogeneous biocatalysis) or can actively participate in tailoring the properties of the enzyme in the pursuit of a synergistic enhancement of the catalytic system.⁴⁵ Today, we know that there are several parameters related to the nature of the polymer, such as the charge, hydrophobicity, length, and functionality, which have a great impact on the performance of the hybrid system, and therefore have to be controlled with high precision.⁵² Importantly, enzyme-polymer conjugates show good substrate/product diffusion, uniform particle size, and prevent particle aggregation. However, the chemical modification of the sequence of the protein, together with the low grafting degree that is usually achieved, are the main hurdles which the enzyme-polymer conjugates face. Therefore, other approaches that keep the enzymes structure unmodified, while providing a favorable environment for the catalysis, are being explored.

1.3.1 Single Enzyme Nanogels (SENs)

This PhD work has been focusing on the use of an alternative way to combine enzymes and tailored polymers into a single material. We investigated the formation of a very fine crosslinked polymeric network, a hydrogel, on the surface of the enzyme, which generates soft nanomaterials called Single Enzyme Nanogels (SENs, **Figure 1-4**).⁵³ These are "core-shell" type hybrid structures with a single biomolecule in the core and a protective hydrogel shell. The diameters of SENs can vary between ca. 10-20 nm in

dependence on the type of enzyme. Furthermore, the shell thickness can be tuned from 0.5 to 10 nm by varying the concentration of monomers and crosslinkers during the synthesis.⁵⁴ It is noteworthy that there are some examples in the literature where 2-3 different enzymes are encapsulated within the same nanogel.^{55,56} The small sizes of SENs make them very interesting for applications such as enzyme delivery *in vivo*, especially to cross the Blood-Brain Barrier (BBB), a highly regulated endothelial structure that protects the brain.⁵⁷

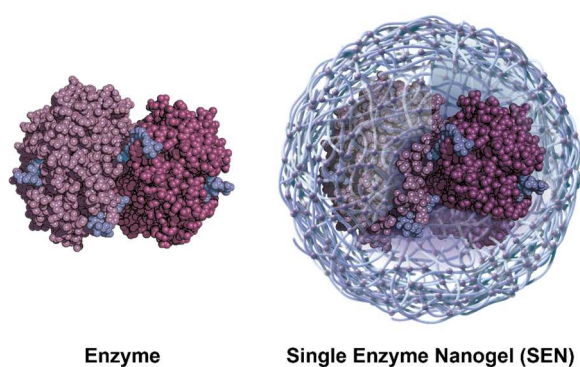


Figure 1-4. Ball model representation of the structure of an unmodified enzyme, i.e., glucose oxidase (GOx, left), and the corresponding Single Enzyme Nanogel (SEN, right). The crosslinked polymeric network is illustrated in blue.

The first paper reporting SENs was published in 2006 by Yan *et al.*⁵⁸ They showed that the kinetic constants (k_{cat} and K_M) of the encapsulated horseradish peroxidase (HRP) were very similar to those showed by the free enzyme, demonstrating that the capsule barely affected the transport of the substrate to HRP, the reaction kinetics, and the product discharge. The main reasons for the conservation of the catalytic performance of the hybrids are likely related to the individual encapsulation of each enzyme, and on the programable porosity and thickness of the hydrogel, which can be tuned to minimize mass transport issues.⁵⁹ In the same paper, Yan *et al.* also demonstrated that HRP nanogels could retain 80% of their initial activity after 90 min of incubation at 65°C, whereas native HRP was completely inactivated under the same conditions. Moreover, in the presence of organic solvents, the HRP activity was also retained due to the

hydrophilic environment provided by the nanogel. The authors attributed the higher thermal stability of the HRP nanogel to the multiple interactions between the polymeric network and the protein along the whole protein surface. It is noteworthy that neither the synthesis procedure, nor the eventual formation of the capsule affected the protein structure, as indicated by the circular dichroism spectra of the protein that remained unaltered after polymerization.⁶⁰ These attractive performances of SENs, which usually outperform the advantages shown by covalent enzyme-polymer conjugates, are explained with the complete entrapment of the enzyme by a polymeric network which at the same time maintains the required protein flexibility for carrying out the catalysis.

1.3.1.1 *Enzymes implemented with SEN technology*

Since 2006, a wide range of enzymes has been individually encapsulated using single enzyme nanogel technology (**Figure 1-5**). SENs were fabricated with therapeutic enzymes such as caspase-3 (CAS3),^{61–63} catalase (CAT),^{64–67} HRP,^{68,69} arginine deaminase,⁷⁰ urate oxidase (UOx),^{71,72} and CRISPR-associated protein 9 (Cas9)⁷³ to treat various diseases such as cancers, gouty arthritis, and COVID-19. Importantly, nanogels formed by therapeutic non-catalytic proteins, e.g., vascular endothelial growth factors (VEGF),^{74,75} anticancer p53,⁷⁶ bone morphogenetic protein-2 (BMP-2),⁷⁷ tumor necrosis factors (TNF),⁷⁸ and monoclonal antibodies,^{57,79–81} have shown great potential for the treatment of diseases such as cancers with central nervous system metastases, lung adenocarcinoma or metastatic B-cell lymphoma. Proteins with other functionalities, e.g., green fluorescent protein (GFP),⁶⁸ bovine serum albumin (BSA),^{68,74} and hemoglobin⁸² have also been successfully applied as templates to form single enzyme nanogels.

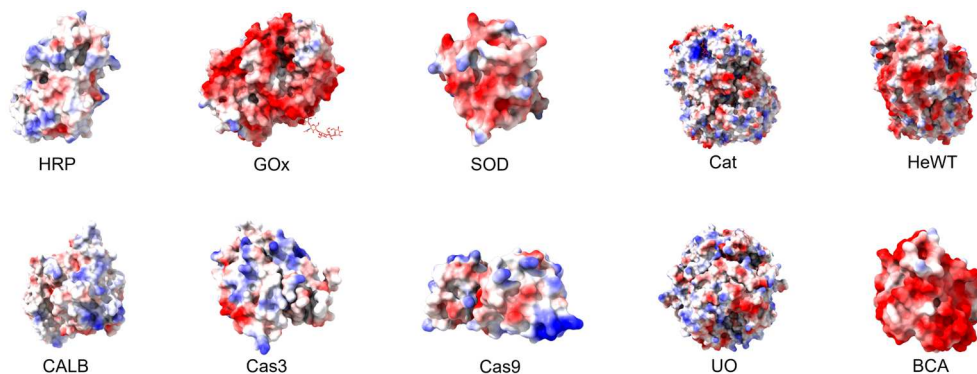


Figure 1-5. Representation of the electrostatic surfaces of the main enzymes used for the fabrication of SENs by now. The negatively charged surface areas are shown in red, while the positive ones are blue.

As enzymes with biotechnological relevance, organophosphorus hydrolase and butyrylcholinesterases SENs were used to treat or prevent organophosphate poisoning.^{83,84} Superoxide dismutase (SOD) nanogels were also investigated for anti-aging processes.⁶⁸ In addition to the biomedical applications mentioned above, SENs have been investigated in other fields. Firefly luciferase (FL) was encapsulated to quantify real-time cell internalization with a kinetic approach.⁸⁵ DNase nanogels effectively degraded biofilms,⁸⁶ and phenol compounds in wastewater were remediated with HRP nanogels.⁸⁷ In another example, GOx and tyrosine kinase were used to improve the stability of the biorecognition of electrochemical biosensors.^{13,88–90} Other enzymes, for example, penicillin G amidase (PGA),⁹¹ lipases,⁹² and bovine carbonic anhydrase (BCA)⁶⁰ were encapsulated to demonstrate that this technology provides great advantages in terms of catalytic stability, which is very convenient for chemical synthesis or environmental purposes.

1.3.1.2 Synthesis of SENs

The most common synthesis procedure of SENs consists of two steps as shown in **Figure 1-6A**. At first, polymerizable vinyl groups are anchored to the enzyme surface by covalent modification of lysine residues, usually achieved by N-acryloxysuccinimide

(NAS). Then, an *in situ* free radical polymerization is carried out on the protein surface by the coaddition of monomers, crosslinkers, the acrylated enzyme, and the initiators of the polymerization, i.e., tetramethylethylenediamine (TEMED) and ammonium persulfate.⁵⁸ The vinyl groups grafted onto the enzyme act as anchor points to hold the nanogel and facilitate the *in situ* polymerization. The underpinning mechanism that leads to the formation of the nanogel was elucidated by molecular simulation and fluorescence resonance energy transfer (FRET) experiments.⁹³ It was shown that monomers and crosslinkers can accumulate locally around the enzyme surface through hydrogen bonding, electrostatic forces, and hydrophobic interactions. The concentration of the monomers close to the surface of the protein permits the *in situ* formation of the polymeric capsule upon addition of the initiators. However, this protocol has some drawbacks. The acrylation step may compromise the stability and bioactivity of the enzyme due to induced structural changes in the protein or to the undesired modification of lysines in the catalytic pocket of some enzymes, e.g., ω -transaminases (ω -TA). Moreover, the chemical modification step is largely dependent on the amount and type of the available amino acid residues of the protein surface, which limits its applicability. Further, the covalent linkage to the polymeric shell impedes the release of therapeutic proteins from the nanogel, limiting their use in biomedical applications.⁷⁴

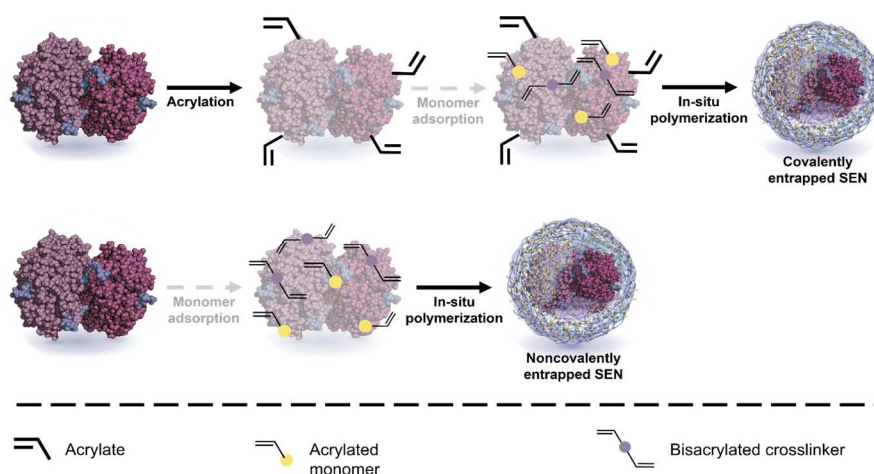


Figure 1-6. Synthesis of single enzyme nanogels (SENs). (A) Covalently entrapped SEN formation consists of two steps: i) acrylation of the enzyme and ii) subsequent in situ radical polymerization in the presence of monomers, crosslinkers, and initiators. (B) Synthesis of non-covalent SEN consists of a single step: the polymerization occurs in the presence of the monomers, crosslinkers, initiators and the unmodified enzyme.

In 2009, the first “noncovalent SEN” was published.⁶¹ It was shown that no enzymatic acrylation step is necessary for the assembly of the nanogel when the interactions between the monomers and the enzyme are sufficiently strong. (**Figure 1-6B**). The surfaces of enzymes are chemically heterogeneous with patches of different wetting properties and charges (**Figure 1-5**).⁹⁴ Thus the use of monomers/crosslinkers or additives that facilitate the physical adsorption and accumulation of polymerizable groups on the surface of the protein, rather than acrylation, is being investigated.^{61,95} Non-covalent nanogels show similar sizes and morphologies to covalently bound nanocapsules.⁶¹ Interestingly, Beloqui *et al.* demonstrated that the addition of small amounts of short carbohydrates, such as saccharose or cellobiose, reduced the repulsion forces between the monomers and the enzymes, thereby facilitating an agglomeration of the monomers at the surface of the protein and thus enhancing the encapsulation yield.⁹⁶ Moreover, they also observed that it was possible to control the thickness of the capsule, regardless of the type of protein utilized, only by varying the monomer concentration. Importantly, they demonstrated that polymeric shells with thicknesses of more than 2 nm exerted significant mass transfer issues and, therefore, were detrimental to the enzymatic activity.

1.3.1.3 Monomers and Crosslinkers

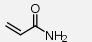
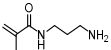
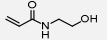
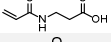
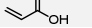
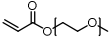
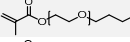
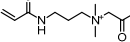
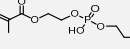
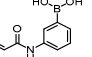
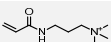
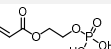
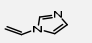
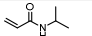
Tailoring the polymeric shell of SENs. The physicochemical properties of SENs are customized by the careful selection of functional monomers (**Table 1-1**) and crosslinkers (**Table 1-2**).¹⁷ The most applied monomer is acrylamide (AA; **Table 1-1a**), used as propagating monomer for the synthesis of polyacrylamide (pAA) in most of the works.⁹⁷ Cationic monomers with primary amines, especially N-(3-aminopropyl)

methacrylamide (APM; **Table 1-1b**), are very beneficial for the internalization of SEN into cells, as well as providing functional groups for eventual covalent post-polymerization modifications.⁶¹ For some applications, such as enzyme therapy, a prolonged circulation time in the bloodstream of the nanomaterial is desired and could be achieved with the design of strongly hydrophilic and biocompatible nanocapsules. In this regard, monomers with hydroxyl groups, i.e., hydroxyethyl acrylamide (HEAA; **Table 1-1c**),⁹⁸ or with carboxylic functional groups, i.e., 2-carboxyethyl acrylate (CEAA; **Table 1-1d**),⁹⁹ or with propenoic acid (PA; **Table 1-1e**),¹⁰⁰ may be appropriate. Moreover, poly(ethylene glycol) (meth)acrylate can also be introduced into the nanogels to increase their flexibility, enhance the antifouling effect, and diminish nanogel immunogenicity (PEG(M)A; **Table 1-1f** and **Table 1-1g**).^{66,73} More importantly, zwitterionic monomers, moieties with equal amount of cationic and anionic groups in one repeat unit, such as carboxybetaine acrylamide (CBAA; **Table 1-1h**) and 2-methacryloyloxyethyl phosphorylcholine (MPC; **Table 1-1i**),⁷¹ lead to strong hydration of the nanogel resulting in excellent anti-fouling properties. For example, Jiang and coworkers demonstrated that uricase encapsulated with a CBAA-based polymer showed improved pharmacokinetic performance in comparison with a uricase-PEG conjugate. Moreover, the use of CBAA caused less serum protein adsorption and lower anti-polymer antibody generation.⁷¹ The use of these ionic monomers leads to high encapsulation efficiencies in the case of noncovalently entrapped SENs due to their spontaneous accumulation on the surface of the protein.^{73,97} 3-acrylamidophenylboronic acid (APBA; **Table 1-1j**) also increases the hydrophilicity of the nanogel binding glucose to phenylboronic acid and, thus, facilitates the diffusion of the substrate.⁷⁰ Another monomer of great interest is the pH-responsive (3-acrylamidopropyl) trimethyl ammonium (APTAC; **Table 1-1k**), which bears a quaternary amine group that can retain negatively charged molecules within the nanogel. Conversely, monomers with phosphates can retain positively charged molecules such as divalent cations like cerium (MAEP; **Table 1-1l**).⁸⁹ Vinyl imidazole (VI; **Table 1-1m**) can be successfully utilized for different purposes such as endosomal escape and the coordination of metal cations.^{73,99}

The second functionality has been fully developed in this thesis. Finally, thermo-responsive enzyme nanogels can be also fabricated for enzyme recycling using N-isopropyl acrylamide as propagating monomer (NIPAM, **Table 1-1n**).¹⁰¹

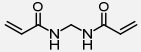
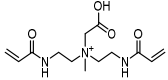


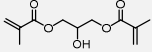
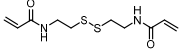
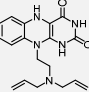
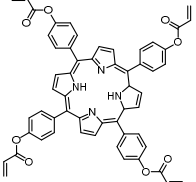
The responsiveness of the SENs can be controlled. Crosslinkers are required to form the nodes of the polymeric gel on the surface of the enzyme. Nondegradable N,N'-methylenebisacrylamide (BIS) was the first crosslinker used to improve the stability of enzymes using the SEN strategy (BIS; **Table 1-2a**) and is still the most widely used today. Bisacrylated carboxybetaine is another common non-degradable crosslinker (CBAAX; **Table 1-2b**).⁷¹ The incorporation of CBAAX increases the hydrophilicity of the system considerably, which makes it greatly interesting for the delivery of enzymes. However, even though SENs are a very versatile platform at the industrial and biomedical levels, the non-degradable network sieves the reagents that are catalyzed, limiting the access of large substrates through the pores of the nanogel.⁹⁷ To address this problem Gu et al. introduced for the first degradable crosslinker, i.e., bisacryloylated peptide (VDEVDTK), into a noncovalently encapsulated CAS3 (**Table 1-2c**).⁶¹ There are further works which show degradation of the crosslinker by environmental proteases (**Table 1-2d**).⁶² Importantly, the residues generated by the degradation of the nanogel are expected to be biocompatible, which is key for biomedical applications.¹⁰² To date, several degradable crosslinkers, responsive to internal/external stimuli, have been designed to facilitate an enzyme release.¹⁷ For instance, glycerol dimethacrylate (GDMA; **Table 1-2e**), responsive to acidic pH, can be successfully employed to release enzymes upon entering acidic endosomes. Redox-responsive crosslinkers have also been developed for the direct delivery of enzymes to the cytosol. Glutathione, an antioxidant present in mammalian cells' cytosol, can break the disulfide bonds of N,N'-Bis(acryloyl)cystamine (BAC; **Table 1-2f**).⁶³ In addition, other crosslinkers can be used for fluorescent tracing (**Table 1-2g**) or PET imaging (**Table 1-2h**).^{66,103}

Table 1-1. Summary of polymeric monomers used to synthesize Single Enzyme Nanogels (SENs).

	<i>Monomer</i>	¹ <i>Abbr.</i>	<i>Structure</i>	<i>Functionality</i>	<i>Enzyme</i>	<i>Reference</i>
a	Acrylamide	AA		Propagating monomer, biocompatibility	1.3.1.1	53–55,58,61–63,67,68,72,74–77,80,82,83,85,91,92,104–120
b	N-(3-aminopropyl) methacrylamide	APM		Cell internalization, post modification	² CAS3, ³ OPH, ⁴ GOx, ⁵ CAT, ⁶ HRP	61–63,65,70,72–75,83,85,86,101,114,117,118
c	Hydroxyethyl acrylamide	HEAA		Hydration	GOx, ⁷ β -Gluc	98,99,108,121
d	2-Carboxy ethyl acrylate	CEAA		Hydration	GOx	99
e	Propenoic acid	PA		Post-polymerization	GOx	100
f	Acrylate methoxy poly(ethylene glycol)	PEGA		Flexibility, hydration, antifouling	⁸ Cas9	73
g	Poly (ethylene glycol) methacrylate	PEGMA		Hydrophilicity	CAT	66
h	Carboxybetaine acrylamide	CBAA		Hydration, antifouling,	Uricase, ⁹ BChE, HRP	71,84,87,116
i	2-methacryloyloxyethyl phosphorylcholine	MPC		Choline and acetylcholine analogs, weaken cell interaction	CAT, ¹⁰ OxO	65,122
j	3-acrylamidophenylboronic acid	AAPBA		Increase substrate diffusion	GOx	70
k	(3-Acrylamidopropyl) trimethyl ammonium	APTAC		Interaction with negative (macro)molecules	¹¹ HeWT	-
l	Monoacryloyloxyethyl phosphate	MAEP		Interaction with positive molecules	GOx	89
m	Vinyl imidazole	VI		Metal ion coordination / endosomal escape	GOx, Cas9	73,98,99,121
n	N-isopropyl acrylamide	NIPAM		Thermoresponse	OPH	101

¹Abbreviation, ²Caspase-3, ³Organophosphorus hydrolase, ⁴Glucose oxidase, ⁵Catalase, ⁶Horseradish peroxidase, ⁷ β -Glucosidase, ⁸CRISPR-associated protein, ⁹Butyrylcholinesterase, ¹⁰Oxalate oxidase, ¹¹ ω -amino transaminase from *Halomonas elongata*.

Table 1-2 Summary of polymeric crosslinkers used to synthesize SENs.

	<i>Crosslinker</i>	<i>Abbreviation</i>	<i>Structure</i>	<i>Responsive to / functionality</i>	<i>Enzyme</i>	<i>Reference</i>
a	N, N'.methylene bisacrylamide	Bis		Stable and neutral capsules	1.3.1.1	55,58,65,66,70,73,83,85,103,111,113,117,118,122
b	Bisacrylated Carboxybetaine	CBAAX		Maximize hydration, Antifouling	Uricase ³ BChE	71,84
c	Bisacryloylated peptide	VDEVDTK		Protease (Cas3)	⁴ CAS3	61
d	Bisacryloylated peptide	Ahx-RVRRSK		Protease (furin)	CAS3	62
e	Glycerol dimethacrylate	GDMA		Acidic environment	⁵ HRP, ⁶ SOD, CAS3	68,116
f	N,N'-Bis(acryloyl)cystamine	BAC		Redox reactions (¹ GSH degradable)	CAS3, ⁷ Cas9	63,73
g	2'-diallylamino-ethyl flavin	DAA-flavin		Fluorescent tracing	⁸ GOx	103
h	Meso-tetra(p-hydroxyphenyl) porphine	THPP		Photosensitizer, ² SPECT imaging	⁹ CAT	66

¹Glutathione, ²Single-photon emission computed tomography, ³Butyrylcholinesterase, ⁴Caspase-3, ⁵Horseshoe peroxidase, ⁶Superoxide dismutase, ⁷CRISPR-associated protein, ⁸Glucose oxidase, ⁹Catalase.

1.3.1.4 *Post polymerization modifications*

The chemistry of SENs can be easily tailored. The incorporation of functional groups that can be modified after the polymerization is a distinctive feature of SENs (summary of several modifications shown in **Table 1-3**). As example, two different amino functionalized nanogels, UOx and CAT, were covalently modified with adamantane-PEG and cyclodextrin-PEG, respectively, to form multienzyme nanoclusters (**Table 1-3a**).⁷² Our group also modified amino functionalized nanogels via amidation (EDC/NHS coupling method) to graft imidazole groups, which is described in more detail in **Chapter 5 (Table 1-3b)**.¹¹⁸ The same chemistry was also utilized to activate carboxyl terminated SENs with pyrrole rings (**Table 1-3c**).¹⁰⁰

SENs are excellent platforms to accommodate functional nanomaterials. The incorporation of amino groups into the nanogel also allowed the conjugation of gold nanoparticles of 8 nm in size (**Table 1-3d**) and fluorescent quantum dots with sizes of 2-3 nm (**Table 1-3e**) through EDC/NHS coupling.^{114,117} The conjugation of the nanoparticles imparted additional functionalities, i.e., enhanced bioluminescence, to the nanogels. In one work by our group, SENs bearing imidazole molecules were used as scaffolds to accommodate and protect organometallic catalysts, i.e., hemin (**Table 1-3g**, see **Chapter 6**) by metal-imidazole coordination.^{99,121} In our latest work, we made use of the amino groups of the nanogel to reversibly bind cofactors, i.e., pyridoxal 5'-phosphate (PLP), around the enzyme, which increased the operational stability of PLP-dependent enzymes (**Table 1-3f**, see **Chapter 7**). We also fabricated cerium loaded SENs as self-responsive glucose bionanosensors (**Table 1-3h**) with a detection limit as low as 73 nM.⁸⁹

Table 1-3. List of SENs modified after the polymerization reaction.

	<i>Enzyme</i>	<i>Monomer</i>	<i>Post-polymerization</i>	<i>Application</i>	<i>Ref.</i>
a	¹ UOx ² CAT	⁶ AA, ⁷ APM	¹¹ Ad-PEG, ¹² CD-PEG	Bienzymatic confinement	72
b	³ HRP	AA, APM	¹³ 4-ICA	Biomineralization	118
c	⁴ GOx	⁸ PA	Pyrrrole	Biosensor	100
d	HRP	APM	¹⁴ AuNC	Bioluminescence	117
e	HRP	AA, APM	¹⁵ CdTe QD	Bioluminescence	114
f	⁵ HeWT	APM, AA	¹⁶ PLP	Cofactor retention	-
g	GOx	⁹ HEAA, VI	Hemin	Bioremediation and cofactor recycling	99,121
h	GOx	AA, ¹⁰ MAEP	¹⁷ Ce (III)	Biosensor	89

¹Urate oxidase, ²Catalase, ³Horseradish peroxidase, ⁴Glucose oxidase, ⁵ ω -transaminase from *Halomonas elongata*, ⁶Acrylamide, ⁷N-(3-aminopropyl)methacrylamide, ⁸Acrylic acid, ⁹N-Hydroxyethyl acrylamide, ¹⁰Monoacryloxyethyl phosphate, ¹¹Adamantane-PEG, ¹²Cyclodextrin-PEG, ¹³4-imidazole carboxylic acid, ¹⁴Gold nanocrystals, ¹⁵CdTe quantum dots, ¹⁶Pyridoxal 5'-phosphate, ¹⁸Cerium.

1.4 ENZYME IMMOBILIZATION

Heterogeneous Biocatalysis. The immobilization of enzymes on insoluble materials has been gaining importance over the last 50 years.¹²³ Immobilized enzyme refers to the state of enzymes in which they are confined within or attached to solid materials. They remain in a solid state while substrates and products can diffuse between the solid and liquid phases. In this way the insoluble enzymes, termed heterogeneous biocatalysts, exhibit properties different from those shown by free enzymes (homogeneous biocatalyst).¹²⁴ The advantages of heterogeneous biocatalysis over the homogeneous counterpart are mainly: (i) the catalysts can be easily separated from the product and can be reused, which is of great importance for all application fields; and (ii) reduction of enzyme inactivation due to high temperatures, extreme pH, organic solvents, or inhibitors, which allows enzymes to be used and stored for a longer time.¹²⁵ For this reason, enzyme immobilization is a very promising approach to overcome the above problems. However, immobilized enzymes usually show impaired activity due to conformational changes of their native structure upon direct physical contact with the solid material¹²⁶ and they may show mass transfer hindrances if entrapped inside solid structures.¹²⁷ To alleviate these impediments, research groups have focused their attention on the development and extensive study of new methodologies, functional materials, and the most suitable chemistries to remove the hurdles found in the enzyme immobilization

procedure.^{128,129} The most used strategies for immobilization of enzymes are the following (**Figure 1-7**): (i) immobilization into prefabricated carriers, (ii) entrapment or encapsulation into organic or inorganic polymer matrixes, and (iii) crosslinking of enzyme aggregates or crystals.^{130–132}

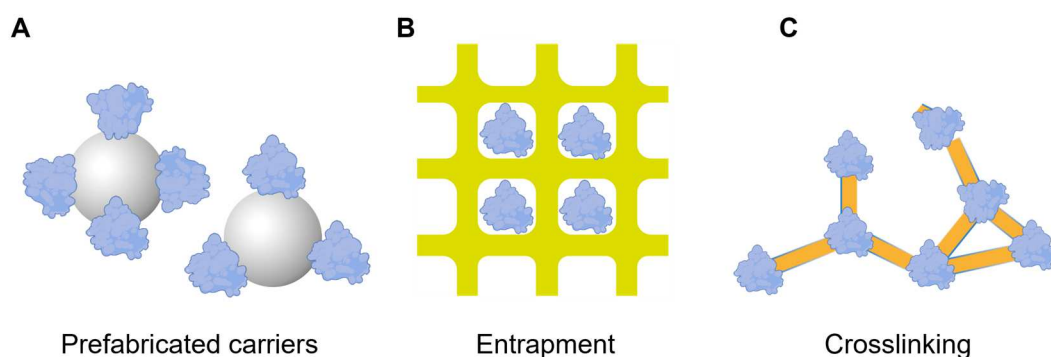


Figure 1-7. Scheme of the most common enzyme immobilization strategies: A) immobilization into prefabricated carriers, B) entrapment or encapsulation, and C) crosslinking of enzyme aggregates or crystals.

1.4.1 Use of prefabricated carriers

The attachment of enzymes to carriers (i) can be done through physical (especially hydrophobic and van der Waals), ionic, or covalent binding (**Figure 1-7A**). Physical adsorption is the easiest approach, but the support-protein interactions are usually too weak to retain the biocatalyst in presence of large amounts of reagents, high ionic strength, or under harsh conditions. In contrast, covalent bonds anchor the enzyme to the support very tightly, which is very convenient to avoid enzyme leaching. Carriers need to be functionalized with vinyl, amine, or epoxy groups, which form covalent bonds with the primary amines present on the surface of the protein.¹³² However, the covalent binding approach has a downside: if the enzyme is irreversibly inactivated, both the enzyme and the often-expensive support are rendered useless. As an alternative approach, affinity-based interactions open further avenues for the fabrication of heterogeneous biocatalysts based on the selectivity and complementarity of

biomolecules, e.g., antibodies/antigens, His-tagged proteins/metal ions (Co^{2+} , Ni^{2+}), etc.¹³³

1.4.2 Entrapment into (in)organic polymeric matrices

Enzyme entrapment (ii) is a bottom-up approach that requires the synthesis of a polymeric network (organic or inorganic) in the presence of the enzyme (**Figure 1-7B**).¹³⁴ The enzymes are confined within the porous structure, allowing their movement and avoiding direct contact with the matrix. In recent years, new materials, i.e., protein-inorganic nanoflowers, have been developed through the synthesis of metal phosphate biominerals, which are eventually used to trap enzymes at the nanoscale. In this case, besides the typical benefits generated from the immobilization, the enzyme activity can be increased due to the cooperative binding of the substrate to the active site.^{135,136}

Enzyme nanoflowers are not only beautiful protein-inorganic hybrids. One of the most successful and innovative nanobiocatalysts are protein-inorganic hybrid nanoflowers (NFs), which are very attractive for many biocatalytic applications, e.g., biosensing and biocatalysis (**Figure 1-8A**).^{136,137} The generation of nanoflowers is a bottom-up approach that exploits the metal ion coordination capacity of specific enzyme residues, e.g., histidine. The formation of these nucleation points allows the subsequent growth of metal phosphate salts that will efficiently entrap the enzyme within 72h. To date, different divalent metal cations, i.e., copper (II), manganese (II), cobalt (II), iron (II), calcium (II) have been used in the presence of phosphate salts to construct these NFs.¹³⁸ The nanoflower synthesis procedure is simple, minimizing the biocatalyst manipulation and immobilization steps. The most outstanding features of the nanoflowers are their 3D spatial configuration, which not only stabilizes the enzyme but also enhances its catalytic activity. This effect is achieved thanks to the high enzyme loading and the synergistic effects between the inorganic and organic components.¹³⁶

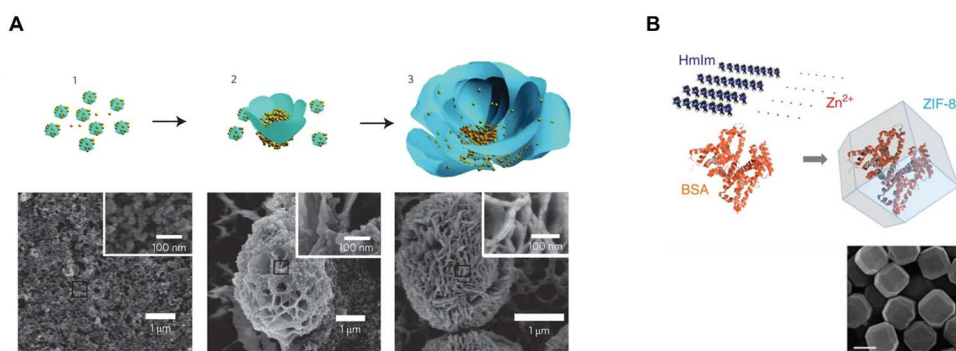


Figure 1-8. Fabrication workflow and SEM images of **A)** protein-inorganic nanoflowers (NFs) and **B)** enzyme-ZIF-8 hybrids.

Metal-organic frameworks (MOFs) are very versatile for enzyme entrapment. MOFs are highly ordered crystalline nanostructures with cavities that allow for immobilization of enzymes.¹³⁹ The synthesis conditions define the distribution of the enzyme within the MOF.¹⁴⁰ Enzymes can be trapped either in a *de novo* approach during MOF formation or following a post-synthesis method in which MOFs are used as carriers. Zeolitic imidazolate frameworks (ZIF-8) are among the most studied MOFs for enzyme immobilization, as they are formed under mild conditions from the ability of zinc ions to coordinate imidazole molecules (**Figure 1-8B**).^{141,142} Importantly, enzyme entrapment by ZIF-8 improves enzyme tolerance towards pH and high temperatures, enabling the enzyme reuse. In some reported cases the enzymatic activity has increased up to tenfold.^{143,144}

1.4.3 Crosslinked of enzyme aggregates

The cross-linking of enzymatic aggregates (iii), known as carrier-free enzyme immobilization, is the only reported strategy in which carriers are not utilized for building heterogeneous biocatalysts (**Figure 1-7C**). In fact, more than 90% (compared to previous approaches) of the total mass of the heterogeneous biocatalyst is eliminated. For the formation of those crosslinked enzyme aggregates (CLEAs), enzymes are usually precipitated with organic solvents and then irreversibly cross-linked with glutaraldehyde. Hence, CLEAs

avoid the use of expensive supports and prevent enzyme leaching.^{145,146} However, the loss of enzymatic activity is usually very significant (less than 50% *vs.* the native enzyme). The chemical modification of the protein structure and the precipitation with organic solvents generally affect detrimentally the catalytic performance. Furthermore, mass transfer issues, caused by enzyme crowding, are also relevant.¹⁴⁷ Therefore, this enzyme immobilization strategy still has much room for improvement.

1.4.4 Multifunctional Nanobiocatalysts

Enzymes coupled to nanocarriers: the size matters. In the last decade, different technologies for the formation and assembly of nanobiocatalysts (NBCs), emerging catalysts that synergistically blend nanotechnology and biotechnology, have been developed.^{127,148–150} Their nanometric size favors enzyme kinetics and selectivity towards substrates, enhancing their catalytic performance considerably.¹⁵⁰ This improvement has been attributed to enzyme confinement effects and to the interfacial interactions between the two moieties that facilitate the integration of two or more activities into the same entity.¹⁵¹ This close positioning of two differently functional (bio)catalysts in a nanoconfined volume is beneficial, for example, for the directional channeling of reaction intermediates.^{99,152}

The fabrication of NBCs is significantly different from that provided by classical enzymatic immobilization. Nanomaterials used as carriers offer high surface area, which favors rapid immobilization as well as high enzyme loadings and low diffusion issues.¹⁵⁰ In addition, NBCs promise exciting advantages regarding enzyme stability and the creation of a favorable microenvironment for the enzyme.¹⁵³ To date, the rapid development of material science allows a tremendous diversity of nanocarriers in terms of the nature of the material and morphology. Metal-based nanomaterials, *i.e.*, gold and Fe₃O₄ nanoparticles (**Figure 1-9A-B**), CeO₂ nanorods, *etc.*, have been widely employed for their high activity and recycling properties.¹⁵⁴ Carbon-based nanosupports, *i.e.*,

graphene nanoflakes and carbon nanotubes (**Figure 1-9C**), are very appropriate due to their excellent thermal stability, biocompatibility, and inertness.¹⁵⁵ Polymer-based nanocarriers, i.e., nanofibers and nanogels, are suitable for the fabrication of NBCs due to their large-scale production, high enzyme loading, and abundant functional groups, i.e., epoxy groups, which allow favorable interactions with enzymes.^{45,131} In addition, mesoporous silica-based nanocarriers have been successfully exploited for enzyme entrapment (**Figure 1-9D**).¹⁵⁶ It is worth mentioning that carrier-less nanoscale systems have also been fabricated as protein-polymer hybrids, which will be discussed in detail throughout this thesis.^{99,108,121}

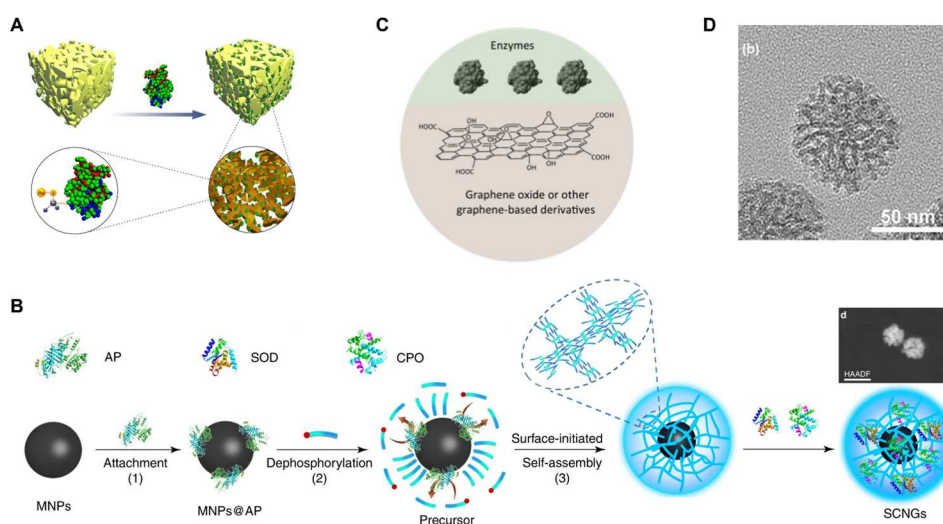


Figure 1-9. Examples of multifunctional nanobiocatalysts. A) Lipase immobilization into nanoporous gold. B) Supramolecular hybrid nanogel around Fe_3O_4 nanoparticles for SOD and chloroperoxidase immobilization. C) Immobilization of enzymes onto graphene-based nanomaterials. D) Mesoporous-silica nanoparticles used to entrap lipase. Figures adapted with permissions from Plos One (2011, A), Nature Communications (2019, B), Trends in Biotechnology (2014, C), and Nano Research (2017, D).^{154,156–158}

Multifunctional nanobiocatalysts to perform cascade reactions. The combination of enzymes with chemical catalysts, i.e., organometallic compounds and metal complexes, in one single entity is a rapidly developing research field.^{159,160} Performing more than one consecutive

reaction in one pot may increase the selectivity of the reactions and the overall yields by shifting the equilibrium in reversible reactions.¹⁶¹ Moreover, the amount of waste is reduced, generating higher economic and environmental benefits. However, chemoenzymatic cascades are quite challenging due to intrinsic incompatibility between the enzyme and the chemical catalyst. On the one hand, metal complexes of noble metals, which are considered efficient chemical catalysts, can bind specific amino acids from enzymes, hampering their activity.¹⁶² On the other hand, the optimum reaction conditions of both catalysts are completely different, e.g., temperature, pressure, presence of organic solvents, etc.¹⁶³

Rational design of chemoenzymatic nanobiocatalysts is needed to confine different (bio)catalysts in very reduced and heterogeneous spaces, avoiding reaction intermediates to diffuse to the bulk media, mimicking organelle operating mode. Likewise, these advanced hybrid nanomaterials will generate synergistic effects between catalysts, as well as enable compartmentalization strategies to solve the problems associated with incompatibility.

1.5 HETEROGENEOUS BIOCATALYST FORMATION FROM SENS

SENSs are of high interest to build heterogeneous biocatalysts. The nanometer scale and ease of functionalization of the nanogel make SENSs ideal building blocks for the fabrication of heterogeneous catalysts. In the literature, there are several examples of SENSs covalently immobilized on carriers of different nature and sizes. Wei et al. immobilized organophosphate hydrolase (OPH) amino-functionalized SENSs on carboxylated cellulose,⁸³ thereby improving the enzyme stability during the recycling and storage. In another work, catalase (CAT) amino-functionalized SENSs were covalently immobilized on cellulose acetate fibers from cigarette filters following EDC/NHS coupling chemistry. Free radicals from tobacco smoke were scavenged while the polymeric

capsule prevented dissociation of the monomer at high temperatures.⁶⁷ Similar SENs were also covalently grafted onto silica microparticles to improve the performance of biocatalytic micromotors.¹⁰⁹ Importantly, the increase of the amount of amino groups on the surface of the catalysts (75% higher in the case of SEN *vs.* free CAT) led to an enhanced immobilization yield, from 8% for free CAT to 25% for nanogels.

The entrapment of SENs has also been fostered for the fabrication of heterogeneous biocatalysts. OPH nanogels were used as building blocks for the synthesis of enzyme-silica nanocomposites with high activity.¹¹¹ In another work, penicillin G amidase (PGA), glucose oxidase (GOx), and horseradish peroxidase (HRP) nanogels were encapsulated in hierarchical mesoporous silica forming hybrid nanomaterials.⁹¹ Moreover, physically crosslinked pH-responsive microgels have been utilized for entrapping SENs for biomedical applications, acting as a shield against immunogenicity, while enzyme stability was enhanced.¹¹⁵ Interestingly, SENs were also entrapped in metal-organic frameworks (MOFs).¹¹⁰ The biocatalytic system exhibited improved stability and recyclability, which were attributed to the synergistic effect generated by the thin polymeric layer and the capsule provided by the MOF.

In addition, patterned films of SENs were formed which were important either to protect enzymes from organic solvents, i.e., the ethanol and chloroform necessary to carry out the film formation or to reduce the non-specific adsorption of unwanted proteins on the surfaces.^{107,112}

Therefore, it is evident that heterogeneous catalysts formed with SENs are becoming increasingly widespread and complex. In this doctoral thesis, harnessing the unique features of SENs, we have applied the previously described immobilization strategies to generate a series of multifunctional nanobiocatalysts. SENs have been covalently immobilized on prefabricated carriers, crosslinked for an assembly into ordered catalytic films, and entrapped in biominerals for obtaining high-performance heterogeneous biocatalysts.

Chapter 2 SCOPE AND OBJECTIVES

A great effort is being invested to facilitate the use and application of enzymes in our daily lives in order to benefit from their enormous catalytic potential. Protein engineering, chemical modification and immobilization of proteins are improving the lifetime and efficiency of enzymes in a number of technological and industrial applications. This PhD thesis focuses on the nanotechnological and biotechnological approaches of relevance for the design and production of advanced biomaterials, one of the priorities established in the RIS3 strategy of the PCTI Euskadi 2030 and Horizon Europe programs.

The main objective of this thesis is to develop innovative biocatalytic materials, which help to simplify, facilitate, and expand the use of enzymes.

The decision to conduct this thesis came about when in the summer of 2017 I stepped into Prof. Knez's Nanomaterials group at CICnanoGUNE BRTA for a two-month internship under the guidance of Dr. Beloqui. She was a Diputación de Gipuzkoa Fellow with a MINECO project (MAT2017-888-08-R) in which the development of nanostructured biomaterials for applications in heterogeneous biocatalysis was planned. The area of research, i.e., hybrid materials, was totally new to me, but I decided to take advantage of that excellent opportunity. Dr. Beloqui helped and taught me many of her skills. Fortunately, I realized that I was fascinated by this field, and I jumped right into the world of catalytic biomaterials. In 2018, I obtained the PhD grant from the Basque Government (PRE_2021_2_0151) and started an exciting full-time scientific career at the same research institute, within the PhD program "*Physics of nanostructures and advanced materials*". In the first part of the PhD (until summer 2019), I focused on the development of heterogeneous catalysts fabricated through the metal-directed self-

assembly of SENs and biomineralization. This stage was very fruitful. In fact, in just over two years, we published 3 high-impact articles. From there on, I focused my work on the synthesis of chemoenzymatic materials, which would help introduce novel functionalities into heterogeneous biocatalysts. In this research line, which was totally new to the group, we designed and manufactured highly efficient biomaterials. It was very motivating that this effort was rewarded with two publications in very prestigious journals. Moreover, I would like to mention that during the months of confinement we did not slow down, and we committed ourselves to the difficult task of writing a review about enzyme-polymer hybrid materials. Finally, in the year 2022, I spent 3 months in Prof. Dr. Paradisi's group at the University of Bern (Switzerland), to work with new enzymes that were never applied with SENs, and to immobilize them into prefabricated supports for their implementation in continuous flow biocatalysis. This stay was supported by a FEBS Short-Term Fellowship.

This PhD thesis focuses on the design, synthesis, and characterization of catalytic biomaterials to improve the properties of enzymes. To achieve the main goal, this PhD thesis targeted the following specific objectives:

- Synthesis of single enzyme nanogels and modulation of their properties by chemical modification of the nanogel. Of particular interest are SENs modified with imidazole molecules, as they may work for macromolecular assembly in the presence of metal cations or incorporation of organometallic catalysts. Functionalization with amino groups will also play a relevant role in this thesis.
- The formation of a wide variety of heterogeneous biocatalyst from single enzyme nanogels. The design and fabrication of i) carrier-free SEN immobilization systems, ii) SEN entrapped in biomineralized scaffolds, and iii) the immobilization of SENs on prefabricated supports will be studied.

- Demonstration of the usefulness of these biomaterials in different applications (biosensors, bioreactors, bioremediation). The final applications will depend on the enzyme selected. Thus, the enzyme horseradish peroxidase (HRP) will be used for the peroxidation of recalcitrant compounds; glucose oxidase (GOx) for the fabrication of glucose sensors, or production of hydrogen peroxide, and a ω -transaminase (HeWT) to produce flavors, e.g., acetophenone.

The first task of this thesis was to search for the state-of-the-art of the main topics to carry out this work: biocatalysis, enzyme modification with polymers, especially single enzyme nanogels, heterogeneous biocatalysts and materials with chemoenzymatic activity. In **Chapter 1** I addressed those topics to give the reader an overview of these fields and to facilitate the reading of this thesis. In addition, in 2020 we wrote a review on enzyme-polymer hybrid materials (**Paper I**),⁴⁵ which was very enriching to broaden the focus of our research and to develop new ideas.

With the aim of facilitating the readability of the results generated in this thesis (**Chapter 4-7**), all materials and methods have been described in **Chapter 3**. The instrumentation used has also been compiled in this chapter.

In **Chapter 4** we explored heterogeneous biocatalysts, exclusively composed of SENSs self-assembled by metal cations, forming carrier-free structures called metal-organic enzyme aggregates (MOEAs). Owing to the low non-catalytic material content, the robust MOEAs showed a low amount of diffusional issues and high catalytic activity, as demonstrated in **Paper II**.¹⁰⁸ In addition, MOEAs were successfully implemented into the fabrication of very robust catalytic films with high stability in the presence of organic solvents and high temperatures. These enzymatic films were used for the fabrication of a glucose electrochemical biosensor and the completion of cascade enzymatic reactions. We collaborated with the *Biomolecular Nanotechnology Lab* of Prof. L. Cortajarena in CICbiomaGUNE BRTA. The results were published in **Paper III**.⁹⁸

Next, we used imidazole and amino-functionalized SENs as building blocks for the fabrication of organic-inorganic enzyme hybrids termed nanosponges. These structures were assembled through metal-imidazole coordination, but also underwent a biomineralization process during the synthesis, entrapping the SENs into the inorganic scaffold. The high concentration of imidazole and amino groups on the enzyme surface accelerated hybrid formation (2h *vs.* 72h of conventional nanoflowers assembled from free proteins) and improved the enzyme loading along with catalytic conversion and system robustness. These results are explained in detail in **Chapter 5** and **Paper IV**.¹¹⁸ Furthermore, the biomineralization with cobalt phosphates was studied varying the composition of the nanogels. This research is still ongoing and will be shortly published. However, those results have not been included in this thesis.

The limited scope of enzymes led us to integrate chemical catalysts, i.e., organometallic, into SENs to increase their functionality. To this end, hemin molecules, which are known to be able to peroxidize many substrates, were combined with GOx-based imidazole-functionalized SENs to form chemoenzymatic nanoreactors. We optimized the design of the nanoreactor, searching for the most active systems, and succeeded in producing carrier-free heterogeneous biocatalysts using hemin as assembly agent. Initially, nanoreactors were used for the degradation of aromatic recalcitrant compounds using glucose and oxygen, as collated in **Chapter 6** and **Paper V**. The high efficiency of the nanoreactors motivated us to continue searching for other applications. We tested the NAD(P)H oxidase activity of the heterogeneous nanoreactors, i.e., NanoNOx, and the results were very positive. In fact, they could be implemented in one-pot reactions coupled to NADH-dependent dehydrogenases. **Chapter 6** and **Paper VI** describes this work.

We attempted to immobilize SENs on prefabricated carriers, i.e., methacrylate and butyl methacrylate microbeads, through covalent bonding. For this purpose, we employed a PLP-dependent ω -transaminase from *Halomonas elongata* (HeWT), which was never

utilized for SEN fabrication. Interestingly, we discovered by serendipity that the phosphate cofactor could be confined in nanogels through imine bonds. Finally, the heterogeneous biocatalysts were evaluated in flow to intensify the biocatalytic process. This research project is still ongoing and further optimization is needed, mainly on the fabrication of the carrier-bound SEN immobilization. The project was carried out in close collaboration with the group of Prof. Paradisi at the Department of Chemistry, Biochemistry, and Pharmaceutical Sciences from the University of Bern. The latest results are described in **Chapter 7** and will be published soon.

2.1 SCIENTIFIC OUTCOME

These results have been published in these scientific articles:

Paper I: Rodriguez-Abetxuko, A.; Sánchez-deAlcázar, D.; Muñumer, P.; Beloqui, A. Tunable Polymeric Scaffolds for Enzyme Immobilization. *Front. Bioeng. Biotechnol.* **2020**, 8 (July), 830. <https://doi.org/10.3389/fbioe.2020.00830>.

Paper II: Rodriguez-Abetxuko, A.; Morant-Minana, M. C.; Knez, M.; Beloqui, A. Carrierless Immobilization Route for Highly Robust Metal-Organic Hybrid Enzymes. *ACS Omega* **2019**, 4 (3), 5172–5179. <https://doi.org/10.1021/acsomega.8b03559>.

Paper III: Rodriguez-Abetxuko, A.; Sánchez-deAlcázar, D.; Cortajarena, A. L.; Beloqui, A. A Versatile Approach for the Assembly of Highly Tunable Biocatalytic Thin Films. *Adv. Mater. Interfaces* **2019**, 6 (18), 1900598. <https://doi.org/10.1002/admi.201900598>.

Paper IV: Rodriguez-Abetxuko, A.; Morant-Miñana, M. C.; López-Gallego, F.; Yate, L.; Seifert, A.; Knez, M.; Beloqui, A. Imidazole-Grafted Nanogels for the Fabrication of Organic-Inorganic Protein Hybrids. *Adv. Funct. Mater.* **2018**, 28 (35), 1803115. <https://doi.org/10.1002/adfm.201803115>.

Paper V: Rodriguez-Abetxuko, A.; Muñumer, P.; Okuda, M.; Calvo, J.; Knez, M.; Beloqui, A. Nanoconfined (Bio)Catalysts as Efficient Glucose-Responsive Nanoreactors. *Adv. Funct. Mater.* **2020**, 30 (35), 2002990. <https://doi.org/10.1002/adfm.202002990>

Paper VI: Rodriguez-Abetxuko, A.; Reifs, A.; Sánchez-deAlcázar, D.; Beloqui, A. A Versatile Chemoenzymatic Nanoreactor That Mimics NAD(P)H Oxidase for the In Situ Regeneration of Cofactors. *Angew. Chemie Int. Ed.* **2022**, 202206926. <https://doi.org/10.1002/anie.202206926>

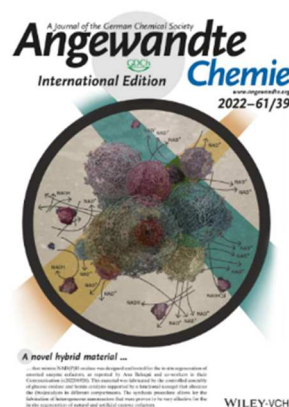


Figure 2-1. Inside cover published in Angewandte Chemie-International Edition 2022-61/39. Picture author: Antonio Reifs

2.1.1 Other papers

Sánchez-deAlcázar, D.; **Rodriguez-Abetxuko, A.;** Beloqui, A. Metal-Organic Enzyme Nanogels as Nanointegrated Self-Reporting Chemobiosensors. *ACS Appl. Mater. Interfaces* **2022**, 14, 27589-27598. <https://doi.org/10.1021/acsami.2c04385>

2.1.2 Papers in Preparation

Rodriguez-Abetxuko, A.; Sánchez-deAlcázar, D.; Beloqui, A. The composition of single enzyme nanogels governs the assembly of organic-inorganic protein hybrids. Manuscript in preparation.

Rodriguez-Abetxuko, A.; Benitez-Mateos, A., Paradisi, F., Beloqui, A. Engineering the surface of an ω -transaminase to confine PLP in continuous flow biocatalysis. Manuscript in preparation.

Chapter 3 MATERIALS AND METHODS

This chapter describes the materials, characterization techniques, and general methods used during this thesis.

3.1 MATERIALS

Reagents for SEN formation: acrylamide (AA; 99.9%, Sigma), N-Hydroxyethyl acrylamide (HEAA; 97%, Aldrich), vinyl imidazole (Vi; >99%, Sigma), N-(3-Aminopropyl)methacrylamide hydrochloride (APM, 98%, Merck), (3-Acrylamidopropyl)trimethylammonium chloride solution (APTAC, 75%, Merck), 2-carboxyethyl acrylate (CEAA, Merck), N,N'-Methylenebis(acrylamide) (BIS; >99%, Sigma), sucrose (<99.5%, Sigma), ammonium persulfate (APS; 98%, Sigma), tetramethylethylenediamine (TEMED; 99%, Sigma), 4-(dimethylamino)antipyrine (98%, ABCR), N-acryloyl succinimide (NAS, >95%, Sigma), H-hydrosuccinimide (NHS-OH, 98%, Sigma), 1-ethyl-3-(3-dimethylaminopropyl)carbodiimide hydrochloride (EDC-HCl, 98%, Sigma), 4-imidazole carboxylic acid (4-ICA, 98%, Sigma), $\text{CuSO}_4 \cdot 5\text{H}_2\text{O}$ (>98%, Sigma), $\text{Ni}(\text{NO}_3)_2 \cdot 6\text{H}_2\text{O}$ (>99%, Sigma), $\text{Co}(\text{NO}_3)_2 \cdot 6\text{H}_2\text{O}$ (>98%, Sigma), $\text{Zn}(\text{NO}_3)_2 \cdot 6\text{H}_2\text{O}$ (>98%, Sigma), $\text{MnCl}_2 \cdot 4\text{H}_2\text{O}$ (>99%, Sigma), $\text{CdSO}_4 \cdot 8/3\text{H}_2\text{O}$ (>99%, Sigma), AgNO_3 (>99%, Sigma), $\text{HAuCl}_4 \cdot 3\text{H}_2\text{O}$ (>99%, Sigma), K_2PdCl_4 (98%, Sigma), and $\text{CrCl}_3 \cdot 6\text{H}_2\text{O}$ (96%, Sigma), hemin (>98%, ACROS organics), epoxy-functionalized methacrylate beads (EP403, Relizyme™), butyl methacrylate beads (ECR8285, Purolite), ethylenediaminetetraacetic acid (EDTA, Sigma).

2,2'-azino-bis(3-ethylbenzothiazoline-6-sulphonic acid) (ABTS, Panreac AppliChem), hydrogen peroxide (35% v/v in water, Carl Roth), D-glucose (>95%, Sigma), benzyl alcohol (99%, ABCR), sodium L-lactate (>98%, Alfa Aesar), sodium pyruvate (>99%, Sigma), β -Nicotinamide adenine dinucleotide (NAD⁺; >97%, PanReac AppliChem), reduced β -Nicotinamide adenine dinucleotide (NADH; >95%, PanReac AppliChem), reduced β -Nicotinamide adenine dinucleotide phosphate (NADPH; >95%, PanReac AppliChem), 1-benzyl-1,4-dihydronicotinamide (BNAH; 95%, ABCR), S-(α)-Methylbenzylamine (S-MBA, Sigma), pyridoxal 5'-phosphate monohydrate (PLP, Sigma),

Acetonitrile (MeCN; VWR), 2-isopropanol (IprOH; PanReac AppliChem), dimethyl sulfoxide (DMSO; Sigma), and dimethyl formamide (DMF, Sigma) were of analytical grade. All buffers were freshly prepared and filtered through 0.22 μ m filters prior to use. Filter membranes (30 kDa MWCO, Amicon®Ultra 15 mL), HisPur NA-Ni resin (ThermoFisher), Sephadex columns (Sephadex™ G-75 and PD-miditrap G25, GE Healthcare), and dialysis membranes (10 kDa MWCO, SnakeSkin, ThermoFisher) were used for concentration and purification of SENs.

Most of the enzymes that have been used along this PhD work are from a commercial source. Glucose oxidase from *Aspergillus niger* (GOx, E.C: 1.1.3.4., 108 U mg⁻¹, Amresco), horseradish peroxidase (HRP, E.C. 1.11.1.7., >1100 U mg⁻¹, Alfa Aesar), catalase from bovine liver (CAT, E.C. 1.11.1.6., >10,000 U mg⁻¹, Merck), β -glucosidase from *Aspergillus niger* (β -Gluc, E.C. 3.2.1.21, 919 U mg⁻¹, Merck) and lactate dehydrogenase (E.C. 1.1.1.27, 1,100 U mg⁻¹, Merck) were dialyzed and filtrated prior to use to remove (NH₄)₂SO₄ and small protein fragments present in most commercial enzymes.¹⁰⁹ In addition, two enzymes were expressed and purified: an alcohol dehydrogenase from *Bacillus stearothermophilus* (BsADH, E.C. 1.1.1.1., 0.06 U mg⁻¹) and

ω -transaminase from *Halomonas elongata* (HeWT, 2.6.1.18., 2.5 U mg⁻¹). The details of both expression and purification processes are explained below.

3.2 INSTRUMENTATION AND CHARACTERIZATION TECHNIQUES

3.2.1 Dynamic light scattering (DLS)

DLS was systematically used to confirm the formation of SENs by measuring the hydrodynamic diameter of the free enzymes and the SENs obtained after each polymerization (**Figure 4-2A**, **Figure 5-2C**, **Table 6-1**, and **Figure 7-2**). It was also used to study the size of some heterogeneous biocatalysts in solution formed through SENs (**Figure 4-3B**).

DLS measurements were performed on a Malvern Zetasizer NanoZS. The dispersant refractive index was set at 1.33 and the viscosity at 1.0041 cP. The experiments were taken in three independent measurements for each sample prepared in sodium phosphate buffer (30 mM, pH 8.0) filtered through 0.22 μm cutoff membranes. The used sample concentration was 0.5-2 μM .

3.2.2 Atomic Force Microscopy (AFM)

AFM measurements revealed the topology and size of SENs (**Figure 4-2B**). The surface roughness of biocatalytic films and nanoreactors was also evaluated by AFM (**Figure 4-9E** and **Figure 6-6**, respectively).

An AFM 5500, Agilent Technologies/Keysight Technologies microscope was used in AC mode with a silicon tip with a force constant of 6 N m⁻¹ and a resonance frequency of approximately 150 KHz. Silicon substrates were cleaned by immersing them in

piranha solution (7:3 mixture of 96% H₂SO₄ and 30% H₂O₂) at 80 °C for 30 min. After that, the substrates were rinsed with Millipore water (MΩ cm) in an ultrasonic bath for 30 min and blow dried with a nitrogen stream. One drop (10 μL, 0.6 μM in water) of SEN solution was spin coated onto a cleaned silicon wafer at 1800 rpm for 0.5 min. The films were measured without any previous modification. The height, phase, and amplitude images were recorded simultaneously. AFM scans were performed at several positions to ensure the representativeness of the sample. The images were processed with the Gwyddion 2.31 software.

3.2.3 Circular Dichroism (CD)

CD was used to evaluate the secondary structure of the enzymes after the formation of nanogels (**Figure 4-2C**) and after film formation (**Figure 4-9B**).

The CD spectra were recorded with a Jasco J-815CD spectropolarimeter. The CD spectra were acquired in a 1 mm pathlength quartz cuvette. All CD spectra were recorded with a bandwidth of 0.1 nm increments, 10 nm min⁻¹ scan speed, 32 s integration time, and 10 accumulations over a wavelength range of 190-260 nm. SENs were prepared in Tris-HCl buffer (5 mM, pH 7) with a final concentration of 1.5 μM. The solid thin film was deposited on a quartz slide of 1 x 1 mm² by spin coating using a Laurell Technologies corporation Model WS-400B-6NPP/LITE, at 1000 rpm for 10 min.

3.2.4 Attenuated Total Reflection Fourier Transform Infrared Spectroscopy (ATR-FTIR)

ATR-FTIR was used to characterize the SENs after formation (**Figure 4-2D**). In addition, ATR-FTIR was used for examining the incorporation of monomers such as VI (**Figure 4-2D** and **Figure 6-2**) and CEAA (**Figure 6-2**) into the nanogel.

Coordination between divalent cations and imidazole was observed (**Figure 4-5B**). It was also utilized for the chemical characterization of the nanoreactors (**Figure 6-3**).

The ATR-FTIR spectra were measured with a PerkinElmer Frontier spectrometer equipped with an ATR sampling stage. 2 μL of the samples (1-5 μM stocks) were drop-casted on silicon wafers and subsequently dried at room temperature. The dropping process was repeated 3 times to obtain sufficient amounts of materials for a readable sample. All spectra were measured with 20 scans from 600 to 4000 cm^{-1} with a resolution of 4 cm^{-1} .

3.2.5 Scanning Electron Microscopy (SEM)

SEM measurements were used for imaging the morphology of nanoparticulated MOEAs (**Figure 4-3**), biocatalytic films (**Figure 4-9**), biomineralized micrometric nanosponges (**Figure 5-3** and **Figure 5-10**), and homogeneous and heterogeneous nanoreactors (**Figure 6-6**).

A Helios NanoLab 450S (FEI) scanning electron microscope was used to analyze the size and morphology of the hybrid materials. The microscope was operated in immersion mode with an acceleration voltage of 5.0 kV and a current of 0.2 nA. The working distance was set to 3 mm. The size estimation was performed using the microscope measurement module. The energy dispersive X-ray analysis (EDX) module (Octane Elect EDS, AMETEK) was used to conduct the elemental analysis. To prepare the samples, a drop (10 μL of a stock solution) was spin-coated onto a 1 x1 mm silicon wafer at 1800 rpm for 0.5 min. The silicon wafers were cleaned with acetone and isopropanol in an ultrasonic cleaner before the deposition.

3.2.6 Transmission electron microscopy (TEM)

The size and morphology of the nanoreactors were examined with TEM (**Figure 6-6B**).

The samples were observed by TEM (JEOL, JEM-1230), stained with 1 % (w/v) uranyl acetate. A carbon coated copper grid was used as support. This work was carried out in collaboration with Dr. Mitsuhiro Okuda from the *self-assembly* group from CIC nanoGUNE BRTA.

3.2.7 Raman spectroscopy

Raman spectroscopy was utilized to elucidate the presence of metal-imidazole coordination of MOEAs (**Figure 4-5A**) and the embedment of hemin molecules within the nanoreactors (**Figure 6-3A**).

The Raman spectra were obtained with a confocal Raman microscope (alpha 300, WITec, Germany). The samples were prepared by drop casting onto a silicon wafer until a sufficiently thick film was formed. The incident laser was a Nd:YAG laser ($\lambda = 532$ nm, 25 mW) illuminating the sample perpendicularly. The spectra were acquired in a 1000-4000 cm^{-1} range with an integration time of 2 s and 20 accumulations.

3.2.8 X-ray photoelectron spectroscopy (XPS)

XPS measurements revealed the oxidation state of metals and composition details, and their coordination with imidazole in MOEA pellets and films (**Figure 4-5C** and **Figure 4-10D**), nanosponges (**Figure 5-7A**), and nanoreactors (**Figure 6-4**).

XPS experiments were performed in a SPECS Sage HR 100 spectrometer with a non-monochromatic X-ray source (Aluminum $K\alpha$ line of 1486.6 eV energy and 300 W), placed perpendicular to the analyzer axis and calibrated using the $3d_{5/2}$ line of Ag with a full width at half maximum (FWHM) of 1.1 eV. The selected resolution for the spectra was 15 eV of pass energy and 0.15 eV/step. All measurements were made in an ultra-high vacuum (UHV) chamber at a pressure around $8 \cdot 10^{-8}$ mbar. The CasaXPS software was used for deconvoluting the spectra. The C 1s peak from C-C sp^3 of adventitious

carbon was employed for charge correction, fixing its binding energy (BE) to 284.8 eV. A Shirley background correction was applied. Peaks were assigned according to NIST DATABASE and xpsfittin.com. The survey spectrum was employed to calculate the relative atomic composition in the samples. Samples were prepared in the same way as for ATR-FTIR. The XPS measurements were performed in the *Surface analysis and fabrication* technological platform from CICbiomaGUNE BRTA.

3.2.9 Inductively coupled plasma mass spectrometry (ICP-MS)

By ICP-MS it was possible to determine the molar ratio between the proteins and the inorganic moiety of the nanosponges (**Figure 5-5A**).

The metal composition in the hybrid materials was determined with a NexION300 (Perkin Elmer Inc.) and the data were acquired using the NeoxION software. The kinetic energy discrimination (KED) mode was used to avoid signal interferences. The instrument was calibrated with the Multielement Calibration Standard 3 (10 $\mu\text{g mL}^{-1}$ stock solution for each element in a range from 0.01 to 1000 ppb in nitric acid (0.5%, 3 mL final volume).

3.2.10 UV-Vis absorption spectroscopy

The UV-Vis absorption spectra of the SENs and the heterogeneous biocatalysts provided us with very important information. The protein concentration of the sample was measured at 280 nm for most of the proteins (450 nm for GOx and 402 nm for HRP). In addition, we observed the presence of FAD in the films (**. A**), the reduction of Ag in the nanosponges (**Figure 5-11D**), and the incorporation and interaction hemin (**Figure 6-5**) and of PLP (**Figure 7-3**) with SENs. Moreover, most of the kinetic characterization was monitored by measuring the disappearance of the substrate or the formation of the product at a certain wavelength.

UV-vis spectroscopy studies were performed using an Epoch 2 Microplate Spectrophotometer (BioTek). The UV-Vis spectra of the samples were acquired in the spectral window from 250 nm to 700 nm with a step size of 2 nm. The concentrations of sample and buffer varied from sample to sample.

3.2.11 Cyclic Voltammetry (CV)

CV was utilized for electrochemical monitoring of glucose (**Figure 4-14A**). Moreover, copper and silver species from nanosponges were studied with this technique (**Figure 5-6** and **Figure 5-11C**).

An electrochemical cell consisting of a three-electrode system (DropSens) was utilized. The measurements were carried out in a range between -0.7 and 0 V, with a scan rate of 0.1 V s^{-1} . With biomineralized samples an electrochemical cell consisting of a three-electrode system deposited onto the cyclic olefin polymer (COP) was used.¹⁶⁴ The measurements were carried out in a range between -0.8 and 0.6 V, with a scan rate of 0.1 V s^{-1} . The CV experiments were monitored with the Autolab electrochemical working station PGSTAT 302N using the Nova 1.9 software version (Eco Chemie). All cyclic voltammetry assays were performed under the same conditions at room temperature.

3.2.12 Zeta-potential

The measurement of the zeta potential was very helpful for assessing the incorporation of monomers into the SENs (**Table 6-1**).

The zeta-potential measurements were performed on a Malvern Zetasizer Nano ZS in auto-mode, at 25 °C, with 5 consecutive measurements at pH 6.5. The samples were diluted to 1.0 mg mL^{-1} in 10 mM KCl.

3.2.13 Sodium dodecyl sulfate-polyacrylamide gel electrophoresis (SDS-PAGE)

SDS-PAGE was the technique used to qualitatively determine the encapsulation yield after SEN formation. SDS-PAGE has only recently started to be used as a method for characterizing SENs, so it was only used in **Chapter 7 (Figure 7-2A)**.

SDS-PAGE was performed using 10% acrylamide gels on the Bio-Rad Mini-PROTEAN tetra system. Free enzymes or SEN (5 mg) were mixed with 5 mL of loading buffer (4x) and heated at 90 °C for 5 min. The samples were loaded on the electrophoresis gel and run at a constant voltage of 100 mV for 1 h. Later, the gel was stained with Imperial protein stain (Thermo Scientific) for 1 h and destained overnight with water.

3.2.14 Proton nuclear magnetic resonance (^1H NMR)

^1H NMR was crucial for assessing the selective oxidation of nicotinamide cofactors (**Figure 6-18A, Figure 6-19C-D, Figure 6-20C**).

NMR spectra were obtained from a Bruker fourier 300 MHz spectrometer. The samples/reaction mixtures containing the cofactors, i.e., NAD(P) and BNA (0.5 – 1 mM), were filtered with 30 kDa MWCO, AmiconUltra (0.5 mL) to remove the catalysts from solution and mixed with 10 % (v/v) of D_2O to reach a final volume of 300 μL in a Norell® Select Series™ 5 mm NMR spectroscopy tube. The spectra were acquired with a 300 MHz radiofrequency pulse at room temperature performing 128 scans with 12 min acquisition time and 1 s relaxation delay. As reference D_2O ($\delta = 4.79$ ppm) was used.

3.2.15 Ultra-performance liquid chromatography mass spectroscopy

UPLC-MS was utilized to monitor the degradation of small aromatic derivatives and dye pollutants with the nanoreactors (**Figure 6-14**, and **Table 3-1**).

The mass spectrometry detection was carried out using a time-of-flight mass spectrometer (ESI-TOF) LCT Premier XE from Waters (Milford, MA, USA) with an electrospray ionization source, working in positive / W mode. The acquired MS range was between m/z 100-1000. The capillary and cone voltages were set to 1000 and 50 V, respectively. The desolvation gas temperature was 350 °C and the source temperature was 120 °C. The desolvation gas flow was set to 600 L h⁻¹ and the cone gas flow was set to 50 L h⁻¹. The Masslynx v4.1 software was used to analyze the chromatograms and spectra (Waters, Milford, MA, USA). The samples were diluted (1:10) in methanol prior to injection. The gradient elution buffers were A (0.1 % formic acid in water) and B (methanol). The gradient method was as follows: 0-0.5 min at 99% A, 0.5-3.5 min to 1% A, 2.5-3 min to 5% A, 4-5 min at 1% A, 4-4.1 min to 99%, 4.1-5 min at 99%. The UV detector wavelengths were set to 302, 317, and 349 nm and the injection volume was 5 µL. The total run time was 5 min and the flow rate was set to 500 µL min⁻¹. The UPLC-MS measurements were performed in the *Mass Spectrometry* technological platform from CICbiomaGUNE BRTA.

3.2.16 High performance liquid chromatography

HPLC was employed to calculate the biocatalytic conversion of BsADH (**Figure 6-20B**) using NanoNO_x as cofactor recycling system.

HPLC measurements were carried out on a HPLC Nexera Lite (SHIMADZU), equipped by a SIL-40C autosampler (SHIMADZU), ACE 3 C18-PFP (length: 150 mm, inner diameter: 4.6 mm) column, and SPD-M40 photo diode array detector

(SHIMADZU). The reaction samples containing benzyl alcohol (BnOH) were filtered (30 kDa MWCO, 10 min, 9000 rpm) and diluted (1:10) in methanol (final concentration of 10% v/v) prior to injection. The injection volume was 5 μL and the flow rate of the mobile phase (35:65; MeOH:H₂O) was set to 1 mL min⁻¹. The column oven temperature was set to 40 °C and the UV detector wavelength was fixed at 215 nm. Consistent results were obtained by measuring the residual BnOH in the reaction. Conversely, the monitoring of benzaldehyde (product of the reaction) showed several inaccuracies in the calculation of the conversion due to its high volatility in the reaction conditions.

The reaction samples containing L-lactate/pyruvate were filtered (30 kDa MWCO, 10 min, 9000 rpm) and diluted (1:10) in the mobile phase (4:96 acetonitrile:phosphate (0.12 M pH 1.5), phosphate solution composed of 49.64 mg mL⁻¹ of Na₂HPO₄·12H₂O and 2.4 % H₃PO₄) before injection. The injection volume was 20 μL and the flow rate of the mobile phase was set to 0.3 mL min⁻¹. The column oven temperature was set to 35 °C and the UV detector wavelength was fixed at 210 nm.

3.3 METHODS

Methods used to produce/modify/characterize enzymes are provided below.

3.3.1 Acrylation of proteins

Horseradish peroxidase (HRP, 50 mg) was dissolved in sodium carbonate buffer (CB, 20 mM, pH 9.15, 5 mL) and dialyzed against the same buffer (**Figure 3-1i**). N-acryloyl succinimide (NAS) was dissolved in DMSO (0.5 mL) and slowly added (20 eq. of NAS per lysine group of the protein) to the protein solution to a final volume of 10 mL. The mixture was further shaken at room temperature for 3 h. The reaction was stopped by

dialysis against PBS. Finally, the acrylated enzyme was gel-filtered through a Sephadex G-25 column, pooling all fractions containing enzyme activity.

3.3.2 General protocol for the synthesis of SENs

We have developed a one-step straightforward route to synthesize SENs with different chemical functional groups such as hydroxyl, carboxyl, amino and imidazole groups. The native enzymes, i.e., glucose oxidase (GOx), β -Glucosidase (β -Gluc), HRP or ω -transaminase from *Halomonas elongata* (HeWT), were mixed with selected monomers and N,N'-methylenebisacrylamide (BIS) as crosslinker. In **Table 3-2**, the molar ratios (relative to mols of the protein) of the monomers, crosslinker, initiators and catalysts for the polymerization (APS and TEMED, respectively) that were used for the reaction, are summarized. The enzyme concentration was adjusted to 20 μ M in most cases and the reaction volume varied from 1 to 10 mL. In the case of HRP, the enzyme was previously acrylated (a-HRP), this being the only case of covalent SENs in this thesis. The monomer ratios were optimized to generate thin polymeric layers and avoid the gelation of the sample. Sucrose (5%, w/v) and dimethyl sulfoxide (10% v/v) were added to the protein/monomer mixture to increase the interaction of the reactants with the enzyme surface and to improve the solubility of some reagents, i.e., APM and BIS (**Figure 3-1ii**). This mixture was deoxygenated with continuous bubbling of N₂. Finally, TEMED and APS (as 10% (w/v) solution) were added (**Figure 3-1iii**). The polymerization reaction was maintained for 2 h. The unreacted monomers were removed by 2 consecutive dialysis steps of 2 L each against 30 mM sodium phosphate buffer pH 8.0 using a 10 kDa MWCO dialysis membrane. The samples were washed 3 times and concentrated using filter membranes (30 kDa MWCO). The SENs were purified with a Sephadex G-75 column to remove non-encapsulated enzymes and protein-free polymer hydrogels. Finally, the nanogels were stored at 4°C in sodium phosphate buffer (50 mM, pH 6.1-8.0).

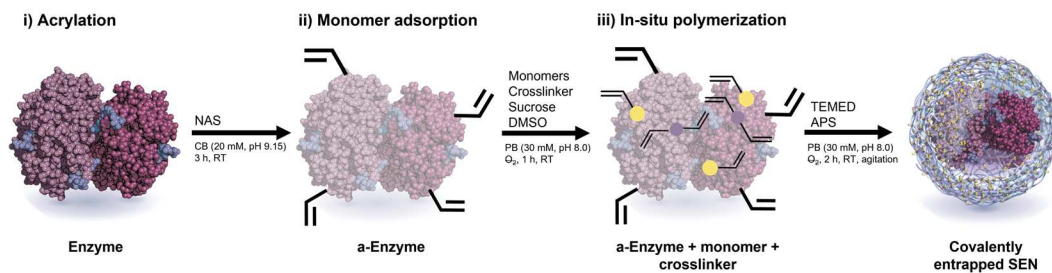


Figure 3-1. Covalently entrapped SEN detailed synthesis procedure divided in i) enzyme acrylation, ii) monomer adsorption to the enzyme surface and iii) in-situ radical polymerization.

Table 3-2. Synthesis conditions utilized in this thesis for the fabrication of the SENs. The protein concentration was set to 20 μ M and sucrose concentration was set to 5 % (m/v). The absence of units refers to the molar excess *vs.* the enzyme.

Code	Chapter (n°)	AA ¹	HEAA ²	CEAA ³	APM ⁴	VI ⁵	BIS ⁶	APS ⁷	TEMED ⁸	Buff. ⁹ (mM; pH)	V _f ¹⁰ (mL)
GOx@pAA-I	4	6000	-	-	-	1000	1000	500	250	12; 6.1	7.0
GOx@pAA-I	4	600	-	-	-	1000	400	400	200	12; 6.1	2.8
GOx@pHEAA-I	4	-	600	-	-	1000	400	400	200	12; 6.1	2.8
β -Gluc@pHEAA-I	4	-	600	-	-	1000	400	400	200	12; 6.1	2.8
a-HRP@pAA-NH ₂	5	2000	-	-	400	-	600	600	300	50; 6.1	10
HeWT@pAA-NH ₂	6	867	-	-	1000	-	400	500	250	30; 8.0	1.0
GOx@pHEAA-I	7	-	600	-	-	2000	400	400	200	50; 8.0	3.1
GOx@pHEAA-I-COOH	7	-	600	2000	-	2000	1000	500	250	50; 8.0	3.1
GOx@pHEAA-I-NH ₂	7	-	600	-	2000	2000	1000	500	250	50; 8.0	3.1
GOx@pHEAA	7	-	2000	-	-	-	400	500	250	50; 8.0	3.1
GOx@pHEAA-I	7	-	800	-	-	4000	600	400	200	50; 8.0	3.1

¹Acrylamide: stock solution of 10% m/v in buffer; ²Hydroxyethyl acrylamide, stock solution of 10% m/v in buffer; ³2-carboxyethyl acrylate: 10% m/v in buffer; ⁴N-(3-Aminopropyl) methacrylamide hydrochloride: 10% m/v in DMSO; ⁵vinyl imidazole: no dilution; ⁶N,N'-Methylenebis(acrylamide): 10% m/v in DMSO; ⁷ammonium persulfate: 10% m/v in buffer. ⁸tetramethylethylenediamine: no dilution. ⁹Buffer were phosphates in all cases; ¹⁰final reaction volume.

Table 3-3. Main features of each SEN and the application they have been used for. In all cases the SENs show higher thermal stability and activity in the presence of organic solvents than the unmodified enzyme.

Code	Chapter (n°)	Main features; application
<i>GOx@pAA-I</i>	4	Self-assemble with divalent metal; formation of MOEAs (NPs and pellets)
<i>GOx@pHEAA-I</i>	4	Self-assemble with di- and tri-valent metals; formation of MOEAs (films)
<i>β-Gluc@pHEAA-I</i>	4	Self-assemble with di- and tri-valent metals; formation of MOEAs (films)
<i>a-HRP@pAA-NH₂</i>	5	Self-assemble and biomineralize with mono-, di-, and tri-valent metals; formation of NSs
<i>HeWT@pAA-NH₂</i>	6	Confinement of cofactor through covalent bonds and enhanced immobilization on prefabricated supports; flow biocatalysis
<i>GOx@pHEAA-I</i>	7	Co-localization of organometallic catalysts
<i>GOx@pHEAA-I-COOH</i>	7	Co-localization of organometallic catalysts
<i>GOx@pHEAA-I-NH₂</i>	7	Co-localization of organometallic catalysts and self-assembly with iron porphyrin; degradation of aromatic compounds
<i>GOx@pHEAA</i>	7	Reduced hydrophobicity
<i>GOx@pHEAA-I</i>	7	Co-localization of organometallic catalysts and self-assembly with iron porphyrin; regeneration of (phosphorylated) nicotinamide cofactors

3.3.3 Post-polymerization modifications of SENs

Some SENs were modified after their synthesis to introduce new functionalities. In the case of HRP@pAA-NH₂, imidazole was introduced through an amidation reaction between the amines of the capsule and the carboxyl of 4-imidazole carboxylic acid (4-ICA, **Chapter 5**). Imidazole incorporated into the nanogels, i.e., GO_x@pHEAA-I, GO_x@pHEAA-I-COOH, and GO_x@pHEAA-I-NH₂, was used to coordinate and anchor iron porphyrins as organometallic catalysts (**Chapter 6**). Finally, more complex molecules such as pyridoxal 5'-phosphate (PLP) cofactor were also introduced to HeWT@pAA-NH₂ through imine bonds (**Chapter 7**). The corresponding protocols are disclosed below.

3.3.3.1 Grafting imidazole moieties to HRP@pAA-NH₂

Primary amines on the polymeric capsule were modified with 4-imidazole carboxylic acid (4-ICA) through an amidation reaction using EDC/NHS coupling chemistry (**Figure 3-2**).¹⁶⁵ For this, a-HRP@pAA-NH₂ (1 mg mL⁻¹) in sodium phosphate (300 mM, pH 8.2) were mixed with EDC-HCl (0.1 M), NHS-OH (0.1 M), and 4-ICA (0.1 M) to obtain imidazole-grafted nanogels. The reaction was kept at 37 °C for 2 h and unreacted reagents were removed by dialysis. Afterwards, the unmodified nanogels were removed using a HisPur™ Ni-nitrilotriacetic acid (NTA) resin (2 mL). The resin was washed with the washing buffer (100 mM sodium phosphate and 150 mM NaCl, pH 6.0) until no protein was eluted. Later, a-HRP@pAA-I, attached to the column, were eluted with 1 M imidazole, 100 mM sodium phosphate and 150 mM NaCl (pH 6.0) containing buffer. Finally, the imidazole was removed by dialysis.

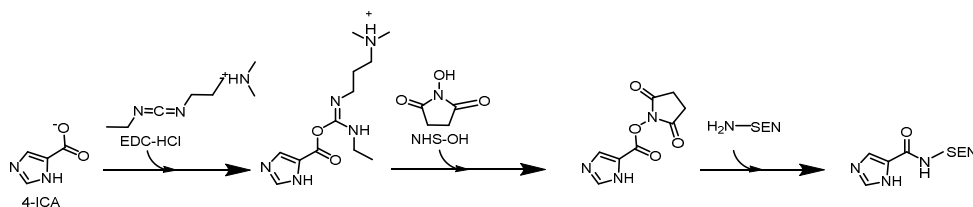


Figure 3-2. Grafting of imidazole moieties to reactive amines from a-HRP@pAA-NH₂. 4-ICA is transformed into an o-acylisourea ester with EDC as coupling agent. NHS-OH transforms the o-acylisourea into an NHS-ester. Finally, the amide bond is formed.

3.3.3.2 *Integration of hemin molecules to SENs*

The organometallic catalyst hemin was incorporated into GOx@pHEAA-I and GOx@pHEAA-I-COOH through coordination with Fe-imidazole (section 6.2.1). SENs (1.5 mL of a stock solution prepared at 1.6 μ M in 40 mM of Tris-HCl buffer, pH 7.0) were mixed with an excess of hemin chloride (molar excess from 0 to 600) at room temperature for 16 h. The hemin stock was freshly prepared at a concentration of 30 mM in a NaOH solution (0.23 M). The homogeneous nanoreactors were passed through a Zeba Spin desalting column (40 kDa, Thermo Scientific) to eliminate the excess of hemin from the sample.

3.3.3.3 *Integration of PLP into HeWT@pAA-NH₂*

The pyridoxal 5'-phosphate (PLP) cofactor was incorporated into HeWT@pAA-NH₂ through imine bonds (see section 7.2.1). HeWT@pAA-NH₂ (300 mL of a stock solution prepared at 1.83 mM in 50 mM potassium phosphate buffer, pH 8.0) was mixed with an excess of PLP (PLP: HeWT@pAA-NH₂ molar ratio from 0 to 250) dissolved in potassium phosphate buffer (50 mM, pH 8.0) at room temperature for 16 h. The samples were not further purified.

3.3.4 **Fabrication of heterogeneous biocatalysts**

This section is divided into three parts, describing the synthesis of different types of heterogeneous biocatalysts (carrier-free SEN immobilization, SEN entrapment in inorganic scaffolds, and immobilization of SEN on prefabricated carriers).

3.3.4.1 *Carrier-free SEN immobilization*

In this section we describe the fabrication of heterogeneous biocatalysts that were formed exclusively through the coordination of imidazole in SENs with cationic metals (Metal-Organic Enzyme Aggregates, MOEAs) or hemin (heterogeneous integrated nanoreactors, INRs).

MOEAs were synthesized at room temperature by the addition of metal salts, i.e., CuSO_4 , $\text{Ni}(\text{NO}_3)_2$, $\text{Co}(\text{NO}_3)_2$, or $\text{Zn}(\text{NO}_3)_2$, into imidazole-functionalized SENs in Tris-HCl buffer (30 mM, pH 7.0, 1 mL) (see section 4.2.2). After incubation overnight, the MOEAs were centrifuged at 5000 xg for 3 minutes and washed. Depending on the metal:nanogel ratio, MOEAs of different sizes were produced. Nanoparticulate MOEAs were fabricated by mixing high metal salt concentrations (5 mM) with rather low amounts of $\text{GOx}@p\text{AA-I}$ (1.6 μM). In contrast, lower metal concentration (0.5 mM) and higher $\text{GOx}@p\text{AA-I}$ (12.5 μM) resulted into insoluble and compact pellets.

Nanoparticulate MOEAs, formed with $\text{GOx}@p\text{HEAA-I}$ (12.5 μM , 1 mL) and metal salts (1.5 mM), were utilized for catalytic film formation (section 4.2.2.1). For that, MOEAs were drop casted (2 μL , 0.09 – 3.00 mg mL^{-1}) onto silicon and glass substrates for the in situ assembly at room temperature. The dried films were washed with water to remove unbound material and used for characterization or activity assays. For the formation of bi-enzymatic films for cascade reaction, typically 2 μL of each MOEA (0.375 mg mL^{-1}) were deposited in each well (96-well plate). Films with different enzyme ratios were fabricated by mixing both MOEAs (25, 50, and 75%) before drop-casting a total of 1.5 μg of the enzyme.

For the fabrication of heterogeneous INRs (see section 6.2.2), $\text{GOx}@p\text{HEAA-I}$ (1.5 mL, 0.25 mg mL^{-1}) in Tris buffer (40 mM, pH 7.0) were mixed with an excess of hemin chloride (molar excess from 0 to 600) at 32°C for 16 h. The hemin stock was freshly

prepared at 30 mM in a NaOH solution (0.23 M). After incubation, the samples were centrifuged at 9000 rpm for 3 min. The supernatant was removed, and the solid was washed with water (1.5 mL). The cleaning process was repeated three times and the NanoNOx were suspended in 1.5 mL of water and stored at room temperature.

3.3.4.2 *SENs entrapped in biominerals*

The general protocol for the formation of nanosponges consists of the addition of $\text{CuSO}_4 \cdot 5\text{H}_2\text{O}$ (1 mM) to a PBS solution with a-HRP@a-iNGs (2.2 μM , 2 mL) (see **Chapter 5**). After 2 h the solution was centrifuged (5000 $\times g$, 5 min), washed with water, and stored at 4°C. The protocol for the nanoflower formation was identical, but using HRP instead of SENs and having an incubation time of 72h.

3.3.4.3 *HeWT@pAA-NH₂ covalently bound to epoxy-functionalized prefabricated carriers*

First, 100 mg of resin, i.e., epoxy-methacrylate and epoxy-butyl methacrylate, were washed 3 times with 10 volumes of phosphate buffer (50 mM, pH 8.0). Then, the resin was incubated overnight with HeWT@pAA-NH₂ (500 μL , 0.2 mg mL⁻¹) in phosphate buffer (50 mM, pH 8.0) under orbital shaking at room temperature. The suspension was filtered and washed 3 times with 10 column volumes of phosphate buffer (50 mM, pH 8.0), keeping the flow-through for further analysis. The immobilized preparation was not blocked with glycine. The SENs were incubated under the same conditions in the absence of beads for comparison. This methodology is related to **Chapter 7**.

3.3.5 Expression and purification of recombinant enzymes

An alcohol dehydrogenase from *Bacillus stearothermophilus* (BsADH, E.C. 1.1.1.1., 0.06 U mg⁻¹ for BnOH) was utilized in section **6.2.5.1**. BsADH was overexpressed in competent *Escherichia coli* BL21. Briefly, 10 mL of an overnight culture of transformed

E. Coli was used to inoculate 750 mL of Luria-Bertani (LB) medium containing kanamycin ($30 \mu\text{g mL}^{-1}$). The resulting culture was aerobically incubated at 37°C with orbital shaking at 200 rpm until the optical density (OD_{600}) reached 0.6. Then, the protein expression was induced with 1 mM of isopropyl β -D-1-thiogalactopyranoside (IPTG) overnight. After the induction time, the cells were harvested by centrifugation at 4000 rpm for 30 min at 4°C . Supernatants were discarded and the pellet was resuspended in sodium phosphate buffer (37.5 mL of 25 mM at a pH 7.0). 2 μL of DNase (stock solution of 1 mg mL^{-1}) and lysozyme (100 μL of a stock solution of 100 mg mL^{-1}) were added and incubated for 1h at 4°C . Then, cells were lysed by sonication using an Ultrasonic sonicator (Bandelin Sonoplus), at 25 % amplitude and 5 s pulse (ON/OFF) for 6 minutes in an ice-water bath. The suspension was then centrifuged at 10000 rpm for 30 min at 4°C .

For the purification of the enzyme, 10 volumes of the collected supernatant were mixed with 1 volume of Ni^{2+} affinity resin for 2 h at 4°C , which was previously cleaned the extraction buffer (25 mM of imidazole and 25 mM of sodium phosphate, pH 8.0). The flow-through was discarded and the Ni^{2+} resin was cleaned 3 times with 10 volumes of phosphate buffer (25 mM, pH 7.0). 3 volumes of elution solution (300 mM of imidazole in phosphate buffer 25 mM, pH 8.0) were added and the resin was incubated for 1h at 4°C . Finally, BsADH was eluted and dialyzed against sodium phosphate buffer (50 mM, pH 8.0) at 4°C (4 x 1 l buffer changes over 40 h). The BsADH concentration was calculated with a NanoDropTM 2000 (Thermo ScientificTM) ($\epsilon_{280\text{nm}} = 133000 \text{ M}^{-1} \text{ cm}^{-1}$; $M_w = 147 \text{ KDa}$) using the Lambert-Beer equation.¹⁶⁶ 10 mL stocks (1 mg mL^{-1} BsADH) were stored at -80°C and were overnight thawed at 4°C before use.

Halomonas elongata ω -transaminase (HeWT, 2.6.1.18., 2.5 U mg^{-1}) was selected as model ω TA to study the PLP confinement effect on the nanogel (see 7.2.1). *Escherichia coli* BL21 competent cells were transformed with the pHESPUC plasmid.¹⁶⁷ The expression was carried out in ZYM-5052 auto-induction medium (300 mL of 1% N-Z-Amine,

0.5% yeast extract, 50 mM KH_2PO_4 , 50 mM Na_2HPO_4 , 25 mM $(\text{NH}_4)_2\text{SO}_4$, 5 mM NaSO_4 , 2 mM MgSO_4 , 0.5% glycerol, 0.05% glucose, 0.2% lactose, 0.2% 1000x trace elements) in presence of ampicillin ($100 \mu\text{g mL}^{-1}$) at 37°C while shaking at 200rpm. The cells were harvested after 16 h and frozen at -20°C . The pellet was thawed and resuspended in the lysis buffer containing potassium phosphate buffer (50 mM, pH 8.0), pyridoxal 5'-phosphate (PLP, 0.1 mM), and imidazole (30 mM). The cells were disrupted by sonication at 4°C using SonicsVCX130 with 8 min 5 s of sonication, at 40% amplitude, and 10 s of cooling. After centrifugation ($38,000\times g$, 4°C , 45 min), the supernatant was clarified by filtration ($0.45 \mu\text{m}$ filter) before chromatography.

Chromatography was performed using an ÄKTA Purifier (GE Healthcare, Little Chalfont, UK). The filtered cellular extract was loaded into a 5 mL column of Ni-NTA Superflow pre-charged with NiSO_4 (0.1 M). The column was washed at a flow rate of 2 mL min^{-1} with at least 10 column volumes of running buffer (50 mM phosphate, 300 mM NaCl, 0.1 mM PLP, and 30 mM imidazole, pH 8.0) and the enzyme was eluted with the elution buffer (50 mM phosphate, 300 mM NaCl, 0.1 mM PLP, and 300 mM imidazole, pH 8.0) after an intermediate step with the 10% of elution buffer to remove non-specifically bound proteins. The fractions containing the enzyme were desalted via dialysis with phosphate buffer (50 mM, pH 8) containing PLP (0.1 mM). The purified enzymes were conserved at 4°C for short term storage or -20°C for long term storage. The enzymatic activity was tested following the spectrophotometric enzymatic assays (see below).

3.3.6 Calculation of SEN immobilization yield

The amount of protein incorporated into the heterogeneous biocatalyst was calculated by measuring the protein concentration in the solution before and after the formation of the heterogeneous catalyst (see equation below). The SEN concentration was measured with a NanoDropTM spectrophotometer at 450 nm ($\epsilon_{450\text{nm}} = 2.61 \times 10^4 \text{ M}^{-1} \text{ cm}^{-1}$

) and in the case of GOx enzyme at 280 nm ($\epsilon_{280\text{nm}} = 2.67 \times 10^5 \text{ M}^{-1} \text{ cm}^{-1}$), using the Lambert-Beer equation ($l = 0.1 \text{ cm}$).^{166,168} The HRP concentration was calculated measuring the absorbance at 402 nm ($1.02 \times 10^5 \text{ M}^{-1} \text{ cm}^{-1}$). The HeWT concentration was measured at 280 nm ($\epsilon_{280\text{nm}} = 1.25 \times 10^5 \text{ M}^{-1} \text{ cm}^{-1}$).

$$\Psi (\%) = \left(\frac{\text{enzyme}_{\text{offered}} - \text{enzyme}_{\text{supernatant}}}{\text{enzyme}_{\text{offered}}} \right) \times 100$$

3.3.7 Calculation of the protein content in heterogeneous biocatalysts (mass fraction)

The protein weight content (in dry solid) was calculated by gravimetry using dry heterogeneous biocatalyst amount with a known enzyme concentration. Specifically, MOEAs ($2.0 - 3.0 \text{ mg mL}^{-1}$, $40 \mu\text{L}$) were freeze-dried and weighted. The protein weight content (%w) was calculated as follows: %w = $100 \times \text{added protein } (\mu\text{g}) / \text{weighed dry solid } (\mu\text{g})$.

In the case of SENs immobilized inside prefabricated carriers the protein load was calculated from the immobilization yield and the amount of carrier utilized. This parameter was defined as $\text{mg}_{\text{enzyme}} \text{ g}_{\text{carrier}}^{-1}$.

3.3.8 Characterization of biocatalytic performance

Standard activity assays of heterogeneous biocatalysts were generally performed in 96-well plates, setting $200 \mu\text{L}$ as the final volume ($l = 0.5 \text{ cm}$) per well. The measurements were carried out in time course mode with an UV-vis spectrophotometer (Epoch2, Biotek). Unless otherwise mentioned in the text, the GOx activity measurements were performed by adding the enzyme (2 nM) to a mixture of glucose (100 mM), ABTS (1 mM), and HRP (0.1 ng mL^{-1}) in sodium phosphate (30 mM , pH 6.0) buffer at $37 \text{ }^\circ\text{C}$

(**Chapter 4** and **Chapter 6**). The color change from oxidized ABTS was monitored at 416 nm ($\epsilon_{416\text{nm}} = 36 \text{ mM}^{-1} \text{ cm}^{-1}$).

The activity of β -Gluc/GOx films was measured using a cellulose/HRP/ABTS assay in sodium phosphate (30 mM, pH 6.0), setting concentrations at 20 mM, 1 μM , and 1 mM, respectively (see section **4.2.2.1**).

The HRP activity assays were performed by mixing enzyme hybrids (0-50 nM), H_2O_2 (0.3 M) and ABTS (1 mM) in sodium citrate buffer (50 mM, pH 5.1) at 37 °C (see section **5.2.3**).

The activity of multifunctional integrated chemoenzymatic nanoreactors (INRs) was measured using INRs (16 nM) in a reaction mixture of glucose (30 mM) and ABTS (1 mM) in sodium acetate (100 mM, pH 6.0) buffer (see section **6.2.2**). The ABTS oxidation was tracked as mentioned earlier. The NADH oxidase activity of INRs was determined by monitoring the NADH oxidation at 340 nm ($\epsilon_{340\text{nm}} = 6.22 \text{ mM}^{-1} \text{ cm}^{-1}$) under aerobic conditions and 37 °C (see section **6.2.5.1**). For that, INRs (2 μL from stock solution, ranging from 0.11 to 1.04 μM) were added to a 200 μL of HEPES buffer solution (100 mM, pH 7.3) containing glucose (25 mM) and NADH (1 mM).

The HeWT activity of SENs, immobilized inside epoxy-functionalized carriers, was measured in 2 ml Eppendorf tubes (see section **7.2.2**). Briefly, 10 mg of resin were mixed with 2 mL reaction solution composed of S-MBA (2.5 mM), pyruvate (2.5 mM), and DMSO (0.25% v/v) in phosphate buffer (50 mM, pH 8.0). The reaction mixture was incubated at room temperature under orbital shaking. The absorbance at 245 nm ($\epsilon_{245\text{nm}} = 12 \text{ mM}^{-1} \text{ cm}^{-1}$) was measured as single readings using Brand UV-cuvettes in a Varian Cary 50 scan spectrophotometer.

3.3.8.1 Calculation of apparent catalytic constants of heterogeneous biocatalysts

MOEAs (Chapter 4). The catalytic constants, i.e., $^{app}K_M$ and $^{app}k_{cat}$, of MOEAs were measured in triplicate at 37 °C using the glucose/(HRP)/ABTS system. The apparent Michaelis-Menten constant ($^{app}K_M$) was calculated by varying the glucose concentration in each well from 0 to 200 mM, keeping ABTS (1 mM) and GOx (2 nM) concentrations constant. In the case of catalytic films, 2 μ l (0.375 mg mL⁻¹) were deposited in each well. The apparent turnover number ($^{app}k_{cat}$) was determined by varying the GOx concentration from 0 to 9 nM, setting the glucose concentration constant (100 mM).

Nanosponges (Chapter 5). The activity of nanosponges based on HRP was measured in triplicate at 37 °C in sodium citrate buffer (50 mM, pH 5.1), varying the H₂O₂ concentration from 0 to 150 mM for the $^{app}K_M$ calculation and varying the HRP concentration from 0 to 50 nM for the $^{app}k_{cat}$ calculation. In all cases the ABTS concentration (1 mM) was set constant.

INRs (Chapter 6). For ABTS oxidation, the kinetic parameters of INRs were measured by monitoring the oxidation of ABTS (1 mM) at 416 nm using a range of concentrations of glucose (0-50 mM) for the $^{app}K_M$ calculation and INRs (0.25 nM) for the $^{app}k_{cat}$ calculation in sodium acetate buffer (50 mM, pH 6.0) at 42 °C.

For the cofactor oxidation in section 6.2.5.1, to measure the $^{app}K_M$ of INR, the catalytic reactions were performed at growing concentrations of glucose, from 0 to 100 mM, while keeping the INR and the NADH concentrations constant (50 nM and 1 mM, respectively) in HEPES buffer (100 mM, pH 7.3) at 37 °C. An equivalent experiment was carried out to determine the $^{app}K_M$ for NADH. For that, the NADH concentration was varied from 0 to 800 μ M while the glucose and INR concentrations were fixed to 5 mM and 50 nM, respectively. The apparent turnover numbers for NADH ($^{app}k_{cat,NADH}$), NADPH ($^{app}k_{cat,NADPH}$, $\epsilon_{340nm} = 6.22 \text{ mM}^{-1}\text{cm}^{-1}$), and BNAH ($^{app}k_{cat,BNAH}$, $\epsilon_{361nm} = 7.24 \text{ mM}^{-1}\text{cm}^{-1}$) were determined.

$^1\text{cm}^{-1}$)¹⁶⁹ were measured at a fixed concentration of glucose and cofactor (25 mM and 1 mM, respectively) in a HEPES buffer solution (100 mM, pH 7.3) at 37°C. Each reaction was tested in a range of concentrations of INR, from 0 to 6.1 $\mu\text{g mL}^{-1}$ (0-0.044 μM).

SENs immobilized inside carriers. In **Chapter 7** only the catalytic constants of SENs (not immobilized) were measured. The catalytic reactions were performed in the presence of DMSO (0.25% v/v) and PLP (0.1 mM) at growing concentrations of pyruvate, from 0 to 5 mM, while keeping the HeWT@pAA-NH₂ and the S-MBA concentrations constant (18 nM and 5 mM, respectively) in phosphate buffer (50 mM, pH 8.0) at 37 °C. An equivalent experiment was carried out to determine the ^{app}K_M for S-MBA. For that, the S-MBA concentration was varied from 0 to 8 mM while the pyruvate and HeWT@pAA-NH₂ concentrations were fixed to 5 mM and 18 nM, respectively.

3.3.8.2 Degradation of small aromatics and dyes

Small aromatics (1 mM) were prepared in a sodium acetate (100 mM, pH 6.0) buffer with glucose (100 mM) and INR (0.78 μM). The reactions were stirred at 42°C in a closed vial. After every 30 min, the vials were opened and oxygenated with fresh air for a maximum response. The samples were centrifuged (13000 $\times g$ for 5 min) and the supernatants passed through a filter (0.2 μm cutoff membrane). The flowthroughs were measured by UV-Vis and analyzed by UPLC-MS.

The decoloring of organic dyes (methyl orange, methylene blue, phenol red, and rhodamine, 10 to 100 μM) was tested using glucose (100 mM) and INR (0.1 μM) in sodium acetate buffer (100 mM, pH 6.0). The bleaching efficiency was defined as the percentage of the difference between the absorbance of the control and the absorbance at different reaction times ($t = x$):

$$\text{Decolorization (\%)} = \frac{[\text{Initial Absorbance} - \text{Absorbance at } t=x]}{\text{Initial Absorbance}} \times 100$$

3.3.8.3 NanoNOx performance coupled with NAD-dependent dehydrogenases

Simultaneous glucose addition. The reaction solution contained NanoNOx (1.5 mg mL⁻¹), BsADH (0.2 mg mL⁻¹), BnOH (10 mM), NAD⁺ (1 mM), glucose (20 mM), and DMSO (5%, v/v) in sodium phosphate buffer (100 mM, pH 8.0, final volume of 500 μ L). The reactions were performed in 2 mL safe lock Eppendorf tubes at 37 °C and under constant agitation (40 rpm in carousel). The experiments were repeated in triplicates.

Sequential glucose addition. The reaction solution contained NanoNOx (1.5 mg mL⁻¹), BsADH (0.2 mg mL⁻¹), BnOH (10 mM), NAD⁺ (1 mM), and DMSO (5%, v/v) in sodium phosphate buffer (100 mM, pH 8.0, final volume of 500 μ L). The reactions were performed in 48-well plates at 37 °C and under constant orbital agitation, with a final volume of 200 μ L. Glucose aliquots (0.2 mM) were added periodically with a sample injector until a final concentration of glucose of 20 mM was reached in each case. The glucose was supplied either every 5 min for 8 h or every 15 min for 24 h.

3.3.9 Stability experiments of heterogeneous biocatalysts

Thermal stability. To study thermal stability of the heterogeneous biocatalysts, i.e., MOEAs (section 4.2.2) and nanosponges (section 5.2.3), 100 μ L (2 μ g mL⁻¹) were incubated in deionized water at 65 °C. At different time intervals (0, 5, 10, 20, 40, and 60 min), sample aliquots were collected and cooled down at 4 °C. Finally, the residual activity of each sample was tested as explained above.

For the thermal stability assay of the GOx-based catalytic films (section 4.2.2.1), initially 75 μ g MOEAs were deposited in each well of a 96-well plate. The films were incubated with glucose (200 μ L, 50 mM) in phosphate buffer (30 mM, pH 6.0) at different temperatures (30-75 °C) to evaluate their catalytic response. After 10 minutes, the reaction products were rapidly removed and kept at 0 °C. A second enzymatic reaction

was carried out with HRP and ABTS at 37 °C to quantify the amount of H₂O₂ formed by GOx films. Six independent films were assayed for each condition. Same experiments were also performed following the same procedure for free GOx.

Organic solvents. Zn@MOEA films (2 μL, 0.375 mg mL⁻¹) were incubated for 1 h at room temperature in the presence of 2-isopropanol (iPrOH), acetonitrile (MeCN), and dimethyl sulfoxide (DMSO) (see 4.2.2.1). Water was used as control. Afterwards, films were washed, and 20 mM of glucose were oxidized in the presence of such organic solvents (200 μL, 90% v/v) for 20 min. After the reaction, 2 μL of the respective solution were added to a HRP/ABTS solution (0.1 ng mL⁻¹ HRP and 1 mM ABTS) in sodium phosphate buffer (30 mM, pH 6.0) to monitor the activity as previously mentioned.

The activity of INRs was tested in the presence of organic solvents (50 and 80%, v/v) (see section 6.2.3). INR (8 μL of a stock solution of 1.6 μM), glucose (5 mM), ABTS (1 mM) or NADH (1 mM), and organic solvents (iPrOH, MeCN, and dimethyl formamide (DMF)) were mixed in sodium acetate buffer (100 mM, pH 6.0) or sodium phosphate buffer (for NADH oxidation, 100 mM, pH 8.0). The catalytic activity was tracked as explained above.

The activity in the presence of organic solvents of HeWT@pAA-NH₂ was tested before their immobilization in prefabricated epoxy-functionalized carriers (section 7.2.1). For that, HeWT@pAA-NH₂ were mixed with S-MBA (2.5 mM), pyruvate (2.5 mM), and DMSO (0.25% v/v) in phosphate buffer (50 mM, pH 8.0) in the presence of 50% (v/v) iPrOH, MeCN, or DMSO.

pH profile. Nanosponges and nanoflowers (section 5.2.3) were dispersed in water, acetate buffer (50 mM, pH 4.0 and 5.0), citrate buffer (50 mM, pH 4.5 and 6.0), and sodium phosphate buffer (50 mM, pH 7.2) to a final HRP concentration of 1 mg mL⁻¹. The samples were kept at room temperature for 5 min, centrifuged (5000 xg, 5 min), and the

supernatant was removed. The remaining pellet was suspended in PBS and used for the activity assay. The relative activity was calculated taking the samples incubated in water (100% of the activity) as reference.

The effect of the pH on HeWT@pAA-NH₂ was tested using a universal buffer containing citric acid (25 mM), potassium phosphate monobasic (25 mM), Tris (25 mM), borax (12.5 mM), and potassium chloride (25 mM) (section 7.2.1). HeWT@pAA-NH₂ were incubated overnight in universal buffer (pH 8.0, 9.0, and 10.0) and the activities were tested as specified above.

3.3.10 Reusability experiments of heterogeneous biocatalysts

The reusability of heterogeneous biocatalysts (MOEAs and INRs) was assessed by ON-OFF experiments. The ON phase started with a reaction mixture containing the reactants specified above. The absorbance at a certain wavelength (416 nm for ABTS oxidation by MOEAs and INRs; 340 nm for NADH depletion by INRs) was measured using the NanodropTM 2000 (Thermo Scientific) spectrophotometer. After a short time interval of around 5 min, the reaction mixture was centrifuged, the supernatant removed, and its absorbance measured every minute (OFF phase). In the case of catalytic films, a centrifugation to separate the reagents from the catalyst was not necessary. After 4-5 min, the supernatant and the heterogeneous biocatalysts were mixed and resuspended, repeating the cycle 5-9 times more.

3.3.11 Flow reactions

In section 7.2.3, continuous flow reactions were carried out in a R2+/R4 flow reactor from Vapourtec equipped with an Omnifit glass column (6.6 mm inner diameter x 42 mm length). The heterogeneous biocatalysts (1 g, 2 mg_{prot} g_{resin}⁻¹) were loaded into the column after being incubated in PLP (1 mM). The mobile phase, consisting of pyruvate (5 mM), S-MBA (12.5 mM), DMSO (1.25 % v/v), and phosphate buffer (50 mM, pH

8.0) was flowed at 0.29 mL min^{-1} , resulting in a retention time of 5 min. A washing step was performed just with phosphate buffer (50 mM, pH 8.0) before flowing the amino-donor and acceptor. The product was analyzed by UV-Vis spectroscopy, tracking the formation of acetophenone at 280 nm. An acetophenone standard curve was utilized to determine the concentration of the product.

Chapter 4 METAL-ORGANIC ENZYME AGGREGATES (MOEAS)

In this fourth chapter of the thesis, I present a new platform for the synthesis of catalytically active hybrid biomaterials, termed metal-organic enzyme aggregates (MOEAs). The MOEA formation is triggered by the metal-driven crosslinking of imidazole-functionalized SENSs. The size and morphology of MOEAs can be tailored from nanoparticles to macroscopic pellets, which are very stable in water and could be disassembled in the presence of complexing agents. Importantly, MOEAs can be subsequently self-assembled into continuous biocatalytic films. The enzyme glucose oxidase (GOx) is selected for the following experiments. The in-depth characterization of the films evidences their exceptional integrity, stability, and reusability. Finally, the thin films are utilized for the fabrication of an electrochemical biosensor of glucose and the study of enzymatic cascade reactions.

Published results: MOEAs with nanoparticle and pellet structure were published in **ACS Omega**.¹⁰⁸ Film formation through MOEAs was published in **Advanced Materials Interfaces**.⁹⁵ Adapted with permission from Adv. Mater. Interfaces 2019, 6, 18, 1900598. Copyright 2019 John Wiley & Sons, Inc.

4.1 FOCUSED INTRODUCTION

The crosslinking of SENs is a very promising approach for the synthesis of high-performance heterogeneous biocatalysts. This novel enzyme immobilization technique can overcome the problems inherent to CLEAs, enzyme aggregates that are chemically and irreversibly crosslinked.¹⁴⁷ On the one hand, the nanogels confine and concentrate specific ligands on the surface of the enzyme. On the other hand, SENs confer high stability to the enzyme, maintaining its catalytic activity almost unaffected.⁵⁸

Nature recurrently applies metal-driven crosslinking between histidine residues and metal ions for the formation of hard unmineralized hierarchical structures, such as mussel byssus or worm jaws, or for the assembly of proteins.^{170–172} Histidine has a side chain consisting of a basic imidazole group, considered as a σ -donor and π -acceptor ligand. This fact facilitates the coordination with metal cations such as Cu(II), Ni(II), and Zn(II).¹⁷³ This approach has been mimicked in the lab by the addition of methylimidazole and metal cations, i.e., Zn(II), to a protein solution. Remarkably, this combination leads to the in situ growth of zeolitic-imidazolate (ZIF-8) MOFs in which the enzyme remains embedded into a supramolecular structure.¹⁷⁴ The MOF-enzyme composites have demonstrated enormous potential in technological and industrial applications.¹⁷⁵ However, enzyme@ZIF-8 hybrids show some shortcomings related to the low protein encapsulation efficiency. Indeed, typical examples of enzyme-MOF composites synthesized in the absence of organic solvents usually lead to the growth of huge amount of noncatalytic material and low protein loadings (1-10 wt %), which eventually cause catalytic diffusion issues.¹⁷⁶

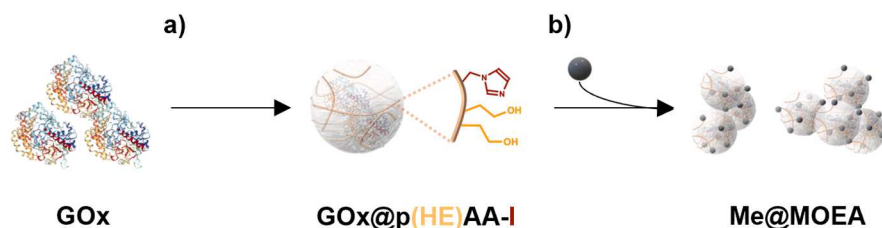


Figure 4-1. Workflow for the MOEA formation. a) enzymes are entrapped within imidazole-functionalized SENs, which are b) further crosslinked by coordination to metal ions for the MOEA formation.

Inspired by the histidine coordination chemistry, this chapter shows the fabrication of catalytic biomaterials by the aggregation of imidazole-modified SENs triggered by metal coordination (**Figure 4-1**). The resulting biohybrids are referred to as Metal Organic Enzyme Aggregates, MOEAs. MOEAs exhibit high enzyme loadings and activity due to their carrier-free nature and unmodified enzyme structure. In addition, MOEAs show enhanced stability at high temperatures or in the presence of organic solvents. These traits feature MOEAs as attractive materials that circumvent the most pronounced problems of immobilization systems such as ZIF-8-enzyme composites or CLEAs. Finally, we show how MOEAs can be assembled into hierarchically structured catalytic films deposited on inorganic surfaces.

4.2 RESULTS AND DISCUSSION

4.2.1 Synthesis and characterization of single enzyme nanogels (SENs)

Following the protocol described in **3.3.2**, non-covalent SENs were fabricated by *in-situ* free radical polymerization, introducing the vinyl imidazole monomer, (GOx@pAA-I, **Table 3-2**), for the very first time.

The size and morphology of the SENs was revealed by DLS (**Figure 4-2A**) and AFM (**Figure 4-2B**), confirming a spherical shape and a diameter of approximately 25 nm. Importantly, CD measurements showed that the secondary structure of GOx was maintained after polymerization (**Figure 4-2C**). The embedment of GOx within the nanogel was also evidenced by ATR-FTIR spectroscopy (**Figure 4-2D**). A rather intense amide I infrared band was detected for GOx@pAA-I sample, which was also

shifted 10 cm^{-1} towards higher wavenumbers in comparison with free GOx. This is attributed to the amide I band of polyacrylamide, which settles at 1644 cm^{-1} and overlaps with the protein band at 1632 cm^{-1} .¹⁷⁷ Moreover, the formation of the nanogel was confirmed by the polyacrylamide N-H stretching vibrations in the $3250\text{-}4000\text{ cm}^{-1}$ area and the band at 1084 cm^{-1} , the latter attributed to the terminal polyvinyl groups of the polymer. The incorporation of imidazole motifs was very clearly revealed by ATR-FTIR, as the emergence of a new band at 917 and 650 cm^{-1} that corresponds to the bending of the imidazole ring could be observed.¹⁷⁸ With all this information, we concluded that GOx was encapsulated within the polymer network. However, as the size of the SENs was triple the size of the free GOx ($\approx 8\text{ nm}$), we could not assure that the encapsulation of only single proteins inside the nanogels occurred, but, most likely, more than one enzyme were entrapped per capsule.

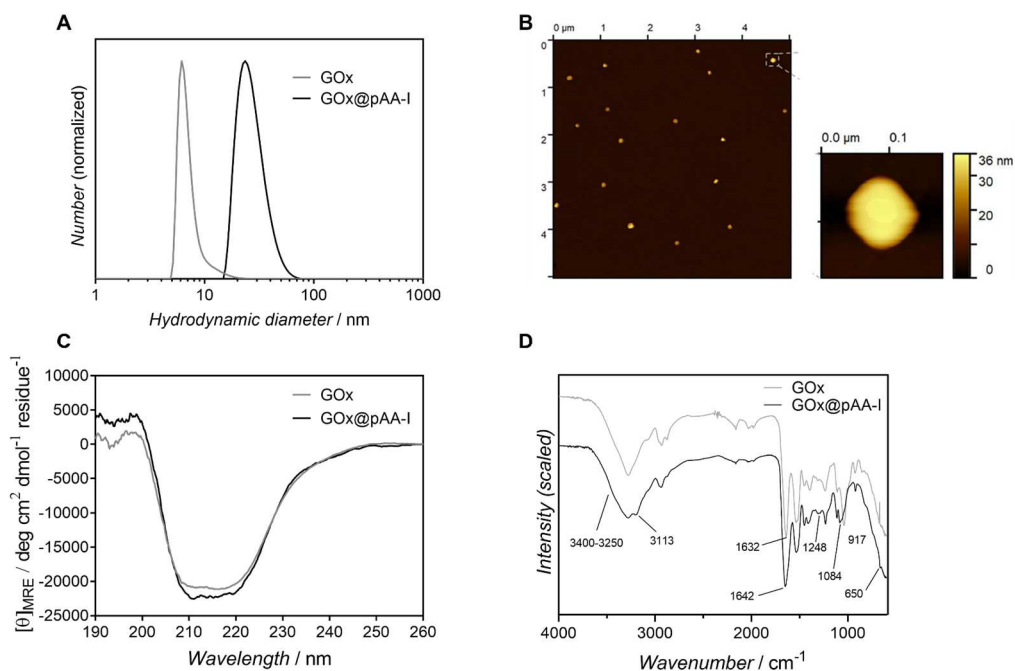


Figure 4-2. Structural characterization of GOx and GOx@pAA-I. A) DLS, B) AFM, C) CD, and D) ATR-FTIR spectra of free and GOx@pAA-I samples.

4.2.2 Synthesis and Characterization of Metal-Organic Enzyme Aggregates (MOEAs)

Nanoparticulated MOEA were synthesized mixing GOx@pAA-I with divalent cations, i.e., Cu(II), Zn(II), Ni(II), and Co(II), in Tris-HCl buffer, as described in 3.3.4.1 (schematic depiction in **Figure 4-1**). All synthesized hybrids yielded nanoparticles of similar size (400-900 nm) but different morphologies, as resolved by SEM and DLS (**Figure 4-3**). Interestingly, this protocol was very efficient in terms of protein immobilization yield (90-97%) and enzyme loadings (30-43%). However, when other buffer compositions were used, i.e., water, sodium acetate (30 mM, pH 5.0), and sodium phosphate (30 mM, pH 6.0), the immobilization yield of the assembly dropped considerably (<50%). Therefore, Tris-HCl buffer facilitates the formation of MOEAs, probably due to its facility to stabilize imidazole-metal coordination.¹⁷⁹

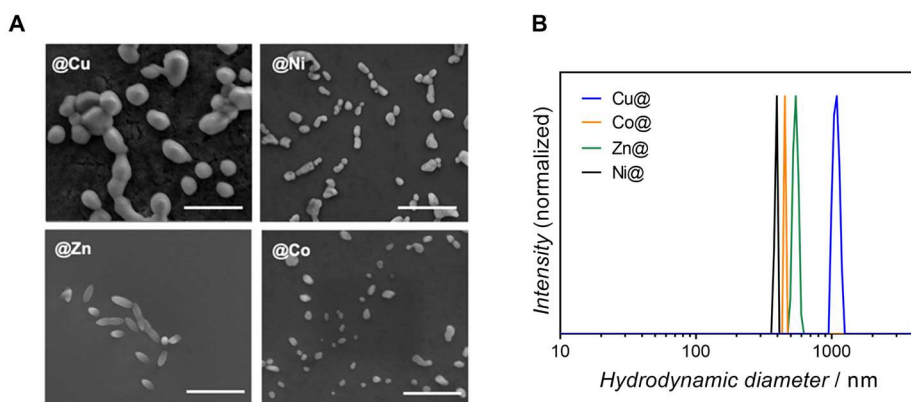


Figure 4-3. Structural characterization of MOEAs. A) SEM images of Cu@, Ni@, Zn@, and Co@MOEA nanoparticles (scale bar 2 μ m). B) Statistical size distribution of the hydrodynamic diameter of Cu@, Co@, Zn@, and Ni@MOEAs measured by DLS.

We observed that the metal:nanogel molar ratio played an important role for the aggregation of the assembled material. Hence, a higher seeding concentration of SENs and a lower metal cation concentration than that used for the fabrication of nanoparticles, led to the formation of insoluble and compact pellets that could not be

dispersed (**Figure 4-4A**). Both types of MOEAs, nanoparticles and pellets, were stable in aqueous solution and could be disassembled in the presence of metal complexing agents such as ethylenediaminetetraacetic acid (EDTA, 2mM). As shown in **Figure 4-4B**, MOEA nanoparticles were rapidly dissolved in the presence of EDTA, but the pellets were much more difficult to disassemble. This effect was most likely caused by i) limited diffusion inside/through the pellet and ii) a stronger crosslinking interaction among the nanogels. Likely, in the case of pellets, metal cations coordinate higher number of nanogels.

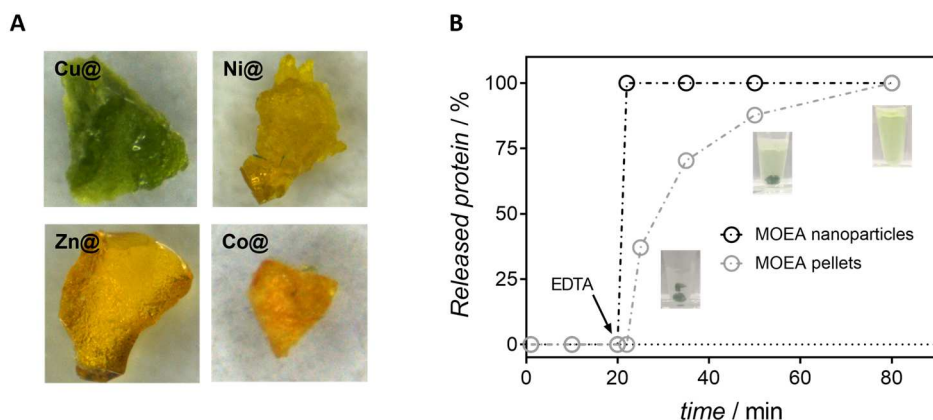


Figure 4-4. (A) Optical images of pelleted MOEAs. (B) Robustness of MOEA nanoparticles and pellets in water in terms of protein release and their disassembly after addition of EDTA. Inset pictures: Cu@MOEA dissolution over time.

The metal-imidazole coordination was assessed by ATR-FTIR spectroscopy (**Figure 4-5A**). The infrared peak attributed to the torsional bending of the imidazole rings, which in the case of the nanogels is at 917 cm^{-1} (blue), had a very clear shift to higher wavenumbers when the imidazole was coordinated to metal cations. This shift varied depending on the type of metal with which the imidazole was interacting. In the case of copper and zinc the peak emerged at 955 cm^{-1} (grey). In contrast, for nickel and cobalt the shift was shorter, settling at 943 cm^{-1} (pink). Moreover, with longer incubation times the peak at 917 cm^{-1} disappeared completely.

We observed an evolution of the color of Cu@MOEAs, from yellow to green (see **Figure 4-4A**). Hence, we performed XPS experiments to ascertain the oxidation state of the Cu within the material (**Figure 4-5C**). The Cu signal of Cu@MOEAs coincided with that typically observed from Cu₃N-based materials, showing a Cu 2p_{3/2} peak at 932.7 eV, which indeed is an unequivocal evidence of the reduction of Cu(II) to Cu(I).^{180,181}

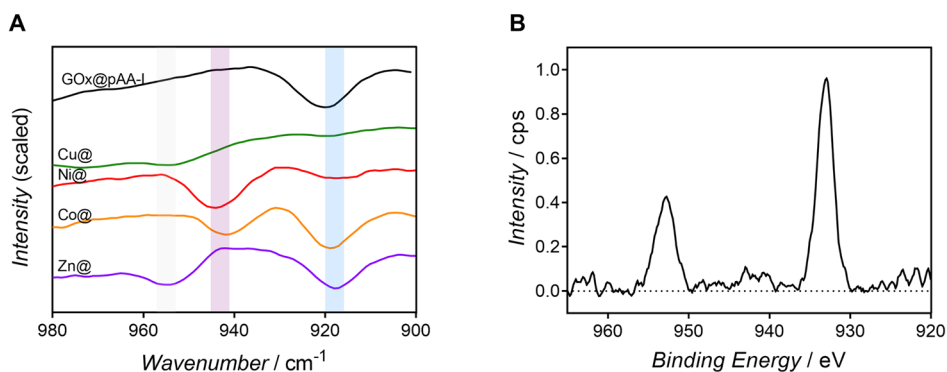


Figure 4-5. Compositional characterization of MOEAs. A) ATR-FTIR spectra of GOx@pAA-I, Cu@, Ni@, Co@, and Zn@MOEAs in the 990-980 cm⁻¹ spectral window. B) XPS of Cu@MOEAs in the Cu2p region.

GOx-embedded ZIF-8 hybrids were synthesized and characterized as reference of analogous metal-organic heterogeneous catalysts. As the performance of the ZIF-8-enzyme composites relies on the approach chosen for their synthesis, we selected two methods to entrap GOx into zeolitic imidazolate frameworks and compared them to MOEAs. The first method to fabricate GOx-ZIF-8#1 hybrid utilizes Brij/cyclohexane/water reverse micelle system for the confinement of the enzyme and reagents in small aqueous volumes.¹⁷⁴ Otherwise, GOx-ZIF-8#2 required the addition of polyvinylpyrrolidone as a capping agent to assist the dispersion and stabilization of protein in methanol.¹⁸² The glucose oxidation performance of the hybrids was studied in-depth using the glucose/HRP/ABTS detection method described in **3.3.8**. The apparent catalytic parameters of MOEAs (nanoparticles) and ZIF-8 hybrids were calculated and are summarized in **Table 4-1**. Overall, all MOEAs outperformed GOx-

ZIF-8s in terms of activity. From all measured hybrids Cu@MOEAs showed the highest catalytic efficiency ($^{app}k_{cat}/^{app}K_M$), comparable to that of free GOx. The difference between Cu@MOEAs and the rest of the hybrids might be attributed to a possible synergistic effect between the GOx and the Cu(I) crosslinker. Indeed, Cu(I)-based materials have been reported as excellent non-enzymatic glucose sensors.¹⁸³

The apparent Michaelis-Menten constant ($^{app}K_M$) values of MOEAs and GOx-ZIF-8#2 were similar or even lower than those from free GOx, meaning an enhanced affinity for the substrate, i.e., glucose. In contrast, GOx-ZIF-8#1 evidenced a detrimental effect on the affinity towards glucose. This effect might be caused by the use of organic solvents, i.e., hexane or detergents, during the synthesis procedure. Moreover, the measurements of apparent turnover numbers ($^{app}k_{cat}$) evidenced more prominent substrate diffusion issues in GOx-ZIF-8 hybrids with significantly lower turnover values. MOEAs also showed lower apparent turnover numbers ($^{app}k_{cat}$) than those of the free enzyme, evidencing diffusion limitations resulting from the SEN crosslinking.

Table 4-1. Measured apparent catalytic parameters for nanoparticulated MOEAs, ZIF-8 hybrids, and GOx.

	Cu@MOEA	Co@MOEA	Zn@MOEA	Ni@MOEA	ZIF-8 #1	ZIF-8 #2	GOx
$^{app}K_M$ (mM)	18.8 ± 5.4	15.0 ± 4.1	21.1 ± 6.3	14.9 ± 2.9	30.2 ± 6.7	19.9 ± 2.3	18.0 ± 1.7
$^{app}k_{cat}$ (x1000; min ⁻¹)	22.8 ± 0.5	10.9 ± 0.3	9.8 ± 0.1	10.9 ± 0.2	1.2	1.3	30.0 ± 1.9
$^{app}k_{cat}/^{app}K_M$ (mM ⁻¹ min ⁻¹)	1218	732	465	735	40	65	1670

The success of MOEAs as heterogeneous biocatalysts hinges upon their recyclability and their ability to be applied in harsh operational conditions. The recycling of MOEAs was studied with an ON-OFF activity assay (**Figure 4-6A**). Cu@MOEA pellets were used to ease the experimental procedure. The reaction was initiated by immersing (ON phase, black circles) the pellets into the reaction solution and removing them after about half a minute (OFF phase, grey circles). The process was repeated 8 times to have 8 reaction cycles. The reaction was completely stopped by removing the pellet, with no

enzyme leaching detected. In addition, the catalytic rate was constant throughout the experiment. Importantly, the integrity and activity of the MOEAs was maintained all along the exchange sequence. Therefore, even though the pellets swell in solution (**Figure 4-6A**, inset picture), there was no observable leakage or inactivation of GOx after 8 cycles.

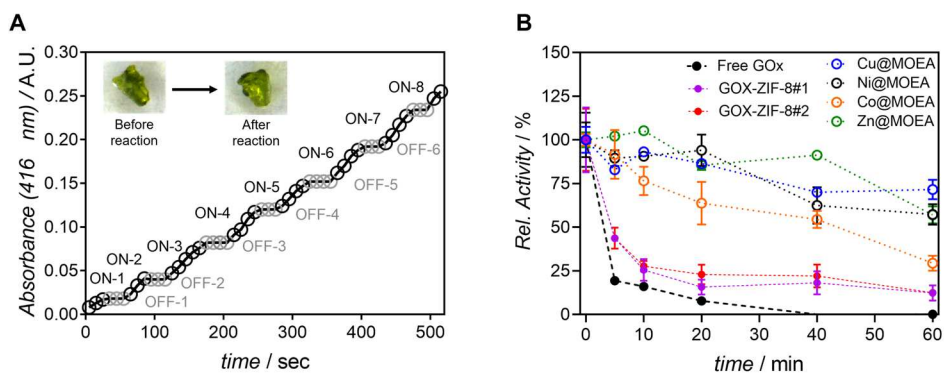


Figure 4-6. Recycling and thermal stability of MOEAs. A) ON-OFF switching experiment showing the immersion (ON) and withdrawal (OFF) of Cu@MOEAs into and out of the reaction mixture. B) MOEA and GOx-ZIF-8 activity evolution after incubation at 65°C for 1h.

Later, we studied the thermal stability of MOEAs and GOx-ZIF-8 hybrids by monitoring their catalytic activity after incubation at 65°C for 1 h. This temperature was chosen because GOx loses its conformation at temperatures higher than 50°C, and therefore, its functionality.¹⁸⁴ As observed in **Figure 4-6B**, only heterogeneous biocatalysts, i.e., MOEAs and GOx-ZIF-8 hybrids, showed activity after 1 h incubation at 65 °C. However, the stability profile was completely different for both types of materials. This disparity in thermal stability was remarkable when hybrids built through Zn(II)-imidazole coordination were compared. GOx-ZIF-8 hybrids lost 75% of the initial activity after 10 min and then the catalytic rate was kept constant for 50 min, probably maintained due to the enzymes entrapped deeper into the ZIF-8. Otherwise, Zn@MOEAs conserved their ability to oxidize glucose (≈ 100 to 80%) even after 60 min. These results demonstrate that the organic component in MOEAs, i.e., the nanogel, and SEN aggregation, provide higher thermal protection than ZIF-8, avoiding

the inactivation of the laden enzyme at high temperatures.

4.2.2.1 Catalytic film formation using MOEAs

Given the good performance of Zn@MOEAs, we decided to exploit their potential by assembling them into thin catalytic films. Zn@MOEAs were drop-casted onto hydrophilic surfaces (glass or activated silicon) following the protocol detailed in **0** (see schematic depiction in **Figure 4-7A**). During the drying process, MOEAs were arranged in parallel layers, turning the turbid unorganized solution into a transparent thin film. Unfortunately, this protocol yielded films that displayed a "coffee ring" configuration (**Figure 4-7B**, left). Next, we modified the polymeric shell of the SENs to increase the hydrophilicity of the hybrids, resulting in uniform and homogeneous films on glass substrates. (**Figure 4-7B**, right). To this end, we successfully synthesized GOx@pHEAA-I as in **3.3.2**, using the HEAA monomer to incorporate hydroxyl functional groups along the nanogel. Importantly, the formation of Zn@MOEAs was effective with GOx@pHEAA-I sample, with almost 100% of the enzyme immobilized and a protein content within the material of ca. 30% (w/w, measured in dry solid). Fortunately, the drop-casting of Zn@MOEAs synthesized from GOx@pHEAA-I on glass resulted into transparent, uniform and homogeneous films. Likely, the hydroxyl groups from the nanogels boosted the nanogel-nanogel and nanogel-substrate interactions. In addition, we confirmed that SENs need to be cross-linked to form well-ordered films (data not shown).

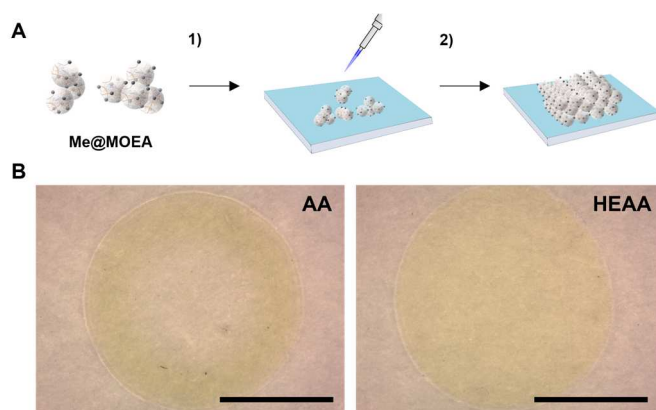


Figure 4-7. Formation workflow and optical pictographs of catalytic films. A) Catalytic film formation entails 1) the drop-casting of MOEAs onto a hydrophilic substrate and 2) the arrangement of the MOEAs during the drying process. Pictographs of films based on GOx@pAA-I (left) and GOx@pHEAA-I (right). Scale bar: 1 mm

The use of other metal cations for the formation of MOEAs and the subsequent formation of films was also evaluated. As observed in **Figure 4-8**, Zn@, Cu@, Co@, and Ni@MOEA assembly resulted in transparent, thin, and homogeneous layers. The use of these cations generated a different degree of non-covalent crosslinking that could affect the flexibility and brittleness of the films, which generated cracks in some of the samples, i.e., Ni@MOEA. Other metal cations with lower affinity for imidazole, i.e., Pd²⁺ and Cr³⁺, were also tested, which formed granular structures.

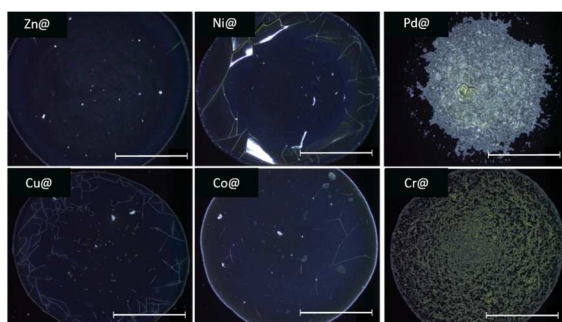


Figure 4-8. Dark-field optical pictographs of catalytic films formed with Zn, Cu, Ni, Co, Pd, and Cr. Scale bar: 1 mm.

An in-depth characterization was carried out to assess the structure and chemical composition of the films. The deposition of 2 μL (0.75 mg mL^{-1} Zn@MOEA) resulted in continuous, homogeneous, and wavy surface films with a thickness of approximately 600 nm (**Figure 4-9A-B**). In contrast, deposition of higher concentrations ($>2 \text{ mg mL}^{-1}$, 2 μL) caused cracks and detachment of the films from the surface (**Figure 4-9C**). With the lowest concentrations used (0.1 mg mL^{-1} , 2 μL) the films were discontinuous (**Figure 4-9D**). Therefore, it was possible to modulate the thickness of the films from 200 nm up to 4 μm by varying the seeding concentration of MOEAs.

The nanostructure of the films was evidenced by AFM imaging (**Figure 4-9E**). AFM images show homogeneous grainy surfaces, with measured root mean square (RMS) roughness values between 6.4 and 12.2 nm, for all divalent metals used for film synthesis. Each of these grains is probably a SEN incorporated into the film structure. Similar images were also obtained by SEM (**Figure 4-9F**). In addition, the deposited MOEAs appeared to self-organize in different layers, as observed in **Figure 4-9G**. Therefore, these results suggest an ordered and homogeneous assembly of MOEAs on the substrate.

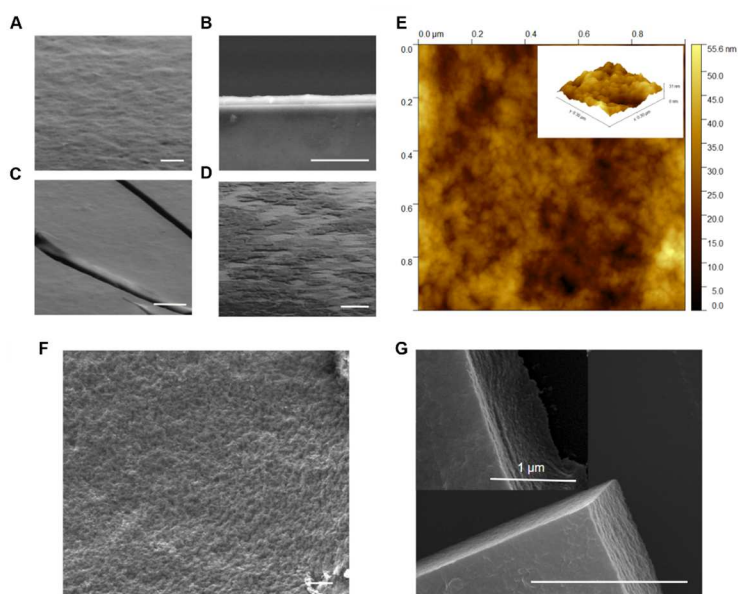


Figure 4-9. Morphology of catalytic Zn-containing thin films. SEM image of the film deposited with 0.75 mg ml⁻¹ in A) top view and B) cross-section view. C) Top view of the film deposited with 2.0 mg ml⁻¹. D) Top view of the film deposited with 0.1 mg ml⁻¹. The aggregation and compactness of nanoscale structures within the film was evidenced by E) AFM and F) SEM. G) Layered structures are observed in cracked films by SEM. Scale bar: 4 μm.

The composition of the film was evaluated by a number of spectroscopic techniques. The UV-vis spectrum of the dried films shows an absorption maximum at 450 nm, typical of GOx due to the presence of the flavin adenine dinucleotide (FAD) cofactor embedded in its structure (**Figure 4-10A**).¹⁸⁵ Circular dichroism measurements showed

the characteristic minimum at 222 and 208 nm, typical of alpha helices, meaning that the secondary structure of GOx was not altered after the SEN formation, crosslinking, and deposition (**Figure 4-10B**). In addition, the conservation of the secondary structure was confirmed by ATR-FTIR spectroscopy. No significant difference was observed in the position or shape of the amide I peak of GOx after the film formation (**Figure 4-10C**). Further compositional information was obtained with XPS measurements, determining 2.9 at% of Zn in the hybrid structures with a binding energy of 1002 and 1045 eV, suggesting the coordination between Zn and imidazole (**Figure 4-10D**).¹⁸⁶ Therefore, the compositional characterization of the films evidences that the enzyme structure is maintained and that the assembly is promoted by metal-imidazole coordination.

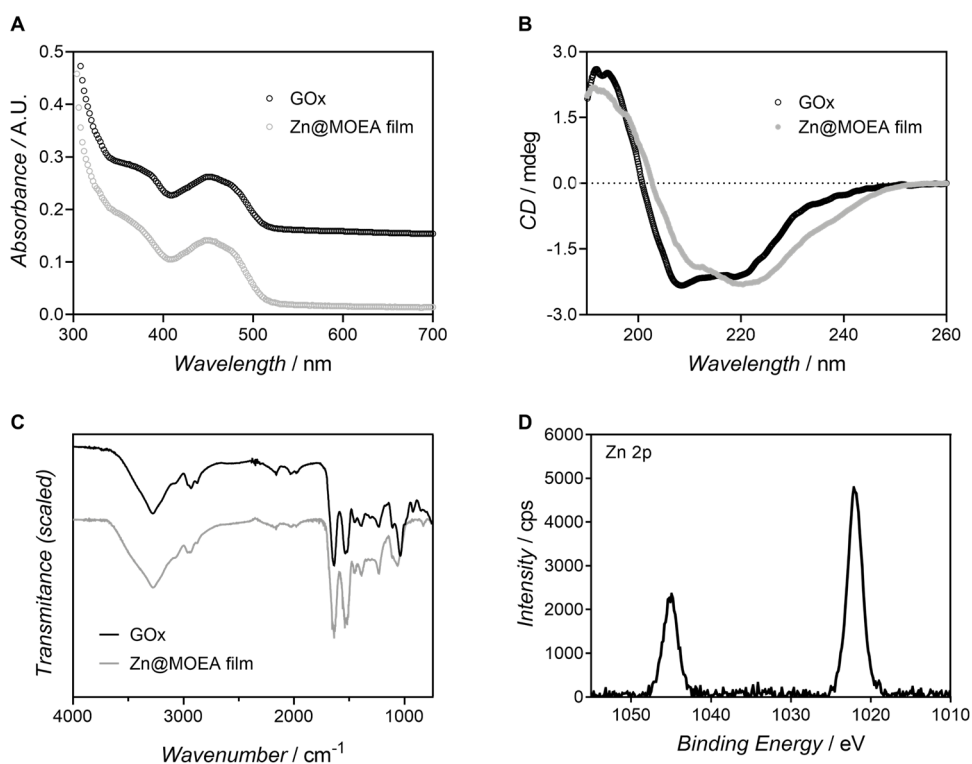


Figure 4-10. Compositional characterization of films. A) UV-vis, B) CD, and C) ATR-FTIR measurements of Zn@MOEA films and free GOx as reference. E) XPS spectrum of a Zn@MOEA films in the Zn 2p spectral region.

The catalytic performance of the films was evaluated measuring their glucose oxidation capacity after the deposition of the films on 96-well plates. The transparency of the thin films for visible light allowed in situ absorbance tracking of oxidized ABTS. Interestingly, a lag-time of 3-6 minutes was observed to reach the highest transformation rates with Zn@MOEA films (**Figure 4-11A**). This effect was dependent on the thickness of the film, since the thicker the film, the longer the delay phase. These substrate diffusion limitations were attributed to film compaction and the need for hydration of the material. Hence, the activity of the films could be increased from 3.2 ± 0.6 to 35.7 ± 1.5 U by decreasing the thickness of the film (from 3 to 0.2 mg mL^{-1} , $2 \mu\text{L}$). The highest activity was shown by non-continuous films (0.1 mg mL^{-1} , $2 \mu\text{L}$), but with very poor reproducibility. In addition, clear differences in activity were observed when comparing films built from the same amount of SENs and different sort of metal cations (**Figure 4-11B**).

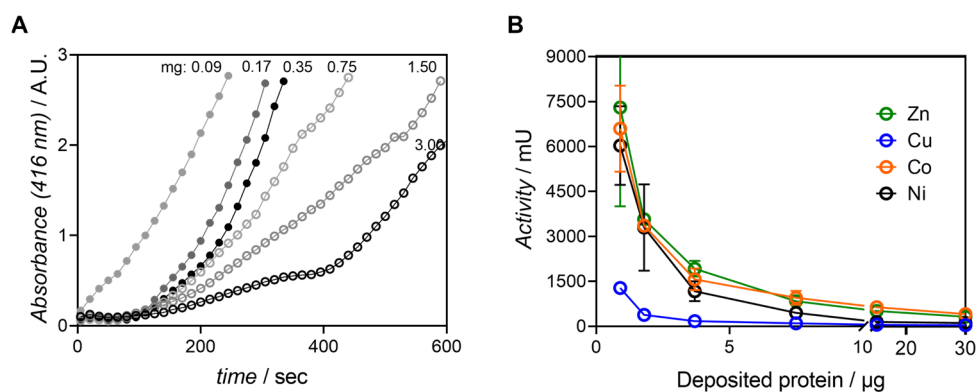


Figure 4-11. Catalytic characterization of MOEA catalytic films. A) Glucose oxidase activity plots of Zn@MOEA films, deposited at a range of protein concentration from 3 mg to 0.09 mg. B) Glucose oxidase activity of assorted Me@MOEA films at different protein concentrations.

The apparent Michaelis constant ($^{app}K_M$) of the four films, i.e., Zn, Cu, Co, and Ni, was calculated to examine the effect of metal cations on the ability of GOx to bind glucose. Interestingly, $^{app}K_M$ values were significantly lower than those calculated for free GOx (**Table 4-2**). Moreover, the differences in V_{max} indicate that the degree of

crosslinking and the compactness of the film can be modulated by the selection of the appropriate divalent metal cation for film formation.

Table 4-2. Measured apparent catalytic parameters for Me@MOEA catalytic films.

<i>Films</i>	<i>Zn@MOEA</i>	<i>Cu@MOEA</i>	<i>Co@MOEA</i>	<i>Ni@MOEA</i>	<i>GOx</i>
$^{app}K_M$ (mM)	2.2 ± 0.3	1.40 ± 0.6	1.1 ± 0.4	3.0 ± 0.7	18.0 ± 1.7
V_{max} ($\mu\text{mol min}^{-1}\text{mg}^{-1}$)	12.5 ± 0.2	1.1 ± 0.1	8.2 ± 0.3	4.0 ± 0.2	>100.0

The integrity and stability of the films is very important to be considered as attractive biomaterials for biotechnological applications.¹⁸⁷ Therefore, the films were evaluated during five long catalytic cycles of 30 minutes each (**Figure 4-12A**). The Zn films lost 15% of their initial activity after the first cycle but the activity was retained in the next cycles. The same experiment was performed with the rest of the films, i.e., Cu, Co, and Ni. Significant differences were observed among the samples. On the one hand, Cu-containing films, despite being the least active, were the most robust, retaining 95% of their activity. On the other hand, the Co films lost activity in each cycle, retaining only 55% after the entire process. These results might be related with the different chelating strength shown by metal cations with imidazole and denoted by their binding constant ($\log K_{\text{Metal-imidazol}}$ of 2.5, 2.6, 3.1, and 4.3 for Co, Zn, Ni, and Cu, respectively)¹⁸⁸. Therefore, high metal-imidazole affinities result detrimental in terms of the activity probably due to a higher mechanical stress of the enzyme, but conversely favors the robustness and reusability of the system. In any case, all the nanoreactors were strongly assembled and firmly attached to the hydrophilic substrate, showing to be robust and recyclable structures.

Also, the solubility and stability of the Zn@MOEA films were tested in organic solvents such as dimethyl sulfoxide (DMSO), 2-isopropanol (iPrOH), and acetonitrile (MeCN). The films were immersed for 1 h in pure organic solvents, cleaned with water, and tested for their performance. Surprisingly, the catalytic performance of the glucose oxidation

in the presence of *i*prOH and MeCN increased by 370 and 50 times, respectively, compared to the activity in water (**Figure 4-12B**).

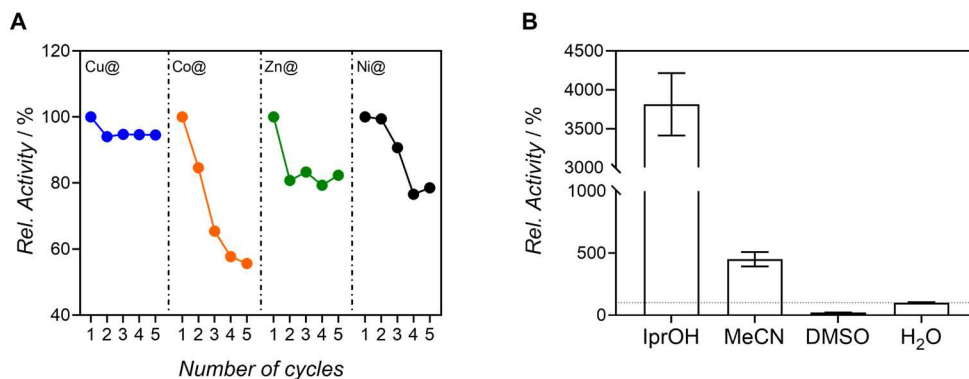


Figure 4-12. Reusability and activity in organic solvents of MOEA catalytic films. A) Reusability of all investigated films after 5 long (30 min) catalytic cycles. B) Relative catalytic performance (compared with water) of Zn@MOEA films in the presence of organic solvents after being incubated in the same solvents for 1 h.

In addition, the thermal stability of the films was also studied. They were still active, even after being heated at 75°C for 10 minutes (**Figure 4-13**). Under the same conditions, free GOx maintained only 8% of its initial activity. The very good performance of the films both in the presence of organic solvents and at high temperatures are very relevant and demonstrate the enormous potential of these hybrid materials as heterogeneous biocatalysts.

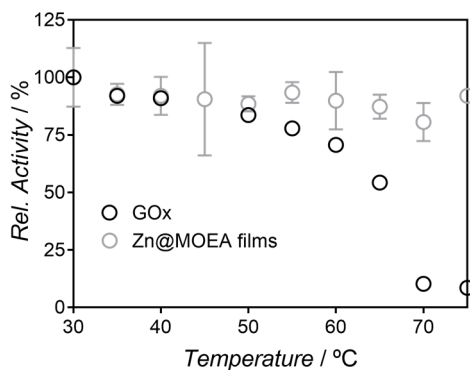


Figure 4-13. Catalytic response of Zn films in a temperature window of 30-75 °C.

Finally, the films were tested for two different applications: 1) the formation of a glucose biosensor, and 2) the study of a catalytic cascade reaction. The glucose biosensor was based on a three-microelectrode system (DropSens® interdigitated gold electrodes). Hence, Zn@MOEA films were homogeneously deposited on the working electrode by drop casting ($15 \mu\text{l}$, 0.75 mg ml^{-1}), washed, and cyclic voltammograms (CV) were acquired for a range of glucose concentrations in PBS (**Figure 4-14A**). The measurements were carried out after equilibration for 200 s with magnetic stirring. The CVs showed a curve with one of the maxima at 330 mV, which was attributed to the reduction of O_2 by the FADH_2 of GOx. Therefore, the CVs suggested a direct electron transfer between the film and the working electrode.¹⁸⁹ The preliminary studies showed that this biosensor can be used to measure the glucose concentration electrochemically in a linear fashion from 0.1 to 1.5 mM (**Figure 4-14B**).

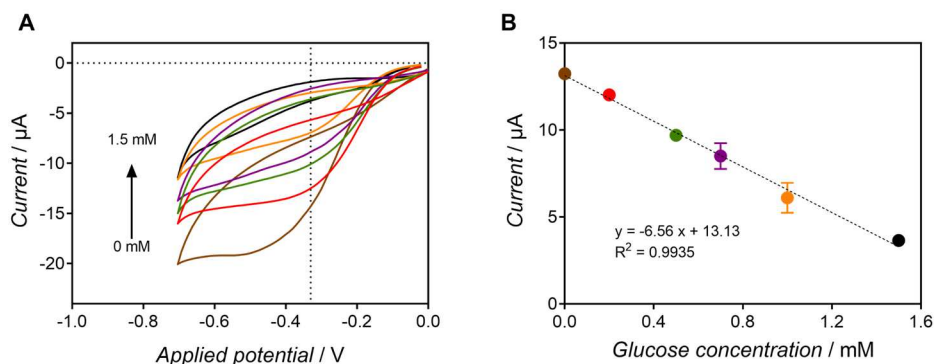


Figure 4-14. Electrochemical glucose biosensing with Zn@MOEA catalytic films. (A) Cyclic voltammogram obtained at different glucose concentrations (0 – 1.5 mM). B) Recorded intensity at each glucose concentration.

Finally, we tested this method for the controlled colocalization of enzymes for cascade reactions. As example, the colocalization of the β -Gluc/GOx duplex was evaluated for the hydrolysis of cellobiose and subsequent oxidation of glucose (**Figure 4-15A**). For that, β -Gluc@pHEAA-I (**Table 3-2**) and the corresponding Co@MOEAs were synthesized as explained in section 3.3.4.1. Moreover, we designed different

arrangements of catalytic films (referred to as “configuration”) for the fabrication of bi-enzymatic films. The first configuration, named GOx/ β -Gluc, consisted of a first layer of GOx film and a second β -Gluc film on top (**Figure 4-15B**). Importantly, SEM/EDX imaging showed that enzymes were compartmentalized in two spatially resolved layers (**Figure 4-15C**). The reverse configuration with GOx on top, was also fabricated (named β -Gluc/GOx). As a second approach, a mix of β -Gluc and GOx MOEAs with different ratios (25, 50, and 75% of β -Gluc) was deposited. Interestingly, different reaction rates were retrieved for each of the configurations. As depicted in **Figure 4-15D**, the β -Gluc/GOx configuration with GOx on top showed an enhancement of the activity of 25% compared to GOx/ β -Gluc and 50% β -Gluc films. This effect is attributed to the compartmentalization of enzymes.¹⁹⁰ The confinement of β -Gluc in the bottom layer forces the cellobiose hydrolysis product, i.e., glucose, to pass through a layer of GOx before it reaches the outer media, which enhances the cascade reaction rate.

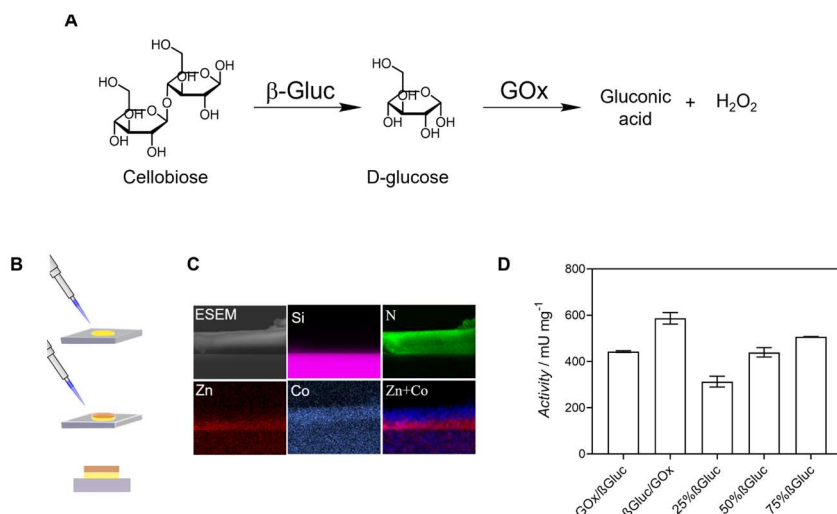


Figure 4-15. Synthesis and characterization of bi-enzymatic films for cascade catalysis. (A) Scheme of the cascade reaction. (B) Drop-casting of two consecutive films on top of each other. (C) EDX-imaging map of the cross-section of the film with the GOx/ β -Gluc configuration. (D) Catalytic rates measured for all configurations. U defined as $\mu\text{mol}_{\text{glucose}} \text{min}^{-1}$.

4.3 CONCLUSION

MOEAs are hybrid materials that show very good catalytic activity and excellent tunability, since their morphology or composition can be varied depending on the intended application. The high activity of these novel heterogeneous biocatalysts is attributed to their good diffusion characteristic and large protein loadings compared to other enzymatic materials, e.g., enzyme-ZIF-8 composites. In addition, the combination of Cu(I) with GOx very clearly enhances glucose oxidation. The thermal stability of nanoparticulate Zn@MOEAs is excellent, and far superior to that of the free enzyme.

MOEAs can be arranged into layered structures for the fabrication of biocatalytic coatings by simple drop-casting. Furthermore, as a versatile method, the thickness of the immobilized film can be altered by adjusting the concentration of the deposited MOEAs. The biocatalytic response and film integrity depends on the thickness and nature of the metal cations used for the SEN assembly. Moreover, the films are stable in aqueous environment, at high temperatures, and in the presence of organic solvents. Therefore, this enzyme immobilization platform increases the protein loading and protects the enzyme from denaturation under harsh conditions. This feature, plus the easy co-localization of enzymes on surfaces and arranged layers suggest that these enzyme films are very good candidates to be used as heterogeneous catalyst in diverse biotechnological applications, as demonstrated in this chapter.

Chapter 5 BIOMINERALIZED ENZYME HYBRIDS

In this fifth chapter, I present a new platform for the development of catalytic organic-inorganic enzyme hybrids, here referred to as nanosponges (NSs), which are based on the imidazole-modified Single Enzyme Nanogels (SENs) entrapment due to a biomineralization process. Compared to other literature-known hybrids, the protein nanoflowers (NFs), the structuring into NSs enhances the catalytic conversion rates, robustness of the material at low pH values, and the thermal stability. Importantly, NS hybrids can be grown with assorted transition metal cations that trigger the mineralization mechanism, which ultimately broadens the chemical and structural diversity of these bioinspired hybrids. The horseradish peroxidase (HRP) enzyme was selected as showcase for this work.

Published work: This work was published in **Advanced Functional Materials**.¹¹⁸ Adapted with permission from Adv. Funct. Mater 2018, 28, 35, 1803115. Copyright 2018 *John Wiley & Sons*, Inc.

5.1 FOCUSED INTRODUCTION

Biomaterials are hierarchical composites based on organic and mineral phases, which are produced by living organisms.¹⁹¹ Typical of biomaterials is a bottom up synthesis strategy, in which the materials are built starting from the atomic or molecular scale, resulting in the formation of nanostructured building blocks that assemble into more complex hierarchies.¹⁹² Biomacromolecules, e.g., proteins, play a key role in the biomaterialization process, as they control the formation, shape, and organization of the mineral phase.^{193,194} Importantly, biomaterials are formed at ambient temperature and pressure. Therefore, the unique characteristics of biomaterials have attracted the attention of researchers to explore and design new bioinspired materials for a variety of applications such as biocatalysis.

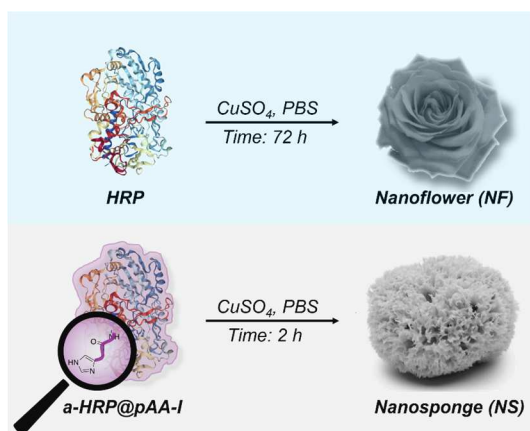


Figure 5-1. Schematic of the formation of both heterogeneous biocatalysts presented in this chapter. Nanoflowers (NF, blue) after biomineralization of free HRP. Nanosponges (NS, grey) were fabricated from nanogels modified with imidazole molecules (a-HRP@pAA-I).

The synergistic effect between enzymes and porous biomaterials leads to a remarkable stabilization and to an improvement of the catalytic activity of the incorporated enzyme. This is the case of the protein-inorganic nanoflowers (NFs, **Figure 5-1**, blue) described in section 1.4.2. However, the success of the NF synthesis depends on the sequence

and conformation of the protein, as specific amino acids, i.e., histidine, are required for the nucleation of the primary crystals.¹⁹⁵ Most NF synthesis involve Cu(II) due to its high affinity to the imidazole in histidine and its ability to form phosphates. However, this circumstance can be detrimental to nanoflowers since Cu(II) inhibits the activity of many enzymes.¹³⁶ Also, in literature there are examples of NFs formed with other divalent metals, e.g., Ca(II), Co(II), Zn(II), Fe(II), Mn(II).¹⁹⁵ In such cases it is required to use high metal concentrations to achieve acceptable biomineralization yields.

In this chapter we propose the use of SENs decorated with imidazole molecules as starting materials for the fabrication of biomineralized hybrid materials, termed nanosponges (NSs, **Figure 5-1**, grey). With SENs we can modify the protein surface artificially, avoiding the use of molecular biology tools to increase the density of more important residues for biomineralization. As in the case of ZIF-8 or MOEAs (see **Chapter 4**), imidazole can undergo stacking interactions with other moieties and bind metal ions. Herein, we show that the presence of imidazole groups grafted all over the SEN promotes the formation of insoluble sponge-like micro-structures in the presence of Cu(II) and PBS. Moreover, through an in-depth characterization of the biohybrid, we investigated the impact of the nanogels on the bioinspired material in terms of robustness, stability, activity, and kinetics of the entrapped enzyme. Finally, we extended the platform to other transition metal salts.

5.2 RESULTS AND DISCUSSION

5.2.1 Synthesis and characterization of single enzyme nanogels (SENs)

The synthesis procedure for the formation of a-HRP@pAA-I entailed 3 steps and are discussed in detail in section 3.3.2 and 3.3.3.1 and compiled in **Figure 5-2A**. The encapsulation and grafting were monitored through DLS (**Figure 5-2B**). Native HRP

showed a hydrodynamic diameter of 5.8 ± 0.3 nm, a-HRP@pAA-NH₂ sample presented 9.7 ± 0.3 nm, while a-HRP@pAA-I showed a similar hydrodynamic diameter of 10.1 ± 0.2 nm, which was barely altered to 10.1 ± 0.2 nm upon grafting reaction (a-HRP@pAA-I sample).

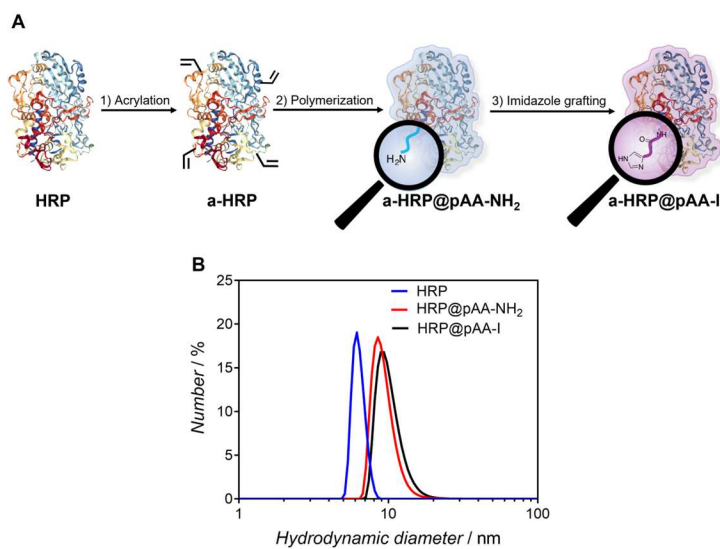


Figure 5-2. Synthesis and characterization of a-HRP@i-aNGs. A) Workflow for the synthesis of a-HRP@i-aNGs consisting of 3 steps: 1) acrylation, 2) polymerization, and 3) grafting. B) Hydrodynamic diameters measured by DLS.

5.2.2 Synthesis and characterization of Nanosponges (NSs)

The nanogels described above were used for the synthesis of nanosponges (NSs). As the objective of our work was to evaluate the effect of the nanogel on the biomineralization process, nanoflowers (NFs) were fabricated from the native enzyme as a reference. The fabrication workflow for both heterogeneous biocatalysts is shown in **Figure 5-1** and described in section **3.3.4.2**.

The addition of CuSO₄ to a-HRP@pAA-I in phosphate-buffered saline (PBS) at room temperature immediately generated a dark brown precipitate (**Figure 5-3A**, left inset picture). As observed by SEM, after 2 h of synthesis, the formed materials showed a

sponge-like morphology (**Figure 5-3A**, NS). As controls, a-HRP and a-HRP@pAA-NH₂ were processed under the same conditions and no solid precipitates were found after 2 h, proving the need of imidazole to facilitate rapid biomineralization. With longer incubation times (72 h) Cu(PO₄)₃·n(H₂O) bluish NFs were formed with free HRP, in agreement with earlier reports in literature (**Figure 5-3A**, NF).^{196,197} The NSs were smaller and more compact than the NFs with sizes of 5 vs. 25 μm, respectively. This effect could be due to the increase of nucleation sites as a result of the availability of more imidazole molecules in the nanogel, which would induce faster biomineralization of individual particles. In fact, the same effect has been observed with nanoflowers by increasing the concentration of the free enzyme.¹³⁵ A higher concentration of protein is equivalent to a higher number of nucleation points, which triggers the formation of smaller biohybrids.¹⁹⁸

The effect of copper concentration on the NS biomineralization was also studied (**Figure 5-3B**). Low copper concentrations (0.1 mM) resulted in NSs with planar structures. Concentrations of at least 0.5 mM CuSO₄ were needed to grow 3D structures. These biohybrids resembled sponges with a hierarchical structure, in which the outer shell is highly porous with interconnected channels. The largest structures (15 μm) were obtained with 10 mM Cu(II). Therefore, higher Cu(II) concentrations generate larger biomaterials.

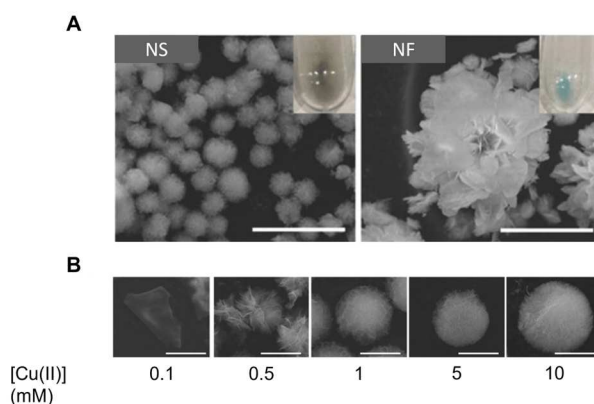


Figure 5-3. Morphological characterization of NS and NF biomaterials. A) SEM images showing

size and morphology of nanospheres (NS) and nanoflowers (NF) (scale bar 20 μm). B) SEM images of NSs grown from different CuSO_4 concentrations (0.1 mM – 10 mM, scale bar: 4 μm).

Later, the immobilization yields of both biohybrids were calculated. The duration of the NF formation was set to 72 h as in previously reported studies. Importantly, NSs showed an immobilization yield of 35% with a metal concentration as low as 0.1 mM, conditions under which NF formation is negligible (**Figure 5-4A**). With a metal concentration of 1 mM, 75% of a-HRP@pAA-I were incorporated into the heterogeneous biocatalyst only after 2 h. Note that the NS reached 100% immobilization yield when the samples were mixed for 72 h. The effect on the immobilization yield when the samples were mixed for 72 h. The effect on the immobilization yield of different enzyme concentrations was also analyzed (**Figure 5-4B**). The results revealed that NSs exhibited constant immobilization performance between 1.5 and 9.0 μM of seeded a-HRP@pAA-I concentration, whereas the immobilization performance of the NFs decreased with the increase of the concentration of HRP.

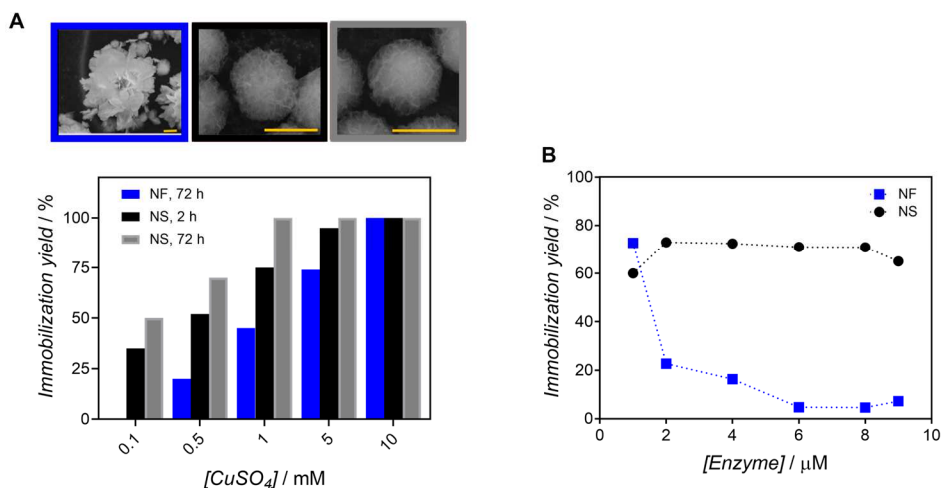


Figure 5-4. Calculation of the protein immobilization yield (%) of NSs and NF. A) Evaluation of immobilized protein at increasing Cu(II) concentrations (from 0.1 to 10.0 mM). Inset picture: morphology of the fabricated hybrids (bar: 5 μm) B) Evaluation of the effect of protein concentration on immobilized yields (from 1.5 to 9 μM).

Both heterogeneous biocatalysts were characterized by ICP-MS, ATR-FTIR, CV, and XPS to reveal their nature and composition. The HRP/Cu(II) molar ratio ($n_{\text{HRP}}:n_{\text{Cu(II)}}$) was quantified by ICP-MS at different concentrations of the seeded proteins (**Figure 5-5A**). This experiment was possible due to the iron cation present in the prosthetic group of HRP, i.e., heme.¹⁹⁹ The NSs showed higher HRP:Cu ratios in each case, in agreement with protein immobilization yield calculation. In addition, ATR-FTIR measurements showed differences between NSs and NFs (**Figure 5-5B**). The intensity of the amide I peak (i), attributed to proteins (also to polyacrylamide), was much higher in the case of the NSs. In addition, the imidazole peak (ii) was only visible in NSs. At the same time, the peak intensity of the asymmetric and symmetric stretching vibrations of PO_4^{3-} (iii) were lower in the case of NSs.²⁰⁰ Indeed, the ratio of intensities between protein and phosphate bands increased from 0.12 to 1.25 for the NSs. These results indicate that NSs are biomaterials with a much higher enzymatic loading than NFs, confirming the results obtained with other characterization techniques.

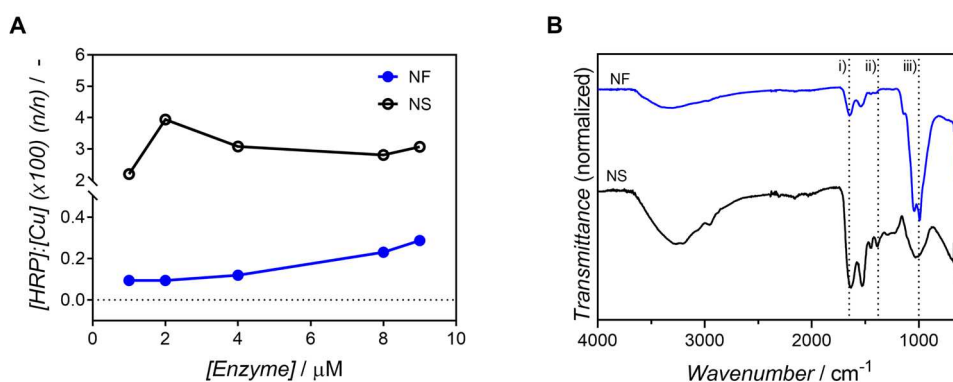


Figure 5-5. Compositional characterization of NS and NFs. A) HRP:Cu molar ratio (n/n) of formed hybrids at different seeded protein concentrations, measured by ICP-MS. B) ATR-FTIR spectra highlighting three spectral regions: i) protein peaks ($1650 - 1550 \text{ cm}^{-1}$), ii) imidazole ($1440 - 1410 \text{ cm}^{-1}$), and iii) phosphate stretching peaks (1031 cm^{-1}).

The electrochemical behavior of the Cu species within the biohybrids was studied by CV (**Figure 5-6**). Both samples were drop-casted on the working electrode and investigated from +600 to -900 mV at a scan rate of 0.1 V s^{-1} . The differences between

NSs and NFs were significant. The reduction peak at -200 mV and the oxidation peak at +300 mV in NFs shifted to -10 and 100 mV for NSs. The differences in the peak potential between both samples (ΔE_{NS} of 150 mV vs ΔE_{NF} of 520 mV) evidenced differences in the electron-transfer process between the working electrode and Cu species present in each hybrid. The main differences hint on the distinct chemical environments that surround the Cu species in each of the hybrids. Indeed, the CVs of the NSs were similar to those obtained for the electrodeposition of Cu in the presence of complexing agents such as amine and imidazole derivatives.²⁰¹

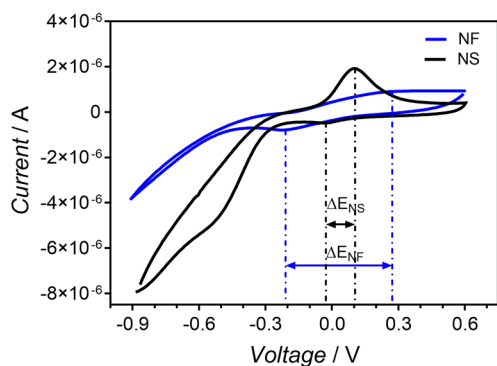


Figure 5-6. Cyclic voltammograms highlighting peak-to-peak separation of NSs (ΔE_{NS}) and NFs (ΔE_{NF}).

The Cu-imidazole coordination was eventually confirmed by XPS. The fitting of the N 1s peak of NSs showed a N-C component at a binding energy of 400.2 eV with a contribution at 398.8 eV, corresponding to a N-Cu bond (**Figure 5-7A**).²⁰² In contrast, NFs had a single component at 400.2 eV, corresponding to the N-C bonds of the protein. In addition, the Cu 2p_{2/3} peak from NFs at 935.1 eV matched well with the signal from Cu₃(PO₄)₂ (**Figure 5-7B**, dark blue). For NSs this peak was shifted to 934.2 eV due to Cu(II)-imidazole interaction (**Figure 5-7B**, black). Further, to demonstrate that imidazole could interfere in the biomineralization of Cu₃(PO₄)₂, Cu(II) was added to PBS at different imidazole concentrations (10, 50, and 100 mM) and the precipitation was evaluated. The XPS spectrum obtained with the highest concentration of imidazole

showed that the Cu $2p_{2/3}$ peak shifted even more (933.1 eV) than in the NSs. When the imidazole concentration was lowered to 50 mM, the binding energy of the Cu $2p_{2/3}$ peak was similar to that in NSs (934.0 eV). These results demonstrate that, while in NFs the Cu(II) contributed only to the growth of inorganic salts, in NSs the Cu(II) also assembles a-HRP@pAA-I sample through coordination with imidazole molecules present in the nanogel.

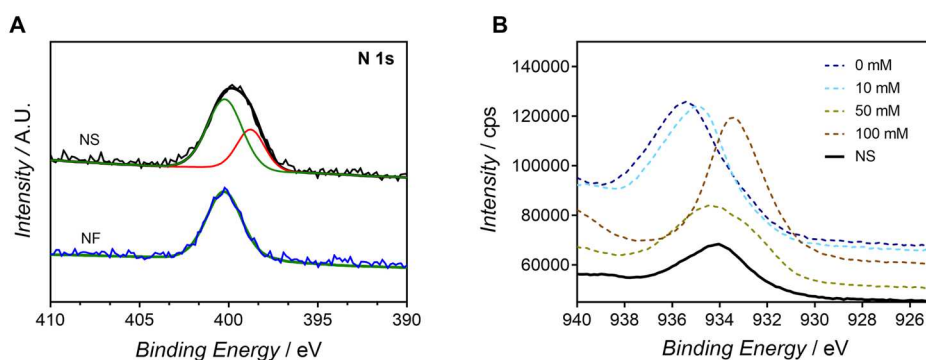


Figure 5-7. Fitted XPS spectra of NS and NFs. A) XPS of the N 1s region. B) XPS spectra of the Cu $2p_{2/3}$ region prepared with 0, 10, 50, and 100 mM of imidazole in a 10 mM CuSO_4 in PBS.

The complete compositional characterization of NFs and NSs elucidated that the assembly mechanism and nature of the hybrids was different. The characterization of the NSs suggested that confinement of the imidazole molecules on the protein surface enabled metal-organic coordination. At the same time, inorganic salts were able to grow around this lattice. This hypothesis matched well with the results obtained from ICP-MS, ATR-FTIR, CV, and XPS, as well as with the reported high protein immobilization yields.

5.2.3 Kinetics, robustness, and thermal stability of nanosponges

The effect of NS composition on the catalytic activity was studied in-depth and compared with NFs. For that, ABTS and H_2O_2 were used as co-substrates. The apparent

turnover number ($^{app}k_{cat}$) and the apparent Michaelis-Menten constant ($^{app}K_M$) of both biomaterials with increasing Cu(II) concentration revealed interesting features (**Figure 5-8**). The turnover number of NSs increased at high copper concentration, from 2700 to 35100 min^{-1} , for 0.1 mM and 5 mM CuSO_4 , respectively (**Figure 5-8A**). Beyond this last value, the turnover number remained constant in the studied range. The $^{app}k_{cat}$ is related to the diffusion of the substrate to the active center of the enzyme, which suggests that the conformation or localization of the protein in the NSs was favored with respect to the NFs.

The calculation of the $^{app}K_M$ of both biomaterials provided insights into the affinity of the substrate towards the active center of the enzymes. The $^{app}K_M$ values of the NSs increased from 0.9 to 45 mM at 0.5 and 10 mM Cu(II) seeding concentration, respectively (**Figure 5-8B**). This means that high concentrations of copper were detrimental for the enzyme activity and this effect was remarkable at copper concentrations higher than 1 mM. Importantly, the enzymes from NSs were less affected than those from the NFs, which is attributed to the shelter provided by the nanogel. Considering both $^{app}k_{cat}$ and $^{app}K_M$, the optimal copper concentration for the catalytic activity was 1 mM since the diffusion of the substrate to the enzyme and the affinity of the substrate for the enzyme was maximized.

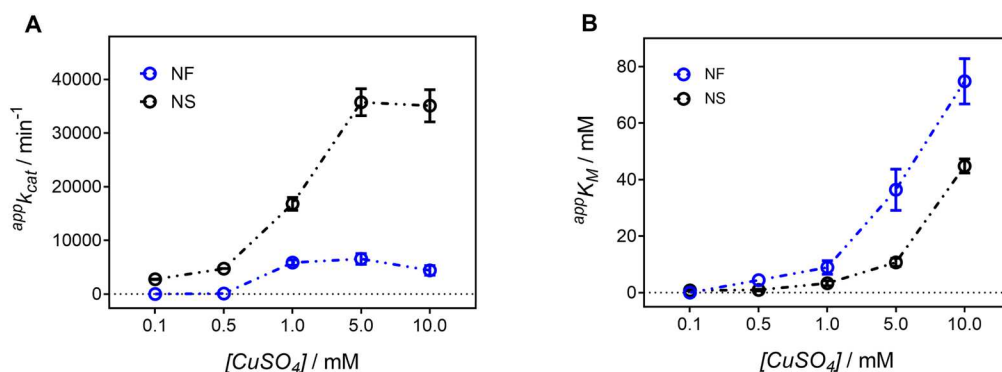


Figure 5-8. Characterization of the catalytic activity of the NSs and the NFs. A) Apparent turnover number ($^{app}k_{cat}$) and B) apparent Michaelis constant ($^{app}K_M$) of both heterogeneous biocatalysts fabricated at increasing CuSO_4 concentrations.

Protein-inorganic composites rely mainly on ionic interactions, making them vulnerable in acidic conditions or in certain buffers, i.e., citrate. To determine the robustness of NSs, both heterogeneous catalysts were incubated in solutions with different pH values and buffers for 5 min. Subsequently, the dispersions were centrifuged to recover the biomaterials and measure their catalytic activity. As expected, the NFs were partially or completely dissolved in citrate buffer and under acidic conditions. In contrast, the NSs remained stable, showing only a 15% decrease in activity in the worst scenario, i.e., in acetate at pH 4.0. (**Figure 5-9A**). In contrast, the NFs lost up to 90 % of their activity. Obviously, the strong Cu-imidazole coordination of NSs provided high robustness to the catalytic biomaterial. This fact is particularly relevant for enzymes that exhibit an acidic optimum pH, as is the case of HRP.²⁰³

The thermal stability of both materials was also studied under conditions where the total inactivation of HRP was expected. NFs, NSs, free HRP, and a-HRP@pAA-I were incubated in various solvents at 65 °C for 60 min and their residual activity tested. The relative initial activity of NSs remained very high, close to 83%. In contrast, the NFs maintained only 20% of their activity (**Figure 5-9B**). Importantly, HRP@pAA-NH₂-I showed a retained activity of around 70%, while free HRP was completely inactivated. Thus, the synergistic contribution of the nanogel and, although to a lesser extent, of the inorganic moiety, largely stabilized HRP under harsh conditions.

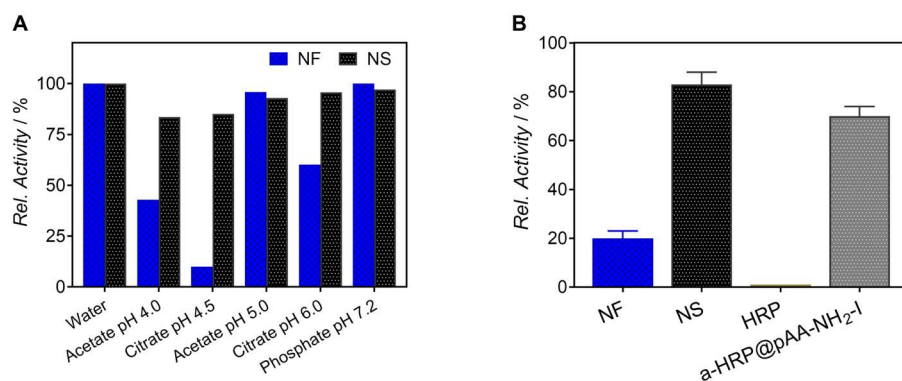


Figure 5-9. Robustness of heterogeneous biocatalysts. A) Relative activity (%) after incubation of

NFs and NSs in various buffers at different pH values. B) Retained initial activity (%) of NFs, NSs, HRP, and a-HRP@pAA-I after incubation at 65 °C for 60 min.

5.2.4 Broadening the chemical nature and morphology of NSs

Finally, we extended the NS formation protocol to other divalent transition metal salts, specifically Mn(II), Co(II), Ni(II), Zn(II), and Cd(II), to study their effect on the biomineralization in the presence of a-HRP@pAA-I and PBS. Besides, monovalent cations, i.e., Ag(I), and trivalent cations, i.e., Au(III) were also evaluated. Generally, different shapes of NSs with similar sizes (5-10 μm) were identified by SEM (**Figure 5-10**). With divalent metals, except for Ni@NSs, the hybrids grew as hierarchically organized microstructures. With a characteristic circular shape, Mn@NSs were similar to Cu@NSs, but with thicker layers. Co(II)-based hybrids also showed circular shapes with disordered layers. Cd@NSs and Zn@NSs showed flat layers that assembled to create flower-like structures of few micrometers. In contrast, the hybrids obtained with Ni and Ag were smaller (<200 nm), and only the constituting units, but no hierarchical structures could be observed. Finally, the gold hybrids showed no flowers, but rather cauliflower-shaped microstructures, apparently formed by agglomeration of spherical particles.

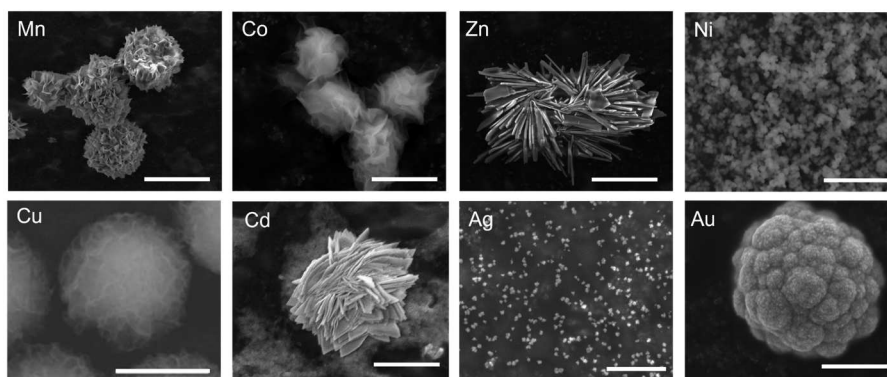


Figure 5-10. SEM images of the resulting hybrid structures after biomineralization with divalent cations: Mn(II), Cu(II), Co(II), Cd(II), Zn(II), Ag(I), Ni(II), and Au(III). Scale bar: 4 μm .

The immobilization yield of each biomaterial is shown in **Figure 5-11A**. The plot shows significant differences among the biohybrids, ranging from 35 to 80%. Those differences can be explained by the binding constant of the cation-imidazole complex ($\log K_{\text{Metal-imidazole}}$ of 1.4, 2.5, 2.6, 2.8, 3.1, and 4.3 for Mn, Co, Zn, Cd, Ni, and Cu, respectively).¹⁸⁸ Attempts to directly prepare hybrids by biomineralization of the free enzyme in the absence of the nanogel led to Mn and Zn nanoflowers with an immobilization yield of only 13 and 8%. Hence, the key role of the imidazole confined on the enzyme surface is to trigger the assembly and biomineralization of the enzyme in the presence of metal cations and phosphates.

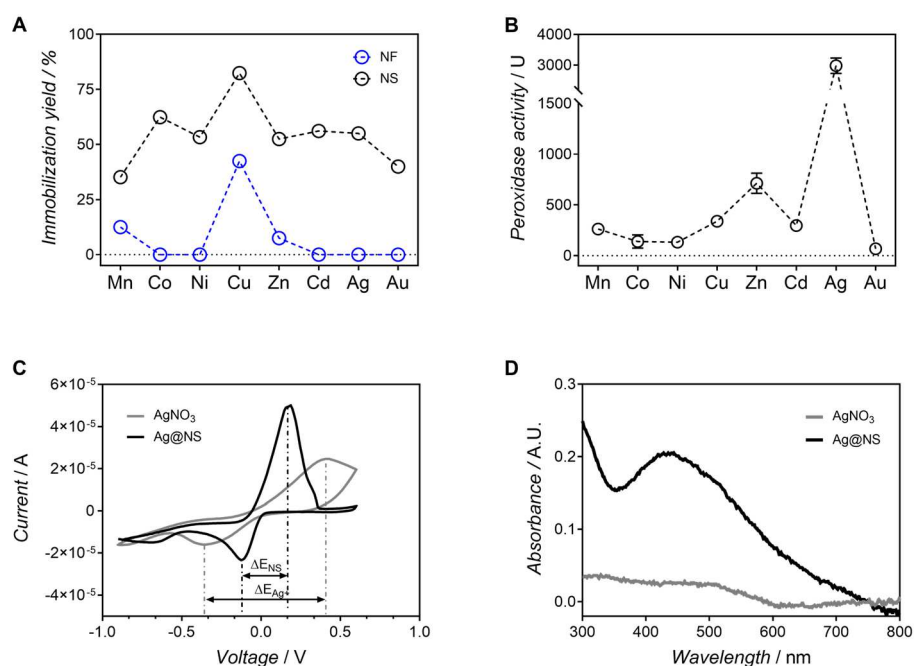


Figure 5-11. Structure-function relationship of biohybrids. A) Protein immobilization yield (%) using free HRP and a-HRP@pAA-I in PBS and different metal salts (MnCl₂, Co(NO₃)₂, NiSO₄, CuSO₄, Zn(NO₃)₂, CdSO₄, AgNO₃, and HAuCl₄). B) Specific peroxidase activity ($\mu\text{mol min}^{-1}$ per mg of protein) of every NS. C) Cyclic voltammograms of AgNO₃ solution and Ag@NSs. D) UV-Vis spectra of AgNO₃ solution and Ag@NSs.

Finally, the structure-function relationship could be assigned for various studied hybrids. The peroxidase activity of biohybrids built from divalent cations showed

intermediate activities, ranging from 140 to 700 U (**Figure 5-11B**). In contrast, trivalent gold showed the lowest activity (68 U), which was attributed to the unfavorable morphology of the material (absence of layers, channels, and pores). Surprisingly, Ag@NSs showed remarkably high peroxidase activity, exceeding the activity of Cu@NSs by the factor of 9. The CV analysis of Ag@NSs suggested the same metal-imidazole interaction as described for Cu@NSs (**Figure 5-11C**). However, its UV-vis spectrum in **Figure 5-11D** showed a peak at 435 nm, meaning that Ag(I) was reduced to Ag(0). It is known that Ag(0) mimics peroxidase activity.²⁰⁴ To evaluate the catalytic activity of Ag(0), Ag@NSs were synthesized with non-catalytic protein nanogels, i.e., a-BSA@pAA-NH₂-I, showing 50 U of peroxidase activity. Therefore, we hypothesize that the high peroxidase activity of Ag@NSs arose from the synergistic effect of the joint peroxidase activity of silver and HRP within the material.

5.3 CONCLUSION

A novel approach is developed to form a new type of heterogeneous biocatalysts, i.e., nanosponges (NSs), resulting from SEN entrapment inside biominerals. The successful fabrication requires the encapsulation of enzymes inside imidazole-decorated nanogels, the assembly triggered by metal-imidazole interactions, and the biomineralization. The deep characterization of NSs elicited fundamental information to understand the interaction between SENs and metal phosphates. Unlike protein-inorganic nanoflowers (NFs), the NSs are built as a consequence of the Cu-imidazole interaction, which coexisted with the growth of Cu₃(PO₄)₂·n(H₂O). Importantly, the SENs provide significant improvements in catalytic conversion, robustness at acidic pHs, and thermal stability of the heterogeneous biocatalysts. It is also demonstrated that this protocol enables the implementation of other metal cations to fabricate NSs. The inorganic counterpart determines the morphology and the catalytic activity of the resulting biomaterial. This fact opens the door to the selection of metal salts not only as a binding agent but also as an element to implement synergistic actions that enhance the catalysis.

Chapter 6 INTEGRATED CHEMOENZYMATIC NANOREACTORS

In the following chapter I report on multifunctional integrated chemoenzymatic nanoreactors (INRs) for the glucose-controlled oxidation of several molecules, i.e., small aromatic derivatives, organic dyes, and reduced nicotinamide cofactors. All the INRs are built of glucose oxidase nanogels which are subsequently modified with hemin molecules. Hemin, the organometallic catalyst, is linked to the flexible polymeric scaffold through coordination to the imidazole groups in the nanogel. The polymeric network works as scaffold material, but also protects both the enzyme and the chemical catalyst from inactivation in the presence of organic solvents. The design of INRs is optimized to increase the effectiveness and the directional channeling at low glucose concentrations.

Published work: the design, synthesis, and characterization of INRs was first published in **Advanced Functional Materials**.⁹⁹ Adapted with permission from Adv. Funct. Mater. 2020, 30, 35, 2002990. Copyright 2020 *John Wiley & Sons*, Inc. Heterogeneous INRs used for the regeneration of nicotinamide coenzymes, i.e., NanoNO_x, were published in **Angewandte Chemie-International Edition**.¹²¹ Adapted with permission from Angew. Chem. Int. Ed. 2022, 61, 39, e202206926. Copyright 2022 *John Wiley & Sons*, Inc.

6.1 FOCUSED INTRODUCTION

In our goal to build highly efficient chemoenzymatic nanoreactors, we have selected polymers as appropriate 3D scaffold material to accommodate and protect both the enzyme and the chemical catalyst from mutual inactivation.^{205,206} Moreover, a convenient confinement of the (bio)catalysts that could foster an efficient reaction cascade in nanometric volume is preferred.²⁰⁷ These demands can be fulfilled with SENs. The functionalization of the nanogel allows for the allocation of the chemical catalyst along the polymer, which will surround the enzyme in proximity.

The catalytic features of hemin, an iron-containing porphyrin, are interesting for its ability to (per)oxidize small molecules.^{69,208–211} In most reported hemin-containing hybrids, the porphyrin molecule is linked through its side groups, i.e., carboxylic or vinyl groups. However, the environmental composition of hemin catalyst affects its performance and, thus, an adequate accommodation within the supramolecular material is of great importance.²¹² In this sense, the coordination of the hemin molecule to imidazole ligands, has shown to boost its catalytic activity drastically.⁶⁹

Great effort is being invested into the design and development of effective systems for the degradation of recalcitrant organic compounds.²¹³ Both small aromatic derivatives and more complex organic dyes are usually poured into wastewater by industries, threatening aquatic living organisms and human health.²¹⁴ To our knowledge, all peroxidase-like systems that have been described to degrade organic compounds are based on the external addition of hydrogen peroxide and, unfortunately, they are usually inactivated in the presence of a high concentration of hydrogen peroxide.²¹⁵ Thus, an alternative that consists in the *in-situ* generation and rapid transformation of H₂O₂ is sought.²¹⁶ In this work, we present multifunctional integrated chemoenzymatic nanoreactors (INRs) for the glucose-controlled oxidation of a broad number of organic compounds. Such hybrid systems are formed by GOx nanogels decorated with

imidazole motifs that anchor and allocate hemin molecules around the enzyme, boosting their catalytic performance. With this confined distribution, INRs are all-in-one hybrid systems in which the GOx enzyme supplies in situ the required co-substrate, i.e., H_2O_2 , to the organometallic catalyst.

Furthermore, the optimization of the aforementioned systems has resulted in heterogeneous INRs capable of mimicking NADH oxidase (NOx) enzymes, biomolecules that efficiently recycle the NADH into NAD^+ just with O_2 as co-substrate²¹⁷ Currently, there are hemin-based hybrid materials that peroxide the NADH successfully. However, they show strong limitations when coupled with NAD-dependent enzymes used in biosynthesis.^{210,218} The main reason is the need and accumulation of H_2O_2 in the medium, which concomitantly inactivates both the NAD-dependent enzyme and the hemin itself.²¹⁹ Confined architectures like heterogeneous INRs, termed under this configuration as NanoNOx, overcome (bio)catalyst deactivation issues combined with a stepwise glucose injection strategy.

6.2 RESULTS AND DISCUSSION

6.2.1 Synthesis and characterization of integrated chemoenzymatic nanoreactors (INRs)

The fabrication of integrated chemoenzymatic nanoreactors (INR) entails the synthesis of imidazole-functionalized SENs and the subsequent attachment of organometallic catalysts, i.e., hemin, to the nanogel through iron-imidazole coordination (**Figure 6-1**).

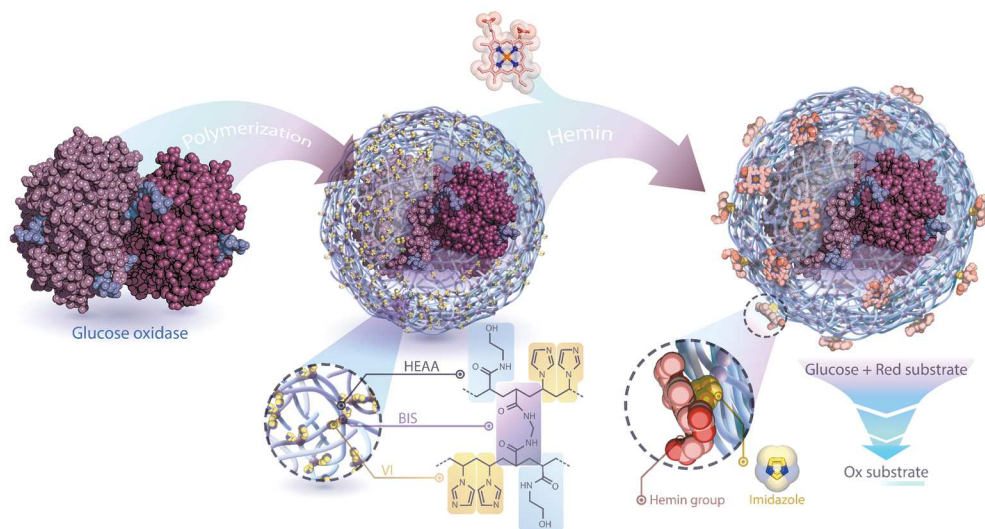


Figure 6-1. Schematic representation of the synthesis procedure and the arrangement of the catalysts within integrated chemoenzymatic nanoreactors (INR). Imidazole-functionalized SENs are synthesized from free GOx and mixed with hemin for the fabrication of chemoenzymatic nanoreactors.

SENs were fabricated from GOx by *in-situ* free radical polymerization as explained in section 3.3.2. The synthesis conditions for SENs are collated in **Table 3-2**. The use of vinyl imidazole (VI) monomer in the *in-situ* polymerization allowed the allocation of imidazole motifs all along the surface of the protein. We also studied the changes caused in the chemical nanoenvironment of the enzyme by 2-carboxyethyl acrylate (CEAA) or N-(3-aminopropyl)methacrylamide (APM) monomers. Further, nanogels with HEAA only as propagating monomer were synthesized as control. Importantly, we aimed at fabricating SENs with polymeric shells of few nanometers to minimize diffusion limitations. Hence, according to DLS measurements, the SENs average hydrodynamic diameters ranged from 9.2 to 13.5 nm, which corresponds to a shell thickness of 1.0 to 3.0 nm, respectively (**Table 6-1**). It was observed that the co-addition of CEAA boosted the polymerization to a thickness of 3.0 nm with higher dispersity (30% compared to around 15% measured for the rest of the samples). This effect could arise from a higher reactivity of CEAA. Similar sizes were measured by SEM and AFM (not shown).

Moreover, the presence of imidazole, carboxylic acid, and amino functional groups within the respective SEN was certified by Zeta-potential (**Table 6-1**).

Table 6-1. Shell thickness and zeta-potential values of synthesized SENs.

	GOx@pHEAA-I	GOx@pHEAA-I-COOH	GOx@pHEAA-I-NH ₂	GOx@pHEAA	Free GOx
Shell thickness (nm)	2.3 ± 0.3	3.0 ± 0.9	1.8 ± 0.2	1.0 ± 0.1	0
Zeta potential (mV)	-8.76 ± 0.35	-10.96 ± 0.58	26.32 ± 1.12	-7.28 ± 0.41	8.79 ± 0.02

The presence of the functional groups was also evidenced by ATR-FTIR (**Figure 6-2**). A broad and intense amide I band at 1642 cm⁻¹ (peak #1) was observed in each case, confirming the incorporation of HEAA into the nanogel.²²⁰ Moreover, the band at 1060 cm⁻¹ (peak #2) was attributed to the terminal polyvinyl groups. Furthermore, the presence of imidazole rings in GOx@pHEAA-I, GOx@pHEAA-I-COOH, and GOx@pHEAA-I-NH₂ samples was clearly evidenced by the bending vibrations at 917 cm⁻¹ and 650 cm⁻¹ (peaks #3 and 4). The presence of carboxylic acids in GOx@pHEAA-I-COOH was clearly evidenced by the band at 1725 cm⁻¹ (peak #5). Finally, the broader bands at 1642 and 3275 cm⁻¹ (peaks #1 and #6) implied the presence of amine groups in GOx@pHEAA-I-NH₂ due to the amide carbonyl (C=O) stretch and NH₂ stretch vibrations, respectively.

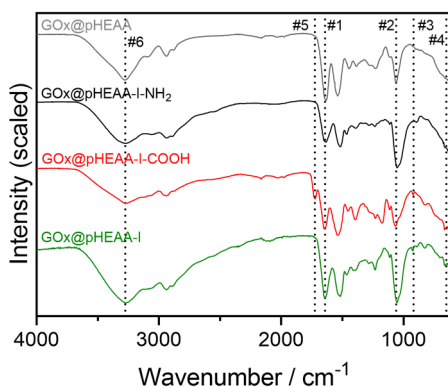


Figure 6-2. ATR-FTIR spectra of SENs. Main peaks are highlighted: #1: 1642 cm⁻¹; #2: 1060 cm⁻¹; #3: 917 cm⁻¹; #4: 650 cm⁻¹; #5: 1725 cm⁻¹; #6: 3275 cm⁻¹.

For the fabrication of the integrated chemoenzymatic nanoreactors (INR, see section 3.3.3.2), hemin was added (molar excess of 100, $n_{\text{hemin}}:n_{\text{SEN}} = 100$) to each nanogel, giving rise to 4 different INRs, termed as INR1-4 (Table 6-2).

Table 6-2. Summary of integrated chemoenzymatic nanoreactors (INRs) used in this work.

	INR1	INR2	INR3	INR4
<i>SEN</i>	GOx@pHEAA-I	GOx@pHEAA-I-COOH	GOx@pHEAA-I-NH ₂	GOx@pHEAA
<i>Organometallic catalyst</i>	Hemin	Hemin	Hemin	Hemin

The chemical composition of each INR was elucidated by several spectroscopic techniques. The embedment of hemin molecules within INRs was first evidenced by Raman spectroscopy (Figure 6-3A). The characteristic Raman D band of hemin shifted to higher wavenumbers (from 1347 to 1360 cm^{-1} in free hemin and INRs, respectively) and its intensity was significantly lowered compared to the G-band, indicating a change in the chemical environment of hemin molecules. Moreover, as observed by ATR-FTIR (Figure 6-3B), the typical infrared band of hemin (1700 cm^{-1} (#1) corresponding to C=O stretch of the carboxylic groups and 710 cm^{-1} (#2) corresponding to C-H bond of the pyrrole ring) evidenced the interaction of the nanogel with hemin molecules.^{221,222}

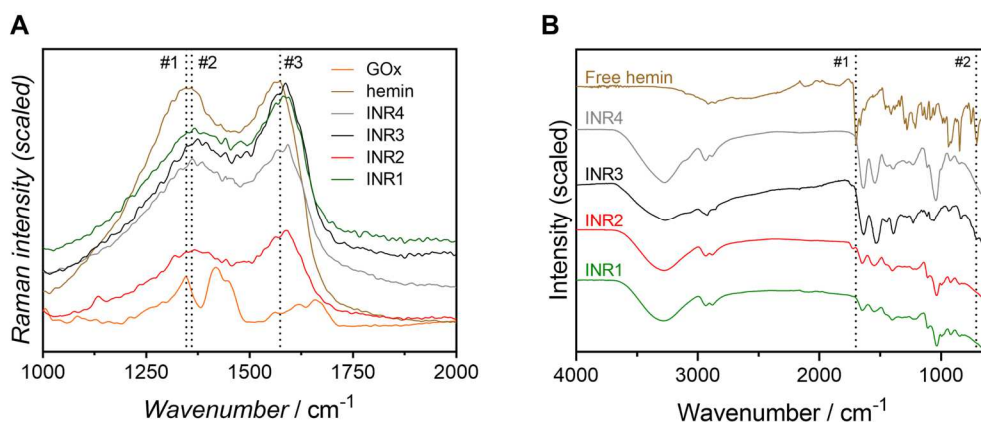


Figure 6-3. Raman and ATR-FTIR of INRs. A) Raman spectra of INRs, hemin, and GOx. The characteristic D band (#1) and G band (#3) of hemin are highlighted at 1347 and 1574 cm^{-1} , respectively.

The D band present in the INRs is highlighted at 1360 B) ATR-FTIR spectra of hemin and INRs. Significant peaks are highlighted at 1700 (#1) and 710 cm^{-1} (#2).

The presence of iron within INRs was confirmed by XPS (1.3-1.7 as atomic %). The hemin used to form INRs was composed of Fe^{3+} and was partially reduced (50%) once dissolved in NaOH (not shown). However, the Fe 2p region of INR showed around 90:10 ($\text{Fe}^{2+}:\text{Fe}^{3+}$) molar composition in each INR, which means the iron was reduced during the assembly process (**Figure 6-4A**). The analysis of the N 1s region evidenced the N-Fe interaction and, thus, the presence of the pyrrolic ring within the network (**Figure 6-4B**).

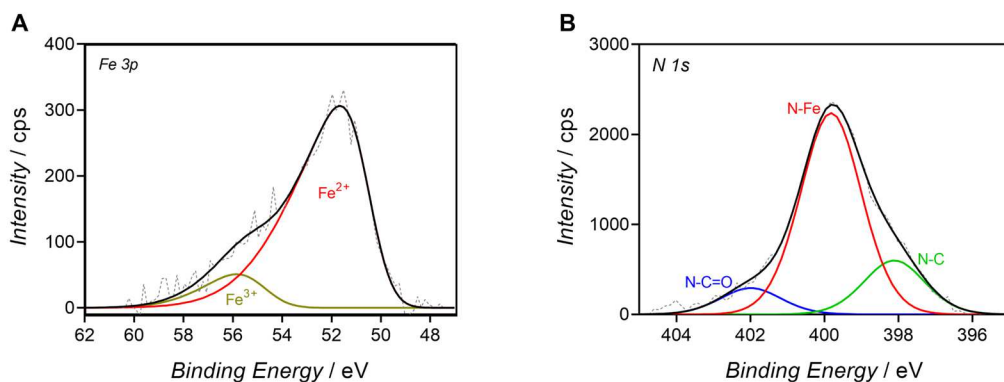


Figure 6-4. Deconvoluted XPS spectra of INR1. A) Fe 3p region. B) N 1s region.

The Fe-imidazole interaction can be detected in the UV-Vis spectra by monitoring the shift of the characteristic Soret band of hemin, usually shifted to the 400-415 nm range when a hemin-histidine complex is formed in proteins.²²³ Thus, UV-Vis absorption spectra were measured to further explore the interactions between hemin and the polymeric network within INR samples. Hence, INR1 with $n_{\text{hemin}}:n_{\text{SEN}}$ ratios ranging from 10:1 to 500:1 was synthesized and characterized. As observed from **Figure 6-5A**, the samples prepared with $n_{\text{hemin}}:n_{\text{GOx@pHEAA-I}}$ ratios up to 150 (0.15 mg mL^{-1} of hemin) showed a maximum of the Soret band at 412 nm. However, higher molar excess of hemin led to a gradual shift of the maxima of the Soret peak towards lower wavelengths (from 412 to 396 nm for a hemin excess of 150 and 500, respectively). Moreover, a band

shoulder at 356 nm emerged in the samples prepared with a $n_{\text{hemin}}:n_{\text{GOx@pHEAA-I}}$ ratio above 150. The detected maxima at 356 and 390 nm are assigned to hemin hydroxide monomers and μ -oxo bridged hemin dimer compounds, respectively.²²⁴ Importantly, the bathochromic shift of the characteristic Soret band to higher wavelengths was only observed in INRs formed from imidazole-bearing SENs (INR1-3, **Figure 6-5B**). In addition, the rise of low intensity satellite peaks of the Soret band (Q bands) at 533 and 565 nm (zoomed inset in **Figure 6-5B**) supported the hemin-imidazole interaction in INR1, INR2, and INR3 samples.²²⁵ Moreover, the comparison of UV-Vis spectra of imidazole-bearing samples showcased the influence of the chemical environment on the hemin-imidazole interaction in INRs. The presence of carboxylic acids (INR2) led to a slight shift of the Soret peak by 2 nm (from 412 to 410 nm in INR1 and INR2 samples, respectively). Yet, the visible light absorption spectrum of the INR3 sample, with amino groups contained in its structure, was significantly different. Besides the shift of a broader Soret band to 408 nm and a shift in the Q bands, a shoulder was observed at 390 nm, which might indicate the presence of stacked hemin molecules. Contrastingly, the spectrum of the INR4 sample, with no imidazole molecules in its structure, fits with that shown by free hemin.

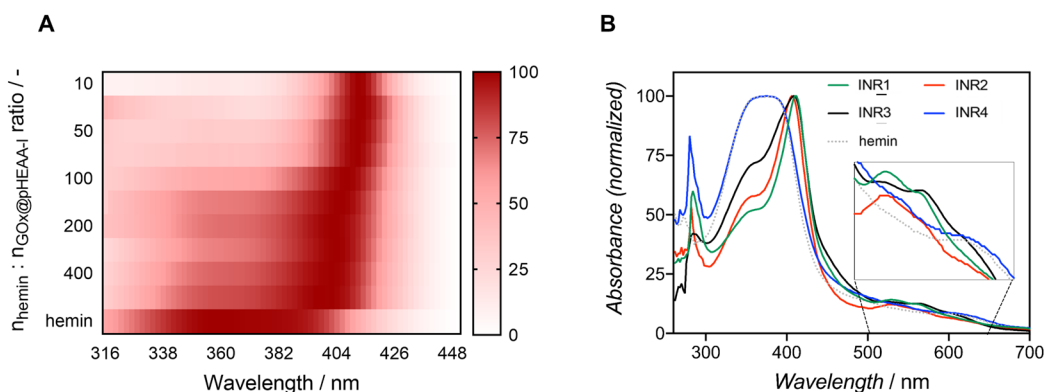


Figure 6-5. UV-Vis analysis of INRs. A) Scaled heat-map representation of the intensity of the UV-Vis spectra of INR1 samples synthesized at a range of hemin:GOx@pHEAA-I molar ratios from 10 to 500. B) Spectra of INRs in comparison to free hemin (non-continuous black line). Zoom at the 500-650 nm region showing the Soret band satellite peaks.

Then, the sizes and morphologies of the INRs were characterized by SEM, TEM, AFM, and DLS. SEM and TEM images of INR1 suggested homogeneous and spherical particles with an average size of 13.7 ± 1.8 nm (**Figure 6-6A-B**). The pseudo-spherical morphology of INR1 was elucidated by high-resolution AFM (**Figure 6-6C**). Similar diameter sizes and shapes were found by SEM, AFM and DLS for INR2 and INR4 samples (summarized in **Table 6-3**). Yet, the INR3 sample showed completely different morphology and dimension. Indeed, the addition of hemin (excess of ≥ 400) to GOx@pHEAA-I-NH₂ triggered the complete aggregation of the nanogels. Under these conditions, SEM pictographs of INR3 showed the formation of polydisperse particles with sizes from 100 nm to $> 1 \mu\text{m}$ (data not shown). Plus, high-resolution AFM images of a 100 nm sized particle suggested the presence of smaller units of $\approx 10\text{-}20$ nm, which likely correspond to individual GOx@pHEAA-I-NH₂ nanogels (**Figure 6-6D**).

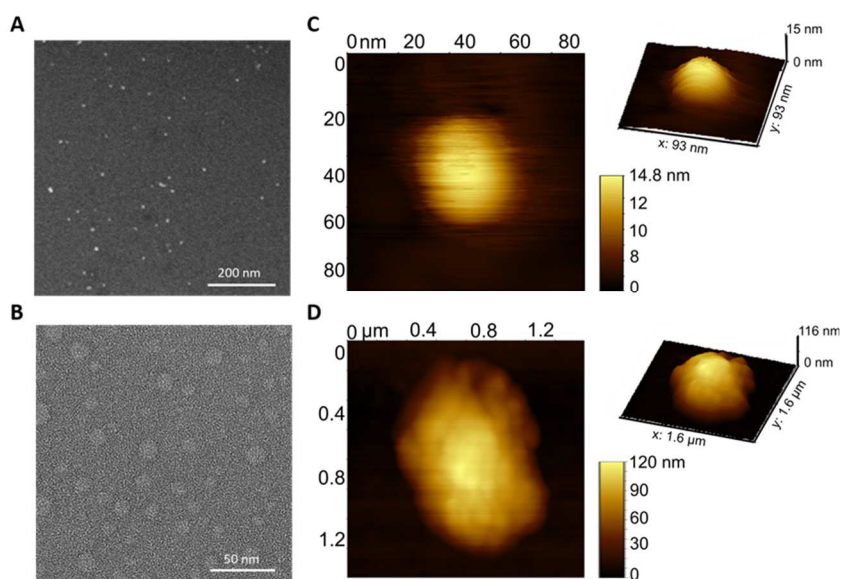


Figure 6-6. Structural characterization of INRs. Sample homogeneity and morphology of INR1 was revealed by A) SEM, B) TEM, and C) high-resolution AFM. The inset image shows the 3D reconstruction of a single INR1 particle. D) High-resolution AFM image and the corresponding 3D reconstruction of one small aggregate within the INR3 sample.

Table 6-3. Diameters measured for INRs using different techniques.

<i>Hybrid</i>	<i>DLS (nm)</i>	<i>AFM (nm)</i>	<i>SEM (nm)</i>	<i>TEM (nm)</i>
<i>INR1</i>	14.8 ± 1.2	13.4 ± 2.9	12.6 ± 1.9	11.6 ± 2.5
<i>INR2</i>	13.5 ± 1.8	11.2 ± 0.8	16.7 ± 3.9	---
<i>INR3</i>	> 100 (multidisperse)	> 100 (multidisperse)	> 100	---
<i>INR4</i>	9.4 ± 0.7	9.1 ± 1.6	12.4 ± 2.8	---

Thus, we demonstrated a dual function of the hemin molecule within the INR3 hybrid. Besides providing the peroxidase-like functionality, hemin played a structural role by triggering the assembly of the nanoreactors into heterogeneous chemoenzymatic catalysts. Such assembly could be fostered by the amino groups within the polymeric mantle and further π - π^* stacking interactions between the hemin pyrrolic rings, as suggested by the band at 390 nm in the UV-Vis spectrum of INR3 sample (**Figure 6-5B**).²²⁶ Compared to homogeneous chemoenzymatic catalysts (i.e. INR1, INR2, and INR4), which are dispersed in the reaction media, INR3 was a recyclable system where the nanoreactors can be easily isolated from the products and reused through a simple rejuvenation process, as demonstrated in the following experiments.

6.2.2 Integrated chemoenzymatic catalysis

The aim of this work was to synthesize integrated chemoenzymatic nanoreactors with high catalytic performance. It is known that the coordination of hemin to imidazole ligands boosts the peroxidase-like activity of the catalyst.²²⁷ However, as the hemin molecules were allocated around the enzyme, the overload of those could block the polymeric pores and induce mass transfer issues, interfering with the enzymatic reaction that takes place in the core. Thus, an adequate $n_{\text{hemin}}:n_{\text{SEN}}$ ratio that provides high peroxidation performance with low substrate diffusion issues was sought for the sake of the concurrent chemoenzymatic reaction.²²⁸ Therefore, in order to optimize the composition of the nanoreactors, one-pot sequential reactions were carried out with INRs synthesized at increasing hemin loads (**Figure 6-8A**). Noticeably, chemoenzymatic nanoreactors bearing imidazole groups, i.e., INR1-3, improved the activity measured for the INR4 sample by up to 800% in the assayed range. The low

cascade activity found for INR4 is a result of the unspecific adsorption of hemin molecules to the polymeric network. Moreover, high loads of hemin (above a $n_{\text{hemin}}:n_{\text{SEN}}$ ratio of 400) led to a drop in the performance of the sequential reaction (**Figure 6-8A**).

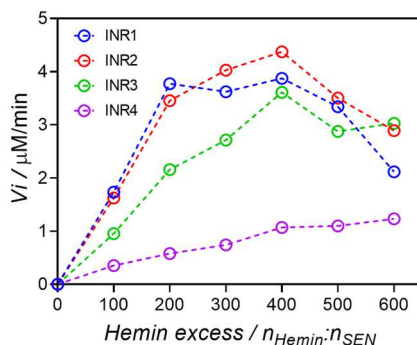


Figure 6-7. Activity plots of INRs synthesized at increasing hemin loadings. One-pot concurrent reaction of INRs representing initial velocities (V_i) of each INR.

These features were also found when the peroxidase-like and glucose oxidase functionalities of the hybrids were tested independently (**Figure 6-8A** and **Figure 6-8B**, respectively), evidencing the peroxidation as the limiting step in the concurrent reaction. According to these activity profiles, the $n_{\text{hemin}}:n_{\text{SEN}}$ ratio of 400 was identified as the best condition for the fabrication of INRs with the highest catalytic performance. Therefore, this composition was used in this work for further catalytic characterization of the hybrid nanoreactors.

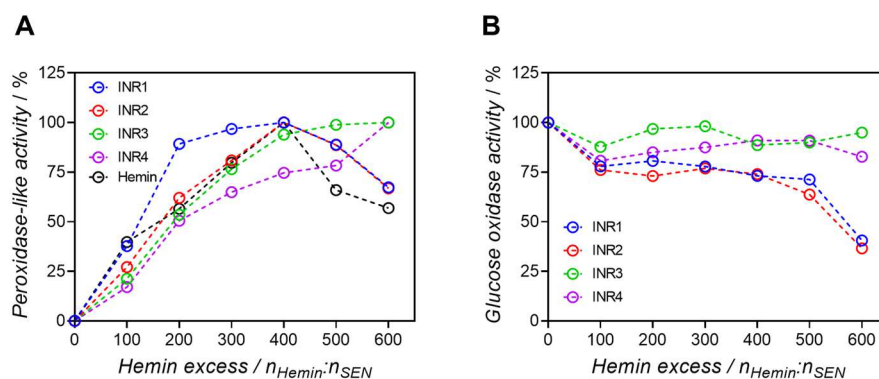


Figure 6-8. Activity plots of INRs synthesized at increasing hemin loadings. A) Peroxidase and B) glucose oxidase activity of INRs.

The measurement of the kinetic parameters corresponding to the one-pot reaction pointed out interesting features (**Table 6-4**). Surprisingly, the best catalytic efficiency was found for the heterogeneous catalyst, i.e., INR3, with a $^{app}k_{cat} / ^{app}K_M$ ratio of $364 \text{ min}^{-1} \text{ mM}^{-1}$. Even though the aggregation of the nanoreactors triggered substrate diffusion limitations (V_{max} of 2.2 vs. $3.6 \mu\text{M min}^{-1}$ and $^{app}k_{cat}$ of 270 vs. 317 min^{-1} measured for INR3 and INR1, respectively), the high affinity towards substrates observed for the INR3 sample ($^{app}K_M$ of 0.7 vs. 2.7 mM for INR3 and INR1, respectively) boosted its catalytic efficiency. Moreover, significantly lower apparent Michaelis-Menten constant values ($^{app}K_M$) were obtained, if compared to the one-pot reaction performed with free GOx/HRP enzymes (0.7 to 2.7 vs. 31.9 mM for nanoreactor and free enzyme systems, respectively). This effect could be explained by the confinement of both catalysts within the nanoreactor.

Table 6-4. Kinetic parameters measured for INR samples and the free GOx/HRP system.

Sample	$^{app}K_M$ (mM)	V_{max} ($\mu\text{M min}^{-1}$)	$^{app}k_{cat}$ (min^{-1})	$^{app}k_{cat} / ^{app}K_M$ ($\text{min}^{-1} \text{ mM}^{-1}$)
INR1	2.7 ± 0.8	3.6 ± 0.3	317 ± 15	118
INR2	1.4 ± 0.3	3.2 ± 0.2	370 ± 25	265
INR3	0.7 ± 0.2	2.2 ± 0.1	270 ± 10	364
INR4	1.2 ± 0.4	1.2 ± 0.2	54 ± 2	45
GOx/HRP	32.0 ± 7.0	20.0 ± 4.0	26080 ± 1910	817

Reaction conditions: catalyst (concentration range 1-25 nM) and glucose (0-50 mM) are mixed in sodium acetate (100 mM, pH 6.0) containing ABTS (1 mM) as chromogenic substrate.

Our core-shell system involves the arrangement of hemin molecules around the enzyme. Thus, the product of the enzymatic reaction is likely further transformed on its way to leave the nanoreactor through the hemin-decorated shell, increasing the overall performance of the concurrent reaction. This effect was clearly evidenced at highly diluted conditions (**Figure 6-9**). Despite showing lower catalytic performance than the free-enzyme system under the assayed conditions (364 vs. $817 \text{ min}^{-1} \text{ mM}^{-1}$ for INR3 and free enzyme system, respectively), the high efficiency of the concurrent reactions in colocalized and confined catalysts allowed us to detect the presence of glucose at catalyst concentrations lower than 20 pM , which resulted impossible for the mix of free enzymes.

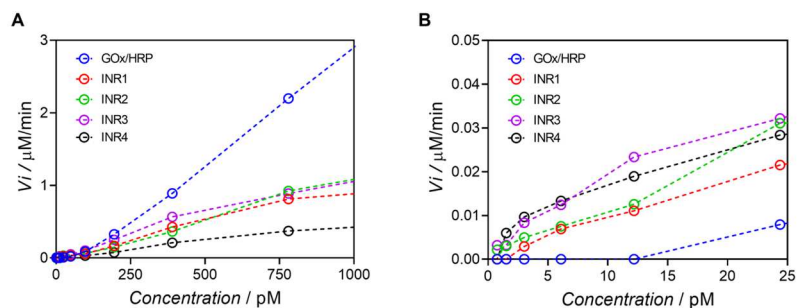


Figure 6-9. Activity plots of the one-pot chemoenzymatic reactions performed at very diluted conditions. A) 0-1000 pM catalyst region. B) Zoom in the 0-25 pM catalyst region. INRs were compared to a mix of GOx and HRP enzymes at equivalent concentrations.

Next, we analyzed the effect of the pH on the hemin-imidazole interaction within the INR samples and on their performance as cascade catalyst. The hybrids were stable at a wide pH range (pH 5.0 to pH 9.0) by measuring the UV-Vis spectra in different buffers (**Figure 6-10A**). At pH 3 the intensity of the Soret band decreased and shifted dramatically to lower wavelengths, showing a free hemin-like spectrum. Also, it was observed that the catalytic performance of INRs was strongly dependent on the pH value. The optimum conditions for the chemoenzymatic reaction were found at pH 6.0 in sodium acetate buffer (**Figure 6-10B**). The decrease of activity observed at pH < 5.0 could be related to cleavage of the Fe-imidazole bond due to the protonation of the coordinated imidazole ligands.²²⁹ Above pH 7.0, a strong decrease of the activity was noticed. Since the glucose oxidase activity of the encapsulated GOx is almost constant up to pH 9.0,⁹⁶ this loss of activity was likely to be related to the hemin catalyst.

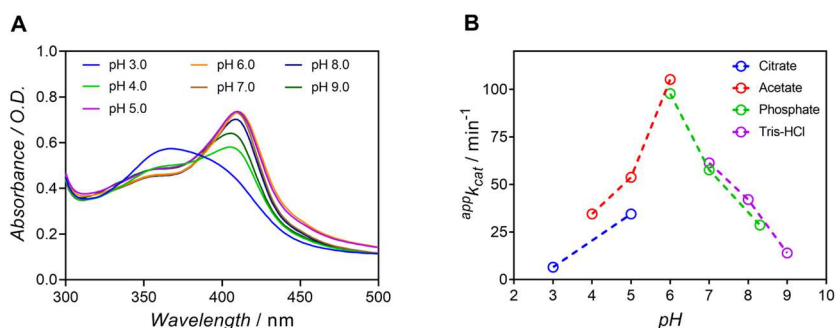


Figure 6-10. Effect of pH on INRs. A) UV-Vis spectra at different pH values and B) pH activity profile.

The presence of bubbles in the reaction vessels at alkaline conditions suggested a side-reaction occurring in INRs (**Figure 6-11A**, inset). The presence of bubbles probably resulted from the dismutation of the hydrogen peroxide, which could be explained by the catalase-like activity of the hemin catalyst under these conditions. Indeed, a weak catalase-like activity of the nanoreactors was confirmed using the appropriate colorimetric activity assay (Invitrogen™ Catalase Colorimetric Activity Kit, **Figure 6-11A**). As mentioned above, at basic pH, the GOx remained active (90% of the activity at the optimum pH 6.0)⁹⁶, releasing thereby hydrogen peroxide, which is accumulated in the medium. It is known that, under these two premises, i.e. basic pH and high hydrogen peroxide concentration, peroxidases mimic catalases and are able to disproportionate H_2O_2 at low rates, producing O_2 bubbles thereupon.²³⁰ Unfortunately, we found that the hemin catalyst was inactivated after the catalase reaction, which precluded the reusability of INRs under these conditions (**Figure 6-11B**).

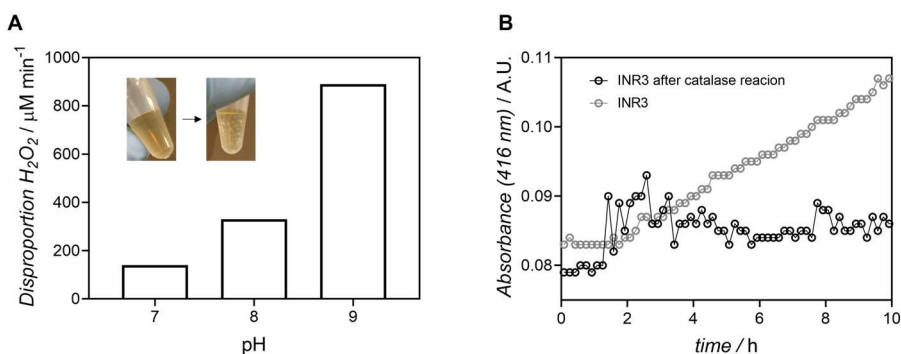


Figure 6-11. Catalase-like activity of INR3 at alkaline conditions. A) Catalase activity measured at pH 7, 8, and 9. Inset pictures: INR3 sample before and after the addition of glucose at pH 9. B) ABTS oxidation ability of INR3 sample before and after catalase reaction.

6.2.3 Stability in organic solvents and reusability of INRs

The ability of the hybrid nanoreactors to work in different reaction media is key for their application in industry.²³¹ We tested the ability of INRs to peroxidize ABTS using glucose in presence of different organic solvents, such as *iprOH*, MeCN, and DMF. As

observed in **Figure 6-12A**, the stabilizing effect of the polymeric scaffold is evident. Compared to the free enzyme system, which lost its ability to oxidize ABTS in organic solvents, INRs kept reasonably good activity in 50% (v/v) solutions of MeCN and *i*prOH, with $\geq 75\%$ of the activity retained, as measured in acetate buffer. Surprisingly, only $\approx 20\%$ of the activity was lost using 80% (v/v) MeCN as co-solvent. In general, except for the case of DMF, it was observed that the effect of the solvents in the encapsulated GOx was moderate owing to the structural protection provided by the polymer (data not shown). Although to a lower degree, the hemin catalyst was also stabilized within the polymeric network. This effect was especially observed when ACN was used as co-solvent (**Figure 6-12B**).

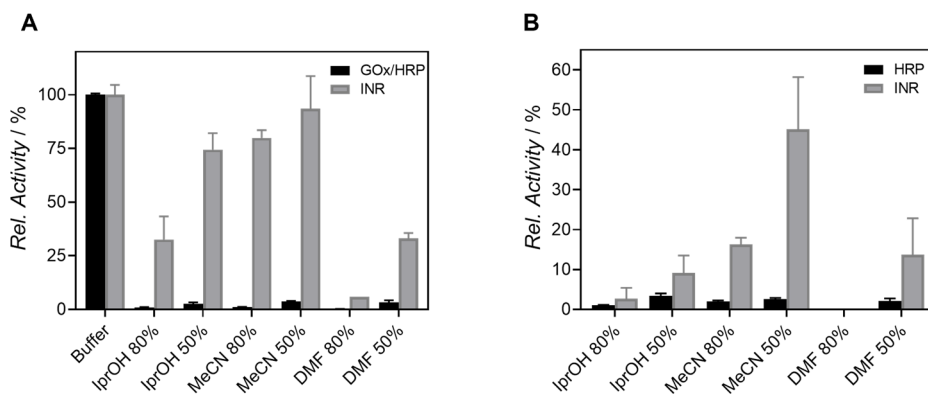


Figure 6-12. Relative activity of INRs and free enzyme system in different organic solvents. A) One-pot concurrent cascade activity. B) Peroxidase activity.

The robustness and reusability of INR3 as heterogeneous chemoenzymatic catalyst was tested in sequential cyclic reactions and ON-OFF switching activity assays (**Figure 6-13**). The reaction started with the addition of INR3 to a glucose/ABTS solution (ON phase) and stopped the reaction by centrifugation after 30 s (OFF phase). This process was repeated 5 times to obtain 5 reaction cycles. The reaction stopped completely upon the withdrawal of the catalyst, meaning a minimal loss of the catalyst over the cycles. Moreover, the catalytic rate of INR3 derived from the slope of the curve in each ON cycle (k in **Figure 6-13**) was constant for the first 3 cycles. Thereafter, the performance

dropped by 12% and 47% in cycle 4 and 5, respectively. Consequently, INR3 were efficiently reused (activity loss < 15%) for up to 4 cycles.

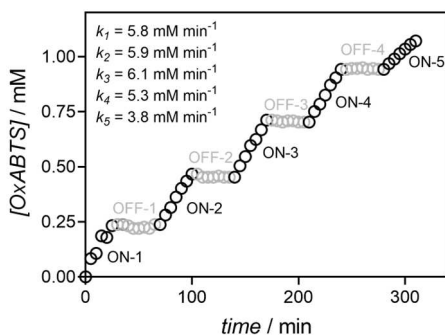


Figure 6-13. ON-OFF switching experiment in the presence (ON) and absence (OFF) of INR3. The values of k represent the catalytic rate of INR3 in each of the 5 ON phases.

6.2.4 Removal of small aromatic derivatives and dye pollutants

The degradation potential of INRs towards phenolic derivatives was tested using glucose as fuel. For this experiment, INR3 was utilized due to its high catalytic turnover and to facilitate an efficient removal from the reaction solution. First, the degradation rate of phenol was assayed. A concentration-dependent catalytic initial rate and a typical fast-then-slow catalytic profile was observed. As observed in **Figure 6-14A**, ~ 50% of phenol was degraded after 2 h of reaction using a catalyst concentration as low as 0.78 μM (which corresponds to 25 μg of GOx enzyme).

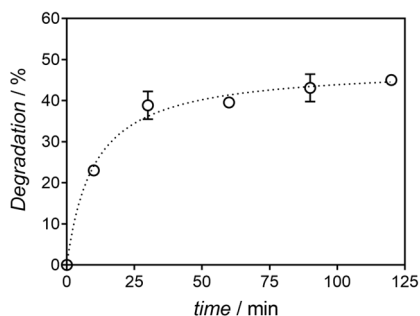
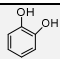
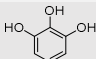
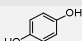
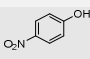
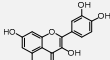
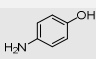
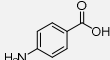
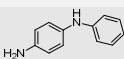


Figure 6-14. Degradation kinetics of 1 mM phenol by INR3.

The ability of INRs to act over a broad number of aromatic compounds would increase their impact. Thus, the degradation of a total of 8 phenolic and aniline derivatives and 4 complex organic dyes was tested. As collated in **Table 6-5**, a wide range of aromatic compounds could be successfully degraded. Thus, ortho-, i.e., catechol and pyrogallol, and para-, i.e., hydroquinone, substituted phenolic compounds showed high transformation yields of 100 % and 88 %, respectively. Only medium degradation rates were observed when 4-nitrophenol (46%) was tested. This effect could be explained by the presence of the nitro group, which electronic withdrawal reduces the reactivity of the aromatic ring.²³² Further, high degradation values were also obtained for complex polyphenols such as quercetin. Interestingly, unlike reported examples using peroxidases, i.e., HRP,²³³ high conversion yields were also achieved when aniline derivatives were assayed. We measured almost complete degradation of 4-aminophenol (98%) and almost complete (93%) or reasonable (67%) degradation of non-phenolic secondary (N-phenyl-p-phenylenediamine) and simple (4-aminobenzoic acid) anilines, respectively. The lower reactivity on 4-aminobenzoic acid can be also explained by the electron withdrawal effect produced by the carboxylic acid on the ring.

Table 6-5 Chemical structures of assayed aromatic compounds and degradation efficiency

Compound	Chemical Structure	Degradation (%)
Catechol		100
Pyrogallol		100
Hydroquinone		88
4-Nitrophenol		46
Quercetin		100
4-aminophenol		98
4-aminobenzoic acid		67
4-phenyl-p-phenylenediamine		93

Furthermore, it has been reported that the direct addition of H_2O_2 (1 mM) to HRP shows very low phenol degradation rates (less than 10%) due to the inactivation of the catalyst unless the enzyme is protected.¹¹⁶ Thus, the good degradation yields found with INRs can be explained by the sheltered hemin catalyst and the progressive release of H_2O_2 , which ensures a low concentration of the peroxide in solution. Hence, these results are comparable to other (chemo)enzymatic cascades with in-situ H_2O_2 production reported in the literature, yet the enzyme concentration is usually higher in those (e.g., 8 mg of peroxidase is needed for a maximum degradation of p-aminophenol of 50% after 7 h of reaction).²¹⁵ Further, INRs provided similar or better degradation yields compared to an equivalent chemical system in which free hemin was used as catalyst (data not shown).

Motivated by the high degradation potential of the hybrids using small aromatics, we tested the ability of INR3 to decolorize methyl orange (MO). The rapid disappearance of the absorption at 466 nm suggested that the chromophores responsible for the typical orange color of MO were degrading (**Figure 6-15A**). These successful results persuaded us to test other organic dyes with different chemical structures. Thus, in contrast to anionic MO, we assayed cationic methylene blue (MB) and rhodamine B (Rho), and phenol red (PR) as anionic and phenolic dye.²³⁴ Gratifyingly, complete bleaching of PR, and MB dyes, added as 50 μM solutions, was observed after overnight reaction (**Figure 6-15B-C**). Lower, but still acceptable degradation rates were obtained when Rho was used, with a maximum of 70% of degradation (**Figure 6-15D**).

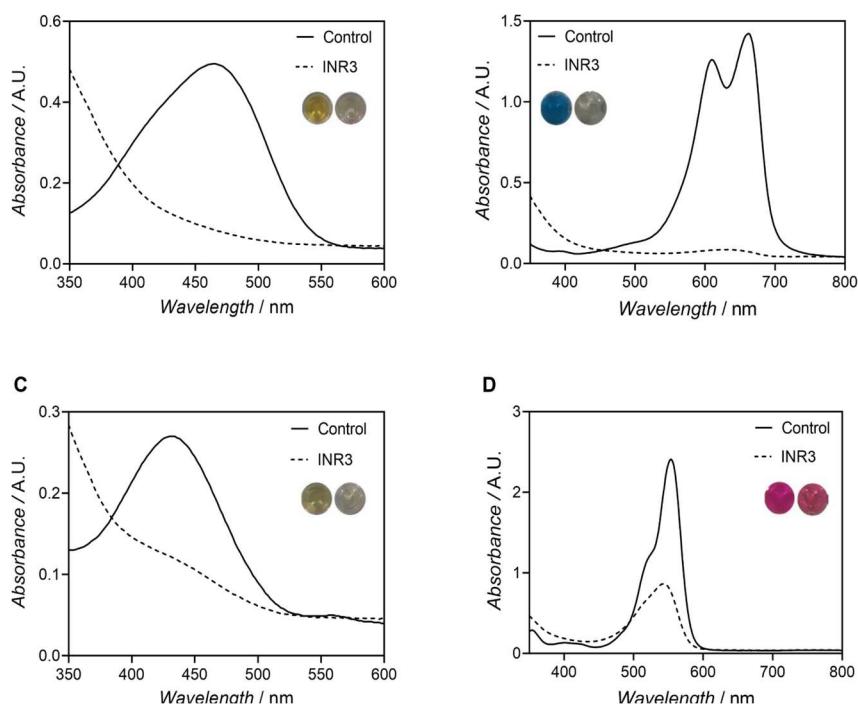


Figure 6-15. Degradation of aromatic dyes by INR3. UV-Vis spectra of 50 μM of dyes A) methyl orange (MO), B) methylene blues (MB), C) phenol red (PR), and D) rhodamine (Rho) before and after overnight reaction.

6.2.5 In situ regeneration of nicotinamide cofactors

Next, the integrated chemoenzymatic nanoreactors were utilized in a completely different application: the *in-situ* regeneration of oxidized nicotinamide cofactors. An extensive study was conducted to gain insight into the potential of INRs in this field. In terms of nanomaterial fabrication, readjustments were made in the synthesis of the nanogels, increasing the VI ratio of GOx@pHEAA-I from 2000 to 4000 (see **Table 3-2**). Remarkably, these SENs were assembled in the presence of small amounts of hemin ($n_{\text{hemin}}:n_{\text{GOx}} \leq 350$), giving rise to insoluble INRs, which we named NanoNOx, due to their ability to mimic NADH oxidase (NOx) enzymes (**Figure 6-16**). After an arduous morphological and compositional characterization, it was observed that the heterogeneous NanoNOx showed similar morphology to INR3 presented before.

However, NanoNOx were precipitated exclusively by hemin-directed crosslinking of individual nanogels. Furthermore, the NanoNOx were able to incorporate higher hemin loadings than previously presented INRs, thus favoring their catalytic efficiency. For NanoNOx morphological and chemical characterization details see supplementary material of **Paper VI**.¹²¹

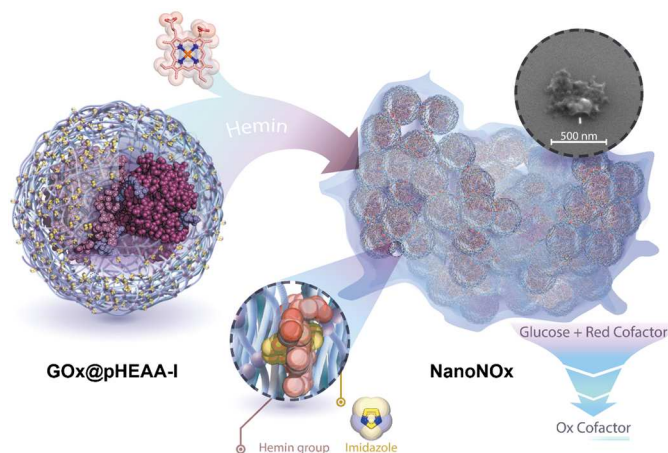


Figure 6-16. Workflow for NanoNOx formation. The addition of hemin to GOx@pHEAA-I (formed from $n_{Vi}:n_{GOx} = 4000$) renders solid materials by the hemin-directed crosslinking of individual nanogels (details in SEM inset image). In the presence of glucose, a concurrent cascade reaction is implemented, releasing oxidized nicotinamide cofactors to the medium.

The kinetic parameters of the NO_x-like activity of NanoNOx were experimentally revealed under aerobic conditions and in the presence of glucose by monitoring the consumption of the NADH cofactor at 340 nm. The apparent Michaelis-Menten constants of 0.39 ± 0.08 mM and 57.85 ± 17.8 μ M for glucose and NADH substrates, respectively, evidenced an enzyme-like first order kinetic behavior (**Figure 6-17**). The NADH oxidation rate depended linearly on the concentration of NanoNOx ($^{app}k_{cat,NADH} = 498 \pm 14$ min⁻¹). In comparison to other described NADH (per)oxidase-like artificial systems, NanoNOx showed the highest apparent turnover number found in literature.¹²¹ Remarkably, when contrasted with the reported hemin-based NO_x mimetics, i.e., hemin/G-quadruplex hybrid,²¹⁰ NanoNOx showed up to 2000 times

higher activity towards NADH oxidation. We hypothesize that such improvement might arise from the combination of several benefits exhibited by our system. First, NanoNOx permitted high loads of organometallic catalyst per enzyme. Further, the accommodation of iron porphyrins through metal-ligand coordination to imidazole ligands, resembling the strategy chosen by Nature to design hemoproteins, boosted the efficiency of the system.^{152,235} Finally, the confinement of the catalysts in the nanospace permitted the in situ injection of H₂O₂ from the core towards the iron porphyrin through a guided diffusion mechanism.

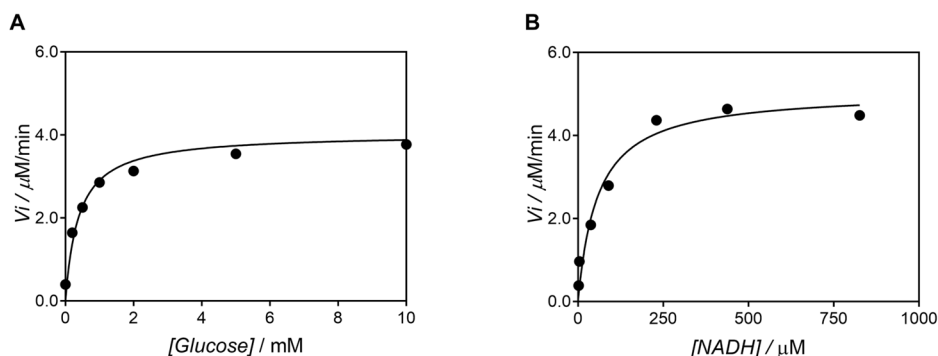


Figure 6-17. Calculation of the apparent Michaelis-Menten constant ($^{app}K_M$) of NanoNOx. A) $^{app}K_M$ of glucose and B) $^{app}K_M$ of NADH.

The catalytic results described above are based on the extinction coefficient of NADH. Nevertheless, non-selective oxidations or overoxidations of the cofactors would likewise be monitored as a drop in the measurements at 340 nm.²³⁶ Importantly, such non-selective oxidation of NADH would imply the unsuitability of NanoNOx as recycling system. Conversely, the oxidation selectivity of NanoNOx assessed by ¹H NMR spectroscopy unequivocally evidenced the yield of the biologically relevant oxidized cofactor, i.e., the 1,4-NAD⁺ regioisomer (**Figure 6-18A**).

Moreover, we corroborated experimentally that the biologically active NAD⁺ cofactor was achieved. For this purpose, NanoNOx were added to a reaction mixture that contained glucose and NADH in phosphate buffer and incubated at 37°C for 90

minutes. As depicted in **Figure 6-18B**, the system reached complete depletion of NADH. Thereafter NanoNO_x were removed from the mixture by centrifugation and a NAD-dependent alcohol dehydrogenase from *Bacillus stearothermophilus* (BsADH; PDB: 1RJW) was added together with its substrate, i.e., iprOH, (injection indicated by an arrow in **Figure 6-18B**). We observed a recovery of NADH in the solution, confirming therefore that biologically active NAD⁺ was yielded with NanoNO_x.

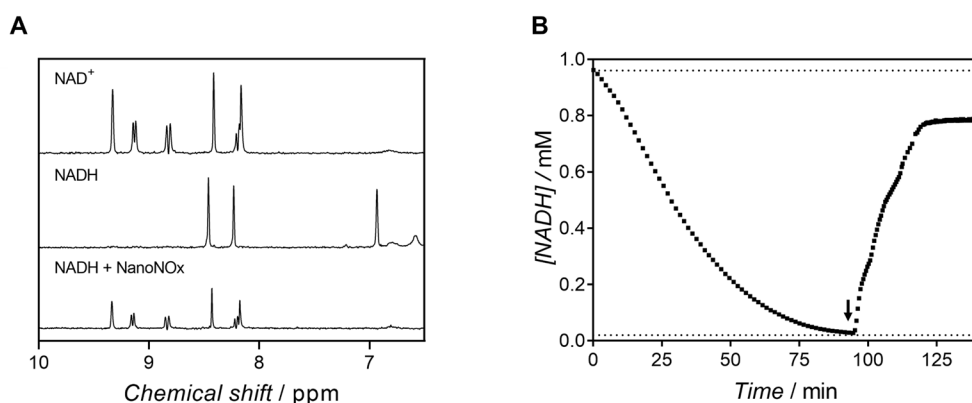


Figure 6-18. Bioavailability test of NADH. A) ¹H-NMR spectra of 1,4-NAD⁺, 1,4-NADH, and changes of 1,4-NADH after oxidation with NanoNO_x (NADH+NanoNO_x). B) Complete NADH oxidation catalyzed by NanoNO_x followed by the NAD⁺ reduction accomplished by BsADH using iprOH as substrate. Reactions were followed at 340 nm.

Only few wild NO_x are capable of oxidizing both phosphorylated and/or synthetic cofactors, so there is considerable interest in developing universal nicotinamide regeneration artificial systems.²³⁷ In this work, we explored the ability of NanoNO_x to oxidize both NADPH and a synthetic cofactor, i.e., 1-benzyl-1,4-dihyronicotinamide (BNAH), which is bioactive, cheaper and more stable than natural cofactors.^{238,239} The oxidation of NADPH by NanoNO_x displayed a meaningful catalytic performance (^{app} $k_{cat,NADPH} = 273 \pm 5 \text{ min}^{-1}$, **Figure 6-19A**), similar to that found in evolved mutant NADPH oxidases.²⁴⁰ Moreover, the oxidation of BNAH was certainly efficient. NanoNO_x showed 37 to 103 times higher activity than artificial systems, i.e., PtNP@MWCNT, hemoproteins, and reported NO_x with BNAH oxidation ability

($^{app}k_{cat,BNAH} = 374 \pm 20 \text{ min}^{-1}$, **Figure 6-19B**).^{241–243} Importantly, after studying the reaction products by ^1H NMR, we conclude that a regioselective oxidation of NADPH and BNAH was achieved, giving rise to the formation of biologically active cofactors (**Figure 6-19C** and **Figure 6-19D**, respectively). Overall, these results highlighted the extraordinary performance and the unparalleled versatility of NanoNOx to oxidize nicotinamide-based cofactors.

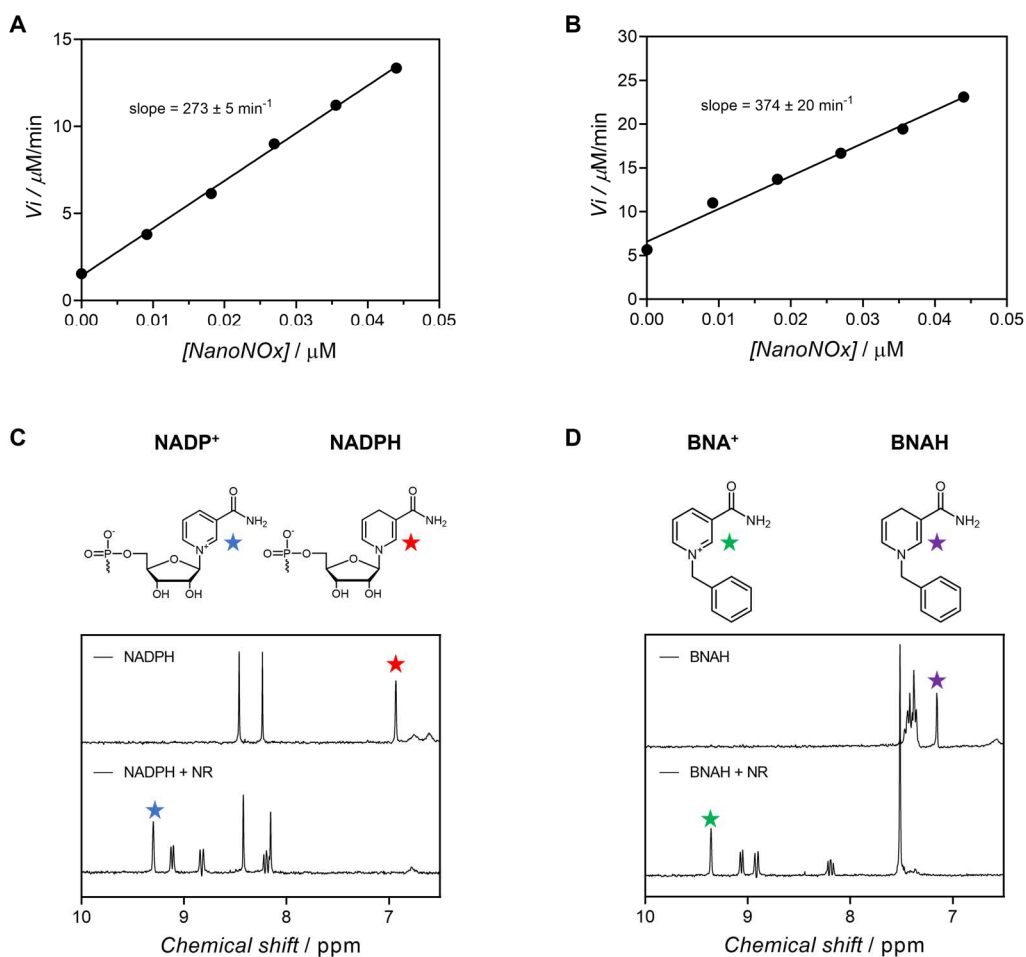


Figure 6-19. Calculation of the turnover number and regioselectivity of NanoNOx. A) $^{app}k_{cat,NADPH}$ calculation using NADPH as substrate B) $^{app}k_{cat,BNAH}$ calculation using BNAH as substrate. C) Changes in the ^1H -NMR spectra of NADPH after oxidation with NanoNOx. D) Changes in the ^1H -NMR spectra of BNAH after oxidation with NanoNOx. Stars designate monitored hydrogens (H-2) of the biologically active nicotinamide (oxidized and reduced) moieties.

6.2.5.1 *NanoNOx performance coupled with NAD-dependent dehydrogenases*

Further, we assessed the feasibility of heterogeneous NanoNOx as NADH regeneration system in combination with BsADH enzyme for the oxidation of benzyl alcohol (BnOH) to benzaldehyde. In a successful recycling, our NOx biomimetic would keep the cofactor pool in its oxidized form, namely, NAD⁺ (**Figure 6-20A**). In a first one-pot experiment, we aimed at converting 10 mM of BnOH by adding 1 mM of NAD⁺ and 20 mM of glucose to the reaction mixture without and with NanoNOx (**Figure 6-20B**). After 2 h of reaction, the non-recycled system reached low yields, with only 2.3 % of the BnOH oxidized (orange rhombus). The addition of NanoNOx to the reaction (optimized amount of 0.25 U mL⁻¹) prompted the yield to 19%, which gives a total turnover number (TTN) of almost 2 for NAD⁺ (red circles). However, the reaction progress was stopped after 2 h. As observed in **Figure 6-20C**, a ¹H-NMR inspection of the reaction mixture evidenced that the NADH cofactor was fully oxidized at this stage, ready to be utilized by the BsADH enzyme (absence of the peak at 6.93 ppm (red) attributed to reduced NADH). With this information, we hypothesized that the progression of the reaction could be affected by the inactivation of the biocatalyst due to the accumulation of H₂O₂ in the reaction medium. Thus, the BsADH was isolated from the reaction and characterized. We determined a drop in the initial catalytic performance of ca. 38% using iprOH as substrate. Further, in a separate experiment, we observed that 5 mM H₂O₂ decreased the activity of BsADH around 35%, which also supported our hypothesis. We observed that the accumulation of H₂O₂ also damaged the NanoNOx (by a factor of 29.4%).

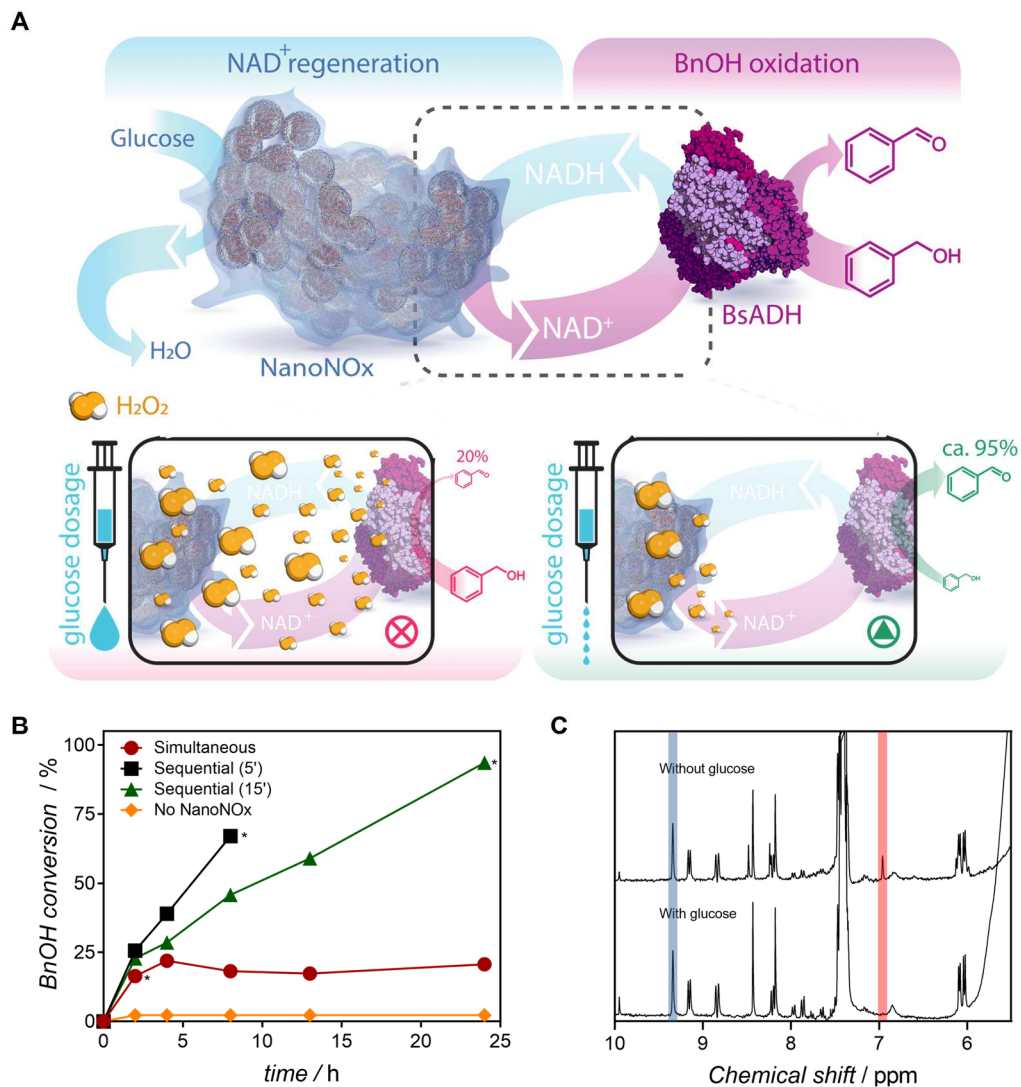


Figure 6-20. Study of the applicability of NanoNOx in NAD-dependent coupled oxidations. A) Illustration of coupled NanoNOx-BsADH biocatalytic system for the formation of NADH and the concomitant regeneration of NAD⁺ that boosts the oxidation of BnOH. A single dose of glucose generates copious amounts of H₂O₂ in the medium, which halts the reaction progress (left). The sequential addition of small concentrations of glucose generates low levels of H₂O₂, which are directionally channeled to the organometallic catalyst without damaging the biomolecules present in the reaction (right). B) BnOH oxidation kinetics with different glucose addition mode: simultaneous (20 mM), 0.2 mM every 5 min and 15 min, and without NanoNOx. Asterisks represent the point at which [glucose] = 20 mM. C) Evaluation of the cofactor by ¹H NMR after BnOH oxidation with glucose simultaneous addition.

A high concentration of H_2O_2 in the medium reflects an unbalanced catalytic equilibrium among all catalytic figures. Here, the oxidation performed by NanoNOx was faster than the oxidation of BnOH accomplished by BsADH, which leads to the accumulation of H_2O_2 (**Figure 6-20A**, left). Therefore, in a next experiment sequence, we sought to reach a balanced catalytic equilibrium by lowering the transformation rate of NanoNOx by means of a stepwise addition of glucose to the reaction. We envisioned that this approach would reduce the release of H_2O_2 to the medium, thereby minimizing the inactivation of the (bio)catalysts (**Figure 6-20A**, right). The supply of glucose (fuel injections of 0.2 mM) every 5 min raised the oxidation performance to 67% (final concentration of glucose of 20 mM, **Figure 6-20B**, black squares). When the doses were spaced every 15 min, the reaction rate decreased, but satisfyingly, a conversion of ca. 95% was obtained within 24 h (**Figure 6-20B**, green triangles). We attributed the improvement of the conversion to the controlled diffusion of H_2O_2 within NanoNOx. Under low fuel concentrations, the H_2O_2 is predominantly used by the hemin molecules to oxidize NADH rather than being released to the medium of the reaction.²⁴⁴

Finally, we aimed to upscale the one-pot reaction to 50 mM of BnOH. The sequential addition of glucose gave rise to a conversion of BnOH of ca. 50% and a TTN of 25 for NAD^+ after 24h. Remarkably, these yields are comparable to the reported values for the enzymatic oxidation of BnOH by NOx-BsADH pairs.²⁴⁵

6.3 CONCLUSION

We have designed and fabricated very versatile integrated chemoenzymatic nanoreactors (INRs) able to degrade small aromatic derivatives and dyes, as well as mimicking NOx enzymes. The advantageous distribution of the (bio)catalysts into a core-shell format leads to a highly efficient cascade reaction. A profound optimization of INRs unveiled that the confined architecture permits the *in-situ* injection of H_2O_2 towards the iron porphyrin catalyst. Moreover, the localization of hemin molecules

through the imidazole ligands of the polymeric mantle boosts the peroxidase activity. Compared to free enzyme systems, INRs show a higher activity under diluted conditions, and noticeably higher stability in presence of organic solvents. However, there is a deep pH dependence of the performance of INRs, with a significant decrease of the activity at pH below 5.0 and above 7.0. Surprisingly, hemin induces the self-assembly of certain SENs into heterogeneous INRs through hemin-imidazole coordination, thus enabling their reuse.

To the best of our knowledge, heterogeneous INRs, i.e., NanoNO_x, show the highest turnover number of all the artificial systems reported for the oxidation of NADH. Albeit displaying lower catalytic activity than NADH oxidase enzymes in terms of $k_{cat,NADH}$, the high robustness, easy recyclability, and the performance in the oxidation of both NADPH and BNAH make NanoNO_x hybrids attractive for the *in-situ* regeneration of oxidized cofactors. Finally, a controlled experimental design based on the stepwise supply of glucose allows for the reduction of harmful peroxide released to the environment. Overall, INRs developed in this work open new avenues for the implementation of hybrid chemoenzymatic catalysts in different fields, e.g., water treatment and regeneration of oxidized nicotinamides.

Chapter 7 COFACTOR CONFINEMENT, PREFABRICATED CARRIERS, FLOW

In this chapter I have increased the complexity of the system by the encapsulation of a dimeric PLP-dependent ω -transaminase enzyme with enormous potential and therefore interest for the chemical synthesis. In this case, the polymeric shell serves as a reservoir of the PLP coenzyme needed to carry out the transamination reaction. The preliminary results showed that the PLP-loaded nanogels, compared to unloaded-nanogels, show higher activity and stability. The SENs were immobilized on prefabricated supports through covalent bonds, giving rise to a novel type of heterogeneous biocatalyst. Finally, a packed-bed-reactor was loaded with the immobilized nanogels to test its performance in flow biocatalysis.

7.1 FOCUSED INTRODUCTION

The covalent attachment of SENs to prefabricated supports, i.e., carrier-bound SEN immobilization, has barely been explored.^{67,83,109} The few published works on this topic lack a detailed characterization of the heterogeneous biocatalyst and are limited to describing their applicability. Indeed, key information, such as the protein immobilization yield or retained activity after immobilization, are not reported in these studies.¹²⁵

Nowadays, there is a wide variety of supports with different composition ((bio)polymer, inorganic silica and alumina, etc.) and traits (particle size, porosity, and functionality) available on the market that could be utilized for the immobilization of SENs.¹³² Methacrylate microbeads are among the most commonly used carriers for enzyme immobilization. The high robustness of methacrylate against high pressures or organic solvents makes them well suited for applications in flow biocatalysis. However, methacrylate often causes the rearrangement of the enzyme structure due to its high hydrophobicity, which lowers the activity of the enzyme.¹²⁶ Likewise, the formation of covalent bonds between the support and the enzyme, although providing high operational stability by preventing enzyme leakage, might also reduce the activity of the biocatalyst by altering the primary structure.⁴⁵ Therefore, we foresee that alternatives such as the immobilization of SENs could alleviate these shortcomings as the encapsulated enzyme would avoid i) direct contact with the resin and ii) the alteration of the primary structure.

Pyridoxal 5'-phosphate (PLP) is the metabolically active form of vitamin B6, necessary in the catalytic mechanism of seven major groups of enzymes, e.g., ω -transaminases (ω TA).²⁸ This class of enzymes catalyzes the transamination reaction between an amine donor and an amine acceptor by using PLP as molecular shuttle (**Figure 7-1A**).²⁴⁶ In

recent years, ω TAs have attracted great interest in the biocatalytic preparation of high value chemicals.²⁴⁷ In fact, ω TAs have already been implemented in industrial processes for the synthesis of sitagliptin and acetophenone,^{248,249} but still pose problems due to their low operational stability. Enzyme inactivation is usually induced by the huge amounts of amino-donors employed to shift the reaction equilibrium to accumulate pyridoxamine 5'-phosphate (PMP) from the stable PLP-enzyme complex (forming an internal aldimine, **Figure 7-1B**).²⁴⁶ Under this unfavorable conditions, ω TAs do not retain the PMP in their catalytic pocket and the resulting catalytic cycle becomes incomplete. Unfortunately, in the absence of the cofactor, the apoenzyme is susceptible to dissociation into monomers and may subsequently precipitate after aggregation. In addition, elevated temperatures and high organic solvent content can also cause the same negative effect. Thus, to mitigate enzyme inactivation, it is imperative that both PLP and PMP remain in the active site.

Flow biocatalysis is performed when reagents are pumped through a reactor filled with immobilized enzymes to yield the final product.²⁵⁰ Flow bioreactors respond well to the process intensification demanded by the industry due to their high productivity, control, and sustainability and, therefore, are a trending topic to enhance biocatalytic transformations in different fields, e.g., pharmaceutical.^{251,252} Flow reactions are accelerated from hours to minutes due to the increased contact of the substrate with the enzyme, faster homogenization of the temperature and diffusion of gases, resulting in up to a 650-fold increase in space-time yields compared to batch reactions.²⁵³ Packed bed reactors (PBRs), which are usually constituted by a hollow pipe filled with heterogeneous biocatalysts, are the most common flow reactors due to their easy handling and stability.

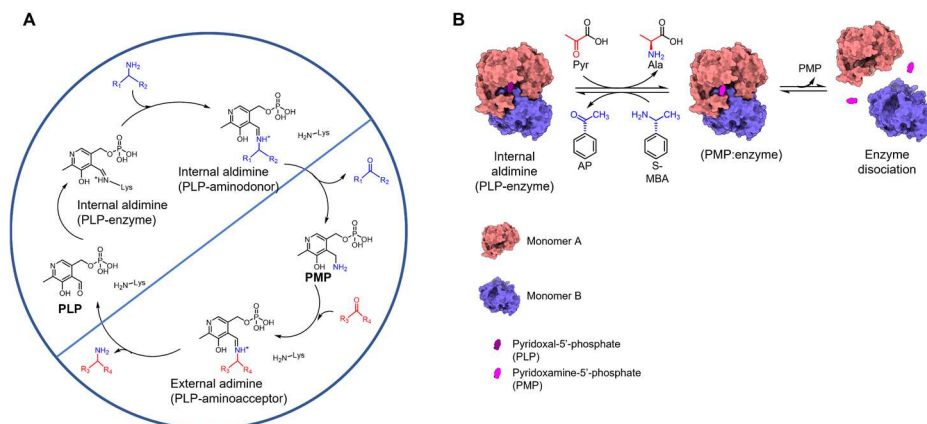


Figure 7-1. Reaction mechanism of ω TAs. A) Catalytic cycle of ω TAs consisting of the PLP half-cycle and the PMP half-cycle. B) Model transamination reaction and inactivation mechanism of dimeric ω TAs.

In this chapter, we propose to use of the SEN technology for two purposes. First, we attempted to increase the operational stability of ω -transaminase from *Halomonas elongata* (HeWT) by protecting its structure, confining the PLP cofactor by imine bonds around the enzyme. Second, for the very first time we immobilized SENs on epoxy-functionalized methacrylate microbeads via covalent bonds to exploit the advantages SENs can offer in this field. Finally, we applied the new heterogeneous biocatalysts in continuous flow biocatalysis.

7.2 RESULTS AND DISCUSSION

7.2.1 Synthesis and characterization of PLP-loaded SENs

The fabrication of HeWT nanogels was first optimized using AA and APM as comonomers and BIS as crosslinker (**Table 3-2**). At a fixed AA and BIS concentration, the APM:HeWT molar ratio was varied from 0 to 3000. The absence of APM in the polymerization resulted in almost completely inactivated hybrids (**Figure 7-2A**, lane 2). Increasing APM concentrations greatly improves the quality of the polymerizations,

encapsulating the dimer very efficiently when an excess of 1000 was used (**Figure 7-2A**, lane 4). HeWT@pAA-NH₂ fabricated under these conditions showed the highest activity, reaching 93% (*vs* non-modified HeWT). Above $n_{\text{APM}}:n_{\text{HeWT}} = 1000$, most of the protein precipitated during the polymerization due to macrogel formation. A second optimization round was carried out to adjust the AA and BIS concentrations. HeWT@pAA-NH₂ produced with 4 times higher AA and APM than those described before resulted in bigger structures with an activity of 70% (*vs* non-modified HeWT). Despite a slight decrease in activity, this sample was selected for further analysis, since thicker nanogels offer greater protection for the enzyme.⁹⁶ SENs with other functionalities, i.e., HeWT@pHEAA-NH₂ and HeWT@pAA-NR₄⁺ were also synthesized (**Table 3-2**), but the retained activities did not exceed 40%. We also found that the addition of PLP excess during polymerization ($n_{\text{PLP}}:n_{\text{HeWT}} = 5$) increased the recovered activity by up to 50%, but disturbed the encapsulation of the enzyme.

To make sure that HeWT@pAA-NH₂ remained as nanogels, their size was estimated through DLS. As observed in **Figure 7-2B**, HeWT and HeWT@pAA-NH₂ showed hydrodynamic diameters of 9.09 ± 1.89 nm and 13.91 ± 3.74 , respectively. This means that the nanogel successfully formed, with a thickness of approximately 2.5 nm.

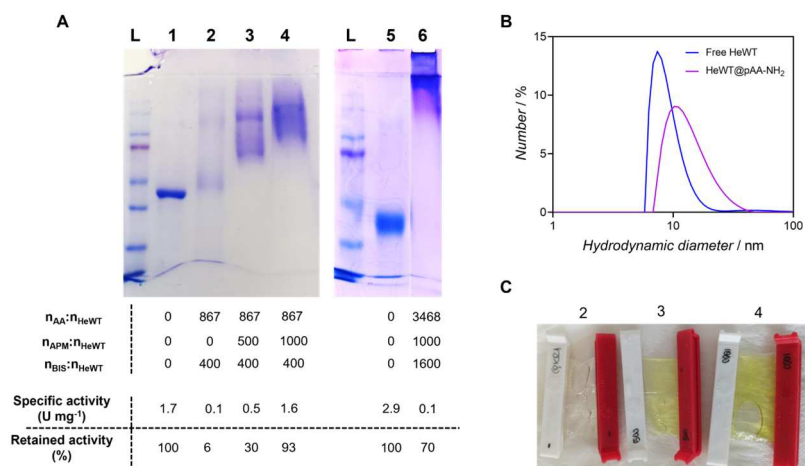


Figure 7-2. Synthesis and characterization of HeWT@pAA-NH₂. A) SDS-PAGE electrophoresis, synthesis conditions, specific and retained activity calculation of HeWT and HeWT@pAA-(NH₂). Lane

L: protein ladder; lane 1 and 5: purified HeWT; lane 2: HeWT@pAA; lane 3, 4, and 6: HeWT@pAA-NH₂. B) DLS spectra of HeWT and HeWT@pAA-NH₂ (lane 6) samples. C) Picture of SENs (lanes 2-4) after dialysis in the presence of PLP.

Next, we studied the interaction of externally added PLP with SENs. For that, during the dialysis step, which is usually performed to stop the polymerization, a fixed amount of PLP was added to the phosphate solution (same as for HeWT). At the first glance it was noticed that the nanogels functionalized with primary amines showed a more intense yellowish color than the remaining samples (HeWT, HeWT@pAA and the PLP solution used for dialysis, **Figure 7-2C**).²⁵⁴ The UV-Vis spectra revealed interesting features (**Figure 7-3**). Despite having the same protein concentration in all samples (measured by Bradford)²⁵⁵, nanogels with amino groups showed the highest intensity in the entire spectrum, especially in the case of HeWT@pAA-NH₂ (1000) (**Figure 7-3A**).

The normalized UV-Vis spectra (**Figure 7-3B**), showed a very pronounced peak at 388 nm for PLP (black spectrum).²⁵⁴ Free HeWT (blue spectrum) exhibited the characteristic protein band at 280 nm and a broad peak at 405 nm, attributed to the imine bond formation of PLP with the ε-NH₂ of catalytic lysine, forming the internal aldimine (**Figure 7-1A**).²⁵⁶ Importantly, the PLP peak in HeWT@pAA, with no amino groups in the polymeric shell, was centered at 388 nm, supporting the hypothesis that PLP leaked during polymerization (**Figure 7-2A**, lane 2). The PLP peak at 388 nm of HeWT@pAA-NH₂ were shifted towards longer wavelengths. The nanogel synthesized with higher amount of APM ($n_{\text{APM}}:n_{\text{HeWT}} = 1000$) showed a stronger peak shift. Moreover, a new peak arose at 278 nm, confirming the imine bond formation between amino-functionalized nanogels and PLP.²⁵⁷ These results suggest that HeWT@pAA-NH₂(1000), besides being the nanogel with the highest retained activity, was able to load high amounts of PLP. The adequate formation of nanogels and the ability to

confine PLP could be of paramount importance to ameliorate the stability problems of the ω Tas. Therefore, we decided to further investigate this system.

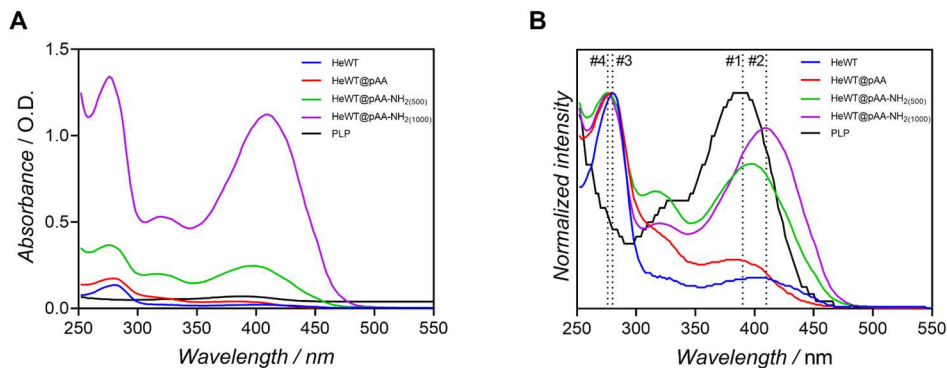


Figure 7-3. UV-Vis spectra of PLP, HeWT and SENs fabricated using AA, (APM), and BIS. A) Spectra fixed at a HeWT concentration of 0.2 mg ml^{-1} ($1.84 \text{ }\mu\text{M}$). The PLP sample was used for dialysis. B) Normalized UV-Vis spectra.

Then, we opted for a controlled incorporation of the cofactor to study the maximum PLP loading of HeWT@pAA-NH₂ (1000). For this purpose, the nanogels were dialyzed in the absence of PLP, and a controlled excess of PLP was thereafter added to the solution (see section 3.3.3.3). As depicted in **Figure 7-4A**, the intensity of the peak at 408 nm increased linearly with increasing PLP concentration. However, from a molar excess of 50, the maximum shifted towards lower wavelengths (**Figure 7-4B**). This effect indicated that no more than 50 PLP molecules could be covalently retained in each nanogel, and in fact, could be confined near the active center. Importantly, HeWT@pAA-NH₂ without external PLP ($n_{\text{PLP}}:n_{\text{HeWT@pAA-NH}_2} = 0$) showed an absorption maximum at 406 nm, demonstrating that PLP is not released during polymerization when APM monomer is utilized and, thus, the activity is preserved.

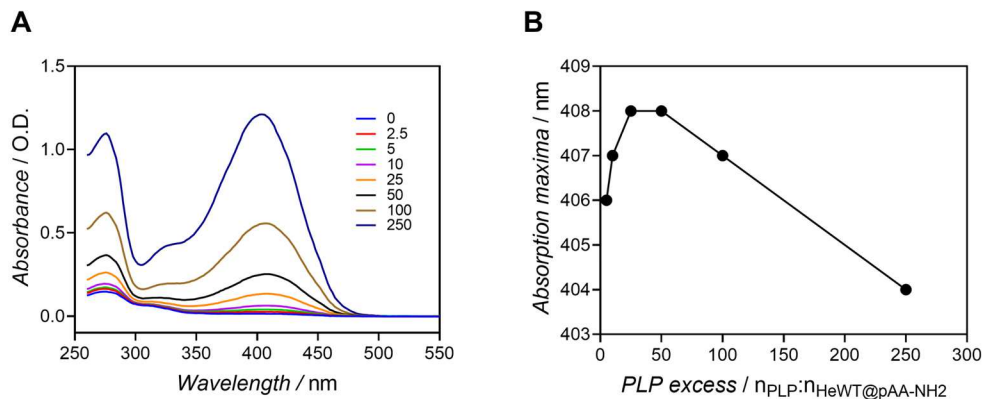


Figure 7-4. UV-vis spectra of HeWT@pAA-NH₂ loaded with different PLP excess (0 to 250).

A) UV-vis spectra of each hybrid. B) Absorption maxima of the PLP peak *vs.* PLP excess.

The activity and long-term stability of HeWT@pAA-NH₂, loaded with different PLP excess, were studied. It was observed that the PLP enhanced the specific activity of HeWT@pAA-NH₂ (**Figure 7-5A**). Importantly, the confinement of PLP in the nanogel worked as a cofactor reservoir for the enzyme. As a control, the unmodified enzyme (HeWT) showed a very different behavior. The increase in PLP concentration negatively affected HeWT activity, as previously observed with this and other ω TAs.^{258,259}

Furthermore, we observed that HeWT@pAA-NH₂ with the highest PLP excess kept its activity better during 35 days of incubation at 4°C (30% more than HeWT@pAA-NH₂ without externally added PLP, **Figure 7-5B**). On the one hand, the PLP reservoir could help maintaining the HeWT conformation, and thereby, its functionality. On the other hand, PLP could stabilize SENSs by capping the primary amines on their surface, since we have observed that the high amine density on the shell can trigger the destabilization of the nanogel and its precipitation. Overall, although the formation of SENSs slightly decreased the HeWT activity, we have demonstrated that they are able to retain PLP and to some extent serve as a reservoir, increasing the activity of the encapsulated enzyme by up to 20%.

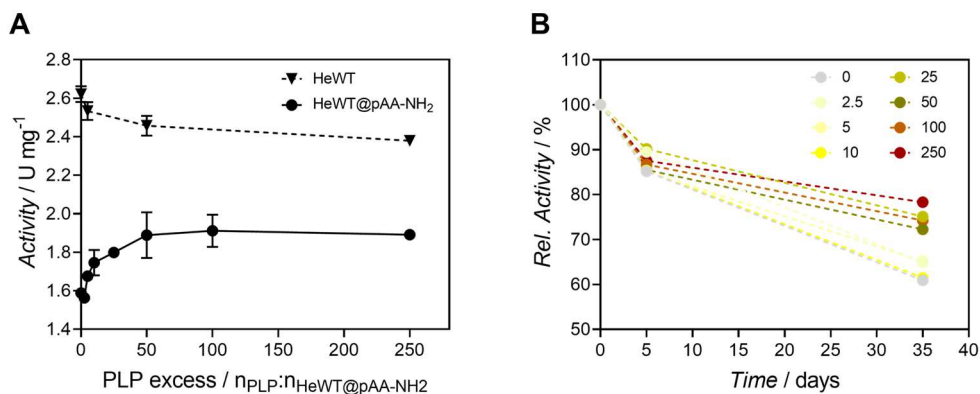


Figure 7-5. Kinetic characterization and stability of HeWT and HeWT@pAA-NH₂. A) Activity of HeWT@pAA-NH₂ loaded with different PLP excess. One unit of HeWT activity was defined as the amount of enzyme that catalyzes the reaction of 1 μmol acetophenone per minute. B) Long-term stability of HeWT@pAA-NH₂ loaded with different PLP excess.

The measurement of the kinetic parameters of HeWT@pAA-NH₂, using pyruvate as amino-acceptor and S-(α)-Methylbenzylamine (S-MBA) as amino-donor, showed interesting features (**Figure 7-6A**).²⁵⁹ Reaction condition are described in detail in section 3.3.8.1. The Michaelis-Menten constant (K_M) was first calculated for varying pyruvate concentrations, while the S-MBA concentration was set constant (**Figure 7-6B**). Free HeWT showed a $K_{M,\text{pyruvate}}$ of 0.58 ± 0.40 mM, in agreement with the values reported in other studies.²⁵⁹ However, the $K_{M,\text{pyruvate}}$ of HeWT@pAA-NH₂ decreased considerably (0.35 ± 0.02). The higher affinity for pyruvate may arise from the positive charges on the nanogel, which favor the substrate enrichment effect.²⁶⁰ The $K_{M,S\text{-MBA}}$ calculation (6.37 ± 1.19 and 8.49 ± 1.66 mM for HeWT and HeWT@pAA-NH₂, respectively) showed a cooperative profile, outlined by the Hill coefficient of 1.7 and 1.5, respectively (**Figure 7-6C**), confirming the dimeric structure of HeWT.

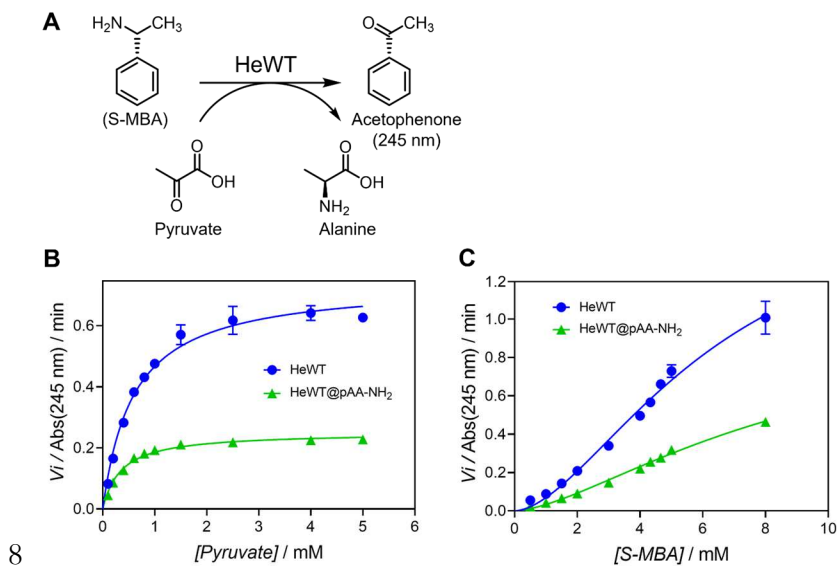


Figure 7-6. Kinetic characterization of HeWT and HeWT@pAA-NH₂. A) Reaction scheme. B) $K_{M,\text{pyruvate}}$ calculation. C) $K_{M,\text{S-MBA}}$ calculation.

To evaluate the stability of nanogels, initially their activity was evaluated in the presence of high concentrations (50%, v/v) of different organic solvents such as 2-isopropanol (iPrOH), acetonitrile (MeCN), and dimethyl sulfoxide (DMSO). As observed in **Figure 7-7**, the relative activity of HeWT@pAA-NH₂ remained higher than that of native HeWT, suggesting that the nanogel provided protection to the enzyme under these unfavourable conditions. This additional protection is important for the synthesis of chiral amines since the reagents are dissolved in relatively high amounts of organic solvents.²⁸

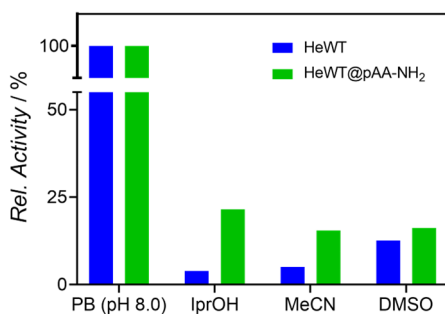


Figure 7-7. Relative activity of HeWT and HeWT@pAA-NH₂ in the presence of 50% (v/v) organic solvents (2-isopropanol (iprOH), acetonitrile (MeCN), and dimethyl sulfoxide (DMSO)). The activity in 50 mM phosphate buffer pH 8.0 was taken as 100%.

Then, HeWT and HeWT@pAA-NH₂ were incubated in toluene (50%, v/v) for 18 h and the activities in the toluene (Tol) and aqueous (Aq) fractions were calculated (**Figure 7-8A**). Unfortunately, under these conditions the nanogels did not protect the enzyme. In another parallel experiment, the free enzyme and nanogels were incubated overnight in aqueous solutions with different pH values (pH 8.0, 9.0, and 10.0. **Figure 7-8B**). It is known that the HeWT activity reaches the maximum activity at pH 10.0, however, it is not stable under those alkaline conditions.²⁵⁹ Therefore, it is of great interest to stabilize the enzyme in alkaline conditions to achieve a more efficient catalytic process. Compared to the free enzyme, the nanogels did not improve enzyme activity after incubation at pH 9.0. Fortunately, the activity was enhanced by approximately 65% at pH 10.0.

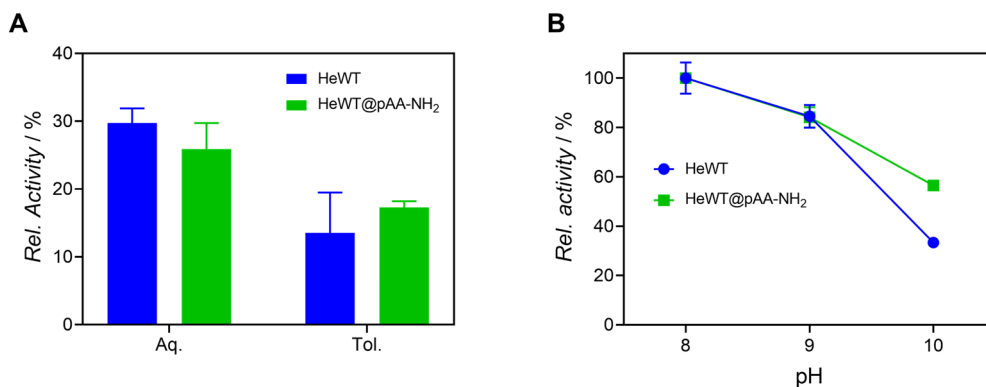


Figure 7-8. Catalytic activity evaluation of HeWT@pAA-NH₂ outside its optimal environment.

A) Activity evaluation after incubation overnight in toluene (50%, v/v) and B) aqueous solution with different pH values (8.0 – 10.0).

7.2.2 Immobilization of HeWT@pAA-NH₂ in epoxy-functionalized resins

For the formation of a heterogeneous biocatalyst, HeWT@pAA-NH₂ were covalently immobilized on solid carriers functionalized with epoxy groups (**Figure 7-9A**). Methacrylate microbeads were utilized first, seeking to improve the immobilized specific activity of HeWT with the SEN technology (fabrication details explained in section 3.3.4.3). The results regarding HeWT and HeWT@pAA-NH₂ immobilization are compiled in **Table 7-1**. HeWT@pAA-NH₂ enhanced the protein immobilization yield by 22% over free HeWT. This effect can be explained with the higher amount of primary amino groups on the surface of the nanogel compared to the free enzyme, which significantly increases the number of covalent bonds with the resin.¹⁰⁹ In addition, the hydrophobic interactions between the carrier and the biomacromolecule might also increase with the nanogel. Indeed, SDS-PAGE experiments proved that nanogels formed stronger interactions with the resin than HeWT (**Figure 7-9B**). For that, the homogeneous catalysts, i.e., HeWT and HeWT@pAA-NH₂, and the respective heterogeneous biocatalysts, i.e., HeWT-MA and SEN-MA, were separately loaded in a polyacrylamide gel. The heterogeneous biocatalysts formed with the free enzyme showed a band corresponding to free HeWT, indicating that there was some non-covalently immobilized HeWT. In contrast, no nanogel band was observed in the SEN-MA lane, which means that all the nanogels are strongly bound to the methacrylate resin.

Table 7-1. HeWT and HeWT@pAA-NH₂ immobilization on epoxy-functionalized methacrylate (MA) and butyl-methacrylate (BMA) supports.

	Resin	¹ ψ (%)	² Imm. spec. act. (U mg _{protein} ⁻¹)	³ Rec. act. (%)	⁴ Biocat. Act. (U g _{resin} ⁻¹)
HeWT	MA	62.99	0.62	27.42	0.39
HeWT@pAA-NH ₂	MA	77.09	0.10	14.54	0.08
HeWT	BMA	>99.00	0.14	6.32	0.14
HeWT@pAA-NH ₂	BMA	>99.00	0.09	12.51	0.09

¹Immobilization yield, ²immobilized specific activity, ³recovered activity, and ⁴biocatalyst activity represented in the columns.

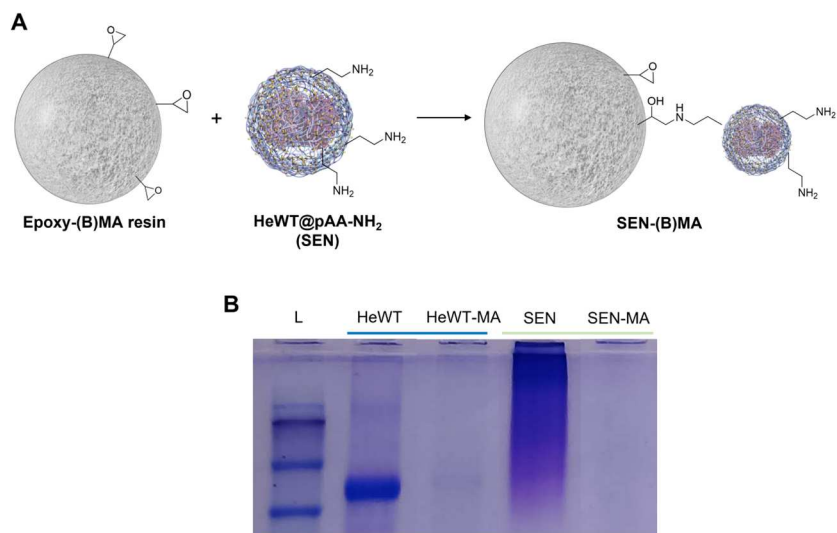


Figure 7-9. SEN immobilization into prefabricated carriers. A) Workflow of the immobilization of HeWT@pAA-NH₂ into epoxy-functionalized insoluble carriers for the formation of heterogeneous biocatalysts (SEN-(B)MA). B) SDS-PAGE of the immobilization of HeWT and HeWT@pAA-NH₂. L: protein ladder; HeWT: free HeWT; HeWT-MA: HeWT immobilized on epoxy-functionalized methacrylate beads; SEN: HeWT@pAA-NH₂; SEN-MA: HeWT@pAA-NH₂ immobilized on epoxy-functionalized methacrylate beads.

However, the immobilized specific activity of SENs decreased considerably, reaching a poor recovered activity of only 14.54% (27.42% for free HeWT). Probably the linker between the nanogels and the support was not long enough, and together with the high number of covalent bonds, made the nanogel rigid, which consequently stiffened the enzyme and therefore decreased its activity.

Afterwards, we investigated an even more hydrophobic support, i.e., butyl methacrylate, also functionalized with epoxy groups. The protein immobilization yield reached almost 100% (see **Table 7-1**), due to stronger hydrophobic interactions between HeWT or HeWTpAA-NH₂ and butyl-methacrylate. Importantly, the nanogels maintained the recovered activity values very similar to those obtained with epoxy-methacrylate, while the HeWT recovered activity decreased to 6.32% (77% drop *vs.* epoxy-methacrylate). This indicates that nanogels may protect HeWT from

hydrophobic interactions with the resin, which eventually inactivated non-modified enzymes almost completely. Therefore, as future work, it would be very interesting to test linkers with various lengths for an in-depth study of the interaction between the resin and nanogel.

7.2.3 Implementation of heterogeneous biocatalyst in flow

A continuous flow packed-bed reactor (PBR) was set-up using co-immobilized HeWT- and SEN-MA resins to produce acetophenone (AP) and L-alanine (L-Ala) from pyruvate (Pyr) and S-methylbenzylamine (S-MBA) (**Figure 7-10A**, details in section 3.3.11). Heterogeneous biocatalysts were fabricated with the same amount of immobilized enzyme ($2 \text{ mg}_{\text{enzyme}} \text{ g}_{\text{carrier}}^{-1}$) and were loaded with PLP. Importantly, it was observed that HeWT@pAA-NH₂ could retain 4 times more PLP per enzyme than HeWT' ($n_{\text{PLP}}:n_{\text{HeWT}} = 267$ and $n_{\text{PLP}}:n_{\text{HeWT}@\text{pAA-NH}_2} = 1093$), thus confirming the PLP retention ability of the nanogel. The maximum conversion in flow was reached after 10-15 column volumes for both HeWT' and HeWT@pAA-NH₂, 100% and 70%, respectively (**Figure 7-10B**), demonstrating that HeWT' was more efficient than HeWT@pAA-NH₂ in flow.

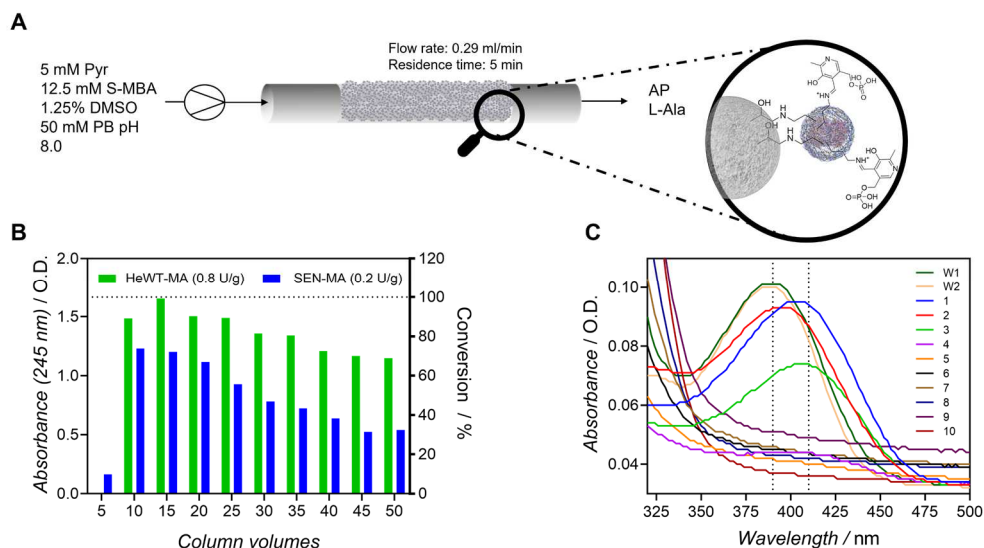


Figure 7-10. Continuous flow deamination by immobilized HeWT/HeWT@pAA-NH₂ on epoxy-methacrylate supports. (A) Schematic of the flow system setup with immobilized HeWT@pAA-NH₂ loaded with PLP. (B) The operational performance of the packed bed reactors. (C) UV-Vis spectra of the 2 washings (W) and first 10 column volumes.

Unfortunately, the acetophenone production decreased over time, ruling out the expected self-sufficient behavior of PLP-loaded nanogels.²⁶¹ Despite the cofactor was having been efficiently retained by HeWT@pAA-NH₂ in batch, it leached out when tested in flow (**Figure 7-10C**). First, it was observed that upon flowing the phosphate buffer (50 mM), PLP already leached from the column. This could be attributed to a too high flow rate for our system, or to an excessive ionic strength, which would reduce possible ionic interactions between PLP and the nanogel. Moreover, S-MBA in the mobile phase competed with HeWT@pAA-NH₂ for the PLP. The absorbance spectra of column volumes 1-3 showed that the PLP peak shifted to longer wavelengths when S-MBA was introduced into the column, as the eluted PLP formed imine bonds with S-MBA. Therefore, our approach still must be fine-tuned to retain PLP also in flow conditions. One possibility could be the introduction of quaternary amines into the system, which is currently being investigated.

7.3 CONCLUSION

In conclusion, the APM monomer is crucial for the efficient encapsulation of HeWT due to its favored interaction with the protein surface. Moreover, the incorporation of amino groups into the nanogel allows the confinement of PLP by reversible imine bonds, increasing the HeWT activity. Importantly, SENs provide resistance in the presence of high concentrations of organic solvents and in alkaline conditions. Unfortunately, the recovered activity of the nanogels after immobilization is much lower than expected, attributed to the short linker between both moieties, which generates high mechanical stress to the enzyme. Therefore, an optimization process to

improve the immobilization of SENs on prefabricated carriers is still needed. The improved heterogeneous catalysts may be of great importance in flow biocatalysis.

Chapter 8 Concluding remarks

The main contribution of this PhD thesis is the design and development of catalytic biomaterials based on Single Enzyme Nanogel (SEN). This innovative enzyme dressing system with rationally designed nanometric hydrogels has opened promising new enzyme immobilization strategies. Ultimately, the heterogeneous biocatalysts developed in this PhD thesis have permitted the successful implementation of enzymes in several technological applications, expanding the use of these extraordinary proteins.

The catalytic biomaterials and the main outcomes derived from this doctoral thesis are summarized below:

- The design of a carrier-free enzyme immobilization platform based on SENs has resulted in highly efficient Metal-Organic Enzyme Aggregates (MOEAs). The excellent tunability of MOEAs in terms of morphology and composition allows them to be arranged in layered structures for the fabrication of biocatalytic coatings. The high activity of these novel heterogeneous biocatalysts is attributed to their good diffusion characteristic and large protein loadings. In addition, the stability of MOEAs is excellent, and far superior to that shown by free enzymes. These features permit the successful implementation of MOEAs in diverse biotechnological applications, i.e., biosensing and biotransformation.
- The entrapment of SENs inside biominerals has led to the rapid formation of the nanosponges (NS). For the construction of these catalytic biomaterials, a high density of imidazole molecules on the enzyme surface is needed, which

can be effectively achieved with SEN technology. Moreover, the SENs provide significant improvements in catalytic conversion, robustness at acidic pH values, and thermal stability of these heterogeneous biocatalysts. Importantly, the use of other inorganic counterparts tunes the morphology and the catalytic activity of the resulting biomaterial.

- The rational design of SENs and the incorporation of chemical catalysts into the nanogel leads to core-shell multifunctional (bio)catlaysts able to perform highly efficient cascade reaction. Moreover, the organometallic catalyst utilized in this PhD thesis, i.e., hemin, induces the self-assembly of imidazole functionalized SENs into INRs, enabling their reuse as heterogeneous catalysts. Importantly, the INRs are successfully applied in the controlled oxidation of small aromatic compounds, dyes, and nicotinamide cofactors.
- We have learnt that the APM monomer is crucial for the efficient dressing of the ω -transaminase from *Halomonas elongata* (HeWT). Importantly, the incorporation of amino groups into the nanogel allows the confinement of the cofactor of the enzyme, i.e., PLP, which is of great importance to increase the operational stability of ω -transaminases. Moreover, the SENs provide resistance in the presence of high concentrations of organic solvents and in alkaline conditions. However, the covalent immobilization of these nanogels into prefabricated carriers needs to be optimized. Although there is still a long way to go, I foresee that these improved heterogeneous biocatalysts will make a major contribution to the flow biocatalysis of the future.

REFERENCES

- (1) Illanes, A. *Enzyme Biocatalysis: Principles and Applications*; Illanes, A., Ed.; Springer, 2008. <https://doi.org/10.1016/B978-0-444-64046-8.00003-3>.
- (2) Husain, Q.; Ullah, M. F. *Biocatalysis*; Husain, Q., Ullah, M. F., Eds.; Springer International Publishing: Cham, 2019. <https://doi.org/10.1007/978-3-030-25023-2>.
- (3) Benítez-Mateos, A. I.; Contente, M. L.; Velasco-Lozano, S.; Paradisi, F.; López-Gallego, F. Self-Sufficient Flow-Biocatalysis by Coimmobilization of Pyridoxal 5'-Phosphate and ω -Transaminases onto Porous Carriers. *ACS Sustain. Chem. Eng.* **2018**, *6* (10), 13151–13159. <https://doi.org/10.1021/acssuschemeng.8b02672>.
- (4) Orth, J. D.; Conrad, T. M.; Na, J.; Lerman, J. A.; Nam, H.; Feist, A. M.; Palsson, B. A Comprehensive Genome-Scale Reconstruction of Escherichia Coli Metabolism-2011. *Mol. Syst. Biol.* **2011**, *7* (535), 1–9. <https://doi.org/10.1038/msb.2011.65>.
- (5) Todd, A. E.; Orengo, C. A.; Thornton, J. M. Plasticity of Enzyme Active Sites. *Trends Biochem. Sci.* **2002**, *27* (8), 419–426. [https://doi.org/10.1016/S0968-0004\(02\)02158-8](https://doi.org/10.1016/S0968-0004(02)02158-8).
- (6) Poulos, T. L. Heme Enzyme Structure and Function. *Chem. Rev.* **2014**, *114* (7), 3919–3962. <https://doi.org/10.1021/cr400415k>.
- (7) Kuhlman, B.; Bradley, P. Advances in Protein Structure Prediction and Design. *Nat. Rev. Mol. Cell Biol.* **2019**, *20* (11), 681–697. <https://doi.org/10.1038/s41580-019-0163-x>.

- (8) Hollingsworth, S. A.; Karplus, P. A. A Fresh Look at the Ramachandran Plot and the Occurrence of Standard Structures in Proteins. *Biomol. Concepts* **2010**, *1* (3–4), 271–283. <https://doi.org/10.1515/bmc.2010.022>.
- (9) Englander, S. W.; Mayne, L.; Bai, Y.; Sosnick, T. R. Hydrogen Exchange: The Modern Legacy of Linderstrom-Lang. *Protein Sci.* **1997**, *6* (5), 1101–1109. <https://doi.org/10.1002/pro.5560060517>.
- (10) Lin, B.; Tao, Y. Whole-Cell Biocatalysts by Design. *Microb. Cell Fact.* **2017**, *16* (1), 1–12. <https://doi.org/10.1186/s12934-017-0724-7>.
- (11) Adrio, J. L.; Demain, A. L. Microbial Enzymes: Tools for Biotechnological Processes. *Biomolecules* **2014**, *4* (1), 117–139. <https://doi.org/10.3390/biom4010117>.
- (12) Sheldon, R. A.; Brady, D. Broadening the Scope of Biocatalysis in Sustainable Organic Synthesis. *ChemSusChem* **2019**, *12* (13), 2859–2881. <https://doi.org/10.1002/cssc.201900351>.
- (13) Dhanjai; Lu, X.; Wu, L.; Chen, J.; Lu, Y. Robust Single-Molecule Enzyme Nanocapsules for Biosensing with Significantly Improved Biosensor Stability. *Anal. Chem.* **2020**, *92* (8), 5830–5837. <https://doi.org/10.1021/acs.analchem.9b05466>.
- (14) Periasamy, D.; Mani, S.; Ambikapathi, R. White Rot Fungi and Their Enzymes for the Treatment of Industrial Dye Effluents; 2019; Vol. 3, pp 73–100. https://doi.org/10.1007/978-3-030-25506-0_4.
- (15) Monteiro, R. R. C.; Arana-Peña, S.; da Rocha, T. N.; Miranda, L. P.; Berenguer-Murcia, Á.; Tardioli, P. W.; dos Santos, J. C. S.; Fernandez-Lafuente, R. Liquid Lipase Preparations Designed for Industrial Production of Biodiesel. Is It Really an Optimal Solution? *Renew. Energy* **2021**, *164*, 1566–1587. <https://doi.org/10.1016/j.renene.2020.10.071>.

- (16) Jung, I. Y.; Kim, J. S.; Choi, B. R.; Lee, K.; Lee, H. Hydrogel Based Biosensors for In Vitro Diagnostics of Biochemicals, Proteins, and Genes. *Adv. Healthc. Mater.* **2017**, *6* (12), 1–19. <https://doi.org/10.1002/adhm.201601475>.
- (17) Zhao, Y.; Li, Q.; Chai, J.; Liu, Y. Cargo-Templated Crosslinked Polymer Nanocapsules and Their Biomedical Applications. *Adv. NanoBiomed Res.* **2021**, *1* (4), 2000078. <https://doi.org/10.1002/anbr.202000078>.
- (18) Zhu, Z.; Kin Tam, T.; Sun, F.; You, C.; Percival Zhang, Y. H. A High-Energy-Density Sugar Biobattery Based on a Synthetic Enzymatic Pathway. *Nat. Commun.* **2014**, *5*. <https://doi.org/10.1038/ncomms4026>.
- (19) Leech, D.; Kavanagh, P.; Schuhmann, W. Enzymatic Fuel Cells: Recent Progress. *Electrochim. Acta* **2012**, *84*, 223–234. <https://doi.org/10.1016/j.electacta.2012.02.087>.
- (20) Duine, J. A. Cofactor Diversity in Biological Oxidations: Implications and Applications. *Chem. Rec.* **2001**, *1* (1), 74–83. [https://doi.org/10.1002/1528-0691\(2001\)1:1<74::AID-TCR10>3.0.CO;2-E](https://doi.org/10.1002/1528-0691(2001)1:1<74::AID-TCR10>3.0.CO;2-E).
- (21) Wu, S.; Snajdrova, R.; Moore, J. C.; Baldenius, K.; Bornscheuer, U. T. Biocatalysis: Enzymatic Synthesis for Industrial Applications. *Angew. Chemie - Int. Ed.* **2021**, *60* (1), 88–119. <https://doi.org/10.1002/anie.202006648>.
- (22) Wu, H.; Tian, C.; Song, X.; Liu, C.; Yang, D.; Jiang, Z. Methods for the Regeneration of Nicotinamide Coenzymes. *Green Chem.* **2013**, *15* (7), 1773–1789. <https://doi.org/10.1039/c3gc37129h>.
- (23) Rodriguez, C.; Lavandera, I.; Gotor, V. Recent Advances in Cofactor Regeneration Systems Applied to Biocatalyzed Oxidative Processes. *Curr. Org. Chem.* **2012**, *16* (21), 2525–2541. <https://doi.org/10.2174/138527212804004643>.
- (24) Ellis, G. A.; Díaz, S. A.; Medintz, I. L. Enhancing Enzymatic Performance

- with Nanoparticle Immobilization: Improved Analytical and Control Capability for Synthetic Biochemistry. *Curr. Opin. Biotechnol.* **2021**, *71*, 77–90. <https://doi.org/10.1016/j.copbio.2021.06.021>.
- (25) Honig, B.; Yang, A. S. Free Energy Balance in Protein Folding. *Adv. Protein Chem.* **1995**, *46* (C), 27–58. [https://doi.org/10.1016/S0065-3233\(08\)60331-9](https://doi.org/10.1016/S0065-3233(08)60331-9).
- (26) Balcão, V. M.; Vila, M. M. D. C. Structural and Functional Stabilization of Protein Entities: State-of-the-Art. *Adv. Drug Deliv. Rev.* **2015**, *93*, 25–41. <https://doi.org/10.1016/j.addr.2014.10.005>.
- (27) Scharnagl, C.; Reif, M.; Friedrich, J. Stability of Proteins: Temperature, Pressure and the Role of the Solvent. *Biochim. Biophys. Acta - Proteins Proteomics* **2005**, *1749* (2), 187–213. <https://doi.org/10.1016/j.bbapap.2005.03.002>.
- (28) Slabu, I.; Galman, J. L.; Lloyd, R. C.; Turner, N. J. Discovery, Engineering, and Synthetic Application of Transaminase Biocatalysts. *ACS Catal.* **2017**, *7* (12), 8263–8284. <https://doi.org/10.1021/acscatal.7b02686>.
- (29) Hartley, C. J.; Williams, C. C.; Scoble, J. A.; Churches, Q. I.; North, A.; French, N. G.; Nebl, T.; Coia, G.; Warden, A. C.; Simpson, G.; Frazer, A. R.; Jensen, C. N.; Turner, N. J.; Scott, C. Engineered Enzymes That Retain and Regenerate Their Cofactors Enable Continuous-Flow Biocatalysis. *Nat. Catal.* **2019**, *2* (11), 1006–1015. <https://doi.org/10.1038/s41929-019-0353-0>.
- (30) Matos, M. J.; Oliveira, B. L.; Martínez-Sáez, N.; Guerreiro, A.; Cal, P. M. S. D.; Bertoldo, J.; Maneiro, M.; Perkins, E.; Howard, J.; Deery, M. J.; Chalker, J. M.; Corzana, F.; Jiménez-Osés, G.; Bernardes, G. J. L. Chemo- and Regioselective Lysine Modification on Native Proteins. *J. Am. Chem. Soc.* **2018**, *140* (11), 4004–4017. <https://doi.org/10.1021/jacs.7b12874>.
- (31) Liu, Q.; Xun, G.; Feng, Y. The State-of-the-Art Strategies of Protein Engineering for Enzyme Stabilization. *Biotechnol. Adv.* **2019**, *37* (4), 530–537. <https://doi.org/10.1016/j.biotechadv.2018.10.011>.

- (32) Chen, Z.; Zeng, A.-P. Protein Engineering Approaches to Chemical Biotechnology. *Curr. Opin. Biotechnol.* **2016**, *42*, 198–205. <https://doi.org/10.1016/j.copbio.2016.07.007>.
- (33) Arnold, F. H. Directed Evolution: Bringing New Chemistry to Life. *Angew. Chemie - Int. Ed.* **2018**, *57* (16), 4143–4148. <https://doi.org/10.1002/anie.201708408>.
- (34) Pucci, F.; Rooman, M. Physical and Molecular Bases of Protein Thermal Stability and Cold Adaptation. *Curr. Opin. Struct. Biol.* **2017**, *42*, 117–128. <https://doi.org/10.1016/j.sbi.2016.12.007>.
- (35) Stepankova, V.; Bidmanova, S.; Koudelakova, T.; Prokop, Z.; Chaloupkova, R.; Damborsky, J. Strategies for Stabilization of Enzymes in Organic Solvents. *ACS Catalysis*. 2013. <https://doi.org/10.1021/cs400684x>.
- (36) Giri, P.; Pagar, A. D.; Patil, M. D.; Yun, H. Chemical Modification of Enzymes to Improve Biocatalytic Performance. *Biotechnol. Adv.* **2021**, *53* (June), 107868. <https://doi.org/10.1016/j.biotechadv.2021.107868>.
- (37) Nwagu, T. N.; Okolo, B.; Aoyagi, H.; Yoshida, S. Chemical Modification with Phthalic Anhydride and Chitosan: Viable Options for the Stabilization of Raw Starch Digesting Amylase from *Aspergillus Carbonarius*. *Int. J. Biol. Macromol.* **2017**, *99*, 641–647. <https://doi.org/10.1016/j.ijbiomac.2017.03.022>.
- (38) Adusumalli, S. R.; Rawale, D. G.; Thakur, K.; Purushottam, L.; Reddy, N. C.; Kalra, N.; Shukla, S.; Rai, V. Chemoselective and Site-Selective Lysine-Directed Lysine Modification Enables Single-Site Labeling of Native Proteins. *Angew. Chemie - Int. Ed.* **2020**, *59* (26), 10332–10336. <https://doi.org/10.1002/anie.202000062>.
- (39) Chalker, J. M.; Bernardes, G. J. L.; Davis, B. G. A “Tag-and-Modify” Approach to Site-Selective Protein Modification. *Acc. Chem. Res.* **2011**, *44* (9), 730–741. <https://doi.org/10.1021/ar200056q>.

- (40) Nwagu, T. N.; Aoyagi, H.; Okolo, B.; Moneke, A.; Yoshida, S. Citraconylation and Maleylation on the Catalytic and Thermodynamic Properties of Raw Starch Saccharifying Amylase from *Aspergillus Carbonarius*. *Heliyon* **2020**, *6* (7), e04351. <https://doi.org/10.1016/j.heliyon.2020.e04351>.
- (41) Shaw, B. F.; Schneider, G. F.; Bilgiçer, B.; Kaufman, G. K.; Neveu, J. M.; Lane, W. S.; Whitelegge, J. P.; Whitesides, G. M. Lysine Acetylation Can Generate Highly Charged Enzymes with Increased Resistance toward Irreversible Inactivation. *Protein Sci.* **2008**, *17* (8), 1446–1455. <https://doi.org/10.1110/ps.035154.108>.
- (42) Liu, J. Z.; Wang, T. L.; Huang, M. T.; Song, H. Y.; Weng, L. P.; Ji, L. N. Increased Thermal and Organic Solvent Tolerance of Modified Horseradish Peroxidase. *Protein Eng. Des. Sel.* **2006**, *19* (4), 169–173. <https://doi.org/10.1093/protein/gzj016>.
- (43) Matsumoto, M.; Nakagawa, T.; Uchida, Y.; Seki, K.; Ohba, M.; Kondo, K. Effect of Modification of Citraconic Anhydrides on Catalytic Activity and Thermostability of Enzymes. *J. Chem. Technol. Biotechnol.* **2016**, *91* (1), 59–64. <https://doi.org/10.1002/jctb.4556>.
- (44) Wright, T. A.; Page, R. C.; Konkolewicz, D. Polymer Conjugation of Proteins as a Synthetic Post-Translational Modification to Impact Their Stability and Activity. *Polym. Chem.* **2019**, *10* (4), 434–454. <https://doi.org/10.1039/c8py01399c>.
- (45) Rodriguez-Abetxuko, A.; Sánchez-deAlcázar, D.; Muñumer, P.; Beloqui, A. Tunable Polymeric Scaffolds for Enzyme Immobilization. *Front. Bioeng. Biotechnol.* **2020**, *8* (July), 830. <https://doi.org/10.3389/fbioe.2020.00830>.
- (46) Gauthier, M. A.; Klok, H. A. Polymer-Protein Conjugates: An Enzymatic Activity Perspective. *Polymer Chemistry*. 2010, pp 1352–1373. <https://doi.org/10.1039/c0py90001j>.

- (47) Krishna, O. D.; Küick, K. L. Protein- and Peptide-Modified Synthetic Polymeric Biomaterials. *Biopolymers* **2010**, *94* (1), 32–48.
<https://doi.org/10.1002/bip.21333>.
- (48) Cobo, I.; Li, M.; Sumerlin, B. S.; Perrier, S. Smart Hybrid Materials by Conjugation of Responsive Polymers to Biomacromolecules. *Nat. Mater.* **2015**, *14* (2), 143–149. <https://doi.org/10.1038/nmat4106>.
- (49) Ding, Z.; Chen, G.; Hoffman, A. S. Unusual Properties of Thermally Sensitive Oligomer-Enzyme Conjugates of Poly(N-Isopropylacrylamide)-Trypsin. *J. Biomed. Mater. Res.* **1998**, *39* (3), 498–505.
[https://doi.org/10.1002/\(SICI\)1097-4636\(19980305\)39:3<498::AID-JBM22>3.0.CO;2-5](https://doi.org/10.1002/(SICI)1097-4636(19980305)39:3<498::AID-JBM22>3.0.CO;2-5).
- (50) Mancini, R. J.; Lee, J.; Maynard, H. D. Trehalose Glycopolymers for Stabilization of Protein Conjugates to Environmental Stressors. *J. Am. Chem. Soc.* **2012**, *134* (20), 8474–8479. <https://doi.org/10.1021/ja2120234>.
- (51) Zhang, Y.; Ge, J.; Liu, Z. Enhanced Activity of Immobilized or Chemically Modified Enzymes. *ACS Catal.* **2015**, *5* (8), 4503–4513.
<https://doi.org/10.1021/acscatal.5b00996>.
- (52) Baker, S. L.; Munasinghe, A.; Murata, H.; Lin, P.; Matyjaszewski, K.; Colina, C. M.; Russell, A. J. Intramolecular Interactions of Conjugated Polymers Mimic Molecular Chaperones to Stabilize Protein-Polymer Conjugates. *Biomacromolecules* **2018**, *19* (9), 3798–3813.
<https://doi.org/10.1021/acs.biomac.8b00927>.
- (53) Ye, Y.; Yu, J.; Gu, Z. Versatile Protein Nanogels Prepared by in Situ Polymerization. *Macromol. Chem. Phys.* **2016**, *217* (3), 333–343.
<https://doi.org/10.1002/macp.201500296>.
- (54) Belouqui, A.; Kobitski, A. Y.; Nienhaus, G. U.; Delaittre, G. A Simple Route to Highly Active Single-Enzyme Nanogels. *Chem. Sci.* **2018**, *9* (4), 1006–1013.

<https://doi.org/10.1039/c7sc04438k>.

- (55) Liu, Y.; Du, J.; Yan, M.; Lau, M. Y.; Hu, J.; Han, H.; Yang, O. O.; Liang, S.; Wei, W.; Wang, H.; Li, J.; Zhu, X.; Shi, L.; Chen, W.; Ji, C.; Lu, Y. Biomimetic Enzyme Nanocomplexes and Their Use as Antidotes and Preventive Measures for Alcohol Intoxication. *Nat. Nanotechnol.* **2013**, *8* (3), 187–192. <https://doi.org/10.1038/nnano.2012.264>.
- (56) Yan, R.; Ren, J.; Wen, J.; Cao, Z.; Wu, D.; Qin, M.; Xu, D.; Castillo, R.; Li, F.; Wang, F.; Gan, Z.; Liu, C.; Wei, P.; Lu, Y. Enzyme Therapeutic for Ischemia and Reperfusion Injury in Organ Transplantation. *Adv. Mater.* **2021**, 2105670. <https://doi.org/10.1002/adma.202105670>.
- (57) Han, L.; Liu, C.; Qi, H.; Zhou, J.; Wen, J.; Wu, D.; Xu, D.; Qin, M.; Ren, J.; Wang, Q.; Long, L.; Liu, Y.; Chen, I.; Yuan, X.; Lu, Y.; Kang, C. Systemic Delivery of Monoclonal Antibodies to the Central Nervous System for Brain Tumor Therapy. *Adv. Mater.* **2019**, *31* (19), 1805697. <https://doi.org/10.1002/adma.201805697>.
- (58) Yan, M.; Ge, J.; Liu, Z.; Ouyang, P. Encapsulation of Single Enzyme in Nanogel with Enhanced Biocatalytic Activity and Stability. *J. Am. Chem. Soc.* **2006**, *128* (34), 11008–11009. <https://doi.org/10.1021/ja064126t>.
- (59) Chapman, R.; Stenzel, M. H. All Wrapped up: Stabilization of Enzymes within Single Enzyme Nanoparticles. *J. Am. Chem. Soc.* **2019**, *141*, 2754–2769. <https://doi.org/10.1021/jacs.8b10338>.
- (60) Ming Yan; Zhixia Liu; Diannan Lu, and; Liu*, Z. Fabrication of Single Carbonic Anhydrase Nanogel against Denaturation and Aggregation at High Temperature. **2007**. <https://doi.org/10.1021/BM060746A>.
- (61) Gu, Z.; Yan, M.; Hu, B.; Joo, K. L.; Biswas, A.; Huang, Y.; Lu, Y.; Wang, P.; Tang, Y. Protein Nanocapsule Weaved with Enzymatically Degradable Polymeric Network. *Nano Lett.* **2009**, *9* (12), 4533–4538.

- <https://doi.org/10.1021/nl902935b>.
- (62) Biswas, A.; Joo, K. Il; Liu, J.; Zhao, M.; Fan, G.; Wang, P.; Gu, Z.; Tang, Y. Endoprotease-Mediated Intracellular Protein Delivery Using Nanocapsules. *ACS Nano* **2011**, *5* (2), 1385–1394. <https://doi.org/10.1021/nn1031005>.
- (63) Zhao, M.; Biswas, A.; Hu, B.; Joo, K. Il; Wang, P.; Gu, Z.; Tang, Y. Redox-Responsive Nanocapsules for Intracellular Protein Delivery. *Biomaterials* **2011**, *32* (22), 5223–5230. <https://doi.org/10.1016/j.biomaterials.2011.03.060>.
- (64) Li, F.; Yan, R.; Wu, J.; Han, Z.; Qin, M.; Liu, C.; Lu, Y. An Antioxidant Enzyme Therapeutic for Sepsis. *Front. Bioeng. Biotechnol.* **2021**, *9* (November), 1–12. <https://doi.org/10.3389/fbioe.2021.800684>.
- (65) Qin, M.; Cao, Z.; Wen, J.; Yu, Q.; Liu, C.; Wang, F.; Zhang, J.; Yang, F.; Li, Y.; Fishbein, G.; Yan, S.; Xu, B.; Hou, Y.; Ning, Z.; Nie, K.; Jiang, N.; Liu, Z.; Wu, J.; Yu, Y.; Li, H.; Zheng, H.; Li, J.; Jin, W.; Pang, S.; Wang, S.; Chen, J.; Gan, Z.; He, Z.; Lu, Y. An Antioxidant Enzyme Therapeutic for COVID-19. *Adv. Mater.* **2020**, *32* (43). <https://doi.org/10.1002/adma.202004901>.
- (66) Wang, H.; Chao, Y.; Liu, J.; Zhu, W.; Wang, G.; Xu, L.; Liu, Z. Photosensitizer-Crosslinked in-Situ Polymerization on Catalase for Tumor Hypoxia Modulation & Enhanced Photodynamic Therapy. *Biomaterials* **2018**, *181* (August), 310–317. <https://doi.org/10.1016/j.biomaterials.2018.08.011>.
- (67) Liu, L.; Yu, W.; Luo, D.; Xue, Z.; Qin, X.; Sun, X.; Zhao, J.; Wang, J.; Wang, T. Catalase Nanocapsules Protected by Polymer Shells for Scavenging Free Radicals of Tobacco Smoke. *Adv. Funct. Mater.* **2015**, *25* (32), 5159–5165. <https://doi.org/10.1002/adfm.201501850>.
- (68) Yan, M.; Du, J.; Gu, Z.; Liang, M.; Hu, Y.; Zhang, W.; Priceman, S.; Wu, L.; Zhou, Z. H.; Liu, Z.; Segura, T.; Tang, Y.; Lu, Y. A Novel Intracellular Protein Delivery Platform Based on Single-Protein Nanocapsules. *Nat. Nanotechnol.* **2010**, *5* (1), 48–53. <https://doi.org/10.1038/nnano.2009.341>.

- (69) Wu, W.; Wang, Q.; Chen, J.; Huang, L.; Zhang, H.; Rong, K.; Dong, S. Biomimetic Design for Enhancing the Peroxidase Mimicking Activity of Hemin. *Nanoscale* **2019**, *11* (26), 12603–12609. <https://doi.org/10.1039/c9nr03506k>.
- (70) Qi, H.; Yang, J.; Yu, J.; Yang, L.; Shan, P.; Zhu, S.; Wang, Y.; Li, P.; Wang, K.; Zhou, Q. Glucose-Responsive Nanogels Efficiently Maintain the Stability and Activity of Therapeutic Enzymes. *Nanotechnol. Rev.* **2022**, *11* (1), 1511–1524. <https://doi.org/10.1515/ntrev-2022-0095>.
- (71) Zhang, P.; Sun, F.; Tsao, C.; Liu, S.; Jain, P.; Sinclair, A.; Hung, H. C.; Bai, T.; Wu, K.; Jiang, S. Zwitterionic Gel Encapsulation Promotes Protein Stability, Enhances Pharmacokinetics, and Reduces Immunogenicity. *Proc. Natl. Acad. Sci. U. S. A.* **2015**, *112* (39), 12046–12051. <https://doi.org/10.1073/pnas.1512465112>.
- (72) Zhang, Z.; Gu, Y.; Liu, Q.; Zheng, C.; Xu, L.; An, Y.; Jin, X.; Liu, Y.; Shi, L. Spatial Confined Synergistic Enzymes with Enhanced Uricolytic Performance and Reduced Toxicity for Effective Gout Treatment. *Small* **2018**, *14* (33), 1–8. <https://doi.org/10.1002/sml.201801865>.
- (73) Chen, G.; Abdeen, A. A.; Wang, Y.; Shahi, P. K.; Robertson, S.; Xie, R.; Suzuki, M.; Pattnaik, B. R.; Saha, K.; Gong, S. A Biodegradable Nanocapsule Delivers a Cas9 Ribonucleoprotein Complex for in Vivo Genome Editing. *Nat. Nanotechnol.* **2019**, *14* (10), 974–980. <https://doi.org/10.1038/s41565-019-0539-2>.
- (74) Wen, J.; Anderson, S. M.; Du, J.; Yan, M.; Wang, J.; Shen, M.; Lu, Y.; Segura, T. Controlled Protein Delivery Based on Enzyme-Responsive Nanocapsules. *Adv. Mater.* **2011**, *23* (39), 4549–4553. <https://doi.org/10.1002/adma.201101771>.
- (75) Zhu, S.; Nih, L.; Carmichael, S. T.; Lu, Y.; Segura, T. Enzyme-Responsive

- Delivery of Multiple Proteins with Spatiotemporal Control. *Adv. Mater.* **2015**, 27 (24), 3620–3625. <https://doi.org/10.1002/adma.201500417>.
- (76) Zhao, M.; Liu, Y.; Hsieh, R. S.; Wang, N.; Tai, W.; Joo, K. Il; Wang, P.; Gu, Z.; Tang, Y. Clickable Protein Nanocapsules for Targeted Delivery of Recombinant P53 Protein. *J. Am. Chem. Soc.* **2014**, 136 (43), 15319–15325. <https://doi.org/10.1021/ja508083g>.
- (77) Tian, H.; Du, J.; Wen, J.; Liu, Y.; Montgomery, S. R.; Scott, T. P.; Aghdasi, B.; Xiong, C.; Suzuki, A.; Hayashi, T.; Ruangchainikom, M.; Phan, K.; Weintraub, G.; Raed, A.; Murray, S. S.; Daubs, M. D.; Yang, X.; Yuan, X. B.; Wang, J. C.; Lu, Y. Growth-Factor Nanocapsules That Enable Tunable Controlled Release for Bone Regeneration. *ACS Nano* **2016**, 10 (8), 7362–7369. <https://doi.org/10.1021/acs.nano.5b07950>.
- (78) Hu, Q.; Sun, W.; Lu, Y.; Bomba, H. N.; Ye, Y.; Jiang, T.; Isaacson, A. J.; Gu, Z. Tumor Microenvironment-Mediated Construction and Deconstruction of Extracellular Drug-Delivery Depots. *Nano Lett.* **2016**, 16 (2), 1118–1126. <https://doi.org/10.1021/acs.nanolett.5b04343>.
- (79) Wen, J.; Wu, D.; Qin, M.; Liu, C.; Wang, L.; Xu, D.; Vinters, H. V.; Liu, Y.; Kranz, E.; Guan, X.; Sun, G.; Sun, X.; Lee, Y. J.; Martinez-Maza, O.; Widney, D.; Lu, Y.; Chen, I. S. Y.; Kamata, M. Sustained Delivery and Molecular Targeting of a Therapeutic Monoclonal Antibody to Metastases in the Central Nervous System of Mice. *Nat. Biomed. Eng.* **2019**, 3 (9), 706–716. <https://doi.org/10.1038/s41551-019-0434-z>.
- (80) Li, S.; Chen, L.; Huang, K.; Chen, N.; Zhan, Q.; Yi, K.; Qi, H.; Liu, C.; Tan, Y.; Hou, X.; Lu, Y.; Zhao, J.; Yuan, X.; Kang, C. Tumor Microenvironment-Tailored Weakly Cell-Interacted Extracellular Delivery Platform Enables Precise Antibody Release and Function. *Adv. Funct. Mater.* **2019**, 29 (43), 1–10. <https://doi.org/10.1002/adfm.201903296>.

- (81) Qin, M.; Wang, L.; Wu, D.; Williams, C. K.; Xu, D.; Kranz, E.; Guo, Q.; Guan, J.; Vinters, H. V.; Lee, Y. J.; Xie, Y.; Luo, Y.; Sun, G.; Sun, X.; He, Z.; Lu, Y.; Kamata, M.; Wen, J.; Chen, I. S. Y. Enhanced Delivery of Rituximab Into Brain and Lymph Nodes Using Timed-Release Nanocapsules in Non-Human Primates. *Front. Immunol.* **2020**, *10* (January), 1–13. <https://doi.org/10.3389/fimmu.2019.03132>.
- (82) Hegedüs, I.; Kiss-Tóth Dojcsak, É.; Juhászné Szalai, A.; Lovrity, Z.; Emmer, J.; Koska, P.; Fodor, B.; Nagy, E. Single Haemoglobin Nanocapsules as Test Materials for Artificial Blood. *Period. Polytech. Chem. Eng.* **2014**, *58* (Supplement), 11–16. <https://doi.org/10.3311/PPch.7284>.
- (83) Wei, W.; Du, J.; Li, J.; Yan, M.; Zhu, Q.; Jin, X.; Zhu, X.; Hu, Z.; Tang, Y.; Lu, Y. Construction of Robust Enzyme Nanocapsules for Effective Organophosphate Decontamination, Detoxification, and Protection. *Adv. Mater.* **2013**, *25* (15), 2212–2218. <https://doi.org/10.1002/adma.201205138>.
- (84) Zhang, P.; Jain, P.; Tsao, C.; Sinclair, A.; Sun, F.; Hung, H. C.; Bai, T.; Wu, K.; Jiang, S. Butyrylcholinesterase Nanocapsule as a Long Circulating Bioscavenger with Reduced Immune Response. *J. Control. Release* **2016**, *230*, 73–78. <https://doi.org/10.1016/j.jconrel.2016.04.008>.
- (85) Wu, D.; Yang, Y.; Xu, P.; Xu, D.; Liu, Y.; Castillo, R.; Yan, R.; Ren, J.; Zhou, G.; Liu, C.; Qin, M.; Du, J.; Hou, L.; Chen, I.; Kang, C.; Jin, L.; Wen, J.; Chen, W.; Lu, Y. Real-Time Quantification of Cell Internalization Kinetics by Functionalized Bioluminescent Nanoprobes. *Adv. Mater.* **2019**, *31* (39), 1–7. <https://doi.org/10.1002/adma.201902469>.
- (86) Liu, C.; Zhao, Y.; Su, W.; Chai, J.; Xu, L.; Cao, J.; Liu, Y. Encapsulated DNase Improving the Killing Efficiency of Antibiotics in Staphylococcal Biofilms. *J. Mater. Chem. B* **2020**, *8* (20), 4395–4401. <https://doi.org/10.1039/d0tb00441c>.
- (87) Zheng, G.; Liu, S.; Zha, J.; Zhang, P.; Xu, X.; Chen, Y.; Jiang, S. Protecting

- Enzymatic Activity via Zwitterionic Nanocapsulation for the Removal of Phenol Compound from Wastewater. *Langmuir* **2019**, *35* (5), 1858–1863. <https://doi.org/10.1021/acs.langmuir.8b02001>.
- (88) Wu, L.; Lu, X.; Niu, K.; Dhanjai; Chen, J. Tyrosinase Nanocapsule Based Nano-Biosensor for Ultrasensitive and Rapid Detection of Bisphenol A with Excellent Stability in Different Application Scenarios. *Biosens. Bioelectron.* **2020**, *165* (May), 112407. <https://doi.org/10.1016/j.bios.2020.112407>.
- (89) Sánchez-deAlcázar, D.; Rodriguez-Abetxuko, A.; Beloqui, A. Metal–Organic Enzyme Nanogels as Nanointegrated Self-Reporting Chemobiosensors. *ACS Appl. Mater. Interfaces* **2022**, No. Iii. <https://doi.org/10.1021/acsami.2c04385>.
- (90) Yang, Z.; Zhang, C. Single-Enzyme Nanoparticles Based Urea Biosensor. *Sensors Actuators, B Chem.* **2013**, *188*, 313–317. <https://doi.org/10.1016/j.snb.2013.07.004>.
- (91) Zhang, F.; Wang, M.; Liang, C.; Jiang, H.; Shen, J.; Li, H. Thin-Layer Polymer Wrapped Enzymes Encapsulated in Hierarchically Mesoporous Silica with High Activity and Enhanced Stability. *Sci. Rep.* **2015**, *4* (1), 4421. <https://doi.org/10.1038/srep04421>.
- (92) Ge, J.; Lu, D.; Wang, J.; Liu, Z. Lipase Nanogel Catalyzed Transesterification in Anhydrous Dimethyl Sulfoxide. *Biomacromolecules* **2009**, *10* (6), 1612–1618. <https://doi.org/10.1021/bm900205r>.
- (93) Ge, J.; Lu, D.; Wang, J.; Yan, M.; Lu, Y.; Liu, Z. Molecular Fundamentals of Enzyme Nanogels. *J. Phys. Chem. B* **2008**, *112* (45), 14319–14324. <https://doi.org/10.1021/jp8053923>.
- (94) Panganiban, B.; Qiao, B.; Jiang, T.; Delre, C.; Obadia, M. M.; Nguyen, T. D.; Smith, A. A. A.; Hall, A.; Sit, I.; Crosby, M. G.; Dennis, P. B.; Drockenmuller, E.; Olvera, M.; Cruz, D.; Xu, T. In Foreign Environments. *Science (80-.)*. **2018**, *1243* (March), 1239–1243. <https://doi.org/10.1126/science.aao0335>.

- (95) Rodríguez-Abetxuko, A.; Sánchez-deAlcázar, D.; Cortajarena, A. L.; Beloqui, A.; Rodríguez-Abetxuko, A.; Sánchez-deAlcázar, D.; Cortajarena, A. L.; Beloqui, A. A Versatile Approach for the Assembly of Highly Tunable Biocatalytic Thin Films. *Adv. Mater. Interfaces* **2019**, *6* (18), 1900598. <https://doi.org/10.1002/admi.201900598>.
- (96) Beloqui, A.; Kobitski, A. Y.; Nienhaus, G. U.; Delaittre, G. A Simple Route to Highly Active Single-Enzyme Nanogels. *Chem. Sci.* **2018**, *9* (4), 1006–1013. <https://doi.org/10.1039/C7SC04438K>.
- (97) Jia, X.; Wang, L.; Du, J. In Situ Polymerization on Biomacromolecules for Nanomedicines. *Nano Res.* **2018**, *11* (10), 5028–5048. <https://doi.org/10.1007/s12274-018-2080-2>.
- (98) Rodríguez-Abetxuko, A.; Sánchez-deAlcázar, D.; Cortajarena, A. L.; Beloqui, A. A Versatile Approach for the Assembly of Highly Tunable Biocatalytic Thin Films. *Adv. Mater. Interfaces* **2019**, *6* (18), 1900598. <https://doi.org/10.1002/admi.201900598>.
- (99) Rodríguez-Abetxuko, A.; Muñumer, P.; Okuda, M.; Calvo, J.; Knez, M.; Beloqui, A. Nanoconfined (Bio)Catalysts as Efficient Glucose-Responsive Nanoreactors. *Adv. Funct. Mater.* **2020**, *30* (35), 2002990. <https://doi.org/10.1002/adfm.202002990>.
- (100) Yang, Z.; Si, S.; Zhang, C. Magnetic Single-Enzyme Nanoparticles with High Activity and Stability. *Biochem. Biophys. Res. Commun.* **2008**, *367* (1), 169–175. <https://doi.org/10.1016/j.bbrc.2007.12.113>.
- (101) Wei, W.; Du, J.; Yan, M.; Hu, Z.; Lu, Y. Thermo-Responsive Protein Nanocapsules for Effective Enzyme Recycling and Delivery. *J. Control. Release* **2013**, *172* (1), e115–e116. <https://doi.org/10.1016/j.jconrel.2013.08.277>.
- (102) Darnell, M. C.; Sun, J. Y.; Mehta, M.; Johnson, C.; Arany, P. R.; Suo, Z.;

- Mooney, D. J. Performance and Biocompatibility of Extremely Tough Alginate/Polyacrylamide Hydrogels. *Biomaterials* **2013**, *34* (33), 8042–8048. <https://doi.org/10.1016/j.biomaterials.2013.06.061>.
- (103) Chen, D.; Huang, Y.; Jiang, H.; Yasen, W.; Guo, D.; Su, Y.; Xue, B.; Jin, X.; Zhu, X. Fabrication of Activity-Reporting Glucose Oxidase Nanocapsules with Oxygen-Independent Fluorescence Variation. *ACS Appl. Mater. Interfaces* **2018**, *10* (31), 26005–26015. <https://doi.org/10.1021/acsami.8b06348>.
- (104) Yan, M.; Liu, Z.; Lu, D.; Liu, Z. Fabrication of Single Carbonic Anhydrase Nanogel against Denaturation and Aggregation at High Temperature. *Biomacromolecules* **2007**. <https://doi.org/10.1021/bm060746a>.
- (105) Liu, C.; Wen, J.; Li, D.; Qi, H.; Nih, L.; Zhu, J.; Xu, D.; Ren, Y.; Zhang, S.; Han, D.; Jia, H.; Zhou, J.; Qin, M.; Wu, J.; Yuan, X.; Liu, J.; Zhao, J.; Kang, C.; Lu, Y. Systemic Delivery of MicroRNA for Treatment of Brain Ischemia. *Nano Res.* **2021**, *14* (9), 3319–3328. <https://doi.org/10.1007/s12274-021-3413-8>.
- (106) Wen, J.; Wang, L.; Ren, J.; Kranz, E.; Chen, S.; Wu, D.; Kanazawa, T.; Chen, I.; Lu, Y.; Kamata, M. Nanoencapsulated Rituximab Mediates Superior Cellular Immunity against Metastatic B-Cell Lymphoma in a Complement Competent Humanized Mouse Model. *J. Immunother. Cancer* **2021**, *9* (2), 1–12. <https://doi.org/10.1136/jitc-2020-001524>.
- (107) Beloqui, A.; Baur, S.; Trouillet, V.; Welle, A.; Madsen, J.; Bastmeyer, M.; Delaittre, G. Single-Molecule Encapsulation: A Straightforward Route to Highly Stable and Printable Enzymes. *Small* **2016**, *12* (13), 1716–1722. <https://doi.org/10.1002/sml.201503405>.
- (108) Rodriguez-Abetxuko, A.; Morant-Minana, M. C.; Knez, M.; Beloqui, A. Carrierless Immobilization Route for Highly Robust Metal-Organic Hybrid Enzymes. *ACS Omega* **2019**, *4* (3), 5172–5179.

- <https://doi.org/10.1021/acsomega.8b03559>.
- (109) Simmchen, J.; Baeza, A.; Ruiz-Molina, D.; Vallet-Regí, M. Improving Catalase-Based Propelled Motor Endurance by Enzyme Encapsulation. *Nanoscale* **2014**, *6* (15), 8907–8913. <https://doi.org/10.1039/c4nr02459a>.
- (110) Du, Y.; Gao, J.; Zhou, L.; Ma, L.; He, Y.; Huang, Z.; Jiang, Y. Enzyme Nanocapsules Armored by Metal-Organic Frameworks: A Novel Approach for Preparing Nanobiocatalyst. *Chem. Eng. J.* **2017**, *327*, 1192–1197. <https://doi.org/10.1016/j.cej.2017.07.021>.
- (111) Li, J.; Jin, X.; Liu, Y.; Li, F.; Zhang, L.; Zhu, X.; Lu, Y. Robust Enzyme-Silica Composites Made from Enzyme Nanocapsules. *Chem. Commun.* **2015**, *51* (47), 9628–9631. <https://doi.org/10.1039/c5cc02053k>.
- (112) Wan, L. S.; Li, Q. L.; Chen, P. C.; Xu, Z. K. Patterned Biocatalytic Films via One-Step Self-Assembly. *Chem. Commun.* **2012**, *48* (37), 4417–4419. <https://doi.org/10.1039/c2cc17451k>.
- (113) Qi, H.; Wang, Y.; Yuan, X.; Li, P.; Yang, L. Selective Extracellular Arginine Deprivation by a Single Injection of Cellular Non-Uptake Arginine Deiminase Nanocapsules for Sustained Tumor Inhibition. *Nanoscale* **2020**, *12* (47), 24030–24043. <https://doi.org/10.1039/d0nr06823c>.
- (114) Du, J.; Yu, C.; Pan, D.; Li, J.; Chen, W.; Yan, M.; Segura, T.; Lu, Y. Quantum-Dot-Decorated Robust Transductable Bioluminescent Nanocapsules. *J. Am. Chem. Soc.* **2010**, *132* (37), 12780–12781. <https://doi.org/10.1021/ja104299t>.
- (115) Gu, Z.; Dang, T. T.; Ma, M.; Tang, B. C.; Cheng, H.; Jiang, S.; Dong, Y.; Zhang, Y.; Anderson, D. G. Glucose-Responsive Microgels Integrated with Enzyme Nanocapsules for Closed-Loop Insulin Delivery. *ACS Nano* **2013**, *7* (8), 6758–6766. <https://doi.org/10.1021/nn401617u>.
- (116) Liu, S.; Huang, B.; Zheng, G.; Zhang, P.; Li, J.; Yang, B.; Chen, Y.; Liang, L.

- Nanocapsulation of Horseradish Peroxidase (HRP) Enhances Enzymatic Performance in Removing Phenolic Compounds. *Int. J. Biol. Macromol.* **2020**, *150*, 814–822. <https://doi.org/10.1016/j.ijbiomac.2020.02.043>.
- (117) Du, J.; Jin, J.; Liu, Y.; Li, J.; Tokatlian, T.; Lu, Z.; Segura, T.; Yuan, X. B.; Yang, X.; Lu, Y. Gold-Nanocrystal-Enhanced Bioluminescent Nanocapsules. *ACS Nano* **2014**, *8* (10), 9964–9969. <https://doi.org/10.1021/nn504371h>.
- (118) Rodriguez-Abetxuko, A.; Morant-Miñana, M. C.; López-Gallego, F.; Yate, L.; Seifert, A.; Knez, M.; Beloqui, A. Imidazole-Grafted Nanogels for the Fabrication of Organic-Inorganic Protein Hybrids. *Adv. Funct. Mater.* **2018**, *28* (35), 1803115. <https://doi.org/10.1002/adfm.201803115>.
- (119) Zhao, Y.; Cai, J.; Liu, Z.; Li, Y.; Zheng, C.; Zheng, Y.; Chen, Q.; Chen, H.; Ma, F.; An, Y.; Xiao, L.; Jiang, C.; Shi, L.; Kang, C.; Liu, Y. Nanocomposites Inhibit the Formation, Mitigate the Neurotoxicity, and Facilitate the Removal of β -Amyloid Aggregates in Alzheimer's Disease Mice. *Nano Lett.* **2019**, *19* (2), 674–683. <https://doi.org/10.1021/acs.nanolett.8b03644>.
- (120) Xu, D.; Tonggu, L.; Bao, X.; Lu, D.; Liu, Z. Activation and Stabilization of a Lipase Nanogel Using GMA for Acryloylation. *Soft Matter* **2012**, *8* (6), 2036–2042. <https://doi.org/10.1039/c1sm06853a>.
- (121) Rodriguez-Abetxuko, A.; Reifs, A.; Sánchez-deAlcázar, D.; Beloqui, A. A Versatile Chemoenzymatic Nanoreactor That Mimics NAD(P)H Oxidase for the In Situ Regeneration of Cofactors. *Angew. Chemie Int. Ed.* **2022**, *61* (39). <https://doi.org/10.1002/anie.202206926>.
- (122) Zhao, M.; Xu, D.; Wu, D.; Whittaker, J. W.; Terkeltaub, R.; Lu, Y. Nanocapsules of Oxalate Oxidase for Hyperoxaluria Treatment. *Nano Res.* **2018**, *11* (5), 2682–2688. <https://doi.org/10.1007/s12274-017-1898-3>.
- (123) Dwevedi, A. 100 Years of Enzyme Immobilization. In *Enzyme Immobilization*;

Springer International Publishing: Cham, 2016; pp 1–20.

https://doi.org/10.1007/978-3-319-41418-8_1.

- (124) López-Gallego, F.; Jackson, E.; Betancor, L. Heterogeneous Systems Biocatalysis: The Path to the Fabrication of Self-Sufficient Artificial Metabolic Cells. *Chem. - A Eur. J.* **2017**, *23* (71), 17841–17849. <https://doi.org/10.1002/chem.201703593>.
- (125) Arana-Peña, S.; Carballares, D.; Morellon-Sterling, R.; Berenguer-Murcia, Á.; Alcántara, A. R.; Rodrigues, R. C.; Fernandez-Lafuente, R. Enzyme Co-Immobilization: Always the Biocatalyst Designers' Choice...or Not? *Biotechnol. Adv.* **2021**, *51* (July 2020). <https://doi.org/10.1016/j.biotechadv.2020.107584>.
- (126) Benítez-Mateos, A. I.; Contente, M. L. Agarose vs. Methacrylate as Material Supports for Enzyme Immobilization and Continuous Processing. *Catalysts* **2021**, *11* (7), 814. <https://doi.org/10.3390/catal11070814>.
- (127) An, J.; Li, G.; Zhang, Y.; Zhang, T.; Liu, X.; Gao, F.; Peng, M. Recent Advances in Enzyme-Nanostructure Biocatalysts with Enhanced Activity. **2020**, 10–13.
- (128) Gonçalves, M. C. P.; Kieckbusch, T. G.; Perna, R. F.; Fujimoto, J. T.; Morales, S. A. V.; Romanelli, J. P. Trends on Enzyme Immobilization Researches Based on Bibliometric Analysis. *Process Biochem.* **2019**, *76* (September 2018), 95–110. <https://doi.org/10.1016/j.procbio.2018.09.016>.
- (129) Garcia-Galan, C.; Berenguer-Murcia, Á.; Fernandez-Lafuente, R.; Rodrigues, R. C. Potential of Different Enzyme Immobilization Strategies to Improve Enzyme Performance. *Advanced Synthesis and Catalysis*. 2011, pp 2885–2904. <https://doi.org/10.1002/adsc.201100534>.
- (130) Homaei, A. A.; Sariri, R.; Vianello, F.; Stevanato, R. Enzyme Immobilization: An Update. *J. Chem. Biol.* **2013**, *6* (4), 185–205. <https://doi.org/10.1007/s12154-013-0102-9>.

- (131) Rather, A. H.; Khan, R. S.; Wani, T. U.; Beigh, M. A.; Sheikh, F. A. Overview on Immobilization of Enzymes on Synthetic Polymeric Nanofibers Fabricated by Electrospinning. *Biotechnol. Bioeng.* **2022**, *119* (1), 9–33. <https://doi.org/10.1002/bit.27963>.
- (132) Zdarta, J.; Meyer, A. S.; Jesionowski, T.; Pinelo, M. A General Overview of Support Materials for Enzyme Immobilization: Characteristics, Properties, Practical Utility. *Catalysts*. Multidisciplinary Digital Publishing Institute February 24, 2018, pp 92–118. <https://doi.org/10.3390/catal8020092>.
- (133) Böhmer, W.; Knaus, T.; Volkov, A.; Slot, T. K.; Shiju, N. R.; Engelmark Cassimjee, K.; Mutti, F. G. Highly Efficient Production of Chiral Amines in Batch and Continuous Flow by Immobilized ω -Transaminases on Controlled Porosity Glass Metal-Ion Affinity Carrier. *J. Biotechnol.* **2019**, *291* (November 2018), 52–60. <https://doi.org/10.1016/j.jbiotec.2018.12.001>.
- (134) Wang, G.; Chen, D.; Zhang, L.; Wang, Y.; Zhao, C.; Yan, X.; He, B.; Ma, Y.; Yang, W. A Mild Route to Entrap Papain into Cross-Linked PEG Microparticles via Visible Light-Induced Inverse Emulsion Polymerization. *J. Mater. Sci.* **2018**, *53* (2), 880–891. <https://doi.org/10.1007/s10853-017-1484-9>.
- (135) Ge, J.; Lei, J.; Zare, R. N. Protein-Inorganic Hybrid Nanoflowers. *Nat. Nanotechnol.* **2012**, *7*, 428–432. <https://doi.org/10.1038/nnano.2012.80>.
- (136) Zhang, M.; Zhang, Y.; Yang, C.; Ma, C.; Tang, J. Enzyme-Inorganic Hybrid Nanoflowers: Classification, Synthesis, Functionalization and Potential Applications. *Chem. Eng. J.* **2021**, *415* (December 2020), 129075. <https://doi.org/10.1016/j.cej.2021.129075>.
- (137) Ge, J.; Lei, J.; Zare, R. N. Protein–Inorganic Hybrid Nanoflowers. *Nat. Nanotechnol.* **2012**, *7* (7), 428–432. <https://doi.org/10.1038/nnano.2012.80>.
- (138) Escobar, S.; Velasco-Lozano, S.; Lu, C. H.; Lin, Y. F.; Mesa, M.; Bernal, C.; López-Gallego, F. Understanding the Functional Properties of Bio-Inorganic

- Nanoflowers as Biocatalysts by Deciphering the Metal-Binding Sites of Enzymes. *J. Mater. Chem. B* **2017**, *5* (23), 4478–4486.
<https://doi.org/10.1039/c6tb03295h>.
- (139) Liu, J.; Liang, J.; Xue, J.; Liang, K. Metal–Organic Frameworks as a Versatile Materials Platform for Unlocking New Potentials in Biocatalysis. *Small* **2021**, *2100300*, 1–21. <https://doi.org/10.1002/sml.202100300>.
- (140) Huang, S.; Kou, X.; Shen, J.; Chen, G.; Ouyang, G. “Armor-Plating” Enzymes with Metal–Organic Frameworks (MOFs). *Angew. Chemie - Int. Ed.* **2020**, *59* (23), 8786–8798. <https://doi.org/10.1002/anie.201916474>.
- (141) Wu, X.; Ge, J.; Yang, C.; Hou, M.; Liu, Z. Facile Synthesis of Multiple Enzyme-Containing Metal–Organic Frameworks in a Biomolecule-Friendly Environment. *Chem. Commun* **2015**, *51* (51), 13408–13411.
<https://doi.org/10.1039/c5cc05136c>.
- (142) Lian, X.; Fang, Y.; Joseph, E.; Wang, Q.; Li, J.; Banerjee, S.; Lollar, C.; Wang, X.; Zhou, H. C. Enzyme-MOF (Metal-Organic Framework) Composites. *Chem. Soc. Rev.* **2017**, *46* (11), 3386–3401.
<https://doi.org/10.1039/c7cs00058h>.
- (143) Wu, X.; Ge, J.; Yang, C.; Hou, M.; Liu, Z. Facile Synthesis of Multiple Enzyme-Containing Metal–Organic Frameworks in a Biomolecule-Friendly Environment. *Chem. Commun.* **2015**, *51* (69), 13408–13411.
<https://doi.org/10.1039/C5CC05136C>.
- (144) Lyu, F.; Zhang, Y.; Zare, R. N.; Ge, J.; Liu, Z. One-Pot Synthesis of Protein-Embedded Metal–Organic Frameworks with Enhanced Biological Activities. *Nano Lett.* **2014**. <https://doi.org/10.1021/nl5026419>.
- (145) Wilson, L.; Illanes, A.; Ottone, C.; Romero, O. Co-Immobilized Carrier-Free Enzymes for Lactose Upgrading. *Curr. Opin. Green Sustain. Chem.* **2022**, *33*, 100553. <https://doi.org/10.1016/j.cogsc.2021.100553>.

- (146) Xu, M. Q.; Li, F. L.; Yu, W. Q.; Li, R. F.; Zhang, Y. W. Combined Cross-Linked Enzyme Aggregates of Glycerol Dehydrogenase and NADH Oxidase for High Efficiency in Situ NAD⁺ Regeneration. *Int. J. Biol. Macromol.* **2020**, *144*, 1013–1021. <https://doi.org/10.1016/j.ijbiomac.2019.09.178>.
- (147) Velasco-Lozano, S.; López-Gallego, F.; Mateos-Díaz, J. C.; Favela-Torres, E. Cross-Linked Enzyme Aggregates (CLEA) in Enzyme Improvement – a Review. *Biocatalysis* **2016**, *1* (1), 166–177. <https://doi.org/10.1515/boca-2015-0012>.
- (148) de Jesús Rostro-Alanis, M.; Mancera-Andrade, E. I.; Patiño, M. B. G.; Arrieta-Baez, D.; Cardenas, B.; Martinez-Chapa, S. O.; Saldívar, R. P. Nanobiocatalysis: Nanostructured Materials – a Minireview. *Biocatalysis* **2016**, *2* (1), 1–24. <https://doi.org/10.1515/boca-2016-0001>.
- (149) Gkantzou, E.; Chatzikonstantinou, A. V.; Fotiadou, R.; Giannakopoulou, A.; Patila, M.; Stamatis, H. Trends in the Development of Innovative Nanobiocatalysts and Their Application in Biocatalytic Transformations. *Biotechnol. Adv.* **2021**, *51* (October 2020), 107738. <https://doi.org/10.1016/j.biotechadv.2021.107738>.
- (150) Misson, M.; Zhang, H.; Jin, B. Nanobiocatalyst Advancements and Bioprocessing Applications. *J. R. Soc. Interface* **2015**, *12* (102). <https://doi.org/10.1098/rsif.2014.0891>.
- (151) Betancor, L.; Luckarift, H. R. Bioinspired Enzyme Encapsulation for Biocatalysis. *Trends Biotechnol.* **2008**, *26* (10), 566–572. <https://doi.org/10.1016/j.tibtech.2008.06.009>.
- (152) Vázquez-González, M.; Wang, C.; Willner, I. Biocatalytic Cascades Operating on Macromolecular Scaffolds and in Confined Environments. *Nat. Catal.* **2020**, *3* (3), 256–273. <https://doi.org/10.1038/s41929-020-0433-1>.
- (153) Bilal, M.; Qamar, S. A.; Ashraf, S. S.; Rodríguez-Couto, S.; Iqbal, H. M. N.

- Robust Nanocarriers to Engineer Nanobiocatalysts for Bioprocessing Applications. *Adv. Colloid Interface Sci.* **2021**, 293.
<https://doi.org/10.1016/j.cis.2021.102438>.
- (154) Wang, X.; Liu, X.; Yan, X.; Zhao, P.; Ding, Y.; Xu, P. Enzyme-Nanoporous Gold Biocomposite: Excellent Biocatalyst with Improved Biocatalytic Performance and Stability. *PLoS One* **2011**, 6 (9), 1–7.
<https://doi.org/10.1371/journal.pone.0024207>.
- (155) Raghavendra, T.; Basak, A.; Manocha, L. M.; Shah, A. R.; Madamwar, D. Robust Nanobioconjugates of Candida Antarctica Lipase B - Multiwalled Carbon Nanotubes: Characterization and Application for Multiple Usages in Non-Aqueous Biocatalysis. *Bioresour. Technol.* **2013**, 140, 103–110.
<https://doi.org/10.1016/j.biortech.2013.04.071>.
- (156) Kalantari, M.; Yu, M.; Yang, Y.; Strounina, E.; Gu, Z.; Huang, X.; Zhang, J.; Song, H.; Yu, C. Tailoring Mesoporous-Silica Nanoparticles for Robust Immobilization of Lipase and Biocatalysis. *Nano Res.* **2017**, 10 (2), 605–617.
<https://doi.org/10.1007/s12274-016-1320-6>.
- (157) Pavlidis, I. V.; Patila, M.; Bornscheuer, U. T.; Gournis, D.; Stamatis, H. Graphene-Based Nanobiocatalytic Systems: Recent Advances and Future Prospects. *Trends Biotechnol.* **2014**, 32 (6), 312–320.
<https://doi.org/10.1016/j.tibtech.2014.04.004>.
- (158) Wu, Q.; He, Z.; Wang, X.; Zhang, Q.; Wei, Q.; Ma, S.; Ma, C.; Li, J.; Wang, Q. Cascade Enzymes within Self-Assembled Hybrid Nanogel Mimicked Neutrophil Lysosomes for Singlet Oxygen Elevated Cancer Therapy. *Nat. Commun.* **2019**, 10 (1), 1–14. <https://doi.org/10.1038/s41467-018-08234-2>.
- (159) Liu, Y.; Ba, F.; Liu, W.-Q.; Wu, C.; Li, J. Plug-and-Play Functionalization of Protein–Polymer Conjugates for Tunable Catalysis Enabled by Genetically Encoded “Click” Chemistry. *ACS Catal.* **2022**, 4165–4174.

- <https://doi.org/10.1021/acscatal.2c00846>.
- (160) Filice, M.; Palomo, J. M. Cascade Reactions Catalyzed by Bionanostructures. *ACS Catal.* **2014**, *4* (5), 1588–1598. <https://doi.org/10.1021/cs401005y>.
- (161) Araújo da Trindade Júnior, A.; Ferraz Ximenes Ladeira, Y.; da Silva França, A.; Octavio Mendonça Alves de Souza, R.; Henrique de Moraes, A.; Wojcieszak, R.; Itabaiana Jr., I.; Silva de Miranda, A. Multicatalytic Hybrid Materials for Biocatalytic and Chemoenzymatic Cascades—Strategies for Multicatalyst (Enzyme) Co-Immobilization. *Catalysts* **2021**, *11* (936).
- (162) Ye, R.; Zhao, J.; Wickemeyer, B. B.; Toste, F. D.; Somorjai, G. A. Foundations and Strategies of the Construction of Hybrid Catalysts for Optimized Performances. *Nat. Catal.* **2018**, *1* (5), 318–325. <https://doi.org/10.1038/s41929-018-0052-2>.
- (163) Litman, Z. C.; Wang, Y.; Zhao, H.; Hartwig, J. F. Cooperative Asymmetric Reactions Combining Photocatalysis and Enzymatic Catalysis. *Nature* **2018**, *560* (7718), 355–359. <https://doi.org/10.1038/s41586-018-0413-7>.
- (164) Morant-Miñana, M. C.; Elizalde, J. Microscale Electrodes Integrated on COP for Real Sample *Campylobacter* Spp. Detection. *Biosens. Bioelectron.* **2015**, *70*, 491–497. <https://doi.org/10.1016/j.bios.2015.03.063>.
- (165) Yan, Q.; Zheng, H. N.; Jiang, C.; Li, K.; Xiao, S. J. EDC/NHS Activation Mechanism of Polymethacrylic Acid: Anhydride versus NHS-Ester. *RSC Adv.* **2015**, *5* (86), 69939–69947. <https://doi.org/10.1039/c5ra13844b>.
- (166) Swinehart, D. F. The Beer-Lambert Law. *J. Chem. Educ.* **1962**, *39* (7), 333–335. <https://doi.org/10.1021/ed039p333>.
- (167) Planchestainer, M.; Hegarty, E.; Heckmann, C. M.; Gourlay, L. J.; Paradisi, F. Widely Applicable Background Depletion Step Enables Transaminase Evolution through Solid-Phase Screening. *Chem. Sci.* **2019**, *10* (23), 5952–5958.

<https://doi.org/10.1039/c8sc05712e>.

- (168) Weibel, M. K.; Bright, H. J. The Glucose Oxidase Mechanism. *J. Biol. Chem.* **1971**, *246* (9), 2734–2744. [https://doi.org/10.1016/S0021-9258\(18\)62246-X](https://doi.org/10.1016/S0021-9258(18)62246-X).
- (169) Mengele, A. K.; Seibold, G. M.; Eikmanns, B. J.; Rau, S. Coupling Molecular Photocatalysis to Enzymatic Conversion. *ChemCatChem* **2017**, *9* (23), 4369–4376. <https://doi.org/10.1002/cctc.201701232>.
- (170) Trapaidze, A.; D’Antuono, M.; Fratzl, P.; Harrington, M. J. Exploring Mussel Byssus Fabrication with Peptide-Polymer Hybrids: Role of PH and Metal Coordination in Self-Assembly and Mechanics of Histidine-Rich Domains. *Eur. Polym. J.* **2018**, *109* (September), 229–236. <https://doi.org/10.1016/j.eurpolymj.2018.09.053>.
- (171) Degtyar, E.; Harrington, M. J.; Politi, Y.; Fratzl, P. The Mechanical Role of Metal Ions in Biogenic Protein-Based Materials. *Angew. Chemie - Int. Ed.* **2014**, *53* (45), 12026–12044. <https://doi.org/10.1002/anie.201404272>.
- (172) Cui, Q.; Karplus, M. Is a “Proton Wire” Concerted or Stepwise? A Model Study of Proton Transfer in Carbonic Anhydrase. *J. Phys. Chem. B* **2003**, *107* (4), 1071–1078. <https://doi.org/10.1021/jp021931v>.
- (173) Chen, Y.; Tao, K.; Ji, W.; Kumar, V. B.; Rencus-lazar, S.; Gazit, E. Histidine as a Key Modulator of Molecular Supramolecular Materials Inspired by Biological Systems. *Mater. Today* **2022**, *xxx* (xx), 1–22. <https://doi.org/10.1016/j.mattod.2022.08.011>.
- (174) Lyu, F.; Zhang, Y.; Zare, R. N.; Ge, J.; Liu, Z. One-Pot Synthesis of Protein-Embedded Metal-Organic Frameworks with Enhanced Biological Activities. *Nano Lett.* **2014**, *14* (10), 5761–5765. <https://doi.org/10.1021/nl5026419>.
- (175) Lian, X.; Fang, Y.; Joseph, E.; Wang, Q.; Li, J.; Banerjee, S.; Lollar, C.; Wang, X.; Zhou, H.-C. Enzyme–MOF (Metal–Organic Framework) Composites.

- Chem. Soc. Rev.* **2017**, *46* (11), 3386–3401.
<https://doi.org/10.1039/C7CS00058H>.
- (176) Chen, G.; Huang, S.; Kou, X.; Wei, S.; Huang, S.; Jiang, S.; Shen, J.; Zhu, F.; Ouyang, G. A Convenient and Versatile Amino-Acid-Boosted Biomimetic Strategy for the Nondestructive Encapsulation of Biomacromolecules within Metal–Organic Frameworks. *Angew. Chemie - Int. Ed.* **2019**, *58* (5), 1463–1467.
<https://doi.org/10.1002/anie.201813060>.
- (177) Jang, J.; Park, H. Formation and Structure of Polyacrylamide-Silica Nanocomposites by Sol-Gel Process. *J. Appl. Polym. Sci.* **2002**, *83* (8), 1817–1823. <https://doi.org/10.1002/app.10116>.
- (178) Ramasamy, R. Vibrational Spectroscopic Studies of Imidazole. *Armen. J. Phys.* **2008**, *8* (1), 51–55.
- (179) Fischer, B. E.; Haring, U. K.; Tribolet, R.; Sigel, H. Metal Ion / Buffer Interactions. *Eur. J. Biochem* **1979**, *530*, 523–530.
- (180) Meng, F. L.; Zhong, H. X.; Zhang, Q.; Liu, K. H.; Yan, J. M.; Jiang, Q. Integrated Cu₃N Porous Nanowire Array Electrode for High-Performance Supercapacitors. *J. Mater. Chem. A* **2017**, *5* (36), 18972–18976.
<https://doi.org/10.1039/c7ta05439d>.
- (181) Lázaro Martínez, J. M.; Rodríguez-Castellón, E.; Sánchez, R. M. T.; Denaday, L. R.; Buldain, G. Y.; Campo Dall’Orto, V. XPS Studies on the Cu(I,II)-Polyampholyte Heterogeneous Catalyst: An Insight into Its Structure and Mechanism. *J. Mol. Catal. A Chem.* **2011**, *339* (1–2), 43–51.
<https://doi.org/10.1016/j.molcata.2011.02.010>.
- (182) Chulkaivalsucharit, P.; Wu, X.; Ge, J. Synthesis of Enzyme-Embedded Metal–Organic Framework Nanocrystals in Reverse Micelles. *RSC Adv.* **2015**, *5* (123), 101293–101296. <https://doi.org/10.1039/C5RA21069K>.

- (183) Liu, C.; Xue, K.; Sun, A.; Chen, D.; Zhang, P.; Cui, G. Cu₂O Ordered Nanoarrays for Non-Enzymatic Glucose Detection. *J. Appl. Sci. Eng.* **2021**, *24* (6), 829–835. [https://doi.org/10.6180/jase.202112_24\(6\).0002](https://doi.org/10.6180/jase.202112_24(6).0002).
- (184) Jiang, X.; Wang, Y.; Wang, Y.; Huang, H.; Bai, Y.; Su, X.; Zhang, J.; Yao, B.; Tu, T.; Luo, H. Exploiting the Activity–Stability Trade-off of Glucose Oxidase from *Aspergillus Niger* Using a Simple Approach to Calculate Thermostability of Mutants. *Food Chem.* **2021**, *342* (December 2019), 128270. <https://doi.org/10.1016/j.foodchem.2020.128270>.
- (185) McCormick, D. B.; Koster, J. F.; Veeger, C. On the Mechanisms of Photochemical Reductions of FAD and FAD-Dependent Flavoproteins. *Eur. J. Biochem.* **1967**, *2* (4), 387–391. <https://doi.org/10.1111/j.1432-1033.1967.tb00150.x>.
- (186) Zhang, Y.; Xie, Z.; Wang, Z.; Feng, X.; Wang, Y.; Wu, A. Unveiling the Adsorption Mechanism of Zeolitic Imidazolate Framework-8 with High Efficiency for Removal of Copper Ions from Aqueous Solutions. *Dalt. Trans.* **2016**, *45* (32), 12653–12660. <https://doi.org/10.1039/c6dt01827k>.
- (187) Kopeček, J.; Yang, J. Smart Self-Assembled Hybrid Hydrogel Biomaterials. *Angew. Chemie - Int. Ed.* **2012**, *51* (30), 7396–7417. <https://doi.org/10.1002/anie.201201040>.
- (188) Kapinos, L. E.; Song, B.; Sigel, H. Metal Ion-Coordinating Properties of Imidazole and Derivatives in Aqueous Solution: Interrelation between Complex Stability and Ligand Basicity. *Inorganica Chim. Acta* **1998**, *280* (1–2), 50–56. [https://doi.org/10.1016/s0020-1693\(98\)00052-8](https://doi.org/10.1016/s0020-1693(98)00052-8).
- (189) Bharath, G.; Madhu, R.; Chen, S. M.; Veeramani, V.; Balamurugan, A.; Mangalaraj, D.; Viswanathan, C.; Ponpandian, N. Enzymatic Electrochemical Glucose Biosensors by Mesoporous 1D Hydroxyapatite-on-2D Reduced Graphene Oxide. *J. Mater. Chem. B* **2015**, *3* (7), 1360–1370.

- <https://doi.org/10.1039/c4tb01651c>.
- (190) Shi, J.; Wu, Y.; Zhang, S.; Tian, Y.; Yang, D.; Jiang, Z. Bioinspired Construction of Multi-Enzyme Catalytic Systems. *Chem. Soc. Rev.* **2018**, *47* (12), 4295–4313. <https://doi.org/10.1039/c7cs00914c>.
- (191) Beniash, E. Biomaterials—Hierarchical Nanocomposites: The Example of Bone. *WIREs Nanomedicine and Nanobiotechnology* **2011**, *3* (1), 47–69. <https://doi.org/10.1002/wnan.105>.
- (192) Aizenberg, J.; Weaver, J. C.; Thanawala, M. S.; Sundar, V. C.; Morse, D. E.; Fratzl, P. Materials Science: Skeleton of *Euplectella* Sp.: Structural Hierarchy from the Nanoscale to the Macroscale. *Science (80-.)*. **2005**, *309* (5732), 275–278. <https://doi.org/10.1126/science.1112255>.
- (193) Beniash, E.; Simmer, J. P.; Margolis, H. C. The Effect of Recombinant Mouse Amelogenins on the Formation and Organization of Hydroxyapatite Crystals in Vitro. *J. Struct. Biol.* **2005**, *149* (2), 182–190. <https://doi.org/10.1016/j.jsb.2004.11.001>.
- (194) Fantner, G. E.; Hassenkam, T.; Kindt, J. H.; Weaver, J. C.; Birkedal, H.; Pechenik, L.; Cutroni, J. A.; Cidade, G. A. G.; Stucky, G. D.; Morse, D. E.; Hansma, P. K. Sacrificial Bonds and Hidden Length Dissipate Energy as Mineralized Fibrils Separate during Bone Fracture. *Nat. Mater.* **2005**, *4* (8), 612–616. <https://doi.org/10.1038/nmat1428>.
- (195) Li, Y.; Wu, H.; Su, Z. Enzyme-Based Hybrid Nanoflowers with High Performances for Biocatalytic, Biomedical, and Environmental Applications. *Coord. Chem. Rev.* **2020**, *416*, 213342. <https://doi.org/10.1016/j.ccr.2020.213342>.
- (196) Lang, X.; Zhu, L.; Gao, Y.; Wheeldon, I. Enhancing Enzyme Activity and Immobilization in Nanostructured Inorganic-Enzyme Complexes. *Langmuir* **2017**, *33* (36), 9073–9080. <https://doi.org/10.1021/acs.langmuir.7b02004>.

- (197) Wei, T.; Du, D.; Zhu, M. J.; Lin, Y.; Dai, Z. An Improved Ultrasensitive Enzyme-Linked Immunosorbent Assay Using Hydrangea-Like Antibody-Enzyme-Inorganic Three-in-One Nanocomposites. *ACS Appl. Mater. Interfaces* **2016**, *8* (10), 6329–6335. <https://doi.org/10.1021/acsami.5b11834>.
- (198) Li, Y.; Fei, X.; Liang, L.; Tian, J.; Xu, L.; Wang, X.; Wang, Y. The Influence of Synthesis Conditions on Enzymatic Activity of Enzyme-Inorganic Hybrid Nanoflowers. *J. Mol. Catal. B Enzym.* **2016**, *133*, 92–97. <https://doi.org/10.1016/j.molcatb.2016.08.001>.
- (199) Berglund, G. I.; Carlsson, G. H.; Smith, A. T.; Szöke, H.; Henriksen, A.; Hajdu, J. The Catalytic Pathway of Horseradish Peroxidase at High Resolution. *Nature* **2002**, *417* (6887), 463–468. <https://doi.org/10.1038/417463a>.
- (200) Yin, Y.; Xiao, Y.; Lin, G.; Xiao, Q.; Lin, Z.; Cai, Z. An Enzyme-Inorganic Hybrid Nanoflower Based Immobilized Enzyme Reactor with Enhanced Enzymatic Activity. *J. Mater. Chem. B* **2015**, *3* (11), 2295–2300. <https://doi.org/10.1039/c4tb01697a>.
- (201) Grujicic, D.; Pesic, B. Reaction and Nucleation Mechanisms of Copper Electrodeposition from Ammoniacal Solutions on Vitreous Carbon. *Electrochim. Acta* **2005**, *50* (22), 4426–4443. <https://doi.org/10.1016/j.electacta.2005.02.012>.
- (202) Carniato, S.; Roulet, H.; Dufour, G.; Palacin, S.; Barraud, A.; Millié, P.; Nenner, I. Electronic Structure of Nitrogen Square Planar Copper Complexes in Langmuir-Blodgett Films. *Thin Solid Films* **1992**, *210–211* (PART 2), 519–520. [https://doi.org/10.1016/0040-6090\(92\)90329-A](https://doi.org/10.1016/0040-6090(92)90329-A).
- (203) Mattoo, A. K.; Modi, V. V. Palmitic Acid Activation of Peroxidase and Its Possible Significance in Mango Ripening. *BBA - Enzymol.* **1975**, *397* (2), 318–330. [https://doi.org/10.1016/0005-2744\(75\)90121-7](https://doi.org/10.1016/0005-2744(75)90121-7).

- (204) Abdel-Lateef, M. A. Utilization of the Peroxidase-like Activity of Silver Nanoparticles Nanozyme on O-Phenylenediamine/H₂O₂ System for Fluorescence Detection of Mercury (II) Ions. *Sci. Rep.* **2022**, *12* (1), 1–9. <https://doi.org/10.1038/s41598-022-10779-8>.
- (205) Poizat, M.; Arends, I. W. C. E.; Hollmann, F. On the Nature of Mutual Inactivation between [Cp*Rh(Bpy)(H₂O)]²⁺ and Enzymes - Analysis and Potential Remedies. *J. Mol. Catal. B Enzym.* **2010**, *63* (3–4), 149–156. <https://doi.org/10.1016/j.molcatb.2010.01.006>.
- (206) Peters, R. J. R. W.; Louzao, I.; Van Hest, J. C. M. From Polymeric Nanoreactors to Artificial Organelles. *Chem. Sci.* **2012**, *3* (2), 335–342. <https://doi.org/10.1039/c2sc00803c>.
- (207) Chen, Z.; Cao, H.; Tan, T. Preparation of Functionalized Star Polymer Nanoparticles by RAFT Polymerization and Their Application in Positionally Assembled Enzymes for Cascade Reactions. *New J. Chem.* **2019**, *43* (22), 8517–8526. <https://doi.org/10.1039/c9nj01122f>.
- (208) Cheng, Y.; Cheng, M.; Hao, J.; Jia, G.; Monchaud, D.; Li, C. The Noncovalent Dimerization of a G-Quadruplex/Hemin DNAzyme Improves Its Biocatalytic Properties. *Chem. Sci.* **2020**. <https://doi.org/10.1039/D0SC02907F>.
- (209) Wang, J.; Chen, Z. Y.; Zhao, M. P.; Li, Y. Z. Catalytical Oxidation of Styrene by Molecularly Imprinted Polymer with Phenylacetic Acid as Template and Hemin as Co-Monomer. *Chinese Chem. Lett.* **2007**, *18* (8), 981–984. <https://doi.org/10.1016/j.ccllet.2007.06.009>.
- (210) Golub, E.; Freeman, R.; Willner, I. A Hemin/G-Quadruplex Acts as an NADH Oxidase and NADH Peroxidase Mimicking DNAzyme. *Angew. Chemie - Int. Ed.* **2011**, *50* (49), 11710–11714. <https://doi.org/10.1002/anie.201103853>.

- (211) Wang, X.; Hou, C.; Qiu, W.; Ke, Y.; Xu, Q.; Liu, X. Y.; Lin, Y. Protein-Directed Synthesis of Bifunctional Adsorbent-Catalytic Hemin-Graphene Nanosheets for Highly Efficient Removal of Dye Pollutants via Synergistic Adsorption and Degradation. *ACS Appl. Mater. Interfaces* **2017**, *9* (1), 684–692. <https://doi.org/10.1021/acsami.6b12495>.
- (212) Wang, Q.; Yang, Z.; Ma, M.; Chang, C. K.; Xu, B. High Catalytic Activities of Artificial Peroxidases Based on Supramolecular Hydrogels That Contain Heme Models. *Chem. - A Eur. J.* **2008**, *14* (16), 5073–5078. <https://doi.org/10.1002/chem.200702010>.
- (213) Jiang, B.; Yao, Y.; Xie, R.; Dai, D.; Lu, W.; Chen, W.; Zhang, L. Enhanced Generation of Reactive Oxygen Species for Efficient Pollutant Elimination Catalyzed by Hemin Based on Persistent Free Radicals. *Appl. Catal. B Environ.* **2016**, *183*, 291–297. <https://doi.org/10.1016/j.apcatb.2015.10.051>.
- (214) Babich, H.; Davis, D. L. Phenol: A Review of Environmental and Health Risks. *Regul. Toxicol. Pharmacol.* **1981**, *1* (1), 90–109. [https://doi.org/10.1016/0273-2300\(81\)90071-4](https://doi.org/10.1016/0273-2300(81)90071-4).
- (215) Rocha-Martin, J.; Velasco-Lozano, S.; Guisán, J. M.; López-Gallego, F. Oxidation of Phenolic Compounds Catalyzed by Immobilized Multi-Enzyme Systems with Integrated Hydrogen Peroxide Production. *Green Chem.* **2014**, *16* (1), 303–311. <https://doi.org/10.1039/c3gc41456f>.
- (216) Burek, B. O.; Bormann, S.; Hollmann, F.; Bloh, J. Z.; Holtmann, D. Hydrogen Peroxide Driven Biocatalysis. *Green Chem.* **2019**, *21* (12), 3232–3249. <https://doi.org/10.1039/c9gc00633h>.
- (217) Rehn, G.; Pedersen, A. T.; Woodley, J. M. Application of NAD(P)H Oxidase for Cofactor Regeneration in Dehydrogenase Catalyzed Oxidations. *J. Mol. Catal. B Enzym.* **2016**, *134*, 331–339. <https://doi.org/10.1016/j.molcatb.2016.09.016>.

- (218) Yuan, Y.; Yuan, R.; Chai, Y.; Zhuo, Y.; Ye, X.; Gan, X.; Bai, L. Hemin/G-Quadruplex Simultaneously Acts as NADH Oxidase and HRP-Mimicking DNAzyme for Simple, Sensitive Pseudobioenzyme Electrochemical Detection of Thrombin. *Chem. Commun.* **2012**, 48 (38), 4621–4623. <https://doi.org/10.1039/c2cc31423a>.
- (219) Rodriguez-Lopez, J. N.; Hernández-Ruiz, J.; Garcia-Cánovas, F.; Thorneley, R. N. F.; Acosta, M.; Arnao, M. B. The Inactivation and Catalytic Pathways of Horseradish Peroxidase with M-Chloroperoxybenzoic Acid. A Spectrophotometric and Transient Kinetic Study. *J. Biol. Chem.* **1997**, 272 (9), 5469–5476. <https://doi.org/10.1074/jbc.272.9.5469>.
- (220) Zhao, C.; Chen, Q.; Patel, K.; Li, L.; Li, X.; Wang, Q.; Zhang, G.; Zheng, J. Synthesis and Characterization of PH-Sensitive Poly(N-2-Hydroxyethyl Acrylamide)-Acrylic Acid (Poly(HEAA/AA)) Nanogels with Antifouling Protection for Controlled Release. *Soft Matter* **2012**, 8 (30), 7848–7857. <https://doi.org/10.1039/c2sm25861g>.
- (221) Barreiro, E. C. V.; López, F. F.; Jover, A.; Meijide, F.; Rodríguez, E.; Tato, J. V. Paramagnetic Epoxy Resin. *Express Polym. Lett.* **2017**, 11 (1), 60–72. <https://doi.org/10.3144/expresspolymlett.2017.7>.
- (222) Devi, L. G.; ArunaKumari, M. L.; Anitha, B. G.; Shyamala, R.; Poornima, G. Photocatalytic Evaluation of Hemin (Chloro(Protoporphyrinato)Iron(III)) Anchored ZnO Hetero-Aggregate System under UV/Solar Light Irradiation: A Surface Modification Method. *Surfaces and Interfaces* **2016**, 1–3, 52–58. <https://doi.org/10.1016/j.surfin.2016.06.003>.
- (223) Liu, Q.; Wang, H.; Shi, X.; Wang, Z. G.; Ding, B. Self-Assembled DNA/Peptide-Based Nanoparticle Exhibiting Synergistic Enzymatic Activity. *ACS Nano* **2017**, 11 (7), 7251–7258. <https://doi.org/10.1021/acsnano.7b03195>.

- (224) Shi, H.; Liu, Y.; Qu, R.; Li, Y.; Ma, R.; An, Y.; Shi, L. A Facile One-Pot Method to Prepare Peroxidase-like Nanogel Artificial Enzymes for Highly Efficient and Controllable Catalysis. *Colloids Surfaces B Biointerfaces* **2019**, *174* (July 2018), 352–359. <https://doi.org/10.1016/j.colsurfb.2018.11.021>.
- (225) Qu, R.; Shi, H.; Wang, R.; Cheng, T.; Ma, R.; An, Y.; Shi, L. Hemin-Micelles Immobilized in Alginate Hydrogels as Artificial Enzymes with Peroxidase-like Activity and Substrate Selectivity. *Biomater. Sci.* **2017**, *5* (3), 570–577. <https://doi.org/10.1039/c6bm00813e>.
- (226) Zhang, Y.; Xu, C.; Li, B. Self-Assembly of Hemin on Carbon Nanotube as Highly Active Peroxidase Mimetic and Its Application for Biosensing. *RSC Adv.* **2013**, *3* (17), 6044–6050. <https://doi.org/10.1039/c3ra22525a>.
- (227) Qu, R.; Shen, L.; Chai, Z.; Jing, C.; Zhang, Y.; An, Y.; Shi, L. Hemin-Block Copolymer Micelle as an Artificial Peroxidase and Its Applications in Chromogenic Detection and Biocatalysis. *ACS Appl. Mater. Interfaces* **2014**, *6* (21), 19207–19216. <https://doi.org/10.1021/am505232h>.
- (228) Bisogno, F. R.; López-Vidal, M. G.; de Gonzalo, G. Organocatalysis and Biocatalysis Hand in Hand: Combining Catalysts in One-Pot Procedures. *Adv. Synth. Catal.* **2017**, *359* (12), 2026–2049. <https://doi.org/10.1002/adsc.201700158>.
- (229) Gkaniatsou, E.; Sicard, C.; Ricoux, R.; Benahmed, L.; Bourdreux, F.; Zhang, Q.; Serre, C.; Mahy, J. P.; Steunou, N. Enzyme Encapsulation in Mesoporous Metal–Organic Frameworks for Selective Biodegradation of Harmful Dye Molecules. *Angew. Chemie - Int. Ed.* **2018**, *57* (49), 16141–16146. <https://doi.org/10.1002/anie.201811327>.
- (230) Campomanes, P.; Rothlisberger, U.; Alfonso-Prieto, M.; Rovira, C. The Molecular Mechanism of the Catalase-like Activity in Horseradish Peroxidase. *J. Am. Chem. Soc.* **2015**, *137* (34), 11170–11178.

- <https://doi.org/10.1021/jacs.5b06796>.
- (231) Schmid, A.; Dordick, J. S.; Hauer, B.; Kiener, A.; Wubbolts, M.; Witholt, B. Industrial Biocatalysis Today and Tomorrow. *Nature* **2001**, *409* (6817), 258–268. <https://doi.org/10.1038/35051736>.
- (232) Ju, K.-S.; Parales, R. E. Nitroaromatic Compounds, from Synthesis to Biodegradation. *Microbiol. Mol. Biol. Rev.* **2010**, *74* (2), 250–272. <https://doi.org/10.1128/membr.00006-10>.
- (233) Van Haandel, M. J. H.; Claassens, M. M. J.; Van Der Hout, N.; Boersma, M. G.; Vervoort, J.; Rietjens, I. M. C. M. Differential Substrate Behaviour of Phenol and Aniline Derivatives during Conversion by Horseradish Peroxidase. *Biochim. Biophys. Acta - Protein Struct. Mol. Enzymol.* **1999**, *1435* (1–2), 22–29. [https://doi.org/10.1016/S0167-4838\(99\)00199-5](https://doi.org/10.1016/S0167-4838(99)00199-5).
- (234) Chiu, Y.-H.; Chang, T.-F. M.; Chen, C.-Y.; Sone, M.; Hsu, Y.-J. Mechanistic Insights into Photodegradation of Organic Dyes Using Heterostructure Photocatalysts. *Catalysts* **2019**, *9* (5), 430–462. <https://doi.org/10.3390/catal9050430>.
- (235) Lin, Y. W.; Wang, J. Structure and Function of Heme Proteins in Non-Native States: A Mini-Review. *J. Inorg. Biochem.* **2013**, *129*, 162–171. <https://doi.org/10.1016/j.jinorgbio.2013.07.023>.
- (236) Harris, A. W.; Yehezkeli, O.; Hafenstine, G. R.; Goodwin, A. P.; Cha, J. N. Light-Driven Catalytic Upgrading of Butanol in a Biohybrid Photoelectrochemical System. *ACS Sustain. Chem. Eng.* **2017**, *5* (9), 8199–8204. <https://doi.org/10.1021/acssuschemeng.7b01849>.
- (237) Petschacher, B.; Staunig, N.; Müller, M.; Schürmann, M.; Mink, D.; De Wildeman, S.; Gruber, K.; Glieder, A. Cofactor Specificity Engineering of *Streptococcus Mutans* NADH Oxidase 2 for Nad(p)⁺ Regeneration in Biocatalytic Oxidations. *Comput. Struct. Biotechnol. J.* **2014**, *9* (14), e201402005.

<https://doi.org/10.5936/csbj.201402005>.

- (238) Drenth, J.; Yang, G.; Paul, C. E.; Fraaije, M. W. A Tailor-Made Deazaflavin-Mediated Recycling System for Artificial Nicotinamide Cofactor Biomimetics. *ACS Catal.* **2021**, 11561–11569. <https://doi.org/10.1021/acscatal.1c03033>.
- (239) Paul, C. E.; Tischler, D.; Riedel, A.; Heine, T.; Itoh, N.; Hollmann, F. Nonenzymatic Regeneration of Styrene Monooxygenase for Catalysis. *ACS Catal.* **2015**, 5 (5), 2961–2965. <https://doi.org/10.1021/acscatal.5b00041>.
- (240) Brondani, P. B.; Dudek, H. M.; Martinoli, C.; Mattevi, A.; Fraaije, M. W. Finding the Switch: Turning a Baeyer-Villiger Monooxygenase into a NADPH Oxidase. *J. Am. Chem. Soc.* **2014**, 136 (49), 16966–16969. <https://doi.org/10.1021/ja508265b>.
- (241) Song, H.; Ma, C.; Wang, L.; Zhu, Z. Platinum Nanoparticle-Deposited Multi-Walled Carbon Nanotubes as a NADH Oxidase Mimic: Characterization and Applications. *Nanoscale* **2020**, 12 (37), 19284–19292. <https://doi.org/10.1039/d0nr04060f>.
- (242) Jia, H. Y.; Zong, M. H.; Zheng, G. W.; Li, N. Myoglobin-Catalyzed Efficient in Situ Regeneration of NAD(P) + and Their Synthetic Biomimetic for Dehydrogenase-Mediated Oxidations. *ACS Catal.* **2019**, 9 (3), 2196–2202. <https://doi.org/10.1021/acscatal.8b04890>.
- (243) Nowak, C.; Beer, B.; Pick, A.; Roth, T.; Lommes, P.; Sieber, V. A Water-Forming NADH Oxidase from *Lactobacillus Pentosus* Suitable for the Regeneration of Synthetic Biomimetic Cofactors. *Front. Microbiol.* **2015**, 6 (SEP), 957. <https://doi.org/10.3389/fmicb.2015.00957>.
- (244) Chen, C.; Vázquez-González, M.; O'Hagan, M. P.; Ouyang, Y.; Wang, Z.; Willner, I. Enzyme-Loaded Hemin/G-Quadruplex-Modified ZIF-90 Metal–Organic Framework Nanoparticles: Bioreactor Nanozymes for the Cascaded

- Oxidation of N -hydroxy- l -arginine and Sensing Applications. *Small* **2022**, *18* (11), 2104420. <https://doi.org/10.1002/sml.202104420>.
- (245) Santiago-Arcos, J.; Velasco-Lozano, S.; Diamanti, E.; Cortajarena, A. L.; López-Gallego, F. Immobilization Screening and Characterization of an Alcohol Dehydrogenase and Its Application to the Multi-Enzymatic Selective Oxidation of 1,-Omega-Diols. *Front. Catal.* **2021**, *1* (July), 715075. <https://doi.org/10.3389/fctls.2021.715075>.
- (246) Börner, T.; Rämisch, S.; Bartsch, S.; Vogel, A.; Adlercreutz, P.; Grey, C. Three in One: Temperature, Solvent and Catalytic Stability by Engineering the Cofactor-Binding Element of Amine Transaminase. *ChemBioChem* **2017**, *18* (15), 1482–1486. <https://doi.org/10.1002/cbic.201700236>.
- (247) Kroutil, W.; Fischereder, E.-M.; Fuchs, C. S.; Lechner, H.; Mutti, F. G.; Pressnitz, D.; Rajagopalan, A.; Sattler, J. H.; Simon, R. C.; Sirola, E. Asymmetric Preparation of Prim -, Sec -, and Tert -Amines Employing Selected Biocatalysts. *Org. Process Res. Dev.* **2013**, *17* (5), 751–759. <https://doi.org/10.1021/op4000237>.
- (248) Savile, C. K.; Janey, J. M.; Mundorff, E. C.; Moore, J. C.; Tam, S.; Jarvis, W. R.; Colbeck, J. C.; Krebber, A.; Fleitz, F. J.; Brands, J.; Devine, P. N.; Huisman, G. W.; Hughes, G. J. Biocatalytic Asymmetric Synthesis of Chiral Amines from Ketones Applied to Sitagliptin Manufacture. *Science (80-.)*. **2010**, *329* (5989), 305–309. <https://doi.org/10.1126/science.1188934>.
- (249) Martin, A. R.; Shonnard, D.; Pannuri, S.; Kamat, S. Characterization of Free and Immobilized (S)-Aminotransferase for Acetophenone Production. *Appl. Microbiol. Biotechnol.* **2007**, *76* (4), 843–851. <https://doi.org/10.1007/s00253-007-1059-9>.
- (250) Benítez-Mateos, A. I.; Contente, M. L.; Roura Padrosa, D.; Paradisi, F. Flow Biocatalysis 101: Design, Development and Applications. *React. Chem. Eng.*

- 2021, 6 (4), 599–611. <https://doi.org/10.1039/d0re00483a>.
- (251) Tamborini, L.; Fernandes, P.; Paradisi, F.; Molinari, F. Flow Bioreactors as Complementary Tools for Biocatalytic Process Intensification. *Trends Biotechnol.* **2018**, 36 (1), 73–88. <https://doi.org/10.1016/j.tibtech.2017.09.005>.
- (252) Devine, P. N.; Howard, R. M.; Kumar, R.; Thompson, M. P.; Truppo, M. D.; Turner, N. J. Extending the Application of Biocatalysis to Meet the Challenges of Drug Development. *Nat. Rev. Chem.* **2018**, 2 (12), 409–421. <https://doi.org/10.1038/s41570-018-0055-1>.
- (253) Jones, E.; McClean, K.; Housden, S.; Gasparini, G.; Archer, I. Biocatalytic Oxidase: Batch to Continuous. *Chem. Eng. Res. Des.* **2012**, 90 (6), 726–731. <https://doi.org/10.1016/j.cherd.2012.01.018>.
- (254) Geders, T. W.; Gustafson, K.; Finzel, B. C. Use of Differential Scanning Fluorimetry to Optimize the Purification and Crystallization of PLP-Dependent Enzymes. *Acta Crystallogr. Sect. F Struct. Biol. Cryst. Commun.* **2012**, 68 (5), 596–600. <https://doi.org/10.1107/S1744309112012912>.
- (255) Bradford, M. M. A Rapid and Sensitive Method for the Quantitation of Microgram Quantities of Protein Utilizing the Principle of Protein-Dye Binding. *Anal. Biochem.* **1976**, 72 (1–2), 248–254. [https://doi.org/10.1016/0003-2697\(76\)90527-3](https://doi.org/10.1016/0003-2697(76)90527-3).
- (256) Roura Padrosa, D.; Alaux, R.; Smith, P.; Dreveny, I.; López-Gallego, F.; Paradisi, F. Enhancing PLP-Binding Capacity of Class-III ω -Transaminase by Single Residue Substitution. *Front. Bioeng. Biotechnol.* **2019**, 7 (October), 282. <https://doi.org/10.3389/fbioe.2019.00282>.
- (257) Gamov, G.; Murekhina, A.; Aleksandriiskii, V. Dephosphorylation of Pyridoxal 5'-Phosphate-Derived Schiff Bases in the Presence of Bovine Alkaline Phosphatase. *Int. J. Chem. Kinet.* **2022**, 54 (1), 58–67. <https://doi.org/10.1002/kin.21541>.

- (258) Shin, J. S.; Yun, H.; Jang, J. W.; Park, I.; Kim, B. G. Purification, Characterization, and Molecular Cloning of a Novel Amine:Pyruvate Transaminase from *Vibrio Fluvialis* JS17. *Appl. Microbiol. Biotechnol.* **2003**, *61* (5–6), 463–471. <https://doi.org/10.1007/s00253-003-1250-6>.
- (259) Cerioli, L.; Planchestainer, M.; Cassidy, J.; Tessaro, D.; Paradisi, F. Characterization of a Novel Amine Transaminase from *Halomonas Elongata*. *J. Mol. Catal. B Enzym.* **2015**, *120*, 141–150. <https://doi.org/10.1016/j.molcatb.2015.07.009>.
- (260) Hwang, E. T.; Lee, S. Multienzymatic Cascade Reactions via Enzyme Complex by Immobilization. *ACS Catal.* **2019**, *9* (5), 4402–4425. <https://doi.org/10.1021/acscatal.8b04921>.
- (261) Velasco-Lozano, S.; Benítez-Mateos, A. I.; López-Gallego, F. Co-Immobilized Phosphorylated Cofactors and Enzymes as Self-Sufficient Heterogeneous Biocatalysts for Chemical Processes. *Angew. Chemie - Int. Ed.* **2017**, *56* (3), 771–775. <https://doi.org/10.1002/anie.201609758>.

